

**Development of Partial Oxidation Catalysts for the Indirect Internal Reforming (IIR) of
Methane in Solid Oxide Fuel Cells (SOFC)**

By Lois Milner-Elkharouf



**UNIVERSITY OF
BIRMINGHAM**

**A thesis submitted to
The University of Birmingham
for the degree of
DOCTOR OF PHILOSOPHY**

**School of Chemical Engineering
College of Engineering and Physical Sciences
The University of Birmingham**

March 2019

UNIVERSITY OF
BIRMINGHAM

University of Birmingham Research Archive

e-theses repository

This unpublished thesis/dissertation is copyright of the author and/or third parties. The intellectual property rights of the author or third parties in respect of this work are as defined by The Copyright Designs and Patents Act 1988 or as modified by any successor legislation.

Any use made of information contained in this thesis/dissertation must be in accordance with that legislation and must be properly acknowledged. Further distribution or reproduction in any format is prohibited without the permission of the copyright holder.

ABSTRACT

Two nickel catalysts were prepared, each adopting a silica support for different functions.

One catalyst consisted of silica spheres onto which nickel nanoparticles were anchored with nickel phyllosilicate bonds ($\text{Ni}/\text{SiO}_{2, \text{sph}}$). The other catalyst adopted a core@shell

configuration whereby nickel nanoparticles were coated in an inert silica shell ($\text{Ni}@\text{SiO}_2$).

Bare nickel nanoparticles, with no silica coating, were also prepared to assess the role of the silica shell in the $\text{Ni}@\text{SiO}_2$ system. The catalysts were characterised by electron microscopy, TGA, XRD, XPS, and surface area analysis. Performance of the catalysts for the partial oxidation of methane was assessed using a gas chromatograph. Methane conversion, and H_2 , CO, and CO_2 product yields were used as performance indicators.

Key findings of the work which add to the understanding of nickel-silica catalysts presented in literature are as follows. Increased nickel loading was shown to improve the activity of the $\text{Ni}/\text{SiO}_{2, \text{sph}}$ catalyst when the catalyst was tested at high GHSV. Nickel particle agglomeration and carbon deposition were both observed in the tested catalysts, and the extent of degradation increased with nickel loading. The SiO_2 shell was shown to be critical in preventing the re-oxidation and redox cycling of active nickel species in the $\text{Ni}@\text{SiO}_2$ system. This catalyst suffered from nickel particle agglomeration due to an incomplete SiO_2 coating. However, the catalyst resisted carbon deposition completely.

For the first time, both catalysts were incorporated into an alumina hollow fibre bundle in an attempt to demonstrate indirect internal reforming within a solid oxide fuel cell. The $\text{Ni}/\text{SiO}_{2, \text{sph}}$ catalyst readily re-oxidised on the alumina fibre thus losing its catalytic activity, whereas

the Ni@SiO₂ catalyst performed well. Indirect internal reforming by partial oxidation was demonstrated as a feasible method of producing syngas to be consumed in a solid oxide fuel cell. This is particularly of interest as the method could be applied to on-board or domestic systems, were direct internal or external reforming might not be feasible.

To my loving family,

Thank you for getting me this far.

ACKNOWLEDGEMENTS

Many thanks to my supervisors Dr. Martin Khzouz and Prof. Robert Steinberger-Wilckens for their support while conducting this work.

For TEM expertise thanks to, Dr. Julie Watts at the Nanoscale and Microscale Research Centre, University of Nottingham and Dr. Gnanavel Thirunavukkarasu at the School of Metallurgy and Materials, University of Birmingham.

For XPS services thanks to, David Morgan at the Harwell XPS facility.

Thank you to Dr. Micheal Lengden at The University of Strathclyde for his willingness to collaborate in developing a device for gas characterisation within an SOFC.

Thank you to Haokun Wang, for his assistance with preparing Ni@SiO₂ catalysts with varying levels of polyvinylpyrrolidone (PVP) during a summer research project.

I am also very grateful to Dr. Tao Li from the Li group at Imperial College London for supplying the alumina hollow fibres.

Finally, I am so grateful that this work was supported by the Engineering and Physical Sciences Research Council (EPSRC) [grant number EP/L015749/1].

CONTENTS

ABSTRACT	i
ACKNOWLEDGEMENTS	iv
LIST OF FIGURES	xi
LIST OF TABLES	xvi
LIST OF ABBREVIATIONS.....	xvii
LIST OF EQUATIONS	xix
Chapter 1: INTRODUCTION	1
1.0 Setting the Scene.....	2
1.1 Fuel Cell Technology.....	5
1.1.1 Solid Oxide Fuel Cells (SOFC)	7
1.2 Barriers to the growth of the hydrogen economy	8
1.3 Hydrogen Production Technologies	10
1.3.1 Hydrocarbon Reforming	11
1.3.2 Carbon Capture and Storage (CCS)	12
1.3.3 Hydrogen roadmaps	13
1.3.4 On-board hydrogen production	14
1.3.5 Catalysis	18
1.4 Scope of the Current Study	19
Chapter 2: LITERATURE REVIEW	20
2.1 Mechanism of Partial Oxidation	22

2.1.1	A Brief History	22
2.1.2	The Role of Support Lattice Oxygen	25
2.2	Factors Affecting Catalytic Activity.....	27
2.3	Catalyst Degradation Mechanisms.....	32
2.3.1	Carbon Deposition	32
2.3.2	Agglomeration of Metal Centres	34
2.4	Core@Shell catalysts	35
2.5	Nickel/Silica Catalysts for POx	37
2.5.1	Nickel Phyllosilicates.....	41
2.6	Coupling SOFC and H ₂ production.....	42
2.6.1	External Reforming (ER).....	43
2.6.2	Internal Reforming.....	44
2.6.2.1	Direct Internal Reforming (DIR).....	44
2.6.2.2	Indirect Internal Reforming (IIR)	46
2.6.3	Thermal Management	47
2.6.4	Integration of IIR catalyst into fuel cells	50
Chapter 3: METHODOLOGY.....		55
3.1	Catalyst Synthesis.....	56
3.1.1	Ni/SiO _{2, sph} Synthesis.....	56
3.1.2	Ni@SiO ₂ Synthesis	58
3.2	Characterisation	59

3.2.1	Imaging	59
3.2.1.1	Scanning Electron Microscopy (SEM).....	59
3.2.1.2	Transmission Electron Microscopy (TEM).....	61
3.2.2	Determination of Nickel Loading and Carbon Deposition	62
3.2.2.1	Thermogravimetric analysis (TGA)	62
3.2.3	Metallic Phase Identification	63
3.2.3.1	X-Ray Diffraction (XRD)	63
3.2.3.2	X-ray photoelectron spectroscopy (XPS).....	64
3.2.4	Surface Area Analysis.....	66
3.3	Determination of Catalytic Activity	68
3.3.1	Gas Chromatography	71
3.3.2	Nitrogen balancing and conversion calculations	74
3.4	Washcoating catalysts onto alumina fibres	75
3.5	Fuel Cell Assembly	76
Chapter 4: CHEMICAL EQUILIBRIUM ANALYSIS		79
4.1	The effect of temperature on Gibbs free energy	81
4.2	Chemical Equilibrium Analysis Results	85
4.2.1	Effect of Temperature on the Composition at Equilibrium	85
4.2.2	The effect of CH ₄ :O ₂ ratio on the equilibrium gas composition	88
4.3	Comparison with experimental data.....	91
4.4	Summary	92

Chapter 5: CATALYST CHARACTERISATION	94
5.1 Microscopy	95
5.1.1 Ni/SiO ₂ , sph	95
5.1.2 Ni@SiO ₂	99
5.2 Thermogravimetric analysis (TGA)	104
5.2.1 xNi/SiO ₂ , sph	105
5.2.2 Ni@SiO ₂	107
5.3 X-ray Diffraction (XRD)	114
5.3.1 xNi/SiO ₂ , sph	114
5.3.2 Ni@SiO ₂	116
5.4 X-ray Photoelectron Spectroscopy (XPS)	118
5.4.1 xNi/SiO ₂ , sph	118
5.4.2 Ni@SiO ₂	122
5.5 Surface Area Analysis	124
5.5.1 xNi/SiO ₂ , sph	124
5.5.2 Ni@SiO ₂	125
5.6 Summary	126
Chapter 6: CATALYTIC PERFORMANCE	128
6.1 Ni@SiO ₂ Catalyst Performance	130
6.1.1 Effect of Temperature on the Performance of Ni@SiO ₂ catalyst	130
6.1.2 Effect of CH ₄ :O ₂ Fuel Feed Ratio on the Performance of Ni@SiO ₂ catalyst	134

6.1.3	Effect of Gas Hourly Space Velocity (GHSV) on the Performance of Ni@SiO ₂ catalyst.....	137
6.1.4	Summary of testing over Ni@SiO ₂	138
6.2	Comparison of nickel nanoparticles and Ni@SiO ₂ for the POx of methane	138
6.3	xNi/SiO _{2, sph} Catalyst performance.....	144
6.3.1	Effect of Nickel loading on the performance of xNi/SiO _{2, sph} catalysts	144
6.3.2	Effect of Gas Hourly Space Velocity (GHSV) on the Performance of xNi/SiO _{2, sph} catalyst	148
6.3.3	Long term testing of xNi/SiO _{2, sph}	153
6.3.4	Summary of testing of xNi/SiO _{2, sph}	158
6.4	Comparison of Catalyst Performance between 3Ni/SiO _{2, sph} and Ni@SiO ₂	159
6.5	Summary	166
Chapter 7: ACHIEVING INDIRECT INTERNAL REFORMING IN A FUEL CELL		168
7.1	Alumina fibres	170
7.2	Washcoating.....	171
7.3	Ex-situ testing of 1Ni/SiO _{2, sph} Fibre reactor	175
7.4	Ex-situ testing of Ni@SiO ₂ Fibre reactor	181
7.5	Ni@SiO ₂ Stub Reactor	184
7.6	Fuel Cell Testing.....	186
7.6.1	Long term testing on fuel cells	188
7.7	In-stream Gas Analysis	191

7.8	Summary	193
Chapter 8: CONCLUSIONS		195
8.1	Further Work	199
APPENDICES		201
Appendix A - Calculation of Gibbs Free Energy of Partial Oxidation Reaction.....		201
Appendix B - Gibbs Free Energy Diagrams		202
Appendix C - Split Ratio		203
Appendix D - Column Flow Rate.....		204
Appendix E - Column Temperature Profile		205
Appendix F - Detector Current		208
Appendix G - Identification of GC peaks		209
Appendix H		210
Appendix I - Product yields of the regeneration cycles of 1Ni/SiO _{2, sph} fibre bundle.		211

LIST OF FIGURES

Figure 1: The Energy Trilemma.....	3
Figure 2: The increasing market share of renewables in the electrical energy sector in the UK [10,11].	3
Figure 3: Energy demand for electricity (red), transport (grey) and natural gas (blue) [12].	4
Figure 4: Solid Oxide Fuel Cell Operation.	7
Figure 5: Overview of hydrogen production pathways [10]	10
Figure 6: Roadmap for Hydrogen Production [49].	13
Figure 7: Isotopic study of ^{18}O labelled Rh/zirconia-doped ceria used in partial oxidation [20].	27
Figure 8: Left, variation in methane conversion with catalyst bed temperature. Right, reducibility of different $\text{Ni/Ce}_x\text{Zr}_{1-x}\text{O}_2$ catalysts, a. $x=0$, b. $x=0.25$, c. $x=0.5$, d. $x=0.75$, e. $x=1.0$ [97].	30
Figure 9: Ranging CH_4/O_2 ratio in order to determine the effect on; Top left: CH_4 conversion. Bottom left: CO selectivity. Top right: Bed exit temperature. Bottom right: H_2 selectivity [121].	31
Figure 10: Effect of feed flow rate on catalytic performance; Left: CH_4 conversion and bed exit temperature. Right: CO / H_2 selectivity [122].	31
Figure 11: Particle size of coated and uncoated catalyst before and after testing [122].	34
Figure 12: Schematic for Core@Shell particle synthesis [135]	36
Figure 13: Structure of 1:1 and 2:1 nickel phyllosilicates [147].	42
Figure 14: System diagram of an external reforming SOFC system [156].	44
Figure 15: Schematic of A. Planar [161] and B. Tubular SOFC configurations both with indirect internal reforming incorporated.	46
Figure 16: Cross-sections of tubular reformers with different catalyst configurations.	51
Figure 17: XPS survey scan of Ni@SiO_2	65
Figure 18: High resolution XPS in the Ni 2P region	65
Figure 19: The origin of peak shapes in XPS	66
Figure 20: The different possible shapes of hysteresis loops [182].	68
Figure 21: Schematic of Gas Chromatography System	72
Figure 22: A. Washcoating apparatus B. Application of back pressure.	76
Figure 23: Assembled fuel cell ready to test.	78
Figure 24: Gibbs free energy of possible reactions occurring during partial oxidation. Zoomed in versions can be found in Appendix B.	83
Figure 25: Gibbs free energy of carbon deposition and removal reactions.	84
Figure 26: Change in enthalpy of partial oxidation with temperature. $\text{CH}_4:\text{O}_2$ ratio = 2, pressure = 1 atm.	85
Figure 27: Effect of temperature on the equilibrium conversion of methane to syngas via partial oxidation	86

Figure 28: Effect of temperature on the CH ₄ conversion, CO ₂ , CO and H ₂ yield for the partial oxidation of methane.....	88
Figure 29: The effect of CH ₄ :O ₂ ratio on methane conversion at different temperatures	89
Figure 30A: Effect of CH ₄ :O ₂ ratio on H ₂ at different temperatures. B: expanded view of the 650°C data.	89
Figure 31: The effect of CH ₄ :O ₂ ratio on equilibrium A. CO and B. CO ₂ yields, at different temperatures.....	91
Figure 32: Equilibrium gas composition at (a) high, (b) stoichiometric and (c) low CH ₄ :O ₂ ratios.....	91
Figure 33: Equilibrium values of CH ₄ conversion and product yield with A. varying temperature B. varying CH ₄ :O ₂ ratio.....	92
Figure 34A-E: SEM micrographs of SiO ₂ batches 1 to 5, respectively F-J: particle size distribution of SiO ₂ batches 1 to 5, respectively.....	97
Figure 35: TEM images of unreduced (1-3)Ni/SiO _{2, sph} respectively, showing whisker like Ni phyllosilicate structures.	98
Figure 36A-C: TEM images of reduced (1-3)Ni/SiO _{2, sph} respectively, a few Ni phyllosilicate structures remain.	98
Figure 37: Increased nickel particle size with increased nickel loading due to lower metal particle dispersion.	99
Figure 38: A-D: TEM micrographs of NiO cores, batches 1 to 4, respectively. E-H: particle size distribution of NiO batches 1 to 4, respectively.	100
Figure 39: TEM images of Ni@SiO ₂ at different magnifications, before reduction.	102
Figure 40: TEM images of reduced Ni@SiO ₂ . Sample was subjected to reduction under 25% H ₂ /N ₂ at 700°C overnight.	104
Figure 41: Typical TGA spectra.	105
Figure 42: TGA results of xNi/SiO _{2, sph} catalysts.....	106
Figure 43: TGA results of uncoated SiO ₂ under reducing conditions.....	107
Figure 44: TGA profiles of Ni@SiO ₂ catalyst and 3Ni/SiO _{2, sph} catalyst.....	108
Figure 45: Results of TGA, BET and TEM analysis of Ni@SiO ₂ when synthesised with full, half and zero PVP.	112
Figure 46: TGA profile of NiO under reducing conditions.	114
Figure 47: XRD analysis of fresh Ni/SiO _{2, sph}	115
Figure 48: XRD analysis of reduced Ni/SiO _{2, sph}	115
Figure 49: XRD spectra of fresh and reduced NiO.....	116
Figure 50: XRD patterns of fresh and reduced NiO@SiO ₂	117
Figure 51: A. XPS survey spectrum of xNi/SiO _{2, sph} catalysts as synthesised. B. Ni 2P 3/2 region with background subtracted.	118
Figure 52: Fitted xNi/SiO _{2, sph} XPS data, Ni 2P 3/2 region.....	120
Figure 53: Reduced xNi/SiO _{2, sph} XPS data, Ni 2P 3/2 region.	121
Figure 54: XPS of fresh Ni@SiO ₂	122

Figure 55: Ni 2P 3/2 peak of reduced Ni@SiO ₂ .	123
Figure 56: BET isotherms of A. 2Ni/SiO _{2, sph} and B. 3Ni/SiO _{2, sph}	124
Figure 57: BET isotherms of fresh and reduced Ni@SiO ₂	126
Figure 58: Effect of Temperature on Ni@SiO ₂ Performance.	131
Figure 59: Average performance of Ni@SiO ₂ with Increasing Temperature	132
Figure 60: Difference in the temperature recorded near to the catalyst surface and the set furnace temperature with increasing furnace temperature.	134
Figure 61: Effect of CH ₄ : x O ₂ ratio on A. catalyst performance and B. reactor temperature.	134
Figure 62: Effect of GHSV on catalyst performance recorded at a constant temperature of 750°C and a CH ₄ :O ₂ ratio of 2.....	137
Figure 63: Comparing the catalytic performance of Ni and Ni@SiO ₂ in terms of A. methane conversion and B-C. H ₂ , CO and CO ₂ yield when tested under partial oxidation conditions at different temperatures. 5B shows results from Ni@SiO ₂ whereas 5C. shows results from uncoated Ni.	139
Figure 64: Partial oxidation proceeding over multiple oxidation states of nickel. Image taken from Ding et al. [95]	139
Figure 65: XRD of reduced and tested uncoated Ni nanoparticles.	140
Figure 66: Redox cycling of nickel when tested for partial oxidation.	142
Figure 67: XRD of reduced and tested Ni@SiO ₂ .	144
Figure 68: Effect of Temperature on (1-3)Ni/SiO _{2, sph} catalyst performance. Tested at a CH ₄ :O ₂ ratio of 2 and a GHSV of 80640 ml g ⁻¹ h ⁻¹	146
Figure 69: Effect of CH ₄ :O ₂ ratio on (1-3)Ni/SiO _{2, sph} catalyst performance. Tested at 750°C and a GHSV of 80640 ml g ⁻¹ h ⁻¹	147
Figure 70: Effect of nickel loading in xNi/SiO _{2, sph} and GHSV on selectivity towards syngas production in the GHSV range 80640 to 214920 ml g ⁻¹ h ⁻¹	148
Figure 71: Effect of nickel loading in xNi/SiO _{2, sph} and GHSV on selectivity towards syngas production in the GHSV range 80640-1705714 ml g ⁻¹ h ⁻¹	151
Figure 72: Effect of Ni loading on CO ₂ yield when (1-3)Ni/SiO _{2, sph} catalysts were tested over a large range of GHSV.	152
Figure 73: Long term stability of xNi/SiO _{2, sph} catalysts tested at 750°C, a CH ₄ :O ₂ ratio of 2 and a GHSV of 80640 ml g ⁻¹ h ⁻¹	154
Figure 74: A. TEM, and B. EDS of tested xNi/SiO _{2, sph} .	154
Figure 75: A. C1s peak from the XPS of tested (1-3)Ni/SiO _{2, sph} catalysts and B. TGA of tested (1-3)Ni/SiO _{2, sph} ; the mass loss at 525°C resulted from carbon oxidation [214].	156
Figure 76: Particle size distribution for reduced and tested (1-3)Ni/SiO _{2, sph} catalysts respectively.	157
Figure 77: Comparison of 1Ni/SiO _{2, sph} and Ni@SiO ₂ catalysts in experiments where A. temperature, and B. CH ₄ :O ₂ ratio was varied.	160
Figure 78: Comparison of 3Ni/SiO _{2, sph} and Ni@SiO ₂ catalyst with varied GHSV	161

Figure 79: Long term stability of 3Ni/SiO _{2, sph} and Ni@SiO ₂ catalysts tested at 750°C, a CH ₄ :O ₂ ratio of 2 and a GHSV of 80640 ml g ⁻¹ h ⁻¹	162
Figure 80: A-B TEM of Ni@SiO ₂ and particle size distributions of C. coated and D. uncoated nickel particles.....	164
Figure 81: BET of fresh, reduced and tested Ni@SiO ₂	164
Figure 82: A. TGA and B. XPS of the tested Ni@SiO ₂ catalyst.	165
Figure 83: Long term testing of Ni@SiO ₂ and 3Ni/SiO _{2, sph} at high GHSV.....	165
Figure 84: Alumina fibre showing dimensions and SEM of cross section.	170
Figure 85: Effect of washcoat circulation duration and circulation speed on catalyst loading.	171
Figure 86: Effect of applying back pressure to catalyst loading of alumina fibre.	172
Figure 87: SEM/EDS of washcoated alumina fibre.	173
Figure 88: high magnification SEM/EDS of coated alumina fibre.	174
Figure 89: Assembled fibre bundle reactor.	175
Figure 90: Photographs of fibre reactors held in quartz tubes and showing the position of thermocouple.....	176
Figure 91: Effect of temperature on 1Ni/SiO _{2, sph} catalyst performance in A. Fibre bundle reactor and B. Fixed bed reactor.....	177
Figure 92: Immediately testing 1Ni/SiO _{2, sph} fibre bundle at 750°C, and a CH ₄ :O ₂ = 2.....	178
Figure 93: 1Ni/SiO _{2, sph} fibre reactor tested at 750°C, CH ₄ :O ₂ = 2.5	179
Figure 94: Regenerating the 1Ni/SiO _{2, sph} fibre reactor by in-situ reduction.	180
Figure 95: Temperature profiles of cycle 1 and 2 of the catalyst regeneration experiment.	180
Figure 96: Ni@SiO ₂ fibre bundle tested at 750°C, CH ₄ :O ₂ = 2.5 GHSV = ml g ⁻¹ h ⁻¹	182
Figure 97: Ni@SiO ₂ fibre reactor showing results after the gas composition was changed to a CH ₄ :O ₂ ratio of 2.	182
Figure 98: Disintegrated Ni@SiO ₂ fibre after testing.	183
Figure 99: SEM of tested fibres showing carbon deposition on the alumina fibre.....	183
Figure 100: Ultra Electronics Ni/YSZ/YSZ/SDC/LSCF tubular fuel cells.....	184
Figure 101: Stub reactor arrangement. Left: Alumina fibre next to the stub Middle: Alumina fibre positioned within the stub Right: Stub reactor in position in the furnace with a thermocouple in place.	185
Figure 102: Comparison of different reactors all testing the Ni@SiO ₂ catalyst at 750°C, CH ₄ :O ₂ = 2 and GHSV approx. 80640 ml g ⁻¹ h ⁻¹	185
Figure 103: Fuel cell operating on H ₂ . IV curve recorded at the start of the experiment and 24 hours later.	186
Figure 104: Increase in maximum power density when the fuel feeds are switched from H ₂ to POx reactants.	187
Figure 105: Fuel cell tested on reformed methane over the course of 48 hours.	187
Figure 106: Alumina fibre reactor removed from the fuel cell after testing.	188
Figure 107: Cell testing under methane, cell death occurred after only 22 hours	189

Figure 108: Fuel cell which has been tested on methane. Left: fuel cell fractured away from the manifold Right: blocked fuel cell tube due to carbon deposition.	189
Figure 109: Long term fuel cell testing on reformed methane.	190
Figure 110: Daily IV curves recorded on fuel cell operated on reformed methane.	190
Figure 111: Initial design of the laser absorption spectroscopy device for determining the composition of gases between the reformer and fuel cell.	192
Figure 112: First attempt at building the gas cell.	192
Figure 113: Effect of temperature on the Gibbs free energy of reactions.	202
Figure 114: Effects of varying split ratio on GC spectrum	203
Figure 115: The effect of column flow rate on GC spectrums flow rates are given in ml.min ⁻¹	204
Figure 116: Effect of initial column temperature on GC spectrums.	206
Figure 117: Effects of Final Column Temperature on GC Spectrums.	207
Figure 118: Detector operation limits	208
Figure 119: Effect of Detector Current on GC Spectrums. Detector currents are given in mA.	208
Figure 120: Spectra from individually sampling each gas in order to obtain the retention time.	209
Figure 121: Catalytic activity of SiO ₂ for partial oxidation of methane.	210
Figure 122: Regeneration of 1Ni/SiO _{2, sph} Fibre bundle showing product yields.	211

LIST OF TABLES

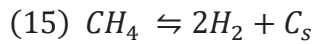
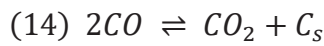
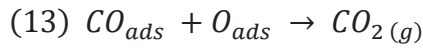
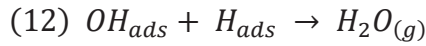
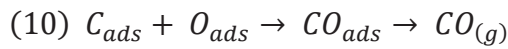
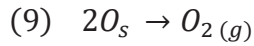
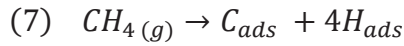
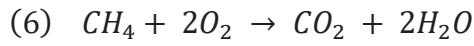
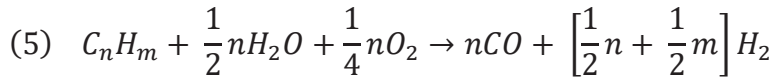
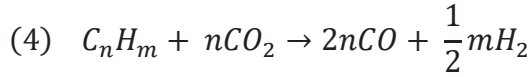
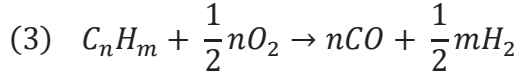
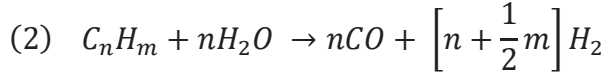
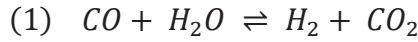
Table 1: Types of Fuel Cell and their Applications [21].	6
Table 2: Comparison of the costs of different hydrogen production processes.	14
Table 3: Advantages and Disadvantage of Different Fuels Reformed in On-board Systems.	17
Table 4: State of current research regarding available anode materials for direct hydrocarbon utilisation [156].	45
Table 5: Advantages and disadvantages of different reforming strategies for SOFC.	47
Table 6: Fundamental difference between different IIR-SOFC systems.	51
Table 7: Volumes of reactants used	57
Table 8: Classification of hysteresis loops [182].	68
Table 9: Flow rates used to test the effect of CH ₄ :O ₂ ratio on catalyst performance.	69
Table 10: Tested gas hourly space velocities.	70
Table 11: GC Method Parameters	73
Table 12: Thermodynamic values of species of interest [181]	81
Table 13: Possible reactions taking place during partial oxidation	82
Table 14: Particle size of SiO ₂ cores.	96
Table 15: Particle size of NiO cores	100
Table 16: Summary of NiO particle size and shell thickness before and after reduction	103
Table 17: Nickel loading of xNi/SiO _{2, sph} catalysts.	106
Table 18: Reported temperatures for the reduction of nickel species supported on silica.	110
Table 19: Effect of varying PVP concentration in Ni@SiO ₂ synthesis	112
Table 20: Ni content at the surface of xNi/SiO _{2, sph} catalysts, measured with XPS	118
Table 21: Oxidation state of Ni species present in xNi/SiO _{2, sph} catalysts after reduction	122
Table 22: Composition of nickel species, determined by XPS, in reduced Ni@SiO ₂ catalyst.	123
Table 23: BET surface area (m ² /g) of fresh, reduced and tested xNi/SiO _{2, sph} catalysts.	124
Table 24: BET surface area (m ² /g) of fresh, reduced, and tested Ni@SiO ₂ catalyst.	125
Table 25: Summary of catalyst physical properties.	127
Table 26: The average Ni particle size of the xNi/SiO _{2, sph} catalysts before, and after testing.	157
Table 27: Range of experiments carried out to determine the effect of back pressure on catalyst loading.	172

LIST OF ABBREVIATIONS

PEFC	Polymer Electrolyte Fuel Cell
AFC	Alkaline Fuel Cell
SOFC	Solid Oxide Fuel Cell
DMFC	Direct Methanol Fuel Cell
MCFC	Molten Carbonate Fuel Cell
PAFC	Phosphoric Acid Fuel Cell
SR	Steam Reforming
POx	Partial Oxidation
DR	Dry Reforming
ATR	Autothermal Reforming
CCS	Carbon Capture and Storage
ICE	Internal Combustion Engine
IIR	Indirect Internal Reforming
DIR	Direct Internal Reforming
Syngas	Synthesis Gas ($\text{CO} + \text{H}_2$)
SMR	Steam Methane Reforming
YSZ	Yttrium Stabilized Zirconia
TPR	Temperature Programmed Reduction
MSI	Metal Support Interaction
PVP	Poly-(vinylpyrrolidone)
Ni-PS	Nickel Phyllosilicate
ER	External Reforming
BoP	Balance of Plant
SEM	Scanning Electron Microscopy
TEM	Transmission Electron Microscopy
TGA	Thermogravimetric Analysis
XRD	X-ray Diffraction
XPS	X-ray Photoelectron Spectroscopy
EtOH	Ethanol
TEOS	Tetra Ethyl Orthosilicate
EDS	Energy Dispersive Spectroscopy
BET	Brunauer-Emmett-Teller
GHSV	Gas Hourly Space Velocity
GC	Gas Chromatography
WGS	Water Gas Shift
HTSR	High Temperature Steam Reforming
RCG	Reverse Coal Gas
SDC	Samarium Doped Ceria
LSFC	Lanthanum Strontium Ferrite Chromium
CEA	Chemical Equilibrium Analysis
ΔG	Gibbs Free Energy
ΔH	Change in Enthalpy
ΔS	Change in Entropy

Comb.	Combustion
CH ₄ Ox.	Methane Oxidation
CO Ox.	Carbon Monoxide Oxidation
H ₂ Ox.	Hydrogen Oxidation
Meth.	Methanation
C _s Ox.	Carbon Oxidation
C _s Ox. (2)	Carbon Oxidation (2)
ICDD	International Centre for Diffraction Data

LIST OF EQUATIONS



$$(16) \quad Y = -1.08(X_1 - 25) + 216.43(X_2 - 0.25) + 12.52(X_3 - 3.95) + 42$$

$$(17) \quad \text{moles} = \frac{\text{mass}}{\text{relative molecular weight (Mr)}}$$

$$(18) \quad \text{Nickel weight \%} = \frac{\text{weight of nickel in sample}}{\text{weight of sample}} \times 100$$

$$(19) \quad \tau = \frac{K\lambda}{\beta \cos \theta}$$

$$(20) \frac{1}{\left[V_a \left(\frac{P_0}{P} - 1\right)\right]} = \frac{C - 1}{V_m C} \times \frac{P}{P_0} + \frac{1}{V_m C}$$

$$(21) n_{total,out}(moles) = \frac{n_{N_2,in}(moles)}{\gamma_{N_2,out}}$$

$$(22) n_{x,out}(moles) = n_{total,out}(moles) \times \gamma_x$$

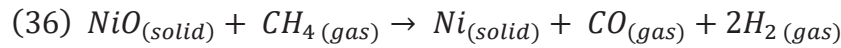
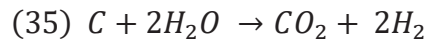
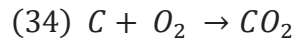
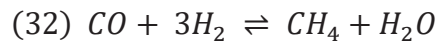
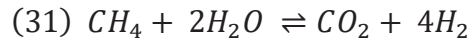
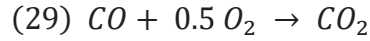
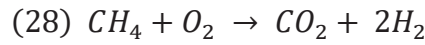
$$(23) CH_4 \text{ conversion } (\%) = \frac{n_{CH_4,in}(moles) - n_{CH_4,out}(moles)}{n_{CH_4,in}(moles)} \times 100$$

$$(24) H_2 \text{ product yield} = \frac{n_{H_2,out}(moles)}{n_{CH_4,in}(moles)}$$

$$(25) CO \text{ product yield} = \frac{n_{CO,out}(moles)}{n_{CH_4,in}(moles)}$$

$$(26) CO_2 \text{ product yield} = \frac{n_{CO_2,out}(moles)}{n_{CH_4,in}(moles)}$$

$$(27) \Delta G (kJ.mol^{-1}) = \Delta H (kJ.mol^{-1}) - T(K)\Delta S (J.K^{-1}.mol^{-1})$$



Chapter 1

INTRODUCTION

1.0	Setting the Scene.....	2
1.1	Fuel Cell Technology.....	5
1.1.1	Solid Oxide Fuel Cells (SOFC).....	7
1.2	Barriers to the growth of the hydrogen economy	8
1.3	Hydrogen Production Technologies.....	10
1.3.1	Hydrocarbon Reforming.....	11
1.3.2	Carbon Capture and Storage (CCS)	12
1.3.3	Hydrogen roadmaps.....	13
1.3.4	On-board hydrogen production	14
1.4	Scope of the Current Study	19

1.0 Setting the Scene

Global primary energy use increased from 1403 to 1921 kg of oil equivalent per capita in the period from 1984 to 2014 [1] and the trend is predicted to continue [2]. This along with the decline of fossil fuel sources [3], is one argument for research into alternative energy generation methods. A second argument is energy security and the potential for international conflict created by a minority of nations controlling the majority of fossil fuel supplies worldwide [4,5]. The third argument in the trio, Figure 1, focuses on the need for preventing a rise in global temperatures which are directly correlated to the concentration of atmospheric greenhouse gasses [6]. Incumbent methods of energy generation from fossil fuels release large amounts of green-house gases to the atmosphere. If this continues, global temperatures will continue to rise causing further climate change and resulting in a more hostile environment for the population of the earth to live in.

In 2015, the Paris Agreement was reached with a goal of mitigating the adverse effects of energy generation on the global climate [7]. It aimed at holding global temperatures well below 2°C more than pre-industrial revolution levels. This further drives a desire for alternative fuels. A more recent environmental driver for change has come in the form of a desire for improving air quality in cities, to promote better public health [8,9].

In response to the energy trilemma, Figure 1, there is a growing market for renewable electricity. In recent years solar and, particularly in the UK, wind energy industries have boomed and renewable electricity has continued to gain a larger market share. In the UK, 33.1% of the electricity generated in quarter 3 of 2018 was from renewable sources. That

value was up from 30.0% the previous year [10], and from 13.6% compared to 2013 [11],
Figure 2.

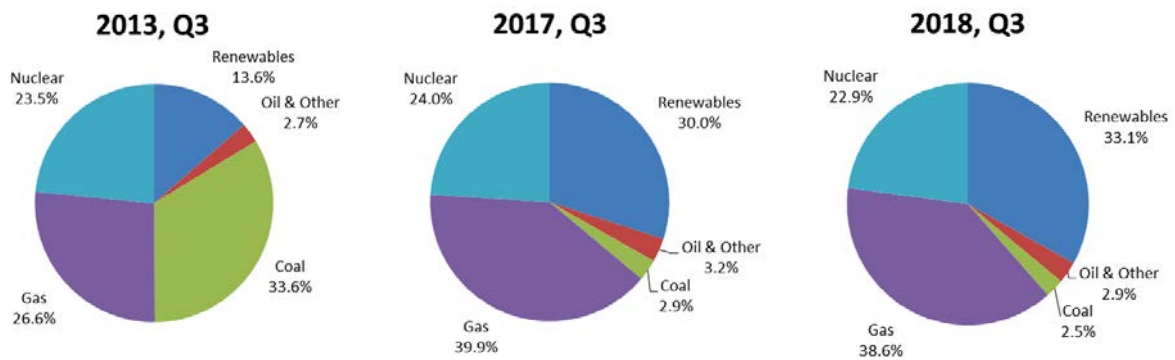
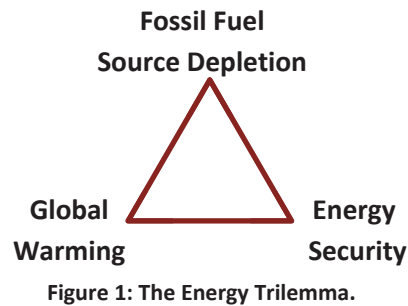


Figure 2: The increasing market share of renewables in the electrical energy sector in the UK [10,11].

With an increasing reliance on renewable electricity, energy storage becomes an issue. Due to the intermittency of renewable energy sources, sufficient energy storage must be in place to meet the energy demand at a time when there is insufficient renewable energy generation.

Additionally, decarbonising heat also remains a problem. The UK predominantly relies on natural gas for domestic heating. Figure 3 shows the demand profile for electricity, transport, and natural gas from 2014 to 2017 [12]. It is evident that the transport and electricity sectors both have relatively stable energy demands across the year. However, natural gas demand is highly volatile. In addition, the scale of the problem is much larger, at

the peak of natural gas demand, four times the amount of energy can be required for heating than is needed for electricity.

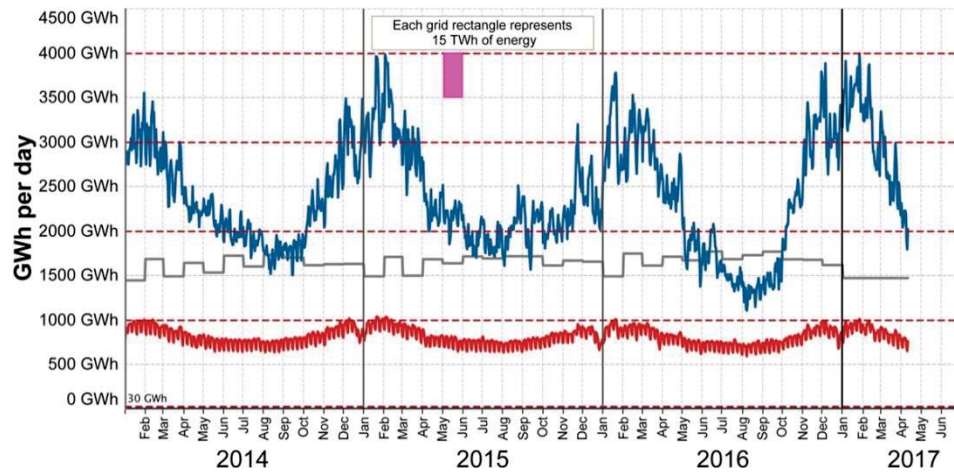


Figure 3: Energy demand for electricity (red), transport (grey) and natural gas (blue) [12].

The natural gas infrastructure contains an inherent storage capacity since gas in the pipeline can be pressurised during times of low demand, in preparation for times of high demand. Decarbonising heat proves to be an incredibly difficult task due to the fluctuating daily and annual demands and the resulting requirement for energy storage. Innovative solutions to heating homes in the UK whilst lowering their carbon footprint include improving the thermal efficiency of homes by insulating them more thoroughly, electrifying heat sources e.g. using heat pumps or using zero carbon gases for heating such as hydrogen [13]. The only method of storing energy mentioned in the UK governments Clean Growth Strategy [13] is to use batteries to store renewable electricity. Alternative methods of energy storage include thermal, pumped hydro power, compressed air, and flywheel systems. An in depth explanation of these technologies is given by Crawley et al. [14].

Hydrogen has the potential to contribute towards a low carbon society, having the potential to combat both the issues of energy storage, and heat decarbonisation. It shows promise as an effective alternative fuel and is projected to play a major role in the future energy sector

[15]. The term “hydrogen economy” is widely used across literature relating to hydrogen production, fuel cells and lowering global CO₂ emissions. It was first coined by scientist John Bockris in the 1970’s. The hydrogen economy was first conceived due to a speculation that it would be more cost effective to transport energy as hydrogen in pipes rather than as electricity in wires [16]. It was later reinvented as a method to provide energy security during the first oil crisis and later, after growing concerns over global warming, the hydrogen economy would lower CO₂ emissions [17]. After so many reinventions Moliner, Lazaro, and Suelves deem the hydrogen economy as no one’s, “‘first choice’ but rather a response forced by environmental and supplying concerns” [17]. It is somewhat reassuring, as a supporter of hydrogen, to think of the hydrogen economy as being an essential inevitability [18].

Hydrogen offers a method of storing renewable electricity for long periods of time.

Hydrogen can be transported between locations with high renewable electricity generation capacity, and those with high demand. Hydrogen even offers a method of part-decarbonising heat with the option of injecting portions of hydrogen into the natural gas grid, thus reducing the release of CO₂ when it is burnt. [19,20]. Fully converting the gas grid to hydrogen and upgrading appliances to operate on this composition is also being investigated in the UK [21]. Hydrogen has the added advantage of being a clean fuel at the point of use. Burning hydrogen or consuming hydrogen in a fuel cell produces only water vapour at the point of consumption, meaning that hydrogen energy can contribute to cleaner cities [22] with zero risk of carbon monoxide poisoning.

1.1 Fuel Cell Technology

Fuel cells are electrochemical energy conversion devices. They are composed of two electrodes (anode and cathode), and an electrolyte. Oxidation reactions take place at the

anode while reduction reactions simultaneously take place at the cathode. The electrolyte is conductive for specific ions. Ionic species combine with each other at either the anode or cathode, depending on the type of fuel cell, to create the products of an electrochemical reaction. The electrolytes are electrically insulating, this means that electrons released during the oxidation reaction at the anode are prevented from passing through the electrolyte. Electrons are driven through an external circuit, delivering electricity from the chemical energy stored in the fuel.

There are several types of fuel cell which operate at different temperatures and meet the requirements of different applications, Table 1 [23]. Typically they are named after the electrolyte which is used.

Table 1: Types of Fuel Cell and their Applications [21].

Name	Acronym	Temperature range/ °C	Efficiency/%	Fuel	Application
Polymer Electrolyte Fuel Cell	PEFC	50-100 Typically 80	60	H ₂ 99.999% purity	Transport Portable power Backup power
Alkaline Fuel Cell	AFC	90-100	60	H ₂	Backup power Transport
Solid Oxide Fuel Cell	SOFC	700-1000	60	H ₂ , CH ₄ , CO, CO ₂	Stationary power Auxiliary power Portable power Transport
Direct Methanol Fuel Cell	DMFC	40-80	20-40	CH ₃ OH	Portable power
Molten Carbonate Fuel Cell	MCFC	600-700	45-50	H ₂ + CO	Stationary power
Phosphoric Acid Fuel Cell	PAFC	150-200	40	H ₂	Stationary power CHP

1.1.1 Solid Oxide Fuel Cells (SOFC)

Solid Oxide Fuel Cells (SOFC) were first proposed in 1890 by Walter Nernst who discovered the ability of stabilised zirconia to conduct ions at high temperatures (600°C -1000°C) [24]. The first SOFC stack followed in the 1930s, made by Baur and Preis [25]. The key principle behind SOFC is that the solid ceramic electrolyte conducts oxide ions whilst remaining electrically insulating. This means that oxide ions are free to cross the electrolyte, from the cathode to the anode, in order to combine with hydrogen ions at the anode. Electrons released from the oxidation of hydrogen or carbon monoxide at the anode, are forced to move around an external circuit, creating current and allowing for reduction of oxygen gas to oxide ions at the cathode.

The high temperature operation of SOFC make them capable of utilising non-hydrogen fuels. As depicted in Figure 4, SOFC are capable of electrochemically oxidising carbon monoxide. This is significant since carbon monoxide is a poison for the catalysts of PEFC. Hydrogen produced to fuel SOFC is therefore not required to be as pure.

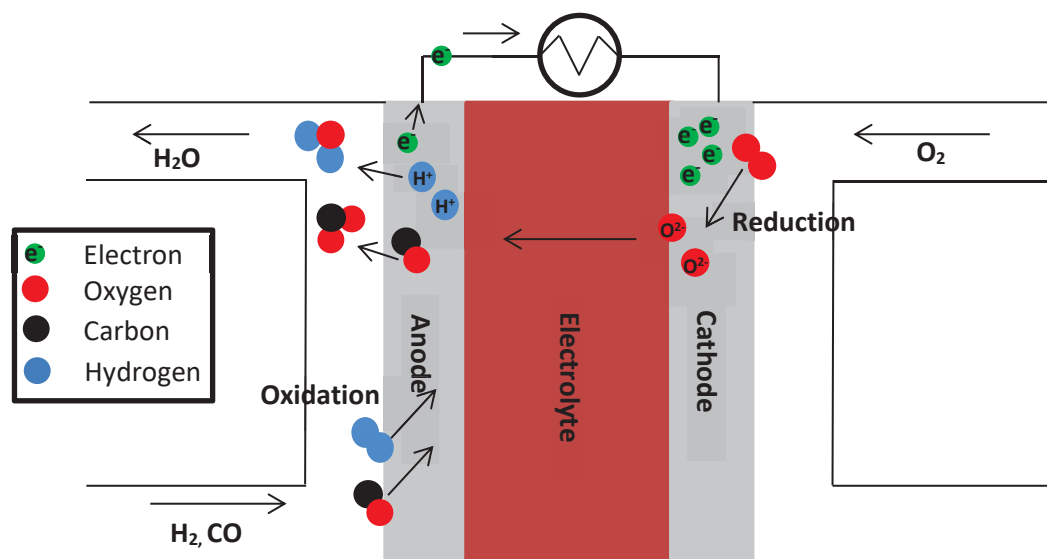


Figure 4: Solid Oxide Fuel Cell Operation.

1.2 Barriers to the growth of the hydrogen economy

The barriers to a hydrogen economy are widely discussed in literature [18,26–38]. Therefore the challenges being faced will not be discussed, in detail, here. However, to give context to the remainder of this thesis the barriers to a hydrogen economy given in literature will be briefly listed. Due reference is given below to papers which discuss specific research challenges not commonly listed in literature.

- Cost: many aspects of the hydrogen economy (green hydrogen production, distribution, and use) face the issue of a lack of economy of scale. A high cost due to specialist materials, and high labour costs due to a lack of mass production reduces the incentive for investment in the technology.
- Chicken vs egg: There is a first mover disadvantage in the transport sector. If infrastructure is first deployed the stations will be underutilised due to a lack of vehicles on the road. If the vehicles come first, there would be a negative consumer experience, due to the limited number of refuelling stations, which could deter future buyers. A lack of policy to reassure investors prevents early growth.
- On-board storage of hydrogen: Hydrogen suffers from a low volumetric energy density. Whilst containing 2.6 times the amount of energy per unit mass, compared to incumbent transportation fuels, hydrogen takes up 4 times the amount of space [39]. Currently, commercial vehicles such as the Hyundai ix35 Fuel Cell [40] and the Toyota Mirai [41] both use compressed hydrogen, stored at 700 bar. However, Gray published concerns that compressed gas will not go far enough to meet the DOE targets on volumetric density, needing to compress the hydrogen to 2550 bar to meet the 2015 target of 81 kg m^{-3} [36].

- A lack of hydrogen infrastructure both in production and distribution. This is coupled with a lack of codes and standards regarding infrastructure.
- Safety: Whilst people acknowledge that hydrogen will be put through stringent tests and will not be commercialised until it is deemed safe, there remains the concern of an explosion due to high profile cases such as the Hindenburg disaster and the hydrogen bomb [42].
- Lock in effect: Hydrogen is competing with established technologies which have “locked” the consumer and some governments into a way of thinking about energy and where it comes from, leading to an “industrial inertia”. Established energy sales are also independent of external costs such as the cost of pollution for the National Health Service. This does not help the economic case for alternatives.
- Environmental impact: the vast majority of hydrogen currently produced is sourced from fossil fuels. Technologies to decarbonise hydrogen production come at an additional cost. The whole system efficiency of a hydrogen based economy could be very low [43]. Low temperature fuel cells (PEFC) require the use of platinum catalyst, a rare earth metal. We could be moving from a dependency on fossil fuels to a dependency on equally finite resources of platinum [44]. Supply security is also an issue with 80% of the worlds platinum resources located in South Africa.
- No strong selling point for fuel cell vehicles: something more is needed than a fuel cell vehicle just being “cleaner” [27].
- Performance, durability and reliability of fuel cells have room for improvement.
- Lack of Policy: A coordinated societal effort is needed which encompasses many different stakeholders and supply chains.

- Lack of operating experience across the hydrogen supply and use chain and a lack of education in these areas.

1.3 Hydrogen Production Technologies

Hydrogen is an energy carrier. Similar to electricity it is not an energy source and therefore, it must be produced in order to be utilised. Hydrogen can be produced in a number of ways from a variety of sources, each method having a different impact on the environment. Recent studies have shown that there could be natural sources of hydrogen under large continents [45], but this is a very fledgling area of investigation. Hydrogen production methodology is well reviewed in literature. The reader is referred to reviews by Dincer and Acar [46], Nikolaidis and Poullikkas [47], and Hosseini and Wahid [48]. A summary of hydrogen production pathways is given in Figure 5 [49]. The green colour indicates pathways with the potential to not increase atmospheric greenhouse gas concentrations.

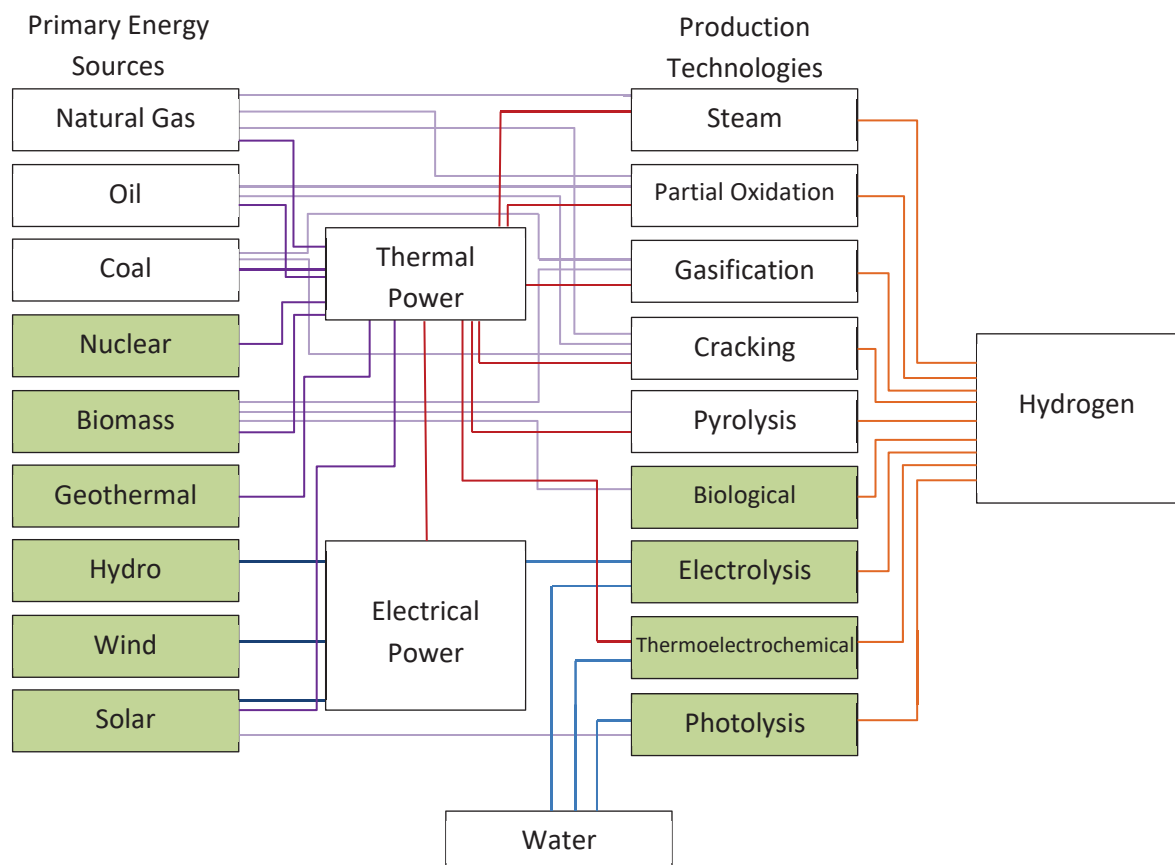


Figure 5: Overview of hydrogen production pathways [47]

The emissions generated during hydrogen production must not be underestimated if hydrogen is to be a positive addition to the energy system. Figure 6 shows the global warming potential of several routes towards hydrogen [50]. Currently, around 95% of hydrogen produced, comes from fossil fuel-based methods [48]. This is deemed a necessary evil in order to reap the long-term carbon emission reductions possible by decarbonisation of hydrogen production. The way in which hydrogen is produced will therefore change with time. Hydrogen from fossil fuels and biofuels with carbon capture and storage are described in sections 1.3.1 - 1.3.3 as bridging fuels towards a hydrogen economy and a low carbon future.

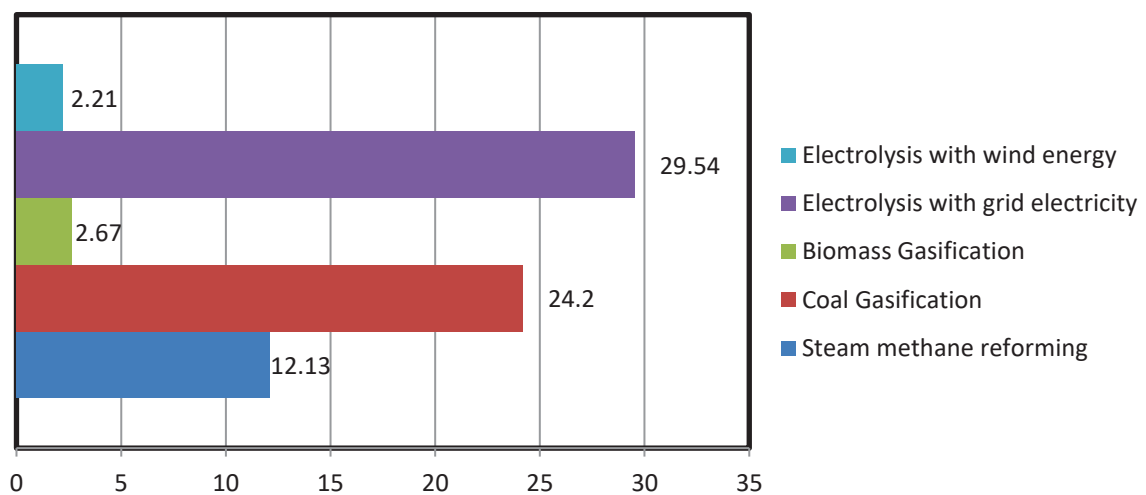
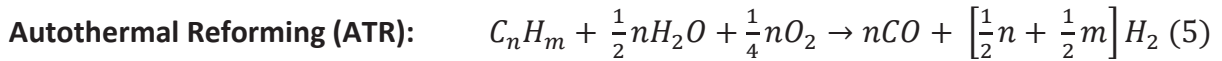
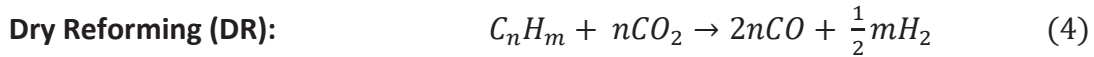
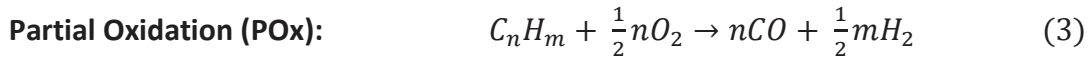
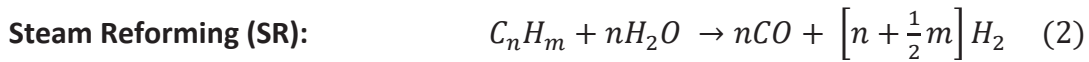


Figure 6: Global warming potential of the emissions created when utilising different methods of hydrogen production [48].

1.3.1 Hydrocarbon Reforming

Hydrocarbon reformation converts the primary feedstock into hydrogen and carbon monoxide, this mixture is commonly known as syngas. There are 4 main technologies for the reforming of hydrocarbons; steam reforming (SR), partial oxidation (POx), dry reforming (DR), and autothermal reforming (ATR). All methods commonly make use of a range of different catalysts (e.g. nickel, noble metals or alloys) and use different oxidants (e.g. O₂, CO₂

or air) at elevated temperatures. Separation of the product gases then takes place in order to obtain pure hydrogen. Additionally, depending on the feedstock, a pre-processing step may be necessary; e.g. desulphurisation. Shift reactors are commonly incorporated after reformation to increase the amount of hydrogen in the reformat, making use of the water gas shift reaction ($\text{CO} + \text{H}_2\text{O} \rightleftharpoons \text{H}_2 + \text{CO}_2$). Each additional step adds cost and complexity to the process. The generic chemical formulas for these processes are given below:



1.3.2 Carbon Capture and Storage (CCS)

With all fossil fuel derived methods of producing hydrogen, carbon capture, storage and utilisation could lower the impact on global emissions. Carbon capture and storage, captures the CO_2 emissions from a process (or less commonly the atmosphere) via a range of methods and sequesters them in long-term storage [51]. CCS can lead to sometimes negative net emissions if used with biomass processing. Long-term applicability is a concern, although CCS could be a viable interim solution to lowering the global CO_2 emissions associated with hydrogen production in the short term [52–54]. However, CCS comes with an additional cost. CCS adds 25-30% to the cost of production [39].

1.3.3 Hydrogen roadmaps

Several roadmaps exist which discuss routes to decarbonising hydrogen production [52,54–57], to reference a select few. Different roadmaps focus on deploying hydrogen in different regions [54,55] or give more focus to the demand side rather than production [52].

However, the roadmaps all have common themes. Whilst envisaging the future for hydrogen production they predict that in the early stage of fuel cell commercialisation hydrogen will be produced in the most cost effective way. At present this means hydrogen will be produced from fossil fuels. Table 2 summarises cost estimates for the hydrogen production methods given in section 1.3. Fossil fuel reformation is by far the cheapest method of production and is the only method to meet US DOE cost targets ($< \$2/\text{kg H}_2$ [58]) and be competitive with incumbent fuels. Biomass derived hydrogen will become more common and so will CCS in attempts to lower CO_2 emissions. Carbon taxes and renewable incentives will play a large part in making these technologies attractive. Green, renewable sources of hydrogen will only be introduced at large scale when gas and carbon prices are prohibitively high and there are large proportions of low cost excess renewable electricity. Figure 7 depicts this trend to low-carbon hydrogen, the significant role that hydrogen from biomass will play is not shown here.

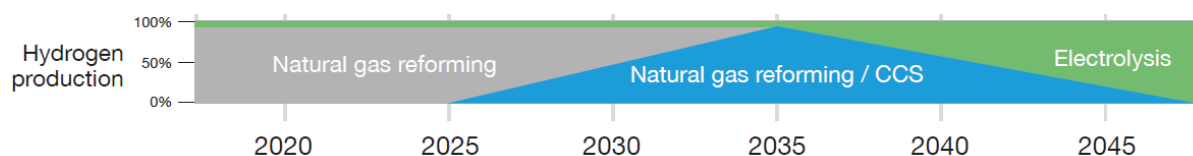


Figure 7: Roadmap for Hydrogen Production [54].

Common in all cited roadmaps is a strong emphasis on deploying hydrogen technologies now even though they are not needed to meet CO_2 reduction targets before 2050.

Table 2: Comparison of the costs of different hydrogen production processes.

Process		Cost of H ₂ (\$US/kg)
Fossil reformation	Fuel	1.03 - 1.48 [47,48,59]
Biomass derived H₂		2.57 - 4.63 [47,48]
Electrolysis		5.78 - 10.49[46,47]

An exception to this generalisation of “low carbon today and zero carbon in the future” [52] is when scale of hydrogen production is taken into account. The cost of compressing, storing and transporting hydrogen is not considered in Table 2. Servicing a small number of vehicles with a centralised SMR plant introduces costs associated with transportation. At this scale on-site electrolysis becomes more cost effective [52]. This is the reason, along with research and demonstration, that some electrolysis is included in Figure 7 from early on.

1.3.4 On-board hydrogen production

Bridging technologies are defined as technologies which progress society towards a new way of thinking (in this case towards the hydrogen economy) whilst utilising some aspects of the incumbent process (in this case energy generation from fossil fuels). In this way bridging technologies reduce the gap created by the barriers to hydrogen that were described in section 1.2. On-board hydrogen production is described here as one such bridging technology.

By producing hydrogen on-board of vehicles many of the challenges faced by the transport sector to utilise hydrogen are overcome. There is no longer an immediate need for overhauling refuelling infrastructure. Safety concerns over handling and storing hydrogen are reduced as the hydrogen can be stored in a more volumetrically dense form, in the form

of hydrocarbons. If the fuel was dispensed as a liquid hydrocarbon (e.g. LNG) then the customer also would not have to adapt to a new method of refuelling.

As discussed in section 1.3.1, large scale stationary reformation is a well-established process. In addition to the high efficiency and durability needed in stationary systems, on-board systems must respond quickly to changes in demand, be compact, have a low cost, and have limited requirements of additional reagents (e.g. H_2O , CO_2) [60]. Other areas of research in the field of on-board hydrogen production, dependent on the method of reformation, focus on reducing thermal stress, inhibiting coke formation, and ensuring homogeneous mixing of reactants [61].

Once on-board, hydrogen can be used in a number of ways, not least to produce electricity using a fuel cell. Hydrogen can be added to combustion fuels and burnt in an internal combustion engine (ICE) or hydrogen can be used as a reducing agent in order to remove NO_x emissions from exhaust streams by converting NO_x to N_2 [62–64].

Since fuel cells are not limited by the Carnot cycle they benefit from higher efficiencies than ICE. Polymer Electrolyte Fuel Cells (PEFC) are the most commonly used fuel cell type for transportation benefiting from low operating temperatures ($40\text{--}80^\circ\text{C}$) [65] meaning rapid start up times. Solid Oxide Fuel Cells (SOFC), operating at $600\text{--}1000^\circ\text{C}$ [65], have been considered for niche transport applications. Applications such as auxiliary power units and buses which have a more predictable load, since rapid start up is not as important in these cases.

Hydrogen benefits from advantageous properties for combustion such as: a low ignition temperature, high diffusivity, high reactivity, and fast burning velocities. Many studies [60,66–71] have therefore shown that adding small quantities of hydrogen to the fuel allows

an ICE to operate with a higher air to fuel ratio and therefore the thermal efficiency of the engine is higher. This reduces the NO_x emissions produced and fuel consumption is lower. Chen et al. [71] report fuel savings of 5-30%, emission savings of 40-50% and exhaust soot reduction of 70%. Using exhaust heat to drive reformation of a small quantity of fuel to hydrogen, which can be reinjected into the fuel stream, has proven to be a highly efficient method of achieving these benefits [66–68,70–73]. Ma et al. [73] not only recycled exhaust heat but also exhaust CO₂ for use as a reagent when dry reforming dimethyl ether.

On-board reforming has been considered for a number of applications across the transport sector, ranging from: ships [74], farm vehicles [75], auxiliary power units on heavy duty vehicles [61,76–78], locomotives [79], submarines [80,81], passenger vehicles [60,62,66,68,82], light duty vehicles (such as taxis and delivery vehicles) [72] to municipal vehicles (such as buses, minivans, refuse collectors, street cleaners and snow removers)[69]. On-board (or possibly more accurately on-site) reforming has also been investigated for portable applications for the military [83,84] and reformation is also common in micro-combined heat and power units [85,86].

Hydrogen can be made on-board from a range of different fuels, a summary is given in Table 3. A common disadvantage to all the listed fuels is the limited environmental benefit when compared with renewably sourced hydrogen.

As well as a range of different fuels, a range of reforming strategies are available. Steam reforming is the widest used and understood process [67,70–72,74,80,84,87,88]. Partial oxidation of hydrocarbons uses oxygen as the oxidant, this can be obtained from air. Coking and hot-spot generation are issues due to the exothermic nature of the reaction [60,62–

64,69,89]. Autothermal reformation is a combination of SR and POx reactions, the heat generated during POx is used to drive SR [61,76–79,82,83].

Table 3: Advantages and Disadvantage of Different Fuels Reformed in On-board Systems.

Fuel	Advantages	Disadvantages	Reference
Methanol	Ease of handling Low pressure storage	Toxic	[71,80,84,87]
Ethanol	Non-toxic Can make use of the established bioethanol industry. Biodegradable Relatively low temperature of reformation. Ease of handling Low pressure storage	Limited solubility with gasoline Carbon formation	[66,70,72,75]
Diesel / gasoline	Well established infrastructure Accepted refuelling experience	Carbon formation	[60,62–64,77–79,81,82]
Jet Fuel (JP-8)	Well established infrastructure Accepted refuelling experience	Need for de-sulphurisation	[83]
Methane (natural gas)	Well established infrastructure Accepted refuelling experience	Boil off of liquefied natural gas reduces system efficiency	[69,74,79,88]
Dimethyl Ether	Non-toxic Similar physical properties to LPG High hydrogen:carbon ratio Easy to transport	Large amounts of CO ₂ in exhaust, needs recirculation.	[73,89]
Ammonia	Liquid at 9 bar and environmental temperature	Low flame speed and temperature Narrow flammability range Toxic	[68,90]

Whilst autothermal reforming is deemed advantageous for on-board reforming due to the ease of thermal management, POx is the only method of reformation which does not require

additional reagents to be carried. Dry reforming uses CO_2 as an oxidant [73]. Plasma assisted reformation has shown promise for on-board reformation, being lightweight, small, and fast to start up [62–64,75,89,91]. During this process, electricity is used to generate more chemically active components from the reactants (ions, electrons and other reactive species). These chemically active species react more readily to give the reaction products. Depending on the fuel and reforming strategy in operation, different catalytic materials are used. Nickel [61,69,72,74,76,88] is commonly used as well as other non-noble transition metals such as copper [66,70,72,80,87], cobalt [90], molybdenum [90] and iron[89]. Noble metals are used in small quantities and commonly in alloys to benefit from their advantageous properties whilst keeping costs to a minimum. Rhodium [78], platinum [62], silver [62], and palladium [87] have all been demonstrated.

1.3.5 Catalysis

By definition, a catalyst increases the rate of a reaction by lowering the activation energy of the reaction by providing a lower energy pathway for the reaction to proceed, without itself being consumed as a reagent. This is depicted in Figure 8.

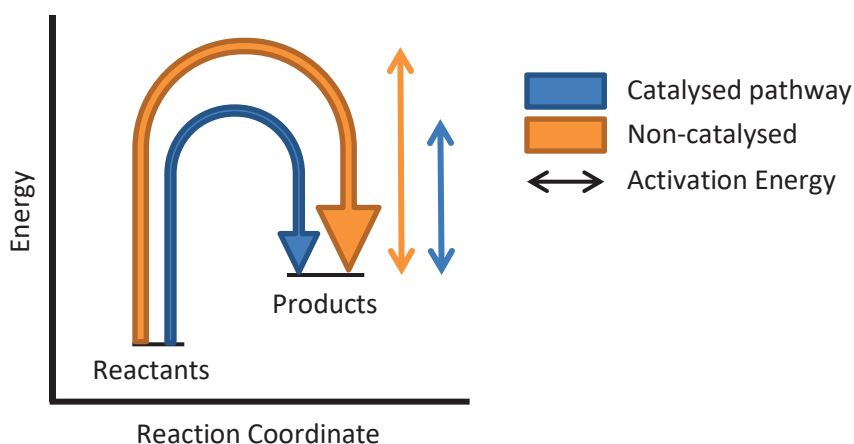


Figure 8: The effects of a catalyst on the activation energy of a reaction.

This study focuses on heterogeneous catalysis, where the reactants are in a different phase to the catalyst itself. As in this study, heterogeneous catalysts often consist of a high surface area solid. The solid provides a surface on which reactants will adsorb, the energy of the adsorbed species is lower than that of the unbound species and this enables the reaction to proceed with a lower energy than would otherwise be required.

1.4 Scope of the Current Study

The current study will explore POx as a potential mechanism for the decentralised reformation of methane to generate H₂ and CO (syngas). The syngas will be generated and directly consumed in an SOFC through a method named Indirect Internal Reforming (IIR). Serving as a proof of concept of IIR by POx this study offers the option of on-board reformation as a promising bridge towards a hydrogen economy.

The mechanism for POx is still questioned; this work aims to expand the understanding given in literature by showing the conditions at which different reaction routes are favoured. In addition, the role of the catalyst support in providing durability against catalyst re-oxidation is explored, something which has been somewhat overlooked thus far in literature. In order to achieve this, differences in the catalytic activity of two nickel catalysts, which employ a silica support for different functions, have been explored.

Chapter 2

LITERATURE REVIEW

2.1	Mechanism of Partial Oxidation.....	22
2.1.1	A Brief History	22
2.1.2	The Role of Support Lattice Oxygen.....	25
2.2	Factors Affecting Catalytic Activity	27
2.3	Catalyst Degradation Mechanisms.....	32
2.3.1	Carbon Deposition.....	32
2.3.2	Agglomeration of Metal Centres.....	34
2.4	Core@Shell catalysts	35
2.5	Nickel/Silica Catalysts for POx.....	37
2.5.1	Nickel Phyllosilicates	41
2.6	Coupling SOFC and H ₂ production.....	42
2.6.1	External Reforming (ER)	43
2.6.2	Internal Reforming	44
2.6.2.1	Direct Internal Reforming (DIR).....	44
2.6.2.2	Indirect Internal Reforming (IIR)	46
2.6.3	Thermal Management.....	47
2.6.4	Integration of IIR catalyst into fuel cells.....	50

Partial oxidation (POx) of methane to CO and H₂, collectively known as synthesis gas (syngas), is an intensely researched area since, as the name suggests, syngas is used as a reactant in a number of industrial reactions. Applications which consume syngas include: synthesis of higher molecular weight hydrocarbons via the Fischer-Tropsch process and, production of methanol. Syngas can also be utilised as a fuel for solid oxide fuel cells (SOFC). In recent years, increased focus has been placed on POx over alternative methods of reforming, namely steam methane reforming (SMR) since POx produces favourable H₂/CO ratios for the previously mentioned applications [92,93]. Another, highly cited reason for favouring POx over SMR is the slightly exothermic nature of POx compared to the highly endothermic nature of SMR [93–101], the lower enthalpy change of POx minimises the effect of thermal gradients on systems. Finally some authors favour POx over SMR, as there is a reduced risk of producing nitrous oxides during the reformation process [95,102]. Nitrous oxides can be produced during SMR in the high temperature burners required for steam generation.

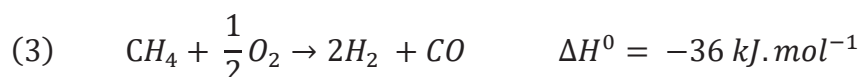
The large commercial market for POx catalysts drives a desire to further understand the mechanism for the reaction. By understanding the mechanism, catalysts with greater fuel conversion efficiencies will be designed with better selectivities for desired products. Catalyst stability is also sought after as the substance must withstand harsh chemical environments, at high temperatures, for long periods of time. Two mechanisms are predominantly debated in this field as will be described in section 2.1.1. There are a number of researchers who claim that the reaction proceeds in a direct manner with the dissociation of methane and oxygen occurring on the catalyst surface. The opposing camp argues that the mechanism proceeds via complete oxidation of methane followed by further

reformation. The following section presents a summary of the history of this mechanism and goes on to review literature concerning areas which lead to how POx will be explored and integrated in this work.

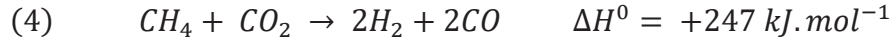
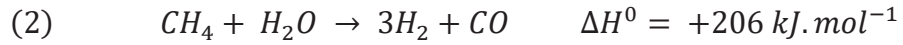
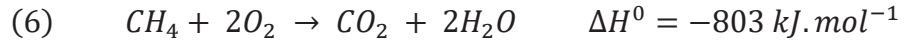
2.1 Mechanism of Partial Oxidation

2.1.1 A Brief History

The first observation of POx of methane to syngas is commonly ascribed to Prettre et al. [103] in 1946. Prettre et al. measured the temperature across a reactor bed containing a catalyst containing 10 wt% Ni. The catalyst successfully converted methane and oxygen into hydrogen and carbon monoxide in a process then called controlled oxidation, now more commonly known as partial oxidation. The authors noted a significant temperature variation across the reactor bed. This indicated to the authors that both endothermic and exothermic reactions were taking place. This led the authors to conclude that the following overall reaction does not sufficiently encapsulate the process occurring:

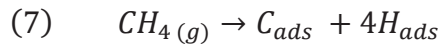


They also reported experiments yielding amounts of carbon dioxide and water vapour, gases which are not present in Equation 3. As a result, the authors determined that POx of methane consists of complete oxidation of a portion of the methane, Equation 6, followed by the remaining methane being reformed by the water vapour and carbon dioxide produced during oxidation, Equations 2 and 4 respectively. Subsequently, many authors have provided evidence for this oxidation-reformation mechanism [92,93,95,97,98,100,102,104,105].

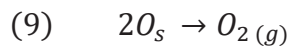


Basile et al. [106] noted the opposite thermal gradient across the reactor bed to Prettre et al., with a hot spot occurring at the bed exit. If the mechanism for the reaction was oxidation followed by reformation, a hot-spot would have occurred at the bed entrance where exothermic total oxidation should have occurred. A cold-spot should have followed further down the reactor due to the endothermic reformation reactions. Basile et al. recorded the opposite leading them to conclude that this disproves the oxidation-reformation mechanism but they remained inconclusive as to what was the true reaction mechanism.

Also contrary to the oxidation-reformation mechanism, around 1992 Hickman and co-workers suggested that the primary products of the partial oxidation reaction were hydrogen and carbon monoxide [94,107,108]. Hickman and co-workers suggested that partial oxidation proceeded via the pyrolysis of the methane, Equation 7, where subscript *ads* denotes a species adsorbed onto the catalyst surface.

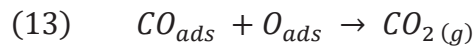
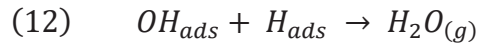
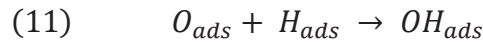


The adsorbed carbon and hydrogen atoms then react with oxygen, or combine, and desorbs from the surface (8-10).





Evidence for this theory was provided from experiments that had very short contact times, 10^{-2} to 10^{-4} s. Since the reactants were only allowed in contact with the catalyst for short periods it was assumed that the composition of the reformat showed the primary POx products. In this case CO and H₂ were predominantly observed. The authors addressed how steam and carbon dioxide can be formed by noting that it is not impossible for surface absorbed oxygen to react with surface absorbed hydrogen or carbon monoxide and go on to produce carbon dioxide and steam, Equations 11-13. However, these processes are more sluggish than the desorption of primary products. They can therefore only occur in reactors with longer contact times.



The direct mechanism is further supported by results indicating that a rhodium catalyst shows a better selectivity towards hydrogen than a platinum catalyst. The activation energy for OH formation on rhodium is much higher than on platinum, 20 kcal/mol vs 2.5 kcal/mol. Therefore deep oxidation occurs more readily on platinum giving a poor selectivity for hydrogen. Drago et al. [109] explain that when the direct mechanism is operational, CO selectivity is favoured only when Equation 10 is favoured over Equation 13. Similarly, H₂ selectivity should remain high due to a low activation barrier for Equation 8 compared with high barriers for water formation. The direct pathway is also supported by Choudhary et al.

[110] who recorded higher selectivities for carbon monoxide and hydrogen than at equilibrium at low temperatures and at high gas hourly space velocities. Many papers support this mechanism [96,99,111]. Generally, experiments which support this mechanism use shorter contact time reactors.

In addition to both the direct and the oxidation-reformation pathway, Balint et al. [112] proposed that there is a change in reaction mechanism as the catalyst is heated to operation temperature. The authors investigated a ruthenium oxide catalyst and concluded that at low temperatures the slow conversion of methane to carbon dioxide and water was promoted whilst the ruthenium oxide was being reduced to ruthenium metal. Once an “ignition” temperature had been reached there was an abundance of ruthenium metal centres with the capability to promote the direct partial oxidation of methane to carbon monoxide and hydrogen. To this day, the mechanism for partial oxidation is still debated in literature. It appears apparent that different reaction conditions and catalyst compositions favour different pathways; this work aims to contribute to the available literature by providing conditions under which each mechanism can be achieved.

2.1.2 The Role of Support Lattice Oxygen

In most cases a catalyst is made up of an active metal loaded onto a support which provides mechanical strength, and also directs the flow of reactants over the reactor bed. Common supports used include perovskites, alumina and silica. All of these supports contain oxygen, a reactant for POx. It is therefore of little surprise that some thought has been given to whether the support actually participates in the catalytic process as an oxidant, or if the support is merely a structural material.

Villalpando, Berry and Cugini [113] used isotopic studies to give insight on this matter. The authors investigated a rhodium and zirconia doped ceria catalyst which was ^{18}O isotopically labelled, and employed the catalyst for POx. During their experiments the reactant mixture used was methane and $^{16}\text{O}_2$. i.e. the only source of ^{18}O was from the catalyst. As POx progressed the carbon monoxide produced was monitored. Figure 9 shows that at first predominantly $^{12}\text{C}^{18}\text{O}$ was observed followed by $^{12}\text{C}^{16}\text{O}$. This gave clear evidence that lattice oxygen was oxidising the methane, this left behind oxygen vacancies which were replenished by gas phase oxygen and this cycle repeated. This mechanism is named the Mars-van Krevelen mechanism. Zhu et al. [114] support this mechanism, their work focussed on the movement of lattice oxygen in ZrO_2 and yttrium stabilised zirconia (YSZ). Again, the authors concluded that methane was selectively oxidised by lattice oxygen and oxygen vacancies were replenished with gaseous oxygen. It was concluded that YSZ was a better catalyst support than ZrO_2 since YSZ has a greater number of oxygen vacancies. The many oxygen vacancies offer the simultaneous activation of methane oxidation, and molecular oxygen towards replenishing oxygen vacancies. Otsuka et al. [115] agree that it is the lattice oxygen which is responsible for the oxidation of methane, the authors went as far as using the ceria support as the oxidant for partial oxidation, in the absence of gaseous oxygen. This required a 2 step reaction in which syngas was produced first by the oxidation of methane to syngas, using the support as the oxidising agent. In the second step the reactant gas stream was changed to allow the reduction of carbon dioxide and water to syngas which replenished oxygen vacancies.

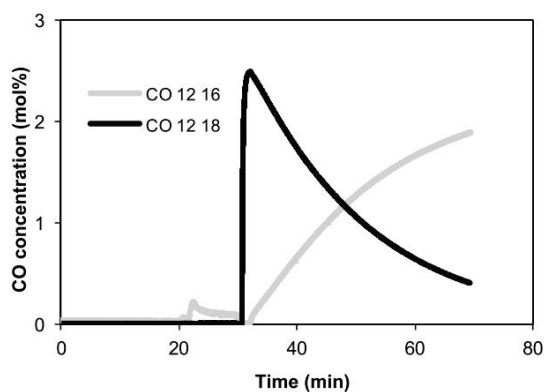


Figure 9: Isotopic study of ^{18}O labelled Rh/zirconia-doped ceria used in partial oxidation [20].

Sadykov et al. [116] noted that whether the reaction proceeded via the direct or oxidation-reformation mechanism could be due to the oxygen mobility in the support material. The authors tested a range of $\text{Pt/Ln}_{0.3}\text{Ce}_{0.35}\text{Zr}_{0.35}\text{O}_{2-y}$ ($\text{Ln} = \text{La}, \text{Pr}, \text{Gd}$) catalysts with varying oxygen mobilities in order to conclude that catalysts with a higher ability to transport oxygen ions promote the direct route to syngas. The direct mechanism is promoted since a high oxygen ion mobility capability stabilises metallic oxides; this promotes the activation of gaseous oxygen on the catalyst surface. Meanwhile metallic sites activate gaseous methane towards oxidation. The combined effect of both metallic and metal oxide sites promoted the direct mechanism for partial oxidation. Catalysts with a low ability for transporting oxygen predominantly displayed metallic sites to the gaseous species, in this way deep oxidation of methane followed by further reformation reactions are favoured.

2.2 Factors Affecting Catalytic Activity

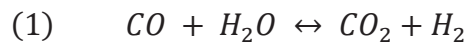
One thing which is not debated in literature is the fact that this catalytic process is highly sensitive to external influences. There are many factors affecting catalytic activity and the conditions of the reaction must be optimised for each catalyst in order to achieve the maximum potential of the catalyst. Factors for optimisation include: reactor bed

temperature, flow rate of reactants, composition of the catalyst, dilution of the catalyst bed with inert material, etc. In this section independent variables affecting catalytic activity will be discussed.

Many authors discuss the effect of the active surface area of the catalyst on its performance. The general trend for all catalysts is the greater the active surface area, the more efficient the catalyst. There are several factors which can affect the active surface area such as calcination temperature, diameter of active metal particle, oxidation state of the active metal, etc. When the catalyst is calcined at low temperatures a smaller active metal particle is produced [100,117]. A smaller metal particle would give rise to a greater surface area and therefore a catalyst capable of higher conversion rates, if the small particles are stable. Ding et al. [100] warn, however, that smaller nickel particles are more easily oxidised and nickel oxide favours the complete oxidation reaction over partial oxidation. In this way the oxidation state of the metal centres affects the active surface area. A compromise therefore has to be made with calcination temperature, it is beneficial to have small particles however, smaller particles are at a greater risk of oxidation. This suggests there is an optimum particle size required in order to obtain a high surface area catalyst which is robust enough to withstand oxidation. The calcination temperature also affects the metal-support interaction; Özdemir et al. showed that increasing the calcination temperature during the preparation of Ni/MgAl₂O₄ strengthens the metal-support interaction by favouring the diffusion of NiO into the bulk. This protects against agglomeration and coking, extending the lifetime of the catalyst [118]. Therefore, it has been shown that an increased calcination temperature can lead to a catalyst with a greater stability but lower activity.

As previously described, partial oxidation of methane to syngas involves the handling of carbon dioxide. It follows therefore that the acidity/basicity of the catalyst has an effect on performance given that carbon dioxide is acidic and will be more attracted to a basic substance. An exaggeration of this effect can be seen when dry reforming conditions are employed. Dry reforming of methane is the conversion of methane to syngas using carbon dioxide, Equation 4.

If a basic support is employed during dry reforming, the rate of CO₂ chemisorption is increased leading to higher activities. Mette et al. employed MgO as a basic catalyst support to achieve this [119]. Carbon dioxide is not a reactant in partial oxidation but as previously described it could be an intermediate product if the oxidation-reformation mechanism is employed. Basicity of the support is therefore still a factor to consider. Increasing the basicity of the catalyst changes the H₂/CO product ratio by promoting the reverse water gas shift (Equation 1) and reverse Boudard reactions, Equation 14 [120].



The basicity of the catalyst also has an effect on the stability of the catalyst by reversing the Boudard equation, Equation 14, this discourages carbon deposition. A variety of basic promoters have been employed for this reason, such as MgO [121], La₂O₃ [122] and ZrO₂ [123].

Although generally, as the catalyst bed temperature is increased methane conversion will increase, temperature variation does not directly correlate to reactant conversion since

there are both exothermic and endothermic reactions at play [124]. Xu et al. [101] tested different catalysts across a range of temperatures from 400 to 800°C. The authors noted that at low temperatures (<600°C) the activity is dependent on the catalyst reducibility, since activity results correlate to temperature programmed reduction (TPR) data. At high temperatures activity is dependent on the surface area and nickel dispersion in the catalysts.

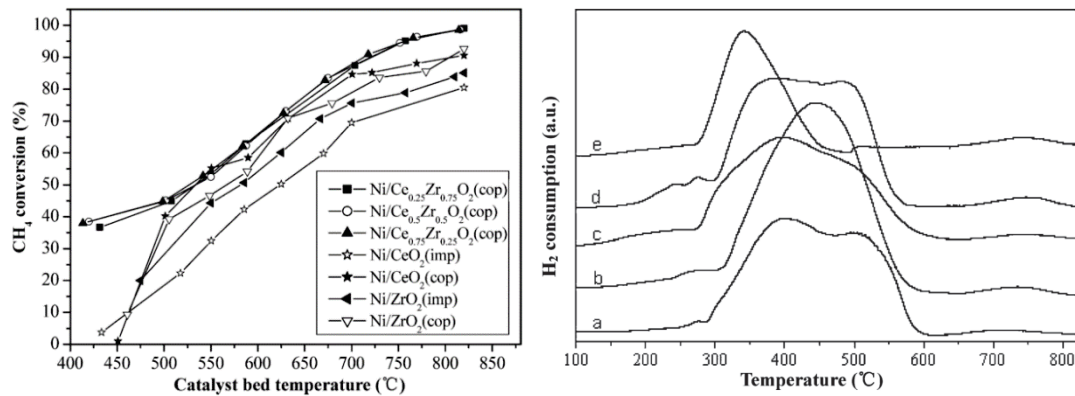


Figure 10: Left, variation in methane conversion with catalyst bed temperature. Right, reducibility of different Ni/Ce_xZr_{1-x}O₂ catalysts, a. x= 0, b. x=0.25, c. x=0.5, d. x=0.75, e. x=1.0 [97]

Related to the reactor bed temperature is the extent to which the catalyst bed is diluted with inert material. By diluting the catalyst itself the likelihood of extreme hot-spots is reduced by dispersing the reaction centres. Many authors adopt this technique in order to achieve an isothermal reactor [100,102,125].

The reactant mix must be optimised to obtain the desired product ratio and extent of reactant conversion. The stoichiometric CH₄/O₂ ratio is 2, as shown in Equation 3. Greater conversions can be obtained when greater than the stoichiometric amount of oxygen is used, as oxygen is the limiting reagent. Verlato et al. [126] show that as the CH₄/O₂ ratio is decreased from 2.6 to 1.4 the methane conversion gradually increases, Figure 11. This comes at a cost however as the CO and H₂ selectivity fall in favour of producing undesired

total oxidation products, H₂O and CO₂. This is coupled with a spike in catalyst bed exit temperature since endothermic reforming reactions are occurring to a lesser extent.

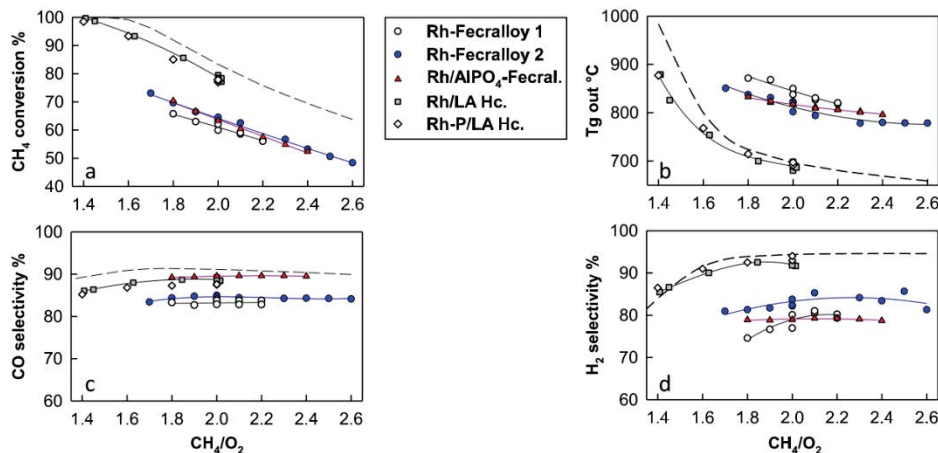


Figure 11: Ranging CH₄/O₂ ratio in order to determine the effect on; Top left: CH₄ conversion. Bottom left: CO selectivity. Top right: Bed exit temperature. Bottom right: H₂ selectivity [121].

In the same publication [126] flow rate was varied in order to evaluate its effect on catalytic performance. It is shown, Figure 12, that when the flow rate exceeds ca. 120 SI/h the change in catalytic performance was negligible. A higher bed exit temperature was noted as there was better thermal efficiency at higher flow rates; fast travelling gases carried thermal energy from the hot spot at the bed entrance, along the reactor more effectively. Due to the increase in reactor temperature it was expected that an increase in catalytic performance might be seen. However, this was absent since any increase in performance was negated as kinetically sluggish reactions are inhibited by the decreasing contact time.

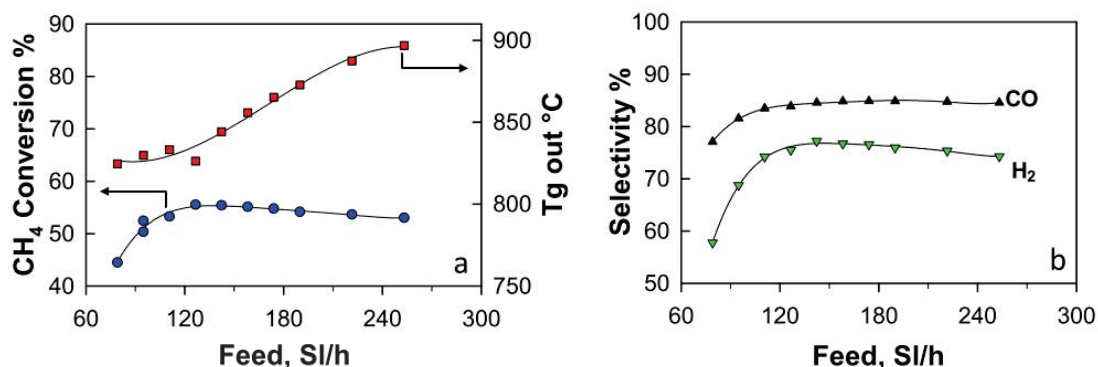


Figure 12: Effect of feed flow rate on catalytic performance; Left: CH₄ conversion and bed exit temperature. Right: CO / H₂ selectivity [122].

2.3 Catalyst Degradation Mechanisms

Many degradation mechanisms are known for partial oxidation catalysts such as carbon deposition, agglomeration of active metal particles, oxidation of active sites, and evaporation of catalyst support. Since the effects of reformer catalyst degradation on its performance in a microtubular SOFC will be investigated in this work, it is important to understand the different methods by which a catalyst can degrade and how these processes can be identified.

2.3.1 Carbon Deposition

Carbon deposition, or coking, is the growth of carbon within the reactor bed to form an additional layer over the catalyst surface. Growth is often in the form of filaments, protruding from the catalyst surface. Carbon deposition reduces the active surface area of the catalyst by blocking active sites and thereby reducing catalytic activity.

Carbon deposition occurs when conditions within the reactor favour undesired reactions. For example coking can ensue when conditions favour the Boudard reaction, Equation 14, or hydrocarbon cracking, Equation 15. The Boudard reaction governs low temperature coking whilst carbon deposition can occur at high operation temperatures via hydrocarbon cracking [127].



Numerous methods are employed to combat this mechanism of degradation. One approach is to physically prevent the growth of carbon on an active site. The metal particles can be

confined to a certain environment, be it within a core@shell particle [128], over-coating a supported catalyst [125] or containing the metal particle within a nanotube [129]. All these protective layers have some sort of microporous structure or other method of allowing the reactant gases to remain in contact with the active metal. Several reasons simultaneously make this “nanoconfinement effect” [129] contribute to the reduction in carbon deposition. Carbon fibres have been shown to preferentially grow on the low-coordinated Ni surface sites, i.e. step and corner sites [130]. The nanotube, shell or coating blocks these corner and step sites reducing carbon fibre growth whilst allowing catalytic reactions to continue on the higher coordinated metal sites. Additionally, the mesopores of the nanotube/shell/coating do not allow space for the carbon fibre to grow. Mesopores range in size from 2-5 nm and carbon filaments are typically 17 nm in diameter, far too large to grow in the mesopores [128].

An alternative to physically preventing carbon deposition is to chemically dope the catalyst to give rise to a surface which either prevents carbon deposition or favours the removal of deposited carbon species. Different dopants have been shown to display this character such as lanthanum [102]. As previously mentioned, doping the catalyst with a basic species contributes to the prevention of carbon deposition by promoting the chemisorption of carbon dioxide and therefore increasing the rates of the reverse Boudard and reverse water gas shift reactions. Many authors conclude that increasing the basicity decreases the extent of carbon deposition [102,120,131,132].

2.3.2 Agglomeration of Metal Centres

Agglomeration is the name given to the aggregation of metal particles. This increases the particle size and decreases the overall active surface area of the catalyst, thereby reducing catalytic performance. Agglomeration is commonly referred to in literature as sintering, this term is avoided in this work to avoid confusion with nickel particle sintering in SOFC which refers to the densification of nickel structures in the fuel cell anode. Agglomeration occurs more readily at higher temperatures and is particularly accelerated above the Tamman temperature, half the melting point of the bulk metal in degrees Kelvin [125]. Coating of a catalyst can prevent agglomeration from occurring, Lu et al. coated a palladium catalyst in alumina and increased the thermal stability of the catalyst. Figure 13 shows that after exposure to reaction conditions, the coated catalyst much more closely resembled the fresh catalyst when compared with the uncoated catalyst. Therefore, it was concluded that the coating helped prevent agglomeration. Other encapsulation techniques have included using phyllosilicate nanotubes[129] and Core@Shell catalysts [117,133–135].

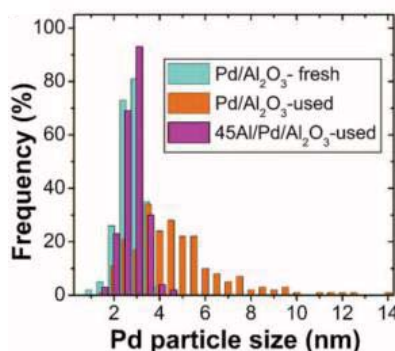


Figure 13: Particle size of coated and uncoated catalyst before and after testing [122].

An alternative approach to lower the risk of agglomeration is to ensure that the metal particles are well distributed on the support, if the metal centres are not in close proximity they will not agglomerate [136]. This can be achieved by having low metal loadings [119].

The metal loading is the ratio of active metal to support. There is a trade-off to be made here between having a stable, agglomeration free catalyst and having a catalyst with a high active surface area to begin with. Strong interactions between the support and the active metal centres ensures that the particles remain dispersed on the catalyst surface [118]. A strong metal-support interaction can be achieved by raising the calcination temperature of the catalyst. However, as previously mentioned, increasing the calcination temperature comes with its own associated disadvantages.

2.4 Core@Shell catalysts

Some of the advantages of core@shell catalysts have already been discussed such as reducing the risk of agglomeration and carbon deposition. Following the current trend to use this advantageous structure, it was attempted to synthesise two inversely oriented core@shell catalysts during this work. This section further discusses the advantages of these structures and briefly discusses how core@shell structures are commonly made.

Chou et al. [137] compared the conversion of methane by platinum/ceria based catalysts on differently shaped alumina supports. The authors compared a tablet shaped catalyst to a ring shaped catalyst with a 30% greater surface area. The increase in surface area resulted in 12-28% improvement in methane conversion depending on the reactant space velocity used. These authors show how by using a core@shell structure of support@catalyst, a large active surface area can be achieved using less material, resulting in lower cost. This is one of the reasons Majewski and Wood [134,138] adopted a core@shell structure when making one of the catalysts attempted to be synthesised in this work, $\text{SiO}_2\text{@Ni}$.

Regarding the synthesis of these structures, as discussed in section 2.3.1, when it is the case where a protective coating is being applied to a catalytic centre, it is important that the reactant gases can still reach the active metal and product gases can also leave the particle. This is achieved through mesopores. Silica is often used as a protective shell as it can be easily made mesoporous during synthesis. Synthesis often occurs in 3 stages: The metal centre is synthesised, using capping agents to regulate the particle size. Secondly the silica shell is added via a polymerisation process and finally the capping agent or pore former is removed by calcination; burning off the capping agent creates mesopores in the shell. This synthetic process is shown in Figure 14.

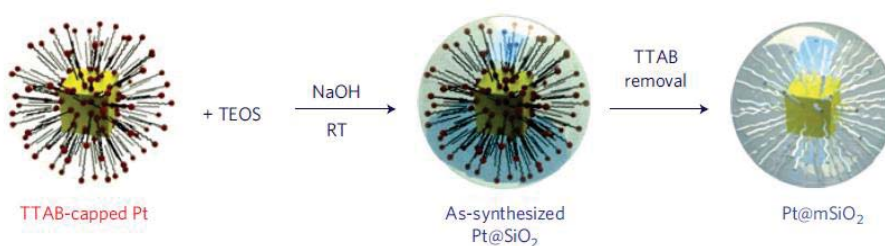


Figure 14: Schematic for Core@Shell particle synthesis [135]

It is shown that capping agents can be somewhat multifunctional in the synthesis of core@shell nanoparticles. Firstly they control the size of the metal centres. Secondly, If carefully selected, capping agents can aid in the coating of the particle; Electrostatic forces between the capping agent and silica precursor can be used to direct polymerisation. Finally, as seen above, the capping agent also acts as a pore-former. Joo et al. used the above method in order to synthesise Pt@SiO_2 [139], in a similar way Cargnello et al. synthesised Pd@CeO_2 [140], and as investigated in this work Li et al. [117], used the method to make Ni@SiO_2 .

Other methods of synthesising core@shell nanoparticles have been tested including chemical vapour deposition [141]. Yu et al. synthesised Au@SnO₂ by first synthesising intermetallic Au/Sn particles and then selectively oxidising the tin which preferentially locates itself on the catalyst surface [142]. Arnal, Comotti and Schüth encapsulated gold in zirconia hollow spheres by firstly coating the gold in silica, then in zirconia and then dissolving the silica framework away [143]. Cargnello also adopted a microemulsion technique to harvest a “more encapsulated” Pd@CeO₂ catalyst which showed a higher stability but reduced activity due to the restriction of reactant/product gas flow to and from the active metal [140].

2.5 Nickel/Silica Catalysts for POx

As previously mentioned, the two catalysts which will be the focus of this work are silica supported nickel catalysts. These catalysts have been chosen due to the affordability and availability of nickel metal compared with other catalytically active metals and also due to the simplicity of the preparation methods, allowing the catalysts to be made in-house giving full control of the catalyst for integration into the microtubular SOFC. This section will review findings of other authors regarding nickel/silica catalysts used for partial oxidation of methane to syngas.

High dispersion of nickel on silica with strong interactions between the two components is vital for preventing nickel particle agglomeration as shown by Xia et al. [144], the authors used two different methods of mounting nickel onto spherical silica particles, impregnation and sol-gel methods. The authors found that the sol-gel method resulted in smaller nickel

particles being bound to the silica surface through silicate structures. This resulted in a more active and stable catalyst.

Encapsulating nickel particles in silica has proven to be beneficial in preventing nickel particle agglomeration and limiting the amount of carbon growth. Li et al. [117] coated different sized nickel nanoparticles in porous silica. The size of the silica pores were controlled by the addition of poly-(vinylpyrrolidone) (PVP). It was found that smaller particles resulted in a thinner shell of silica. Catalysts with a smaller nickel core resulted in higher methane conversions, greater syngas selectivities and had greater a durability. TEM analysis before and after testing showed that particle size growth was kept to a minimum due to the encapsulation. Temperature programmed oxidation of the tested catalysts showed that larger nickel particles with larger cavities between the Ni and SiO₂ resulted in greater proportions of carbon deposition. A smaller pore size in the SiO₂ shell resulted in a more stable catalyst since it was more resistant to carbon deposition. Takenaka et al. [98] reported a similar benefit being claimed from the application of silica shells over nickel nanoparticles. The silica shell ensured a longer catalyst lifetime by increasing the interaction between the metal and support, limiting agglomeration, and the silica shell also prevented the growth of carbon fibres.

Guo et al. [145] confined nickel nanoparticles within an ordered, 3D structure, of mesoporous silica honeycomb in an attempt to encapsulate the nickel particles to prevent agglomeration and coking, while maintaining low diffusion resistances of the reactants to the catalyst surface. ZrO₂ was used to strengthen the interaction between the nickel and silica. The authors found that their honeycomb structured Ni-ZrO₂-SiO₂ catalyst improved

the ability of nickel/silica catalysts to resist agglomeration due to the SiO₂ physically preventing nickel particles from merging. The physical barrier also limited the room available for filamentous carbon growth. The addition of ZrO₂ improved the catalysts performance due to its high oxygen mobility. The strong metal support interaction promoted by ZrO₂ also resulted in smaller more highly anchored nickel particles, again contributing to a higher resistance against agglomeration. Jing and Seng also utilised ZrO₂ to increase the Ni particle dispersion [146], it was concluded that 5 wt% addition of ZrO₂ was optimum for increasing catalyst performance, any additional zirconium would merely block access to Ni active sites.

Sadegh et al. [147] utilised oleylamine as a capping agent when they prepared their Ni/SiO₂ catalysts. Due to the strong hydrophobicity and affinity for metal particles of oleylamine, the capping agent isolated nickel particles and therefore resulted in a catalyst with small, highly dispersed nickel nanoparticles. The oleylamine also produced a catalyst with a strong interaction between the metal and support. The combination of both of these characteristics resulted in a more stable catalyst when compared with a Ni/SiO₂ catalyst which had not utilised oleylamine. Greater stability was shown over a 5 hour time period and the rapid degradation of the unmodified Ni/SiO₂ catalyst was attributed to nickel particle agglomeration due to a weak metal-support interaction.

Ding et al. [93] synthesised nickel/silica catalysts using a range of alkanol solvents as delivery conveyors for the nickel particles onto the silica particles. The alkanol solvents subsequently acted as carbon templates to control the size of the nickel nanoparticles. The authors achieved a range in average nickel particle size from 7-25 nm and concluded that smaller particles give rise to a higher proportion of edge and step metal sites. These low coordinated

sites promote the cleavage of the C-H bond and therefore an abundance of these sites lends itself to higher methane conversions. However, these sites also promoted coking.

In an earlier paper Ding et al. [100] varied the nickel particle size in Ni@SiO₂ catalysts by varying the calcination temperature. Smaller nickel particles were obtained by utilising a lower calcination temperature, these particles were demonstrated as having higher activities towards methane conversion. However, it was shown that the smaller particle sizes were more easily oxidised and this led to the selectivity of the catalyst decreasing rapidly with time on stream. It was concluded that NiO favours total methane oxidation whereas Ni⁰ promotes the partial oxidation. Furthermore the stabilities of a Ni@SiO₂ catalyst was compared with a non-core@shell, silica supported, nickel catalyst. The silica shell was said to resist the re-oxidation of nickel particles and therefore maintain a higher catalytic performance.

Hu et al. [148] used CeO₂ to promote Ni/SiO₂ catalysts. The authors reported greater performances of catalysts with mixed ceria/silica supports than nickel supported on purely silica or ceria. This was attributed to the ease of reduction of NiO due to the high oxygen storage capacity of ceria. The stability of the mixed support was also higher due to the supports weak acidity resisting carbon deposition. Li et al. [149] also investigated Ce as a promoter, the authors concluded that Ce reduced the Ni particle size, thereby increasing activity. The catalysts were tested for the combined partial oxidation and dry reforming, similar conclusions to Hu et al. were made pertaining to the benefits of Ce in resisting carbon deposition. Bimetallic Co-Ni nanoparticle encapsulated in silica were shown to also exhibit a greater performance and carbon resistance than Ni@SiO₂ during POx [150]. CoNi₂@SiO₂ was

shown to be the ideal composition, increasing the cobalt concentration past this point reduced the active surface area of nickel.

A series of different dopants were utilised in the study by Li et al. [151]. The authors observed that La was the best dopant for Ni@SiO₂ from the range studied (La, Ce, Ba, Co, Cu and Fe). A more stable catalyst resulted with a higher catalytic performance. Doping with La lowered the nickel particle size and thus allowed for an improved performance and carbon tolerance. In addition to the carbon tolerance being attributed to the smaller nickel particle size, it was concluded that the La encouraged O₂ and CO₂ to adsorb onto the nickel surface. These would react with any deposited coke, aiding its removal.

2.5.1 Nickel Phyllosilicates

Nickel Phyllosilicates (Ni-PS) have attracted attention in literature pertaining to hydrocarbon reforming. Ni-PS structures offer a stronger metal-support interaction than other silica supported nickel catalysts. They are crystalline structures which are synthesised in two different arrangements. Phyllosilicates are named dependant on the number of layers of tetrahedral SiO₄ crystals present. 1:1 nickel phyllosilicates consist of layers of tetrahedral SiO₄ stacked on top of octahedral NiO₄(OH)₄ [152]. As depicted in Figure 15. The structural formula of the 1:1 arrangement is Ni₃Si₂O₅(OH)₄.nH₂O.

2:1 Nickel phyllosilicates consist of octahedral NiO₄(OH)₄ sheets sandwiched between two tetrahedral SiO₄ sheets [152], as shown in Figure 15. The structural formula of the 2:1 arrangement is Ni₃Si₄O₁₀(OH)₂.nH₂O.

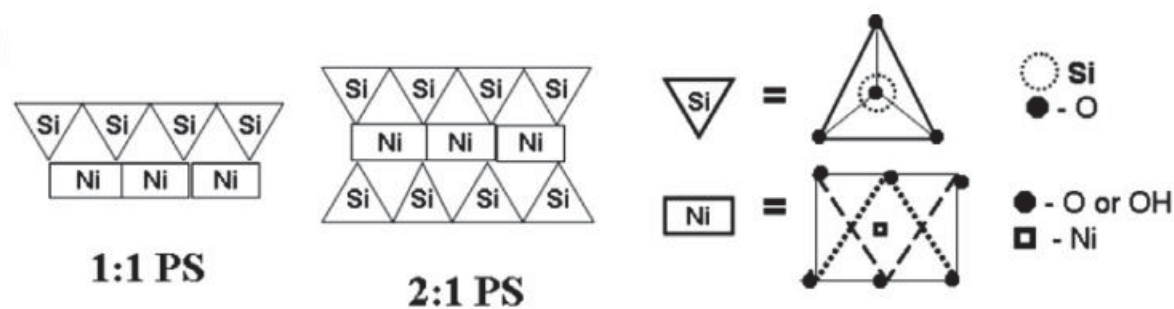


Figure 15: Structure of 1:1 and 2:1 nickel phyllosilicates [147].

Ni-PS structures can be precursors for silica supported nickel nanoparticles. Sivaiah et al. [152] describe how the two arrangements of Ni-PS result in supported nanoparticles with different thermal stabilities. The authors conclude how the 1:1 arrangement results in nickel nanoparticles purely supported on silica, post reduction, whereas the 2:1 arrangement partially reduces at temperatures up to 700°C. This partial reduction results in nickel nanoparticles dispersed between unreduced Ni-PS structures, supported on silica. The availability of –OH groups from the unreduced Ni-PS groups aids the 2:1 Ni-PS derived catalyst avoid coking when tested as a reformation catalyst [153]. Ashok et al. also report the partial reducibility of Ni-PS and the resulting availability of surface –OH groups that creates [154]. The authors suggest that the surface –OH groups promote the water gas shift conversion.

2.6 Coupling SOFC and H₂ production

The high temperature operation of SOFC offers certain benefits over other fuel cell technologies when it comes to coupling the systems with on-site hydrogen production. The main advantage of SOFC, in this sense, is that the high quality waste heat (produced by the oxidation of fuel) can be recycled to drive endothermal reforming reactions. At a cell voltage of 0.78 V the heat evolved by the fuel cell operation is 470 kJ.mol⁻¹ H₂ [155], literature states that 40 to 70% of this heat can be used to drive endothermal reformation reactions in order to achieve a greater system efficiency [156]. If the energies of the fuel cell operation and fuel

reformation are perfectly matched autothermal operation can be obtained whereby heat for reformation is generated by the SOFC [157]. In this way, greater system efficiencies are achieved since the heat for reformation is provided and the cooling demand on the SOFC is reduced. Additionally, SOFC offer greater tolerance to fuel impurities, therefore considerably less purification of reformat is required than in low temperature PEFC systems [158].

On-site/on-board reforming is the decentralised reformation of hydrocarbon fuels in order to produce a hydrogen rich fuel. In this way some of the challenges associated with handling hydrogen such as safety and its inherent low volumetric energy density are overcome. There are several approaches to on-site/on-board hydrogen production for fuel cells, each offering their own advantages and disadvantages. The approaches are named: external reforming (ER), and internal reforming which can either be direct (DIR), or indirect (IIR) in nature. Brief descriptions of these technologies are given in sections 2.6.1 - 2.6.2.

2.6.1 External Reforming (ER)

An external reforming system aims to have a compact reforming unit [159] which fully converts the fuel prior to it entering the fuel cell. As the name suggests the reformer is independent from the fuel cell. Depending to the efficiency strived for, the reformer can be separately heated from the SOFC [157] or it can be thermally linked via a heat exchanger, afterburner [160] or both. An afterburner combusts the excess non-oxidised fuel found in the anode waste stream, producing heat that can be returned to the reformer. Thermal management to ensure high efficiency is a challenge in ER, in addition having more balance of plant (BoP) components is disadvantageous. On the other hand, control of reformation,

and the ability to ensure the quality of the reformat is beneficial. Figure 16 shows a possible system diagram, from literature, which utilises external reforming [161].

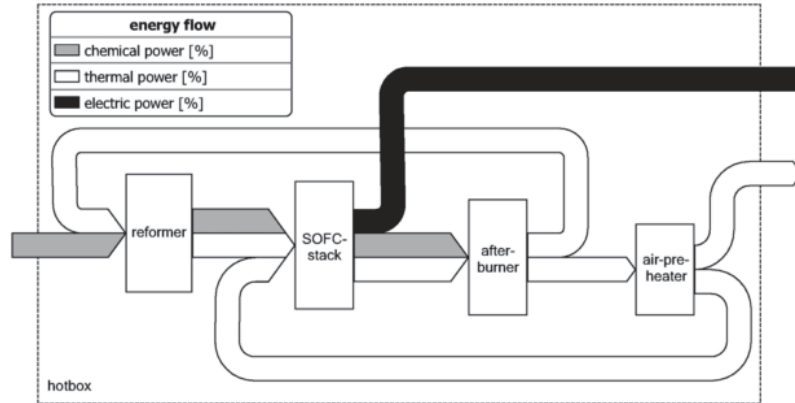


Figure 16: System diagram of an external reforming SOFC system [158].

2.6.2 Internal Reforming

Compared to ER, internal reforming is reported as being a cheaper and more efficient mechanism to generate hydrogen in-situ [162,163]. By eliminating the need for a pre-reformer and shifting the endothermic reformation process to the fuel cell, the cooling demand of the stack is reduced. Generally, SOFC are cooled by blowing air over the fuel cell stack. Eliminating the need for these components either partially, or fully, saves both money and parasitic energy losses.

Depending on the position of the reformer relative to the anode, internal reforming is deemed either direct or indirect.

2.6.2.1 Direct Internal Reforming (DIR)

Some systems reform the fuel directly at the anode either by utilising specialised anode materials or additional catalyst layers, the state of the art research on this topic is summarised in Table 4. The anode simultaneously reforms the fuel and oxidises the

reformat to generate power. The difference in the rates of reformation and electrochemical oxidation however, can lead to difficulties. The conditions of SOFC operation are ideal for reformation (high temperature and the presence of a nickel catalyst), the rate of reformation is therefore high. This causes large proportions of reformation to occur at the fuel cell inlet, inducing a large change in the temperature at this point. Depending on the reformation strategy (SR, DR, POx etc.) adopted, hot spots or cold spots can be generated, leading to mechanical stress in the fuel cell material and potentially material failure.

Transferring heat for reformation is, however, no longer a problem since the reformation occurs exactly at the point where the heat is being generated by the fuel cell. Having fewer system components is advantageous from a cost and efficiency perspective.

Table 4: State of current research regarding available anode materials for direct hydrocarbon utilisation [156].

Classification of anode material	Disadvantages	Areas for development
Ni Cermets	<ul style="list-style-type: none"> • Coke deposition is irreversible 	<ul style="list-style-type: none"> • Scale up of coke resistant anode fabrication methods
Cu Cermets	<ul style="list-style-type: none"> • Fabrication processes are tedious • Poor fuel cell performance due to Cu being essentially inert to fuel oxidation. Materials must be co-impregnated with ceria/noble metals to improve performance. • Instability in operating conditions 	<ul style="list-style-type: none"> • Cost competitive fabrication methods • Long term stability
Oxide Based	<ul style="list-style-type: none"> • Low electrical conductivity • Slow reaction kinetics • Poor redox stability • Currently restricted to electrolyte supported cells. 	<ul style="list-style-type: none"> • Development of electrode supported cells/stacks • Further material developments.

2.6.2.2 Indirect Internal Reforming (IIR)

Indirect internal reforming separates the reforming component from the fuel cell anode but maintains the catalyst within the fuel cell itself. Figure 17 shows a schematic for both a planar [164] and tubular configuration.

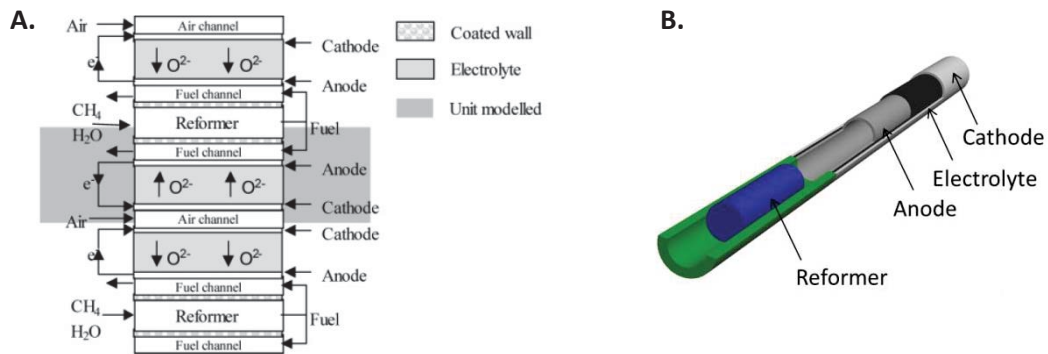


Figure 17: Schematic of A. Planar [161] and B. Tubular SOFC configurations both with indirect internal reforming incorporated.

The reformer is distinct from the anode while being in close thermal contact. This allows for independent tailoring of both the fuel cell and reformation catalysts whilst maintaining the simplicity of the system with integrated heat management.

The advantages and disadvantages of the different approaches to fuel reforming are given in Table 5.

Table 5: Advantages and disadvantages of different reforming strategies for SOFC.

	Advantages	Disadvantages
External Reforming	<ul style="list-style-type: none"> • Control of reformat entering fuel cell • Possibility for reformat purification prior to entering fuel cell. 	<ul style="list-style-type: none"> • Additional BoP • Requires high efficiency heat exchangers • Inherently larger system
Direct Internal Reforming	<ul style="list-style-type: none"> • Compact system • No need for heat exchangers/afterburners to recover SOFC heat [165]. • Consumption of the reformat quickly by the fuel cell encourages further CO/H₂ production [166]. 	<ul style="list-style-type: none"> • Risk of anode coking [167] • Reforming catalyst infiltration of anode can inhibit mass transport of the fuel cell reactants [168] • Mismatch of rates of reformation and electrochemical reactions [169]. Causing thermal gradient across anode[167]. • Anode catalyst must be suitable for both electrochemical and reformation reactions [165].
Indirect Internal Reforming	<ul style="list-style-type: none"> • Reforming Catalyst degradation does not necessarily mean fuel cell failure. • Shift of temperature distributions away from anode • Reduced risk of anode coking • System simplicity • Opportunity to individually optimise both reformer and anode materials. [157] 	<ul style="list-style-type: none"> • Engineering challenge • Mismatch of rates of reformation and electrochemical reactions [157,170].

2.6.3 Thermal Management

A common theme to all systems, especially those involving internal reforming, is the importance of thermal management. Local hot/cold spots can be caused from the endo/exothermic reforming and electrochemical reactions. Since the components of the layered ceramic of the SOFC and catalysts have slightly different coefficients of thermal expansion, changes in temperature affect the stress that the different components inflict on each other. Fischer and Seume modelled these stresses and concluded that for tubular SOFC,

stress due to a local cold spot is more significant than the stress caused by longitudinal thermal gradients across the cell [171]. Such stress can cause cracking of the ceramic layers and can ultimately lead to complete fuel cell failure.

Lim et al. showed several methods of achieving smoother temperature profiles across indirect internal reformers by simulation [164]. The authors utilised the following strategies:

- Lowering the reforming capacity of the catalyst.
- Distributing the activity of the catalyst along the reformer length. Aguiar et al. also adopted this strategy by changing the thickness of the catalyst coating along a wall-coated reformer [156].
- Introducing small amounts of oxygen into the reformer to drive exothermic hydrogen oxidation reactions to heat any cool spots. Dokmaingam et al. also investigated the addition of small quantities of oxygen to a steam reforming IIR system [165]. The authors noted however that care must be taken since adding too much oxygen would consume large amounts of hydrogen and lead to low electrical performance of the SOFC.

Additional strategies for smoothing the temperature profile across the cell include:

- Recycling anode exhaust gas; this lowers the hydrocarbon concentration in the anode and therefore lowers the rate of reformation. This can have several other benefits as described below.
- Staggering the points of fuel entry along the cell.
- Optimising cell construction to enhance heat transfer away from the cell.

- Alternative anodes with lower reforming capabilities; Boder and Dittmeyer showed the promise of infiltrating anodes with copper in an attempt to block some of the nickel sites while maintaining the electrical conductivity. Reforming capacity was shown to reduce while the electrochemical performance of the cell remained comparable to regular Ni/YSZ anodes [169].
- Optimising the flow arrangements of air and fuel in the fuel cell. Dokmaingam et al. [165,170] modelled co-flow and counter flow arrangements and found that a co-flow configuration resulted in a better match between the heat required for reforming and that generated by electrochemical reactions.

The anode exhaust contains both carbon dioxide and steam from the oxidation of carbon monoxide and hydrogen. By recycling the anode gas to the reformer inlet, the following benefits can be taken advantage of [162]:

- Less energy needed for external steam generation
- Fuel utilisation increases.
- Reduced requirement of the system to carry CO₂ on-board for DR.
- The steam content of the exhaust is lower meaning that the waste heat of the fuel cell is of higher quality.
- Means of preventing coking of anode [172].
- Higher system efficiency by up to 10% [172].

Care must be taken with anode gas recycling since the recycled anode gas will dilute the fuel feed which results in lower cell potentials. Fellows designed a concept of overcoming this,

the system involved having two separate anode exhausts, one which is depleted in hydrogen which is not recycled and another which is relatively non-depleted which is recycled [172].

Methane slippage is the term given to the amount of methane which has remained unconverted in the reformer of an IIR system which has then entered the fuel cell. This can occur when an IIR catalyst with a lower activity has been adopted in order to smooth temperature gradients. Under these conditions it is possible to have IIR working simultaneously to DIR. Issues with local cooling of the anode due to DIR still remain. Aguiar et al. modelled an SOFC system which presented both IIR and DIR [173]. The authors varied the amount of methane slippage from 1 to 59% and results showed that independent of the amount of methane entering the fuel cell, complete methane conversion was achieved over the first 10% of the anode. Therefore reducing the catalytic activity of the IIR catalyst was not sufficient to prevent cold spots in the cell. The cold spot was nearly shifted to the anode inlet where DIR took place. The authors showed that lowering the activity of both the IIR and DIR catalysts was preferential for creating a smooth temperature profile.

2.6.4 Integration of IIR catalyst into fuel cells

There are many papers which focus on the modelling of IIR-SOFC systems [160,165–167,174]. Due to the scarcity of literature based on experimental results this section focuses on literature pertaining to IIR systems which utilise all reformation strategies. Since the engineering challenges faced by integrating a catalyst within a high temperature fuel cell environment will be comparable it is envisaged that lessons will need to be drawn from across the literature. However, it is important to remember the fundamental differences between different systems, these are summarised in Table 6.

Table 6: Fundamental difference between different IIR-SOFC systems.

Feature	Comment
Type of Reformation	Depending on the reformation strategy adopted (SR, DR, POx or a combination) the reaction will have different degrees of endo/exothermicity, requiring different approaches to thermal management.
Type of Fuel	Heavier hydrocarbons have a higher tendency towards carbon deposition [155]. However, they have a higher tolerance for sulphur poisoning [175]. The thermodynamics of reforming of different fuels is different therefore different temperature profiles will result [170]. Biogas carries an oxidant within it which can be utilised during reformation [160], up to 50% CO ₂ [161].
Operation Temperature	Different authors have chosen to work at different temperatures, this affects the reformation performance and should be taken into account when making comparisons.
Fuel Cell Arrangement	Tubular/Planar SOFC arrangements require different approaches to IIR, as shown in Figure 17.

Several methods of integrating a catalyst into fuel cells have been trialled. Different reformer designs are depicted in Figure 18.

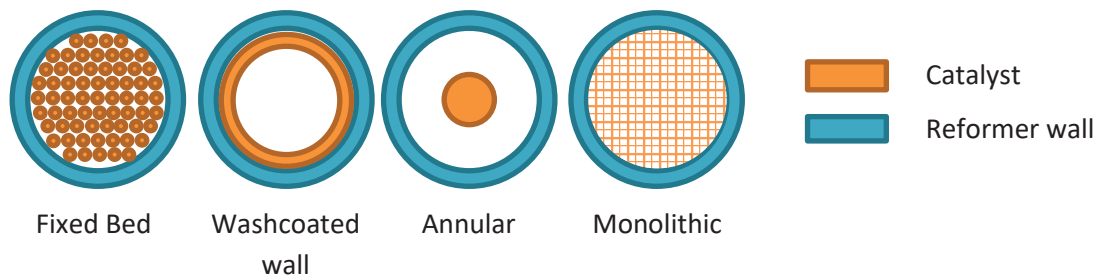


Figure 18: Cross-sections of tubular reformers with different catalyst configurations.

Fixed bed reactors are a packed bed of catalyst coated particles. Whilst the loading of the catalyst into the bed is the easiest of all the reactor designs [176], flow across the reactor is relatively restricted causing issues with pressure drop across the reactor. Restricted flow also means that expulsion of heat from the catalyst bed is limited [177,178]. Due to the large weight of catalyst per unit of volume the reforming capability of fixed bed reactors is generally high. Whilst this sounds preferable, it can actually be a negative attribute since

high proportions of reformation can take place within the relatively short lengths of the reformer. As previously addressed, this can cause a cold/hot spot (depending on the reformation strategy adopted) leading to a sharp thermal gradient. It has been shown that temperature gradients should not exceed $10^{\circ}\text{C.cm}^{-1}$ [170]. The risk of catalyst bed redistribution and gas channelling is also a problem with fixed bed reactors [178]. A fluidised bed is a fixed bed reactor with the special condition that the catalyst particles are constantly circulated. Jing and Zheng reported that this aided with the elimination of hot/cold spots since the movement of particles helps in thermal management [146].

Washcoated wall reactors consist of a channel with a thin layer of catalyst located on its peripheries. They contain less catalyst per unit volume, meaning that their reforming capacity is lower than that of a fixed bed reactor. Reformation therefore takes place over a larger area of the reformer, leading to a smoother temperature gradient. Compared to fixed bed reactors, wall coated reactors have a lower specific activity. Aguiar et al. reported that the reforming reaction for a wall coated reactor was only 8 times faster than the fuel cell reaction, whereas a fixed bed reactor with the same catalyst resulted in reformation being 170 times faster than the fuel cell reaction [156]. The pressure drop across the reactor was lower since the gas flow was less restricted, aiding in improving heat transfer [178].

However, since the amount of catalyst per unit volume was lower than in a fixed bed reactor, longer reactor paths were required to obtain an equal reforming capability. For planar fuel cells this is not an issue since the reforming channel can adopt a serpentine flow configuration. In order to obtain long reformer pathways in tubular cells however, long tubes are necessary. This can increase ohmic losses [179] and add system bulk. Lee et al. showed experimental results of washcoated wall reactors and fixed bed reactors, concluding

that when the effects of the difference in thermal gradients between the two systems were removed the fixed bed reactor was more stable over the 4 hour test period [176].

Monolith reactors are a higher surface area equivalent of washcoated-wall reactors. By maintaining a high surface area the reactors can benefit from similar activities to fixed bed reactors while maintaining the low pressure drop as well as enhanced heat and mass transfer of washcoated-wall reactors [180].

Kim-Lohsoontorn et al. [179] modelled different methods of catalyst integration in order to evaluate the effect of reactor design on the temperature gradient across the reformer, as well as the resulting fuel cell performance. A comparison between fixed bed, wash-coated wall, annular, and a novel annular-washcoated wall hybrid reactor revealed that the annular-washcoated wall design resulted in preferential reformer characteristics. The design utilised a high catalytically active surface area whilst limiting the pressure drop by allowing reactants to flow over the catalyst relatively unhindered.

Settar et al. discuss how the way in which catalyst is positioned on the walls of a tubular reformer impacts the catalyst performance [174]. Settar studied the endothermic steam methane reforming reaction and concluded that by isolating catalyst layers in discrete modules along the walls of a tube, the reactants did not suffer from large degrees of cooling due to the endothermicity of the reaction being spread across the reactor. As such, higher methane conversions and product yields were obtained with minimal thermal gradient.

Fazeli and Behman modelled the performance of two wall coated catalytic micro channel reactors [181]. Each of the reactors had a different geometry, either zig-zag or straight. The authors found that by increasing mass transfer of reactants to the catalyst the zig-zag

geometry resulted in more efficient hydrogen production. Due to the non-parallel alignment of the reactant flow and catalyst layer, the geometry aided in bulk transportation of reactants to the catalyst.

There is a limited amount of literature showing experimental results for the indirect internal reforming of hydrocarbons using partial oxidation. Perhaps since the cooling of the fuel cell stack cannot be achieved using this reforming strategy. However this method of reformation offers other advantages such as not requiring additional reactants, POx can utilise the oxygen from air to oxidise methane. The reaction also has a small enthalpy change; therefore thermal gradients are less extreme. Some authors have adopted this reformation strategy in an IIR system however. Majewski and Dhir tested a nickel catalyst both in a washcoated-wall tube reactor and in a monolith [182]. The authors recorded a hot spot at the fuel inlet 100°C higher than the operating temperature, leading to cell cracking. Operating the fuel cells at a lower temperature of 650°C increased the lifetime of the cells but reduced the power generated. Schwiedernoch used both experimentation and numerical studies to show the temperature gradient across a partial oxidation monolithic reactor [183]. As was reported by Majewski and Dhir, a hot spot at the fuel inlet was observed due to the total oxidation of fuel, followed by reformation. The temperature gradient across the cell should not be so dramatic for internal partial oxidation given the slightly exothermic nature of the reaction [184].

Chapter 3

METHODOLOGY

3.1	Catalyst Synthesis.....	56
3.1.1	SiO ₂ @Ni Synthesis.....	56
3.1.2	Ni@SiO ₂ Synthesis.....	58
3.2	Characterisation	59
3.2.1	Imaging.....	59
3.2.1.1	Scanning Electron Microscopy (SEM).....	59
3.2.1.2	Transmission Electron Microscopy (TEM)	61
3.2.2	Determination of Nickel Loading and Carbon Deposition	62
3.2.2.1	Thermogravimetric analysis (TGA)	62
3.2.3	Metallic Phase Identification.....	63
3.2.3.1	X-Ray Diffraction (XRD).....	63
3.2.3.2	X-Ray photoelectron spectroscopy (XPS)	64
3.2.4	Surface Area Analysis	66
3.3	Determination of Catalytic Activity	68
3.3.1	Gas Chromatography	71
3.3.2	Nitrogen balancing and conversion calculations	74
3.4	Washcoating catalysts onto alumina fibres	75
3.5	Fuel Cell Assembly.....	76

3.1 Catalyst Synthesis

In this work two silica supported, nickel catalysts which employ the silica support for differing functions were attempted to be made following previous work [117,138]. In order to compare the two catalysts it is important to synthesise the catalysts with comparable sizes and metal loadings. Both of these factors affect the active surface area and performance of the catalyst, as discussed in section 2.2. In this section the method for synthesising both catalysts will be presented and the variables that were changed in order to control the active surface area of the catalysts will also be discussed.

3.1.1 Ni/SiO_{2, sph} Synthesis

Spherical SiO₂ particles were made using the Stöber method and subsequently coated in nickel by a precipitation-deposition process as described by Majewski and Wood [138]. The size of the silica particles were controlled using varying concentrations of ammonia from 0.089 mol.L⁻¹ to 1.38 mol.L⁻¹ [185]. The nickel loading was controlled by varying the number of nickel coatings that were applied to the silica core.

To make the SiO₂ particles, an amount of absolute ethanol (EtOH)(VWR Chemicals, 99.79%) was mixed, by magnetic agitation, with an amount of tetraethyl orthosilicate (TEOS) (Sigma Aldrich, 98%) in a 100 ml water jacketed reaction vessel, the temperature of which was maintained at 25°C. An amount of deionised water and ammonia (Fisher, laboratory grade, 35%) were mixed in a separate beaker and were subsequently added to the reaction vessel, dropwise, fairly slowly. An exothermic reaction was induced which was visible by the production of gas bubbles in the reaction vessel and a colour change from a clear colourless solution to a white opaque solution. Equation 16 was used to synthesise a silica particle

predicted to be 20 nm in diameter, see Table 7 for the reactant volumes used. The reaction mixture was stirred at 25°C by magnetic agitation for 48 hours and then aged for 6 hours at 60°C. The SiO₂ particles were then separated from the solution by centrifugation (4000 rpm, 10 mins) and washed 4 times in EtOH. The silica cores were then dried at 50°C overnight.

As discussed by Qi et al. [185] the size of the silica particles produced is dependent on the rate of the hydrolysis and condensation of TEOS. During the Stöber process, TEOS is hydrolysed by the presence of water and ammonia and a siloxane network is then formed from the condensation of these monomer, i.e. a condensation polymerisation reaction produces the final silica particles. Careful balancing of the hydrolysis (monomer creation) and condensation (polymerisation) allows control over the size of the silica particles. Qi et al. discuss many factors which effect the rate of the hydrolysis and condensation reactions including: temperature, TEOS concentration, water concentration, and ammonia concentration. The authors conclude with the following equation for the prediction of silica particle size from preparation by the Stöber method and state that the most reliable way to control the process is to vary the ammonia concentration:

$$(16) \quad Y = -1.08(X_1 - 25) + 216.43(X_2 - 0.25) + 12.52(X_3 - 3.95) + 42$$

Where Y, X₁, X₂ and X₃ represent SiO₂ particle size (nm), temperature (°C), ammonia concentration (mol L⁻¹) and water concentration (mol L⁻¹) respectively.

Table 7: Volumes of reactants used

Predicted particle size	Volume of reactant / ml			
	Ammonia	Water	TEOS	EtOH
20	1.01	8.69	8.26	82.04

Silica particles were then coated in nickel oxide by precipitation deposition. 1.8 g of silica particles were added to 100 ml of deionised water and stirred by magnetic agitation for 10 minutes. Subsequently the particles were sonicated for 30 minutes. During this time, 0.1816 g of nickel nitrate hexahydrate (Sigma Aldrich, >97 %) was dissolved in 10 ml of deionised water. After sonication the silica suspension was transferred to a conical flask, using 6 ml of water to wash the volumetric flask. Whilst stirring, the nickel solution was added dropwise to the conical flask containing the silica suspension. The solution was covered and sonicated for a further 30 minutes and then heated to 95°C. Once 95°C had been established 0.3604 g of urea (Fisher, 99%) dissolved in 4 ml deionised water was added to the reaction vessel dropwise, whilst stirring. The solution was magnetically agitated and held at 95°C for 4 hours. Particles were then separated by centrifugation (6000 rpm, 10 mins, 25°C) and washed 4 times with deionised water. The product was dried at 80°C, overnight. Coating of the silica particles was repeated a number of times, following the above protocol, to achieve the desired nickel loading. The catalyst was calcined in air at 700°C for 4 hours and reduced in-situ under 25 % H₂/N₂ at 700°C overnight before testing.

3.1.2 Ni@SiO₂ Synthesis

Nickel oxide particles were prepared by a chemical precipitation method, they were then coated in silica by a modified Stöber method as reported by Li et al. [117]. First, 2.9 g of nickel nitrate hexahydrate was dissolved in 40 ml of deionised water. Alongside this, in the reaction vessel, 330 mg of polyethylene glycol (molecular weight = 20,000) (Sigma Aldrich) and 1 g of sodium hydroxide (Sigma Aldrich, 97%) were dissolved in 100 ml of deionised water. The reaction vessel was subject to continuous magnetic agitation whilst the nickel

solution was added, dropwise. The solution was further stirred for 1 hour. Nickel particles were then collected by centrifugation (5500 rpm, 10 mins, 25°C), washed twice with ethanol, twice with deionised water and finally dried at 50°C overnight.

After calcination of the nickel particles in air at 350°C for 2 hours, 1 g of the NiO particles were suspended in a solution containing 5 g of polyvinylpyrrolidone (PVP)(Sigma Aldrich, k29-32) and 500 ml of absolute ethanol. The solution was stirred for 12 hours. 50 ml of 25 wt% ammonia was then added to the NiO solution and sonicated for 30 minutes. A solution of 0.5 ml TEOS and 25 ml EtOH was then injected into the nickel solution and further sonicated for 1 hour. The product was collected by centrifugation (5500 rpm, 10 mins, 25°C), washed twice in ethanol and twice in water, then dried at 80°C for 6 hours. The catalyst was reduced in-situ at 700°C overnight under a flow of 25 % H₂/N₂.

3.2 Characterisation

3.2.1 Imaging

3.2.1.1 Scanning Electron Microscopy (SEM)

Electron microscopy is similar to optical light microscopy; the difference in the two techniques comes from the radiation which is used to observe the sample. Light microscopy uses a beam of light to illuminate the sample whereas in electron microscopy an electron beam is used. The wavelength of an electron beam is much smaller than that of a beam of light, as a result much greater resolution images can be obtained by electron microscopy.

During SEM an electron beam is focused onto the sample and reflected electrons are collected by detectors to build up an image. The name scanning, electron microscopy, is

assigned as the electron beam scans pixel by pixel in order to build up an image. At each pixel the detectors will record the number of back scattered or secondary electrons created and display this. The more electrons that are created the brighter that pixel appears [186]. SEM is used typically used to visualise micron scale features. In this work it was used to size silica particles which are 100s of nanometres in diameter, SEM also revealed the location of the catalyst after it was deposited on the alumina fibres.

Two microscopes were used for SEM in this work. A Hitachi table top TM3030 and also a Philips XL-30 (LaB6) when greater resolution images were required.

Samples for SEM either consisted of a powders or solid tubes. Powdered samples were simply held in position on carbon tape. Tubular samples were mounted in epoxy resin (Beuhler, EpoThin 2), they were then polished using a Beuhler EcoMet polisher with various polishing pads and diamond solutions from 75 μm -0.03 μm in size. Samples were exposed from the resin and made planar using the 75 μm pad. The grade of the pad was then reduced and the sample polished for 3 minutes before moving to the next smallest diamond grade. The epoxy was secured to the SEM stub using carbon tape and any non-conductive SEM samples were then sputter coated with gold or platinum before imaging.

During SEM, X-rays can also be produced from the sample via the absorption of the electron beam energy. These X-rays can be used for elemental identification of the sample, since the X-ray emitted is unique to the energy difference between two electron orbitals within the atom from which it has been emitted. This is unique to each element, allowing elemental identification. This technique is called Energy Dispersive Spectroscopy (EDS). For EDS

measurements on the Hitachi SEM, QUANTAX software was utilised whilst Oxford Instrument's INCA was used for the Philips SEM.

Particles and features were sized from images using ImageJ software. When particles were sized an average diameter of over 100 measured particles was taken.

3.2.1.2 Transmission Electron Microscopy (TEM)

During TEM a single layer of sample is subjected to an electron beam, the beam passes through the sample and is imaged on a phosphorescent screen. The opacity of the sample to the electron beam allows different features of the sample to be visualised. Darker regions showing heavier elements. TEM allows nanoscale features to be visualised. It was therefore used to observe the nano-sized catalysts and observe carbon growth on the catalysts.

TEM was carried out using two different instruments. A FEI Talos 200X and also a JEOL 2100F were utilised. Both were operated at 200kV.

Samples were prepared by suspending the catalyst in ethanol at a concentration of $1\text{mg}_{\text{sample}}\cdot\text{ml}_{\text{EtOH}}^{-1}$. The sample was well dispersed in the ethanol by sonification. 8 μl of solution was then micro-pipetted onto a commercial TEM grid. The grids used were purchased from EM Resolutions, copper 300 mesh grids were used with a carbon film support. The sample was allowed to settle onto the grid for 1 minute before excess solvent was removed using filter paper. Grids were then dried under a lamp and stored under vacuum until they were imaged. When using the JEOL 2100F, copper TEM grids with a lacey carbon support and graphene oxide coating were utilised in order to obtain the best contrast between nickel, silica and any carbon which may have been deposited after testing.

TEM also produces X-rays during imaging, allowing EDS to be performed. EDS was carried out using Oxford Instrument's INCA software. In the same way as SEM, particles/features were sized using ImageJ.

3.2.2 Determination of Nickel Loading and Carbon Deposition

3.2.2.1 Thermogravimetric analysis (TGA)

TGA comprises of a high accuracy mass balance which is located inside a furnace to which a gas supply or vacuum can be applied. TGA is used to determine the temperatures at which thermally driven processes such as reduction or oxidation occur by recording the change in mass with respect to temperature. It also allows determination of the amount of substance reduced/oxidised.

Thermogravimetric analysis (TGA) was performed using a Netzsch TG 209 F1, retrofitted with a ceramic furnace in order to enable samples to be measured under a flow of hydrogen, to observe reduction processes. Samples of 5 to 8 mg were held in an alumina crucible and exposed to 40 ml.min⁻¹ 5% H₂/N₂ in order to examine reduction processes and the same flow rate of air was used to evaluate the extent of carbon deposition, by carbon oxidation. Samples were heated to 900°C at a rate of 10 K.min⁻¹.

In order to calculate the nickel loading of a sample from the TGA data, the percentage weight loss associated to nickel oxide reduction was converted to a mass loss in grams using the sample mass. This was used to determine the number of moles of oxygen in the sample given that:

$$(17) \quad \text{moles} = \frac{\text{mass}}{\text{relative molecular weight (Mr)}}$$

The number of moles of Ni was then determined using the chemical formula of the species present, determined by XPS or XRD. The chemical formula determined the ratio of Ni:O in the sample, for example; the number of moles of nickel is equal to the number of moles of oxygen when the molecular formula of the nickel species present is NiO. When the nickel species present were determined to be Ni(OH)₂ the Ni:O ratio of 1:2 was used. Using the number of moles of nickel in the sample, the mass of nickel was then calculated using the above formula and the final nickel weight percent was calculated using:

$$(18) \text{ Nickel weight } \% = \frac{\text{weight of nickel in sample}}{\text{weight of sample}} \times 100$$

3.2.3 Metallic Phase Identification

3.2.3.1 X-Ray Diffraction (XRD)

During XRD samples are illuminated with X-rays and the amount by which any crystal lattice structures present diffracts the X-ray is measured. The detector rotates around the sample to collect diffracted radiation at different angles of 2θ . The diffraction pattern created is characteristic of samples and so XRD is used for sample identification via pattern matching to libraries of XRD data. Particle size can also be determined. In this work XRD was used to observe how the crystalline structures within the catalyst change pre and post reduction and testing. Particle sizes were also determined in order to observe agglomeration.

XRD data was collected on a Bruker D8 diffractometer fitted with a Cu source. Diffraction was conducted between 5 and 90° 2θ .

The software package EVA was used to interpret XRD data and the International Centre for Diffraction Data (ICDD) pdf 2 database was used to pattern match.

Particle size, τ , was obtained from the extent of peak broadening in the diffraction pattern using the Scherrer equation:

$$(19) \quad \tau = \frac{K\lambda}{\beta \cos\theta}$$

Where K is a dimensionless shape factor of 0.9, λ is the X-ray wavelength, β is the full width half maximum of the diffraction peaks of the particle you are interested in and θ is the diffraction angle of that peak.

3.2.3.2 X-ray photoelectron spectroscopy (XPS)

XPS is used to determine surface specific structural information. XPS irradiates a sample with X-rays, the sample absorbs the energy of these X-rays causing electrons to be emitted from the sample. The binding energy of the detected photoelectrons are measured and this is used to give information about the environment in which the atom, that the photoelectron was emitted from, is in. XPS is surface specific since photoelectrons quickly lose their energy by interacting with other matter. Only electrons emitted from around the first ~3-10 nm of a sample are able to reach the detector. For this reason XPS is especially useful in catalysis, where most reactions occur on surfaces of species. XPS was therefore used to show structural groups present at the sample surface.

Survey scans were first recorded between 0 and 1350 eV, this was a low resolution scan covering a wide range of binding energies in order to observe what species were present in a sample. From this survey regions were selected that indicate the presence of a certain element, Ni for instance at around 860eV, as shown in Figure 19. The regions were then

scanned with high resolution in order to more accurately determine the state in which the elements present are found, oxides, hydroxides etc.

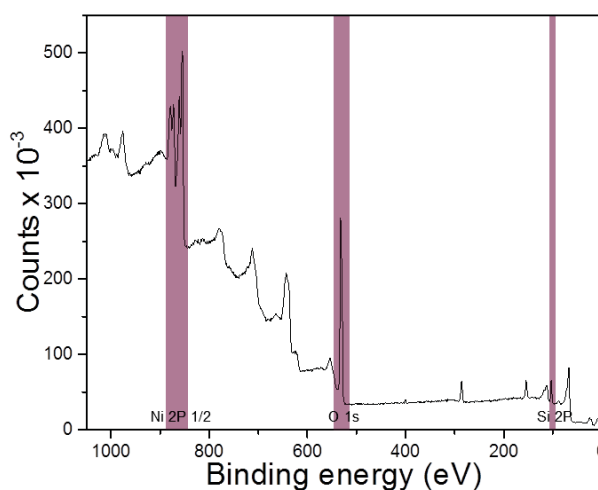


Figure 19: XPS survey scan of Ni@SiO₂

Figure 20 shows an example of a high resolution XPS spectrum measured over the region of the nickel 2P binding energy.

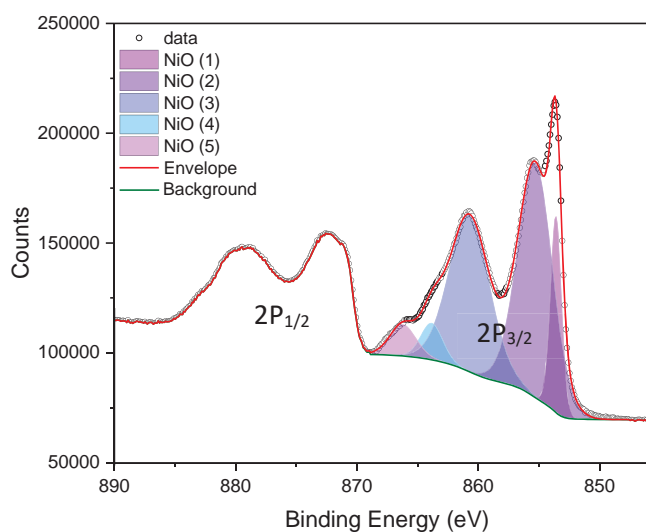


Figure 20: High resolution XPS in the Ni 2P region

X-ray photoelectron spectroscopy (XPS) was performed on a Thermo Fisher Scientific K-alpha+ spectrometer. Samples were analysed using a micro-focused monochromatic Al X-ray source (72 W) over an area of approximately 400 microns. Data was recorded at pass

energies of 150 eV for survey scans and 40 eV for high resolution scan with 1 eV and 0.1 eV step sizes respectively. Charge neutralisation of the sample was achieved using a combination of both low energy electrons and argon ions. Samples were introduced to the spectrometer as a powder, lightly compacted into the holder using a spatula.

Data analysis was performed in CasaXPS using a Shirley type background and Scofield cross sections, with an energy dependence of -0.6. Figure 20 shows a spectra with an applied background onto which components have been added, the purple/blue coloured peaks. Each component represents photoelectrons emitted from different environments or shows the effect of multiplet and shake up peak splitting as represented in Figure 21 [187].

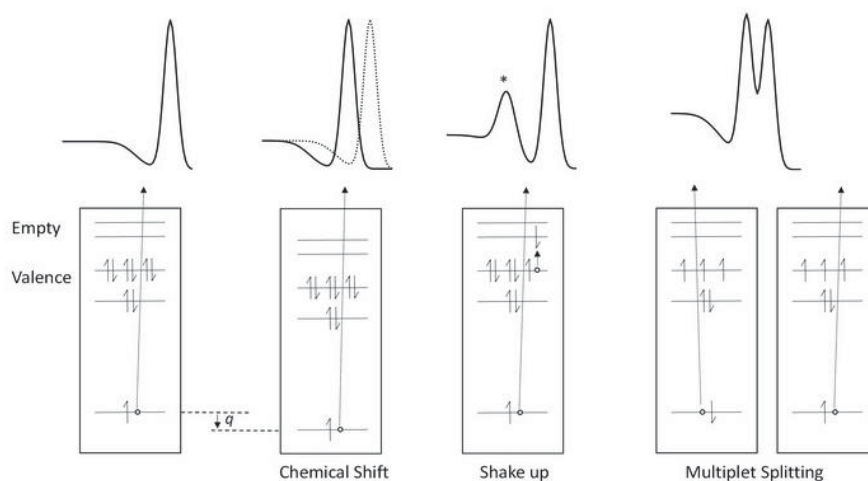


Figure 21: The origin of peak shapes in XPS [185].

3.2.4 Surface Area Analysis

The surface area of the catalysts was determined by N₂ adsorption-desorption using a Micrometrics 3Flex. 100 point adsorption/desorption isotherms were recorded at -196°C. Samples were degassed at 150°C under vacuum for 4 hours prior to analysis.

N₂ adsorption works on the principle that molecules of nitrogen adsorb onto the surface of powders when pressure is applied to the system. The amount of nitrogen which is absorbed onto the surface is measured relative to the pressure applied, while temperature is held constant. When a monolayer of nitrogen molecules has been adsorbed onto the surface the Brunauer-Emmett-Teller (BET) formula, equation 20, is applied in order to calculate the surface area. Where P is the partial pressure of nitrogen in equilibrium with the surface at 77.4 K, in pascals. P₀ is the saturated pressure of nitrogen, in pascals. V_a is the volume of gas adsorbed at standard temperature and pressure (STP) in ml. V_m is the volume of gas adsorbed at STP to produce a monolayer on the sample surface in ml. C is a dimensionless constant that is related to the enthalpy of adsorption of nitrogen gas onto the powder sample.

$$(20) \quad \frac{1}{\left[V_a \left(\frac{P_0}{P} - 1 \right) \right]} = \frac{C - 1}{V_m C} \times \frac{P}{P_0} + \frac{1}{V_m C}$$

The pressure is further increased until the surface is fully saturated with nitrogen. At this point micro and mesopores are filled with nitrogen. The manner in which nitrogen desorbs from the surface can give information about the shape of the pores present. Differently shaped hysteresis loops can be observed in the isotherms, Figure 22. Table 8 summarises the pore shape which would give rise to each of the hysteresis loops [188].

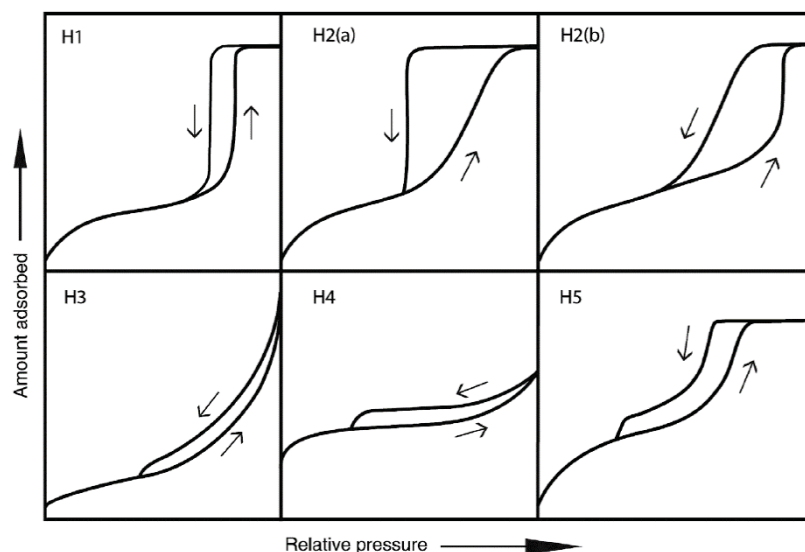


Figure 22: The different possible shapes of hysteresis loops [182].

Table 8: Classification of hysteresis loops [182].

Hysteresis Loop Classification	Pore shape
H1	Materials with a narrow range of uniform mesopores.
H2(a)	Pore-blocking caused by narrow pore necks.
H2 (b)	Pore-blocking caused by narrow pore necks, neck size has a wider range than H2(a).
H3	Non-rigid clusters of plate-like particles.
H4	Similar to H3 but the space between plates is smaller.
H5	Pore structures containing both open and partially blocked mesopores.

3.3 Determination of Catalytic Activity

The catalytic reactor used in this work consisted of an electrical horizontal tube furnace containing a quartz tube with an inner diameter of 6 mm. An amount of catalyst was loaded into the quartz tube and held in place by inert quartz wool. To compare the performance of different catalysts, each catalyst was subjected to the same two day test procedure which varied temperature as well as the $\text{CH}_4:\text{O}_2$ ratio. The exhaust gas composition was constantly analysed during this period by gas chromatography (Shimadzu, GC2014). On day 1 of testing, after in-situ reduction as previously described in section 3.1.1 and 3.1.2, the furnace was

cooled to 550°C with a ramp rate of 5°C.min⁻¹. The gas flow was then changed from a reducing atmosphere to a flow of molar ratio 1:0.5 CH₄:O₂, N₂ was used as a carrier gas. The total flow rate used was 67.2 ml.min⁻¹ (gas hourly space velocity (GHSV) = 80640 ml.g⁻¹.h⁻¹). As such flow meters were set to deliver 10.1 ml.min⁻¹ O₂, 20.2 ml.min⁻¹ CH₄ and 37.0 ml.min⁻¹ N₂. During day 1 the temperature was varied from 550°C to 950°C in 100°C intervals, each temperature was maintained for 2 hours. The actual temperature within the rig was tested using a K-type thermocouple which was positioned in the middle of the catalyst bed, touching the external wall of the quartz tube. After the furnace had held the catalyst at 950°C for 2 hours the rig was cooled to 750°C and maintained at that temperature overnight, the exhaust gas continued to be monitored by GC during this time. Day 2 of testing was used to evaluate the effect of varying CH₄:O₂ ratio on catalyst performance. Temperature was maintained at 750°C whilst the CH₄:O₂ ratio was varied from 3.33 to 1.43. During this time the GHSV remained 80640 ml.g⁻¹.h⁻¹, mass flow meters were set to deliver the quantities given in Table 9. Each test level was maintained for a minimum of four GC measurements, approximately 1 hour.

Table 9: Flow rates used to test the effect of CH₄:O₂ ratio on catalyst performance.

CH₄:O₂ Ratio	O₂ / ml min⁻¹	CH₄ / ml min⁻¹	N₂ / ml min⁻¹
3.33	6.0	20.1	41.0
2.5	8.1	20.1	39.0
2	10.1	20.1	37.0
1.67	12.1	20.1	34.9
1.43	14.1	20.1	32.9

It is clear from the literature [95,100,102,111,125,189] that a thermal gradient across the reactor bed is problematic for comparison of results and determining a reaction mechanism. Multiple experimental tricks can be adopted to combat this. Looij et al. diluted the fuel gases

to just 1% methane and 0.5% oxygen [95] this was also adopted by other authors [102]. Alternatively, the catalyst bed itself can be diluted with an inert substance [100,102,125]. Care must be taken when doing this as it has been shown that this can reduce catalytic activity [189]. Another method of obtaining an isothermal reactor which has been adopted is to pulse the fuel feed gas rather than maintaining a constant feed gas supply [111]. In this study diluting the reactants with N₂ was used.

GHSV was varied by changing the flow rates of reactants over the catalysts. 750°C and a CH₄:O₂ ratio of 2 were maintained during these experiments. Table 10 shows the flow rates tested. To achieve high GHSV the weight of the catalyst tested was reduced. Weights tested are also given in Table 10.

Table 10: Tested gas hourly space velocities.

Weight of Catalyst (g)	Total Flow Rate (ml.min ⁻¹)	Gas Hourly Space Velocity (ml.g ⁻¹ .h ⁻¹)
0.05	67.2	80640
0.05	89.6	107520
0.05	112.0	134400
0.05	134.3	161160
0.05	156.7	188040
0.05	179.1	214920
0.0125	67.2	322560
0.0125	89.6	430080
0.0125	112.0	537600
0.0125	134.3	644640
0.0125	156.7	752160
0.0125	179.1	859680
0.0063	67.2	640000
0.0063	89.6	853333
0.0063	112.0	1066666
0.0063	134.3	1279047
0.0063	156.7	1492380
0.0063	179.1	1705714

3.3.1 Gas Chromatography

Gas chromatography is a technique used for determining the composition of gas mixtures by separating the mixture into single gas portions and recording the abundance of each gas present. An aliquot of the sample is carried from the injector onto the column by a carrier gas. The column separates the mixture since each gas within the sample has a different affinity towards the column. After the column there is a detector, which will show the abundance of each gas portion as it leaves the column. The gases are therefore separated by retention time; the time that it takes each gas to pass through the column and reach the detector. Results are presented as a series of peaks in a spectrum with intensity on the y axis and retention time on the x axis. The area of the peaks directly correlates to the concentration of the analyte present at that retention time. It is important to understand that the detector simply measures the presence of any species different to the carrier gas, it does not identify the species. Therefore, both the column and the detector are vital for quantitative analysis and good calibration is crucial.

In this work a Shimadzu GC2014 was upgraded and used. The upgrade included fitting a heated gas sampling loop, replacing the injector and replacing the column itself. A gas sampling valve sits on the exhaust line of the catalytic reactor, Figure 23. When the valve is in position 1 (blue pathway) gas from the reactor will flow through the sampling loop and to the exhaust. When the valve is switched to position 2 (pink pathway) the gas in the sampling loop is transferred into the injector by the carrier gas. In this way a constant volume of sample is injected into the instrument for each measurement, the sampling loop used in this study had a volume of 1 ml. The sample loop allows for measurements to be recorded approximately every 12.5 minutes, over long periods of time. The measurement time is

limited by the amount of time taken for different gases in the sample to be separated on the column and reach the detector. The injector itself was replaced with a split injector. A split injector allows samples to be diluted to avoid overloading the column. When the column is “overloaded” peaks appear broad and may overlap, this makes integration difficult and ultimately the results are less reliable. Finally, the column was replaced with a ShimCarbon ST micropacked column which is capable of separating methane, carbon monoxide, carbon dioxide, nitrogen, and hydrogen in a single measurement. The instrument was already fitted with a thermal conductivity detector, TCD. This detector measures the variation in thermal conductivity of two filaments. Both filaments are held within a temperature controlled cell, having independent gas streams flowing over them. One filament is the reference and is kept within a flow of carrier gas, in this case argon. The other filament is exposed to the stream of gas leaving the column. This stream contains the carrier gas and any separated analytes from the sample. When an analyte leaves the column the thermal conductivity of the gas surrounding the filament is lowered and the filament heats up. This makes the resistance of the column filament differ from that of the reference and thus a response signal is generated. Figure 23 shows a schematic of the GC system used in this work.

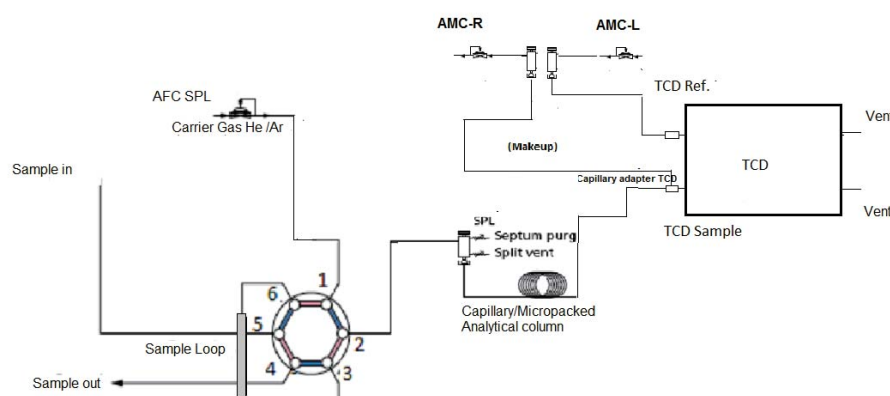
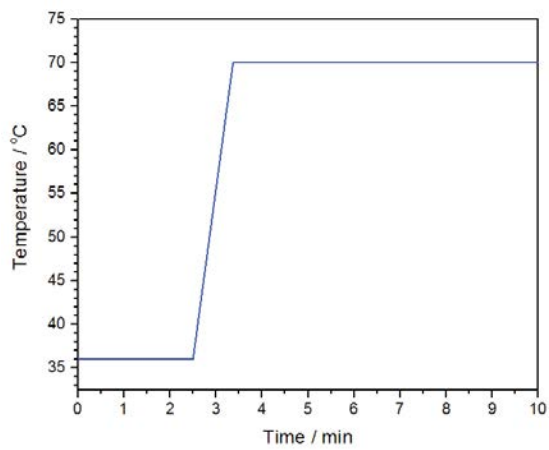


Figure 23: Schematic of Gas Chromatography System

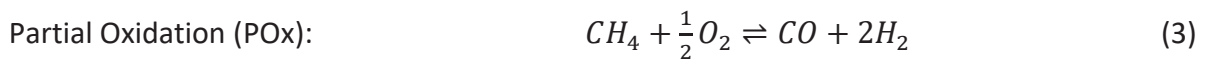
When poor separation occurs in the column, peaks overlap one another and quantitative analysis of the results is not possible. Therefore it is necessary to create a method specifically designed for the mixture of gases being tested. Several method parameters can be modified in order to ensure good separation of a sample. The following parameters were optimised for this work and they are discussed in turn in Appendix C to F: Column flow rate, column temperature profile, split ratio and detector current. The method parameters used in this work are summarised in Table 11 below.

Table 11: GC Method Parameters

Parameter	Unit	Set
Injector Temperature	°C	100
Column flow	ml min ⁻¹	4.81
Split ratio	N/A	35.0
Total flow	ml min ⁻¹	173.0
Pressure	psi	53.9
Column Temperature Profile	°C	 <p>Initial : 36 Ramp rate: 45 °C min⁻¹ Final : 70</p>
Detector Temperature	°C	75
Detector Current	mA	75
Sample Loop heater Temperature	°C	60
Detector Reference Gas Flow	ml min ⁻¹	20
Make up gas flow	ml min ⁻¹	17.6

3.3.2 Nitrogen balancing and conversion calculations

As equation 3 shows, as POx progresses the total number of moles in the system changes since there are 3 moles of products formed for every 1.5 moles of reactants consumed. This is disregarding any side reactions that could occur, such as total oxidation, steam methane reforming (SMR), dry reforming (DR), water gas shift (WGS), or methane cracking which could all contribute to the number of moles in the system changing.



Since the total number of moles in the system varies we must determine the number of moles of reformat from the GC data in order to convert the composition of reformat from mole fraction to the number of moles of each species in the gas mix.

Measuring the flow rate of the exhaust gas from the reactor would be one method of calculating the total number of moles in the exhaust. However, this is time consuming and unrealistic given the timescale of the experiments conducted in this work. Atom balancing is another method which achieves the same end. In this method the amount of atoms of a certain element are calculated before a reaction and are accounted for in the products.

Assuming no nuclear reactions occur any atom that is present in the reactants will be present in the products. Nitrogen was selected as the atom with which to balance in these experiments. Nitrogen is an inert gas in the feedstock; it does not participate in the reaction therefore $n_{N_2,in} = n_{N_2,out}$, where n_x is the number of moles of species x and in and out denote a reactant or product, respectively. We can also accurately measure the amount of nitrogen in the exhaust using the gas chromatograph making it the ideal candidate for atom balancing. Nitrogen atoms were balanced as below, where γ_x is the mol fraction of species x .

$$(21) \quad n_{total,out}(moles) = \frac{n_{N_2,in}(moles)}{\gamma_{N_2,out}}$$

The number of moles of each product was then calculated by:

$$(22) \quad n_{x,out}(moles) = n_{total,out}(moles) \times \gamma_x$$

Percentage methane conversion along with H₂ and CO yields were calculated as follows.

$$(23) \quad CH_4 \text{ conversion } (\%) = \frac{n_{CH_4,in}(moles) - n_{CH_4,out}(moles)}{n_{CH_4,in}(moles)} \times 100$$

$$(24) \quad H_2 \text{ product yield} = \frac{n_{H_2,out}(moles)}{n_{CH_4,in}(moles)}$$

$$(25) \quad CO \text{ product yield} = \frac{n_{CO,out}(moles)}{n_{CH_4,in}(moles)}$$

$$(26) \quad CO_2 \text{ product yield} = \frac{n_{CO_2,out}(moles)}{n_{CH_4,in}(moles)}$$

3.4 Washcoating catalysts onto alumina fibres

Washcoat solutions were prepared by dispersing catalysts in ethanol at a concentration of 1g.L⁻¹. The washcoat was subjected to sonication for 1 hour in order to ensure good dispersion of the catalyst in the solution.

The alumina fibres to be washcoated were dried in an oven at 120°C for more than 1 hour before being weighed and then inserted into the washcoating apparatus, Figure 24A. The apparatus consists of a rotary pump and silicon tubing from which the alumina fibres were hung. The washcoat was prepared in conical flask and agitated using a magnetic stirrer bar and plate.

0.5 L of washcoat was magnetically agitated at 300 rpm whilst being circulated through the fibre for different lengths of time, at different circulation speeds, with or without the application of back pressure onto the fibre. Backpressure was applied to the alumina fibre by attaching a second length of tube to the outlet of the alumina fibre and securing a crocodile clip to that, Figure 24B. After coating, the fibres were dried in an oven at 50°C overnight. The dried fibres were then reweighed in order to determine the catalyst loading. Fibres were finally calcined in air at 350°C for 2 hours.

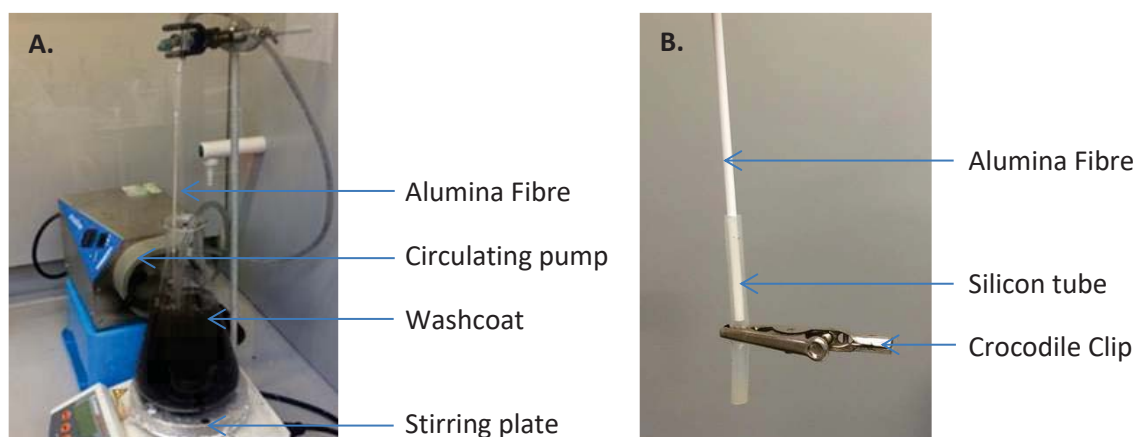


Figure 24: A. Washcoating apparatus B. Application of back pressure.

3.5 Fuel Cell Assembly

Tubular fuel cells were purchased from Ultra Electronics for this work. The cells are anode supported and are delivered as full cell consisting of a layered ceramic tube of NiO-YSZ/YSZ/SDC/LSFC (Anode/Electrolyte/Buffer/Cathode). The cells do not have any current collectors or manifolds and therefore these must be added.

Firstly, to add the anode current collector, a 10 mm section of the electrode is removed from the centre of the cathode using a razor blade. A 1 mm section of the electrolyte is filed away in order to expose the anode to the exterior of the tube. A non-porous silver paint (Shanghai Research Institute of Synthetic Resins, DAD-87) was applied to the exposed anode. The paint

was dried in air at 100°C for 1 hour. During this time a four strand wire of 0.375 mm silver wire was wound with a loop at one end. The wire was produced to be long enough to connect to the anode and extend out of the furnace. The fuel cell was removed from the oven and allowed to cool, then the previously prepared wire was connected to the anode using the loop in the wire. A second layer of non-porous silver paint was applied over the anode current collector. The silver paint provided both electrical conductivity and a barrier for gas diffusion, again the paint was dried in air at 100°C for 1 hour.

The exposed cathode was painted in a thin layer of porous silver paint (STI, silver conductive paint) to create an electrical contact. The paint was dried in air at 100°C for 1 hour. A 4 strand wire was prepared using 0.25 mm silver wire. This was prepared with a bridge in its centre to create a cathode current collector which would straddle the anode connection. A longer double stranded silver wire was prepared using 0.25 mm silver wire, long enough to connect to the current collector bridge and extend out of the furnace. After the fuel cell was removed from the oven and cooled, the current collector was secured in place using six silver wire ties (90 mm lengths of double stranded 0.25 mm silver wire). The longer wire was then secured at the current collector bridge. Quartz insulating sheaths were placed over the anode and cathode current collectors to prevent short circuiting in the furnace.

Alumina tubes were used to connect the fuel cell to the gas supply and exhaust. They were cut to the appropriate length and secured to the fuel cell using a high temperature glue (PI-KEM, Ceramabond 552). The Ceramabond was dried in air for several hours followed by being cured at 93°C for 2 hours and then at 260°C for 2 hours. A Glass seal (Schott, G018-354) was then applied over the Ceramabond and also around the anode current collector to

prevent gas crossover. The glass was fired at 850°C for 4 hours. A 25% H₂/N₂ gas mix was passed over the anode during this time to prevent oxidation.

A second layer of glass seal was applied to both the Cerambond connections and the anode current collector and fired as above before testing. A fully assembled fuel cell is shown in Figure 25.

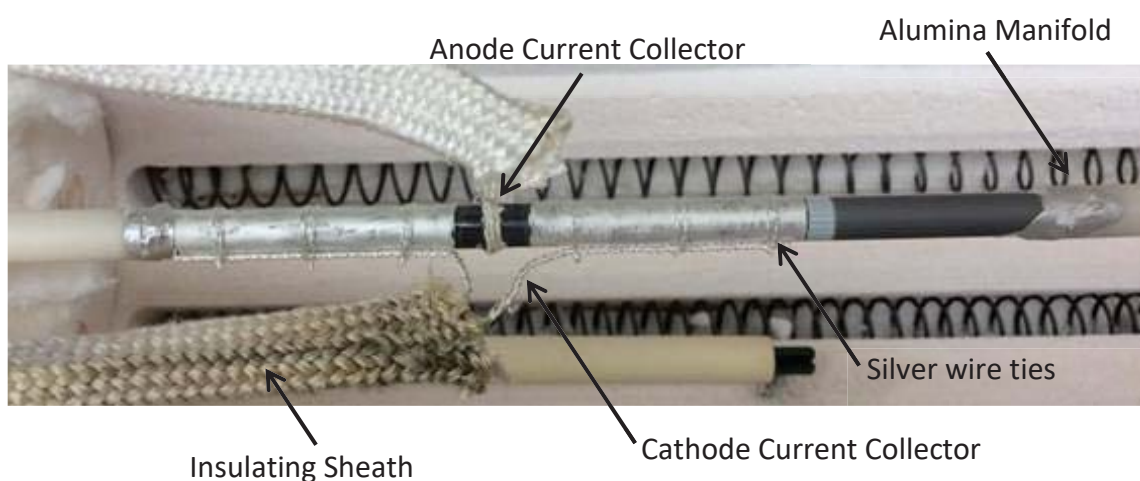


Figure 25: Assembled fuel cell ready to test.

The electrochemical performance of the fuel cells was assessed using a Solartron 1470E CellTest System (Solartron Analytical) and a 125 W booster (Solartron Analytical).

Chapter 4

CHEMICAL EQUILIBRIUM ANALYSIS (CEA)

4.1	The effect of temperature on Gibbs free energy	81
4.2	Chemical Equilibrium Analysis Results.....	85
4.2.1	Effect of Temperature on the Composition at Equilibrium	85
4.2.2	The effect of $\text{CH}_4:\text{O}_2$ ratio on the equilibrium gas composition.....	88
4.3	Comparison with experimental data	91
4.4	Summary	92

Chemical equilibrium analysis (CEA) was performed for the partial oxidation (POx) of methane in order to predict trends in the reformat composition which could be expected when varying the catalyst operating temperature and the feedstock gas ($\text{CH}_4:\text{O}_2$ ratio). CEA provides a target by which to measure improvements made in POx by the catalyst [190]. The equilibrium compositions were calculated using the freely available NASA CEA software (found at: <https://www.grc.nasa.gov/WWW/CEAWeb/>). The software uses the minimum Gibbs free energy of reactants and all possible products in order to give the expected equilibrium product concentrations. The composition of the reactant mixture, along with a range of temperatures wished to be observed, and pressure is input to the software. Results are given as a list of gas compositions in mol fraction, each set of values referring to the equilibrium composition at the temperature of interest. These values have been used to calculate the percentage of methane conversion along with H_2 , CO , and CO_2 product yields using the method given in section 3.3.2. H_2 and CO yields are particularly interesting, having the potential to supply fuel cells, CO_2 yield is recorded to highlight where undesirable side reactions occur. Due to the extremely low concentrations, HCN and NH_3 were omitted as possible products of the reaction and any product with a concentration lower than 1×10^{-4} mol% were not reported by the software. It was later confirmed that no products other than those given in the results of this section were observed experimentally; no additional, unidentified peaks were observed in GC. This supported the decision to omit products lower with concentrations than 1×10^{-4} mol%.

4.1 The effect of temperature on Gibbs free energy

As previously mentioned the CEA software used, minimises the Gibbs free energy in order to predict the equilibrium product composition. It is known that Gibbs free energy varies with temperature according to the following equation:

$$(27) \quad \Delta G (kJ.mol^{-1}) = \Delta H(kJ.mol^{-1}) - T(K)\Delta S(J.K^{-1}.mol^{-1})$$

Where ΔG is the change in Gibbs free energy, ΔH is the enthalpy change of the reaction and ΔS is change in entropy of the reaction. ΔH and ΔS are calculated by subtracting the sum of enthalpies/entropies of the reactants from the products of a reaction. Table 12 shows the thermodynamic values of the species of interest. An example calculation is given for the partial oxidation reaction in Appendix A.

Table 12: Thermodynamic values of species of interest [181]

Species	Enthalpy of formation, ΔH_f^0 (kJ.mol ⁻¹)	Entropy, S (J.mol ⁻¹ .K ⁻¹)
CO (g)	-110.54	197.9
CO ₂ (g)	-393.51	213.68
CH ₄ (g)	-74.85	186.27
H ₂ (g)	0	130.59
C (s)	0	5.69
H ₂ O (g)	-241.82	188.72
O ₂ (g)	0	205.03

As has already been identified in section 3.3.2, partial oxidation is not entirely described by a single chemical equation. The number of contributing reactions to POx varies in literature [191,192] a list of possible reactions and side reactions are presented in Table 13. Although it is apparent that there are many possible side reactions and reactions which could lead to

carbon deposition, it is accepted that the main side reactions of partial oxidation are the water gas shift, steam reforming and dry reforming reactions [191].

Table 13: Possible reactions taking place during partial oxidation

Oxidation			
Partial Oxidation	POx	$CH_4 + 0.5 O_2 \rightarrow CO + 2H_2$	(3)
Combustion	Comb.	$CH_4 + 2O_2 \rightarrow CO_2 + 2H_2O$	(6)
Methane Oxidation [191]	CH ₄ Ox.	$CH_4 + O_2 \rightarrow CO_2 + 2H_2$	(28)
Carbon Monoxide Oxidation [191]	CO Ox.	$CO + 0.5 O_2 \rightarrow CO_2$	(29)
Hydrogen Oxidation [191]	H ₂ Ox.	$H_2 + 0.5 O_2 \rightarrow H_2O$	(30)
Side reactions			
Steam Reforming	SR	$CH_4 + H_2O \rightleftharpoons CO + 3H_2$	(2)
High Temperature Steam Reforming [192]	HTSR	$CH_4 + 2H_2O \rightleftharpoons CO_2 + 4H_2$	(31)
Dry Reforming	DR	$CH_4 + CO_2 \rightleftharpoons 2CO + 2H_2$	(4)
Water Gas Shift	WGS	$CO + H_2O \rightleftharpoons CO_2 + H_2$	(1)
Methanation [192]	Meth.	$CO + 3H_2 \rightleftharpoons CH_4 + H_2O$	(32)
Carbon Deposition			
Methane Cracking		$CH_4 \rightarrow C + 2H_2$	(15)
Boudouard		$2CO \rightleftharpoons CO_2 + C$	(14)
Reverse Coal-Gas [192]	RCG	$H_2 + CO \rightleftharpoons C + H_2O$	(33)
Carbon Removal			
Carbon Oxidation 1	C _s Ox.	$C + O_2 \rightarrow CO_2$	(34)
Carbon Oxidation 2	C _s Ox. (2)	$C + 2H_2O \rightarrow CO_2 + 2H_2$	(35)

The Gibbs free energy, at different temperatures, of the different reactions listed in Table 13 was calculated. Graphs were plotted using these values; the graphs show the processes which are favoured, as temperature increases. A process with a lower Gibbs free energy is thermodynamically favoured over ones with higher Gibbs free energies. The reactions are split into 2 graphs for clarity, one showing oxidation and side reactions, Figure 26, and another concerning carbon deposition and removal, Figure 27.

When assessing the effect of temperature, a larger temperature range was evaluated (50-1000°C) than was experimentally observed and a smaller temperature interval was selected (50°C). This decision was made due to the ease of obtaining equilibrium data with use of the CEA software/Excel and so that a comprehensive assessment of trends could be made. Conditions where carbon deposition should be expected could also be found in this way. The range of temperatures observed goes beyond the ranges reported in literature where the thermodynamics of partial oxidation is usually considered at higher temperatures (>750°C) [190,192].

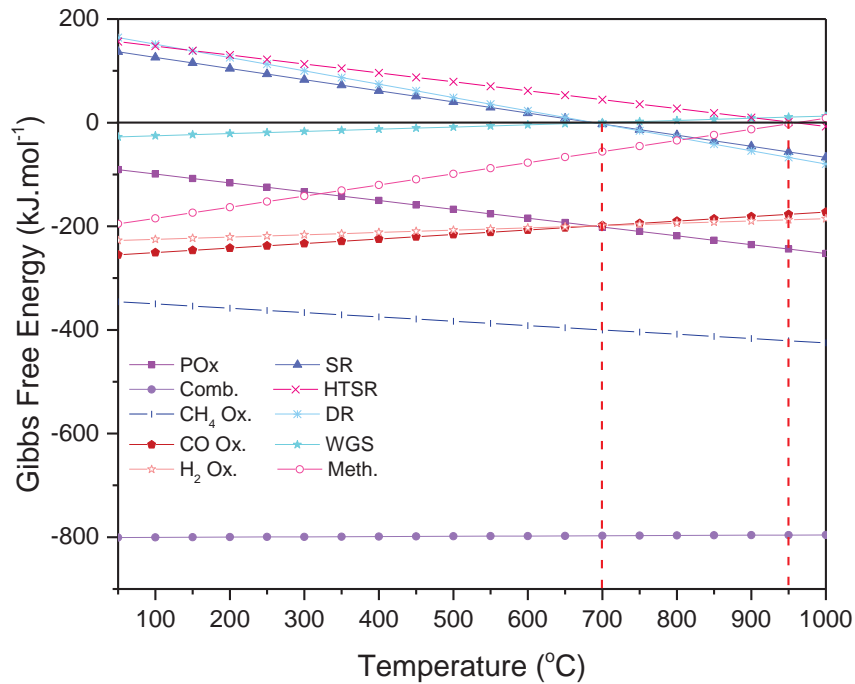


Figure 26: Gibbs free energy of possible reactions occurring during partial oxidation. Zoomed in versions can be found in Appendix B.

Figure 26 shows that combustion is energetically favoured at all temperatures. It follows then that partial oxidation would be a two-step process, at equilibrium, as argued in literature [193] as opposed to direct POx. Firstly, oxygen is quickly consumed in the complete combustion of methane to carbon dioxide and water. Dependant on the

temperature, the now mixture of CO_2 , H_2O and CH_4 will go on to participate in reforming and conversion reactions (Table 13).

At low temperatures, Figure 26 shows that the WGS, POx, methanation, CH_4 Ox., CO Ox. and H_2 Ox. reactions are thermodynamically viable, all having negative Gibbs free energies.

Oxygen is rapidly consumed in the energetically favourable combustion of methane [194], therefore the contribution of direct POx, CO Ox. and H_2 Ox are all negligible due to the lack of availability of oxygen. It is suggested that a small contribution of POx along with WGS and methanation determine the final product composition at low temperature [191].

There are two tipping points one at 700°C and another $>950^\circ\text{C}$. At 700°C SR, DR and cracking become viable while the Gibbs free energy of WGS becomes positive. At $>950^\circ\text{C}$ the high temperature SR reaction becomes viable whilst methanation become thermodynamically disfavoured.

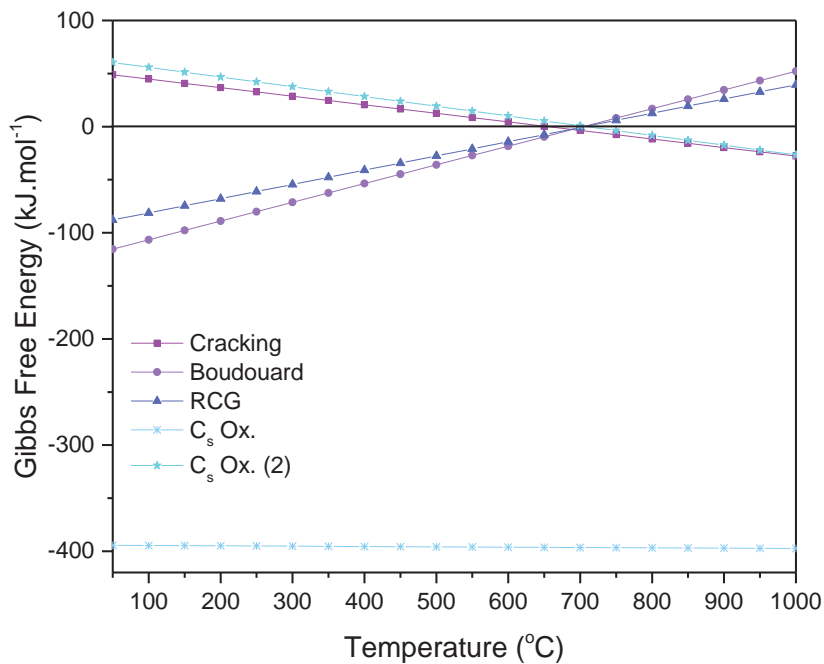


Figure 27: Gibbs free energy of carbon deposition and removal reactions.

Figure 27 shows how any low temperature carbon deposition can be associated with the Boudard and RCG reaction whilst high temperature carbon deposition would be as a result of cracking.

4.2 Chemical Equilibrium Analysis Results

The feedstock composition input to the CEA software to examine the effect of temperature was 9×10^{-4} moles CH_4 , 4.5×10^{-4} moles O_2 and 1.65×10^{-3} moles N_2 . Flow cannot be taken into account in the CEA software. The number of moles of species which enter the reactor per minute experimentally, were selected as the input variables. Pressure was set to 1 atm for all equilibrium analysis.

4.2.1 Effect of Temperature on the Composition at Equilibrium

Figure 28 shows the variation in enthalpy change of the partial oxidation reaction at different temperatures. Values were taken from the CEA software at $\text{CH}_4:\text{O}_2$ ratio = 2. The enthalpy of the reaction becomes slightly positive at $T > 850^\circ\text{C}$. This indicates that endothermic reactions dominate in this region [191]. This is consistent with the results given in Figure 26 which show that SR and DR have the lowest Gibbs free energy of all the side reactions given in Table 13 which do not require the presence of oxygen at 850°C .

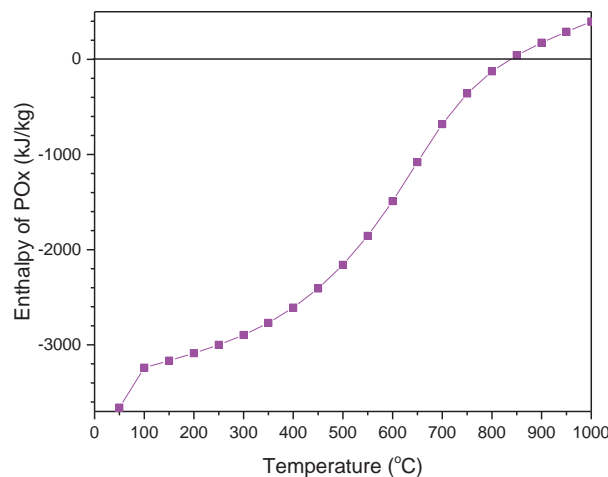


Figure 28: Change in enthalpy of partial oxidation with temperature.
 $\text{CH}_4:\text{O}_2$ ratio = 2, pressure = 1 atm

Figure 29 shows how the composition at equilibrium changes with increasing temperature as a result of the change in Gibbs free energy of all possible reactions. It is a simulation of the consequences of Figure 26 to Figure 28 in terms of number of moles of species present at equilibrium.

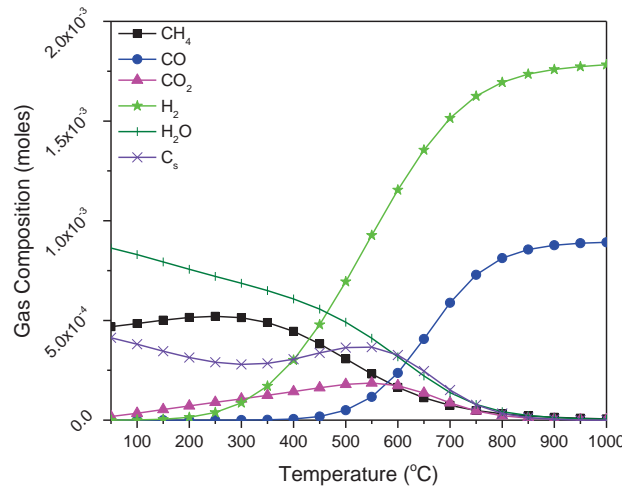


Figure 29: Effect of temperature on the equilibrium conversion of methane to syngas via partial oxidation

Figure 29 shows that carbon deposition is likely to occur at low temperatures and dramatically decreases at temperatures greater than 550°C to near zero by 800°C, this is consistent with literature [191,195]. As previously stated low temperature carbon deposition can be ascribed to the Boudouard and reverse coal-gas reactions since these reactions have negative Gibbs free energy at these temperatures.

Analysing the thermodynamics of carbon formation is important for the validity of results pertaining to the extent of carbon deposition on the catalysts, it shows feedstock gas should be turned on only when the catalyst is at temperature and switched to an inert gas before the catalyst is cooled down. In this way post mortem characterisation of the catalyst

accurately represents carbon deposition from the tests which have been conducted rather than that which has occurred during heating and cooling.

From Figure 29 it is visible that hydrogen is produced at very low temperatures ($<350^{\circ}\text{C}$), this is as a result of the WGS reaction. This is evidenced by the increase in H_2 and CO_2 coupled with the decrease in H_2O and low-zero concentrations of CO present. As well as the WGS reaction having the lowest Gibbs free energy reactants as previously described. At $T < 650^{\circ}\text{C}$ CO concentration is much lower than that suggested by the reaction for partial oxidation, reaction (3), i.e. there is not 2 moles of CO for every 1 mole of H_2 . This evidences that the direct POx pathway is not dominant. CO concentrations remain low due to the viability of several CO consuming reactions at these temperatures. Namely the WGS, Boudouard, RCG and methanation. CO is produced in rapidly increasing amounts at temperatures higher than $\sim 450^{\circ}\text{C}$ as the Gibbs free energies of these reactions becomes more positive and reforming reactions become more viable.

At the first “tipping point” at 700°C , Figure 29 shows the composition of the reformat at equilibrium is predominantly CO and H_2 . Minor quantities of CO_2 , H_2O , CH_4 and C remain at this temperature until the Gibbs free energies of SR and DR have fallen below that of RCG and methanation at $\sim 850^{\circ}\text{C}$, and the enthalpy of the reaction becomes positive indicating the dominance of endothermic SR and DR reactions. At this temperature the amount of H_2 and CO produced plateaus as H_2 and CO become the sole products of the reaction [193].

For comparison with experimental results which will be presented in terms of CH_4 conversion, and CO, CO_2 , and H_2 yield, Figure 30 shows the effect of temperature on these parameters. H_2/CO yield is also given, this emphasises that at $T < 650^{\circ}\text{C}$ significantly more

hydrogen is produced than the expected stoichiometric amounts found in equation 3. As previously described this is due to the lower temperature promoting the Boudouard and WGS conversion which both produce H_2 and consume CO . At higher temperatures H_2 and CO are produced in the stoichiometric amounts of partial oxidation as SMR and DR become viable and WGS and Boudouard reactions become thermodynamically non-viable [191].

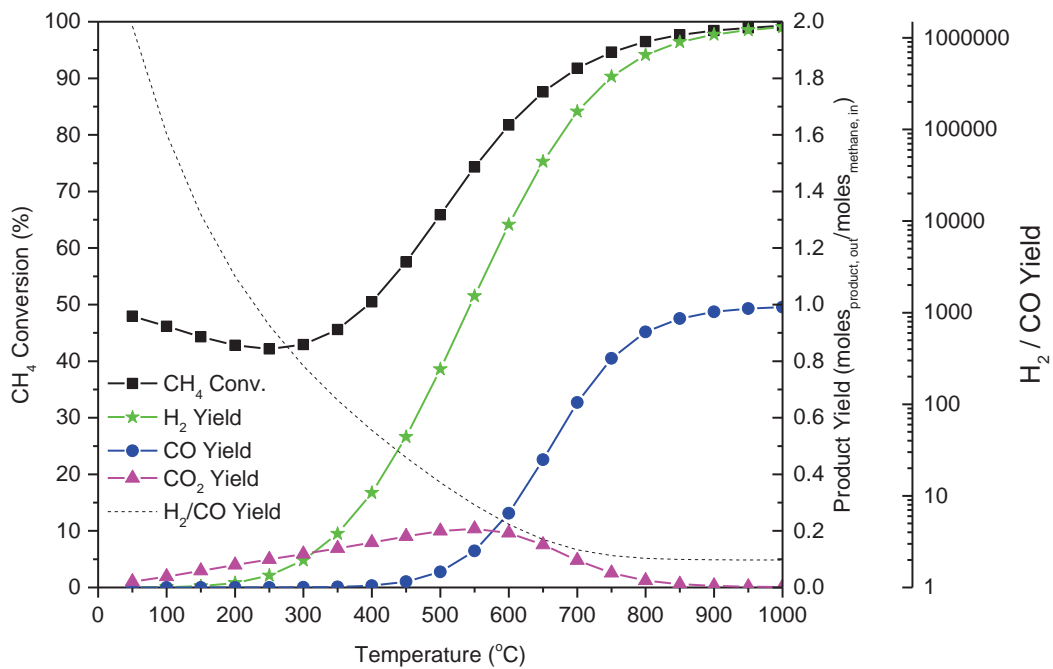


Figure 30: Effect of temperature on the CH_4 conversion, CO_2 , CO and H_2 yield for the partial oxidation of methane.

4.2.2 The effect of $CH_4:O_2$ ratio on the equilibrium gas composition

Figure 31 shows the effect of changing the $CH_4:O_2$ ratio on the conversion of methane at different temperatures. Methane conversion increases with increasing oxygen content in the feed gas supply (lower $CH_4:O_2$ ratio), as would be expected and is found in literature [196] due to the oxidising conditions.

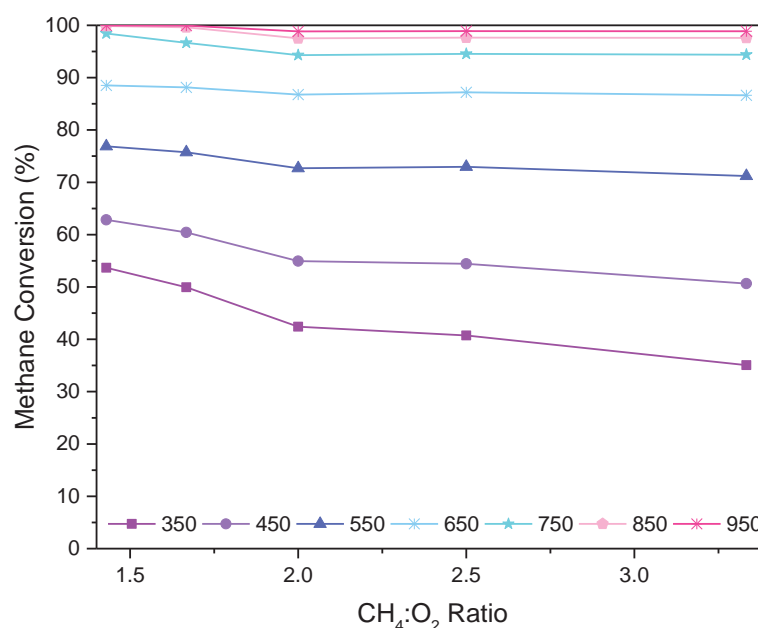


Figure 31: The effect of CH₄:O₂ ratio on methane conversion at different temperatures

The extent to which the CH₄:O₂ ratio effects methane conversion decreases with increasing temperature. At lower temperatures, a more oxidising environment favours methane conversion by promoting combustion [194]. Two regimes seem apparent, one where the CH₄:O₂ ratio <2 and one where the CH₄:O₂ ratio >2. Zhu et al. report how fuels with a higher oxygen content promote total oxidation whilst fuels with the stoichiometric ratio of CH₄:O₂ for POx give rise to syngas products, ratios exceeding this stoichiometry result in excess methane, lower methane conversion [193]. These two regimes are more visible at temperatures lower than 650°C, past this temperature methane conversion is not so greatly dependant on the oxygen content in the feedstock as complete conversion is approached.

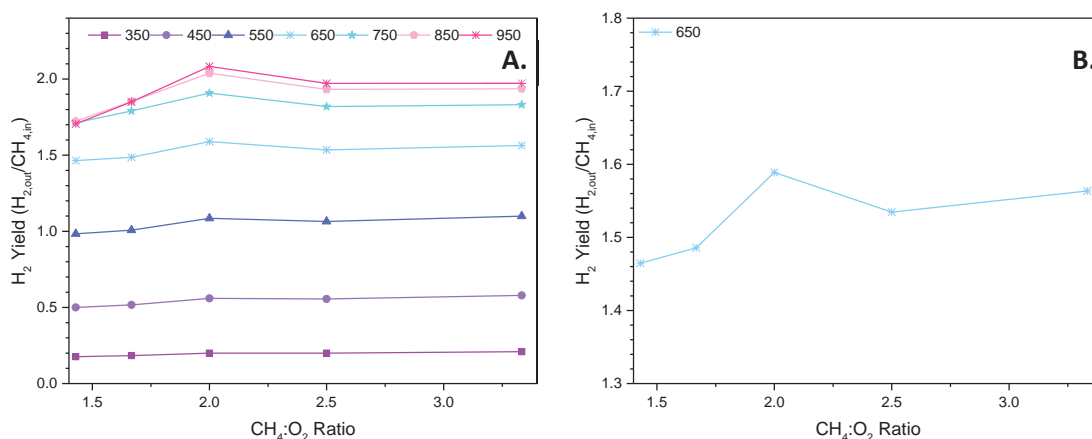


Figure 32A: Effect of CH₄:O₂ ratio on H₂ at different temperatures. B: expanded view of the 650°C data.

Oxygen supply continues to significantly affect the selectivity of the reaction towards certain products at higher temperatures however [197]. Figure 32 shows the effect of $\text{CH}_4:\text{O}_2$ ratio on H_2 yield at different temperatures. Hydrogen yield, generally, gradually decreases as oxygen content in the feedstock increases. In addition to this trend there is a peak in H_2 yield at a $\text{CH}_4:\text{O}_2$ ratio of 2 [191]. This is not obvious from Figure 32A therefore the y-axis has been expanded for the 650°C data in Figure 31B. The peak in hydrogen yield is more pronounced at higher temperatures as reforming reactions become more viable. The decrease in hydrogen yield at higher oxygen contents ($\text{CH}_4:\text{O}_2 < 2$) is sharper with increasing temperatures, due to the conditions favouring complete oxidation. In these conditions H_2O production is favoured over H_2 production [191].

Figure 33 shows the effect of $\text{CH}_4:\text{O}_2$ ratio on equilibrium CO and CO_2 yields. Generally, the amount of CO produced increases with increasing feedstock oxygen content. The rate at which CO production grows, increases with increasing temperature. The CO yield begins to plateau and subsequently begins to decrease when conditions exceed 750°C and $\text{CH}_4:\text{O}_2 = 2$. Again, this is observed since conditions favour the complete oxidation of methane to carbon dioxide. This is confirmed in Figure 33B where at $T > 750^\circ\text{C}$, little CO_2 is formed until $\text{CH}_4:\text{O}_2$ ratio drops below 2. The same trend in CO_2 yield with increasing temperature is seen across all $\text{CH}_4:\text{O}_2$ ratios, CO_2 yield increases up to 550°C and subsequently starts to decrease as SR and DR are activated.

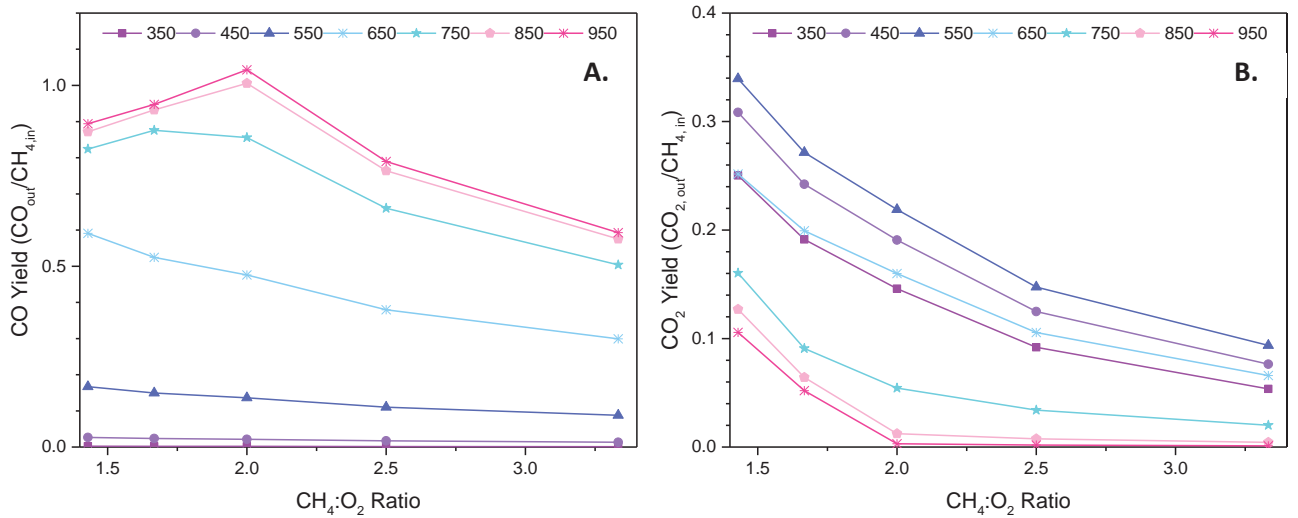


Figure 33: The effect of $\text{CH}_4:\text{O}_2$ ratio on equilibrium A. CO and B. CO_2 yields, at different temperatures.

Figure 34 shows the complete gas composition at equilibrium at high, stoichiometric for POx and low $\text{CH}_4:\text{O}_2$ ratios. At low oxygen content, high $\text{CH}_4:\text{O}_2$ ratio, there is solid carbon in the equilibrium composition at all temperatures, at the stoichiometric ratio solid carbon

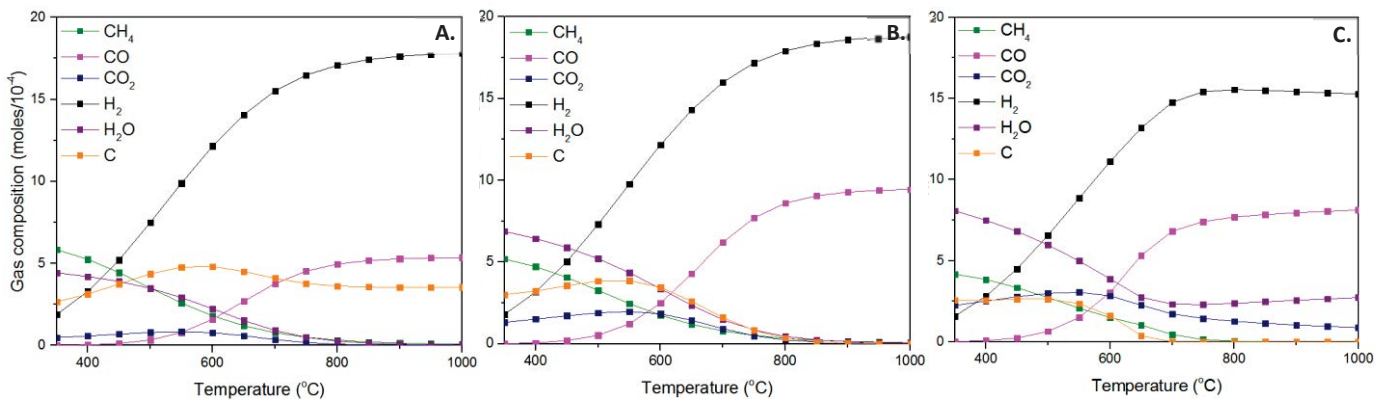


Figure 34: Equilibrium gas composition at (a) high, (b) stoichiometric and (c) low $\text{CH}_4:\text{O}_2$ ratios.

4.3 Comparison with experimental data

For comparison with experimental data solid carbon and H_2O were then omitted as products of the reaction from the CEA software. This allows for comparison with experimental data since we cannot measure these two products as a function of time with the available equipment. By omitting them from the CEA software it is possible to see the theoretical H_2 , CO and CO_2 yields if water and carbon were not being formed. Differences in the experimental and theoretical values can then be accounted for by water vapour and carbon

formation. The equilibrium data used for comparison with experimental data in subsequent chapters is shown in Figure 35.

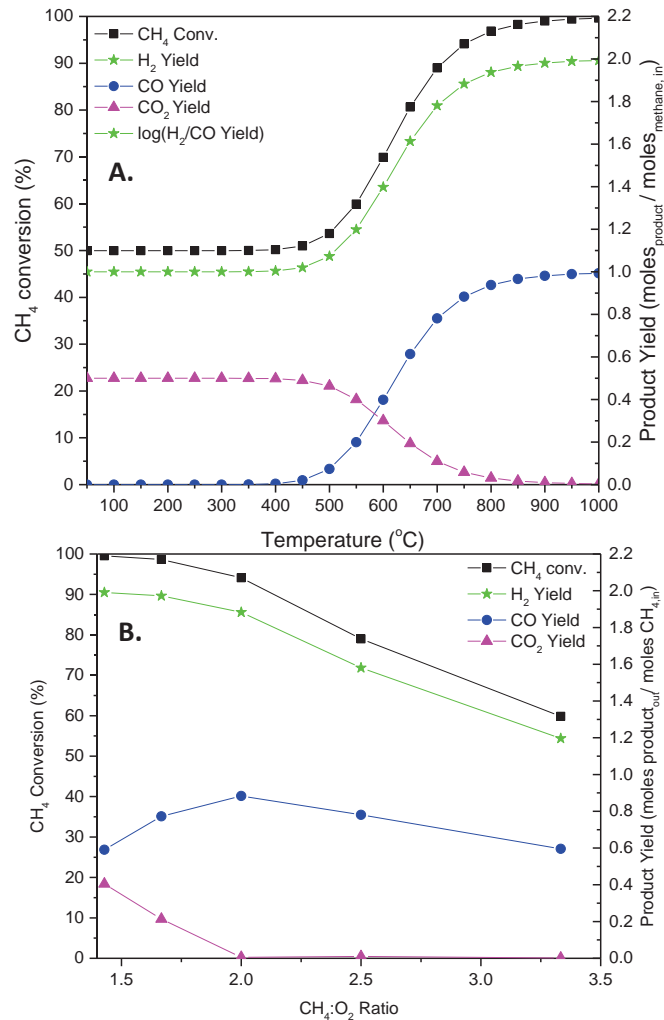


Figure 35: Equilibrium values of CH₄ conversion and product yield with A. varying temperature B. varying CH₄:O₂ ratio

4.4 Summary

The effect of temperature and CH₄:O₂ ratio on the equilibrium composition of partial oxidation reactants has been investigated using CEA software. The results show that in different conditions different reactions from the list given in Table 13 are favoured.

At all temperatures oxygen is rapidly consumed in the combustion of methane to carbon dioxide and water vapour, POx occurs to a minor extent generating some carbon monoxide.

At low temperatures the WGS also has a significant contribution in consuming CO and producing additional H₂.

As SR and DR become more viable at $T > 550^{\circ}\text{C}$, CO₂ and H₂O are consumed in producing H₂ and CO at close to the stoichiometric 2:1 ratio given in the POx equation. When temperatures are high and there is a high CH₄:O₂ ratio, complete oxidation is favoured over partial oxidation, resulting in CO₂ and H₂O increasing in abundance.

From this study on the equilibrium composition of partial oxidation reaction products, it appears that the mechanism for partial oxidation is likely to be oxidation-reformation at equilibrium. Amounts of complete oxidation occur and subsequent dry and steam reforming reactions ensue to produce CO and H₂. This is not to say that at non-equilibrium conditions the mechanism will not change. As has been found in previous work where extremely high GHSV have been used, equilibrium is not allowed to establish, and the mechanism is concluded to be of a direct nature [94,96,99,107,108,110,111].

It is clear from this study and literature previously mentioned in section 2.1.1, that the mechanism for partial oxidation is highly complex and very sensitive to operating conditions due to the abundance of reactions which are simultaneously occurring. In this work, close to equilibrium conditions are attempted and as such the mechanism can be perceived to be close to oxidation-reformation.

Chapter 5

CATALYST CHARACTERISATION

5.1	Microscopy	95
5.1.1	Ni/SiO ₂ , sph	95
5.1.2	Ni@SiO ₂	99
5.2	Thermogravimetric analysis (TGA)	104
5.2.1	xNi/SiO ₂ , sph	105
5.2.2	Ni@SiO ₂	107
5.3	X-ray Diffraction (XRD)	114
5.3.1	xNi/SiO ₂ , sph	114
5.3.2	Ni@SiO ₂	116
5.4	X-ray Photoelectron Spectroscopy (XPS)	118
5.4.1	xNi/SiO ₂ , sph	118
5.4.2	Ni@SiO ₂	122
5.5	Surface Area Analysis	124
5.5.1	xNi/SiO ₂ , sph	124
5.5.2	Ni@SiO ₂	125
5.6	Summary	126

Two nickel catalysts supported on silica, employing the support for differing functions were synthesised in this study. In order to reliably conclude that it was the different structures impacting the catalytic performance, firstly, it was important to confirm that two different catalysts had been prepared. Secondly, it was necessary to verify that other variables, which could affect activity, were kept constant. Therefore, surface area of the catalysts, nickel loading, and active particle size were ensured to be similar by characterisation of the prepared catalysts. More details as to the effects of these variables on catalyst performance can be found in section 2.2. Insights gained by characterising the catalysts before testing are offered in this chapter.

5.1 Microscopy

As described in chapter 3, both catalysts were prepared in two stages. Firstly, the cores were prepared, and then the outer layers were reduced onto them. To obtain a large enough sample size without introducing complications associated with scale up [198], cores were made in batches until 1 g of sample was obtained. Preparing the cores in batches also allowed the repeatability of the methodology to be observed. Batches were imaged by electron microscopy to confirm they were of comparable particle size distribution, before mixing them and adding the coatings.

5.1.1 Ni/SiO₂, sph

The silica cores were prepared in 5 batches. The cores were imaged by SEM and examples of the images are given in Figure 36, as well as the resulting size distributions. The size distributions were generated by measuring the particle size of over 100 particles from a range of images; this was deemed a sufficiently large number to represent the sample

[93,199]. Table 14 summarises the SiO₂ particle size. Table 14 shows that all batches have similar size ranges, and the average particle size in the batches deviated by a maximum of 35.5 nm. The resulting size distributions were comparable and as such the batches were deemed to be similar enough to be mixed to continue the synthesis, coating them in NiO.

Table 14: Particle size of SiO₂ cores

Batch no.	Average particle size (nm)	Min. measured (nm)	Max. measured (nm)	Standard Deviation (nm)
1	156.7	115.8	263.4	27.8
2	153.2	90.8	335.9	40.5
3	143.2	84.9	240.9	32.2
4	169.1	98.4	309.9	37.8
5	133.6	89.5	191.6	25.8

Figure 37 shows TEM images of the silica cores coated with increasing numbers of nickel coatings before the catalyst was reduced. The nickel binds to the surface as a phyllosilicate. As previously reported [154,199–202], phyllosilicates appear as whiskers on the surface of the support when visualised by TEM. The phyllosilicate whiskers are shown in Figure 37, where the silica cores appear wrinkled. On reduction, the whisker-like structures reduce into nanoparticles, as shown in Figure 38.

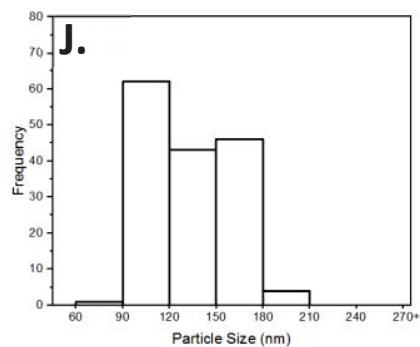
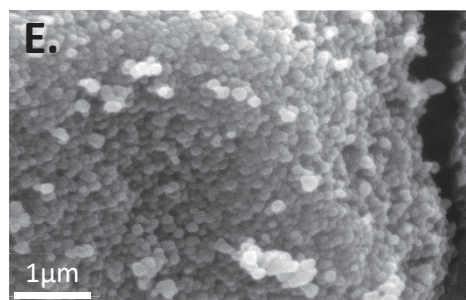
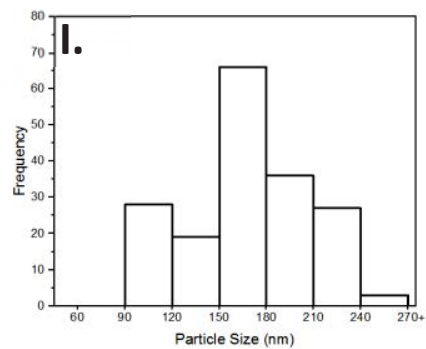
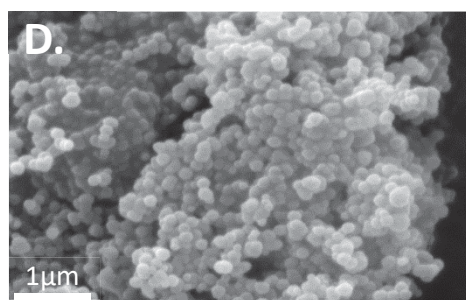
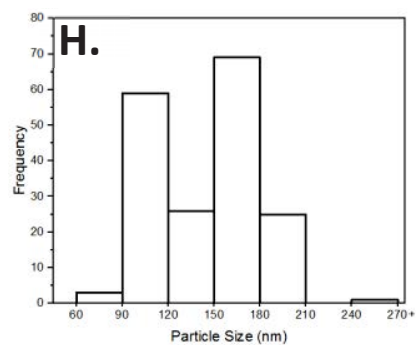
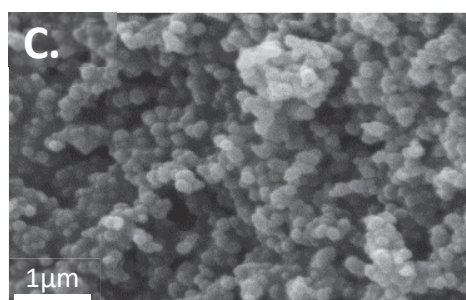
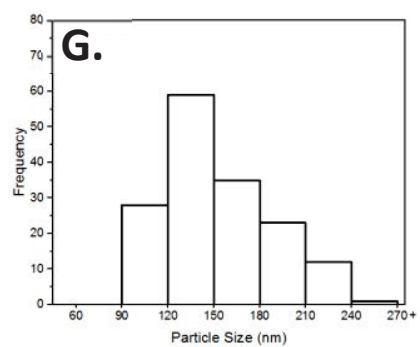
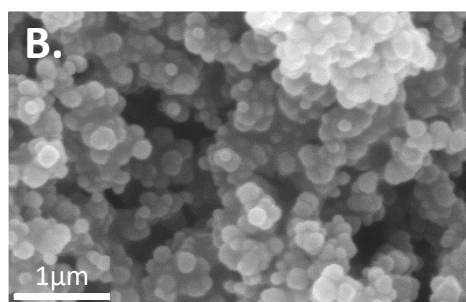
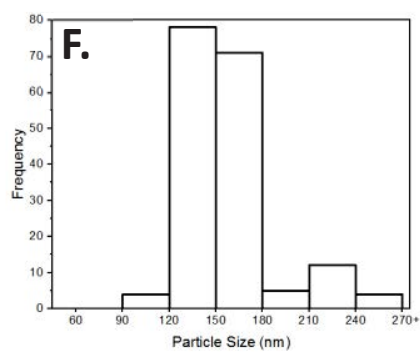
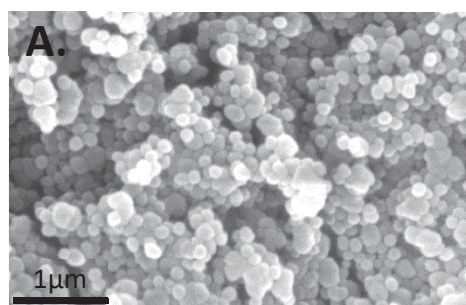


Figure 36A-E: SEM micrographs of SiO₂ batches 1 to 5, respectively F-J: particle size distribution of SiO₂ batches 1 to 5, respectively.

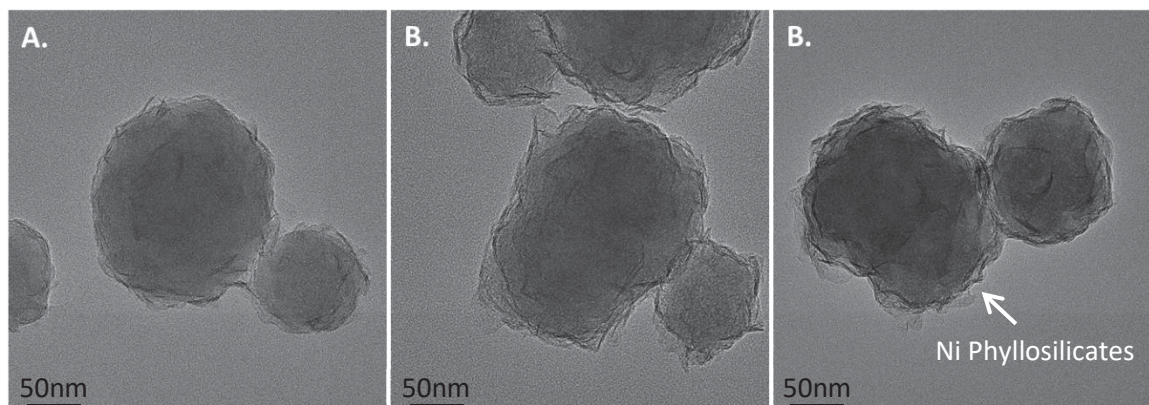


Figure 37: TEM images of uncoated (1-3)Ni/SiO_{2, sph} respectively, showing whisker like Ni phyllosilicate structures.

It is clear that repeating the coating process increases the nickel loading, as was expected from literature [138]. The density of both the whisker-like phyllosilicate structures, and the resulting nickel nanoparticles, increased. The images of the reduced catalysts, Figure 38A-C, shows the presence of some remaining whisker-like structures. This suggests that the reduction procedure did not fully reduce the catalysts. Burattin et al. [203] and Zhao et al. [204] report how this is beneficial in maintaining the metal particle dispersion on the catalyst surface. The uncoated phyllosilicate structures anchor the nickel nanoparticles to the silica, thereby resisting nickel particle agglomeration.

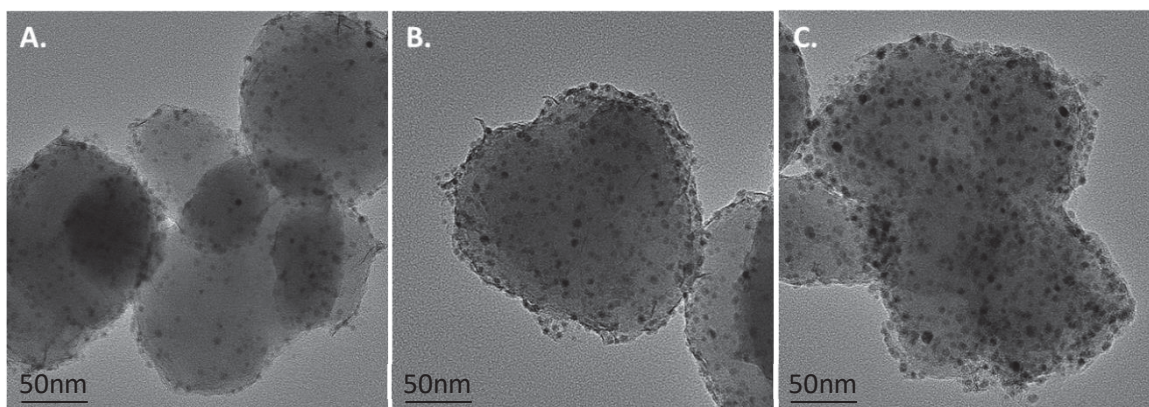


Figure 38A-C: TEM images of reduced (1-3)Ni/SiO_{2, sph} respectively, a few Ni phyllosilicate structures remain.

The nickel particle size was measured; Figure 39 shows how the nickel particle size increased with increasing nickel loading. The average nickel particle size was 4.90, 5.61, and 6.36 nm for the single, double, and triple coated silica particles, respectively. Increased nickel particle sizes have been previously reported in samples with increased nickel loading since generally, dispersion decreases with increased loading [138,205,206]. At higher nickel loadings, it is therefore easier for particles to agglomerate as they are spatially closer to one another in greater concentrations.

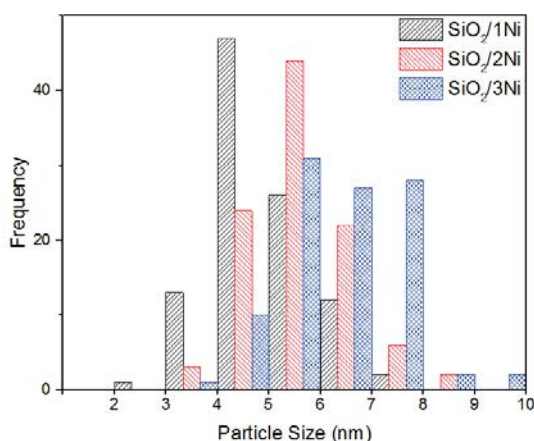


Figure 39: Increased nickel particle size with increased nickel loading due to lower metal particle dispersion.

The TEM images, Figure 38A-C, show that nickel does not coat the entirety of the silica surface. The catalyst therefore does not display a core@shell structure. The catalyst is more accurately described as nickel nanoparticles supported on spherical silica particles. As such, the catalysts are named as xNi/SiO_{2, sph}, where x represents the number of nickel coatings.

5.1.2 Ni@SiO₂

Figure 40A-H show examples of the TEM images taken of the 4 batches of NiO particles used to prepare the Ni@SiO₂ catalyst, as well as the particle size distributions. Table 15 summarises the average particle size, and size range of these 4 batches.

Table 15: Particle size of NiO cores

Batch no.	Average particle size (nm)	Min. measured (nm)	Max. measured (nm)	Standard Deviation (nm)
1	5.175	2.072	9.054	1.240
2	6.207	3.367	9.998	1.318
3	5.795	2.883	9.189	1.402
4	5.250	2.553	9.982	1.246

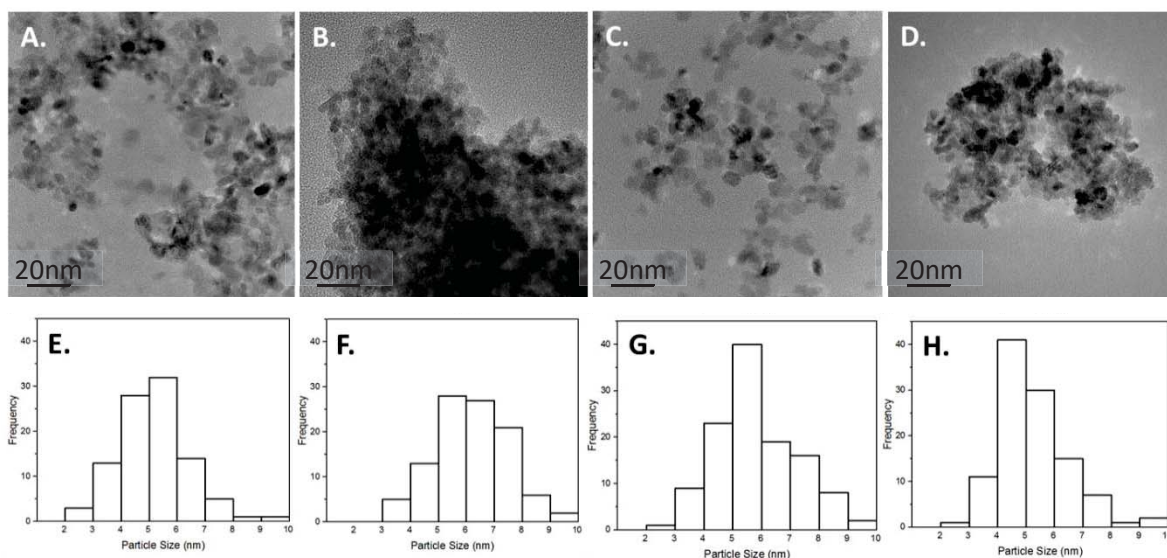


Figure 40: A-D: TEM micrographs of NiO cores, batches 1 to 4, respectively. E-H: particle size distribution of NiO batches 1 to 4, respectively.

The average particle size and ranges in each batch were comparable; the synthesis method described in section 3.1.2 was therefore reasonably repeatable. Batch number 2, represented in Figure 40B, was measured to have the largest particle sizes. As can be seen from the TEM image of this batch, the particles agglomerated on the TEM grid more than in the other samples. This made it more difficult to measure the particle size accurately; this could be a reason for the slight deviation in size from the other batches. In the same way as the SiO₂ cores, the batches of NiO were deemed comparable and so were mixed to continue the synthesis.

Figure 41 shows TEM images of the coated Ni@SiO₂ samples before reduction. These samples were imaged on copper grids with a holey carbon film covered in a graphene oxide support. Imaging the sample hanging over a hole in the carbon film allowed for better contrast. The sample agglomerated significantly on the grid, this made focusing the entire image difficult in parts.

Figure 41A and B are relatively low magnification images showing a large area of sample. The sample is clearly non-homogeneous. The figures show both coated and uncoated nickel particles were present. Nickel particles appear as dark, sharp edged, features under bright field TEM whilst the amorphous silica appears more translucent and irregular in shape.

Uncoated nickel particles can be clearly seen in the higher magnification image, Figure 41C. The uncoated nickel particles were measured to clarify that the features suspected to be nickel nanoparticles were just that by comparing their size with the uncoated samples. The average particle size of the uncoated nickel oxide particles was measured to be 5.30 nm, very close to that of the nickel oxide particles before the coating procedure was carried out (5.61 nm on average). This confirmed that the darker, relatively crisp edged shapes were uncoated nickel oxide.

Figure 41D shows silica forming a sphere around multiple nickel oxide nanoparticles. On average these nickel oxide particles were measured to be 4.98 nm and the shell was measured to be 7.17 nm thick. A third type of nickel oxide particles is shown in Figure 41E. This image shows nickel oxide particles coated in a thin shell of silica. The silica shell was measured to be 1.71 nm and the average nickel oxide particle was measured to be 5.09 nm. Again, the nickel oxide particles were on the same order of magnitude as the uncoated

particles. The non-homogenous sample was therefore deemed to be made up of 3 types of nickel oxide particles: uncoated particles, thinly coated particles, and multi-core, thickly coated particles.

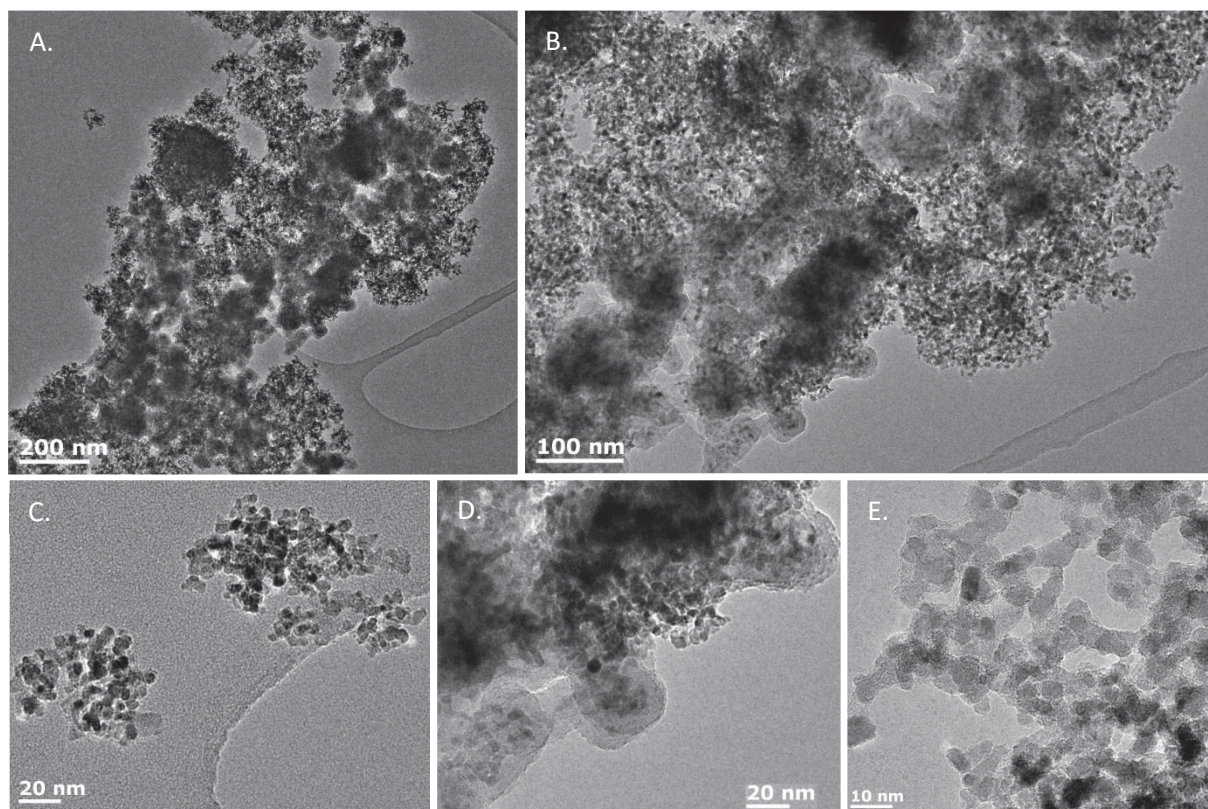


Figure 41: TEM images of Ni@SiO₂ at different magnifications, before reduction.

On reduction, the three different types of nickel particles remained apparent. Nickel oxide particles which were not coated with silica reduced into large nickel agglomerates, as are highlighted in Figure 42B, E, and F. The average length of these particles was measured to be 29.50 nm. Silica spheres which contained multiple nickel oxide particles reduced into nickel particles with thick silica shells as shown in Figure 42A, C, and D. The particles and shells were measured to be 9.19 nm and 8.54 nm, respectively. Finally, nickel oxide coated in a thin silica shell reduced into larger nickel particles with thin silica shells. The particles and shells were measured to be 11.80 nm and 2.70 nm, respectively. Figure 42B and F show this type

of particles. The TEM images confirmed that a Ni@SiO₂ structured catalyst was successfully made.

The Ni@SiO₂ sample was inhomogeneous and contained some uncoated large nickel particles. The nickel oxide and nickel particle sizes as well as silica shell thicknesses for the three types of particles are summarised in Table 16.

Table 16: Summary of NiO particle size and shell thickness before and after reduction

State	Thick SiO ₂ coating average NiO particle size (nm)	Thick SiO ₂ coating average shell thickness (nm)	Thin SiO ₂ coating average NiO particle size (nm)	Thin SiO ₂ coating average shell thickness (nm)	Uncoated NiO average particle size (nm)
Fresh	4.98	7.17	5.10	1.71	5.30
Reduced	9.19	8.54	11.80	2.71	29.51

Table 16 shows that significant nickel particle agglomeration occurred for the uncoated particles due to the heat of reduction. These particles increased in size by a factor of 5.6. The well-coated particles also grew in size but to a lesser extent. The thin shelled particles increased in size by a factor of 2.3, whilst the thickly coated particles only grew by a factor of 1.8. This provides evidence for the silica shell protecting the nickel particles against agglomeration. This observation also suggests that the thicker the silica shell, the better it is at resisting agglomeration, as has been previously observed [207].

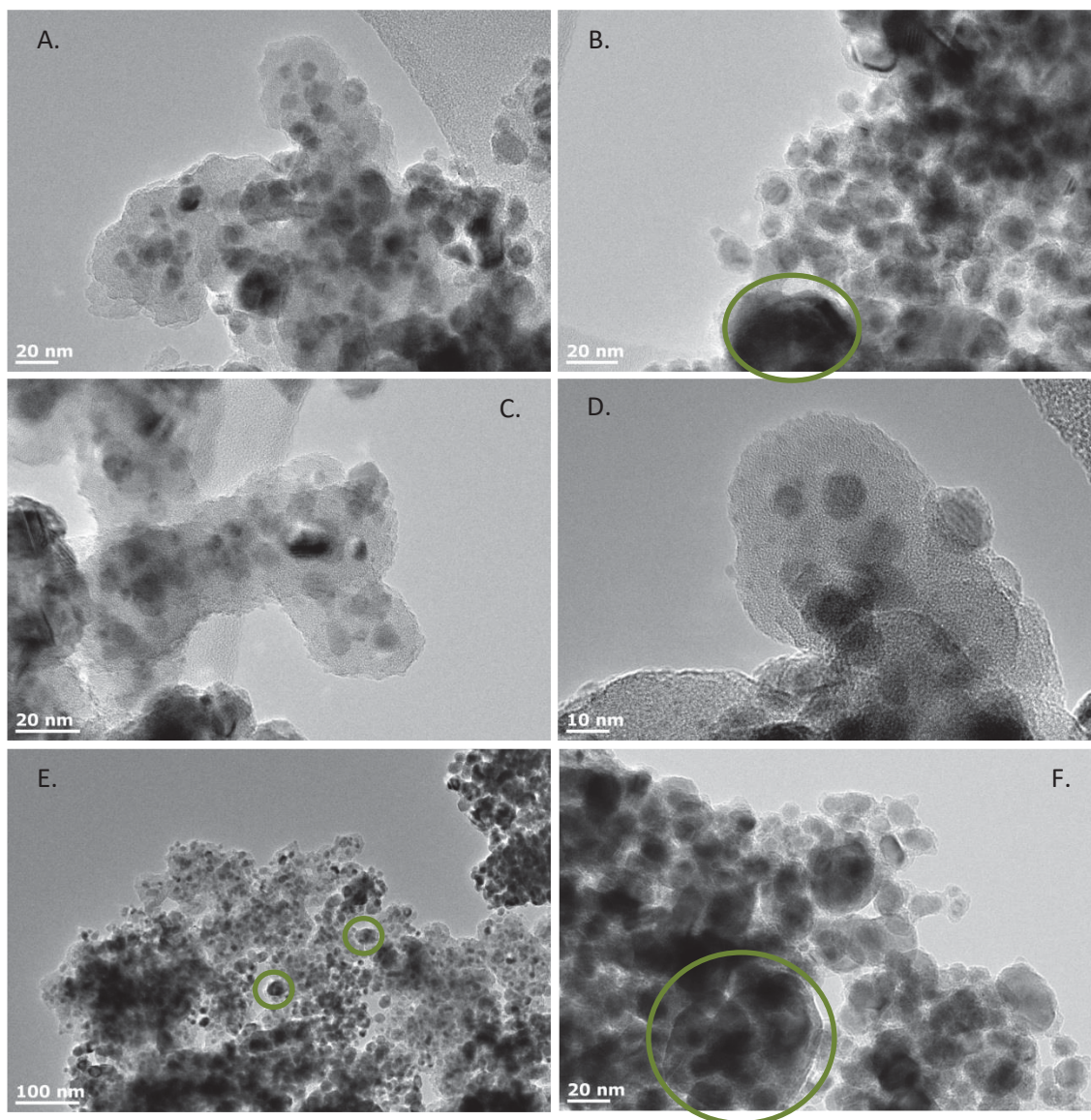


Figure 42: TEM images of reduced Ni@SiO₂. Sample was subjected to reduction under 25% H₂/N₂ at 700°C overnight.

5.2 Thermogravimetric analysis (TGA)

TGA was carried out under reducing conditions (5% H₂ / N₂) to show the reducibility of the catalysts and to confirm the nickel loading. Typical spectra, Figure 43, show a mass loss at low temperatures (<150°C) which corresponds to water evaporating from the sample [138,206,208], followed by high temperature mass losses which are assigned to Ni²⁺/Ni³⁺ reduction [152,209] or silica evaporation [210]. The derivative of the mass loss spectra more clearly identifies the temperatures at which processes occur. The data in subsequent TGA

profiles were adjusted to account for the variable water content in the samples since this was not important to the results. Typically, 2-3 wt% was water adsorbed onto the surface of the samples. The mass loss associated with water evaporation, at $T < 150^{\circ}\text{C}$, was added to the data to align the profiles. In addition, profiles are only shown at temperatures greater than 150°C to avoid any distraction from the results created by this mass loss.

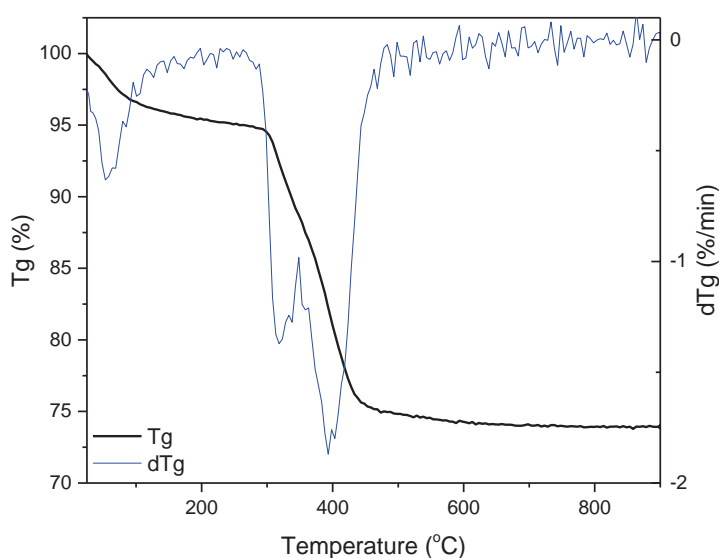


Figure 43: Typical TGA spectra.

5.2.1 $x\text{Ni}/\text{SiO}_{2, \text{sph}}$

Figure 44 confirms that the nickel loading on the $x\text{Ni}/\text{SiO}_{2, \text{sph}}$ catalysts was proportional to the number of times that the Ni coating procedure was carried out. This result was consistent with TEM imaging and as expected [138]. The mass loss centred at 750°C was attributed to nickel phyllosilicate reduction in accordance with literature [138,199,202,204,211]. This mass loss peak increased in intensity with each additional nickel coating. The high temperature of reduction is indicative of 2:1 nickel phyllosilicate structures having been formed [152,206,211]. Other studies have shown reduction to occur at a much higher temperature in nickel phyllosilicates as opposed to other silica supported nickel nanoparticles [201,212]. 2:1 nickel phyllosilicates have the chemical formula $\text{Ni}_3\text{Si}_4\text{O}_{12}\text{H}_2$.

This formula was used to determine the ratio of Ni:O and therefore the nickel loading of the samples from the TGA data recorded, using the method given in section 3.2.2.1.

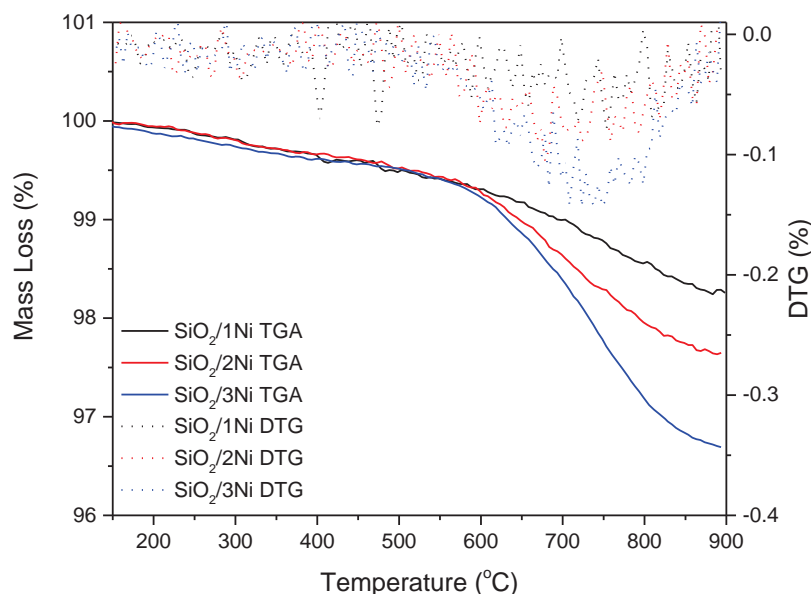


Figure 44: TGA results of $x\text{Ni}/\text{SiO}_{2, \text{sph}}$ catalysts.

The nickel loading obtained from each coating is given in Table 17. The nickel loading initially calculated assumed that complete reduction had occurred. Later it was understood that complete reduction had not taken place. The true nickel loading is therefore likely to be slightly higher than that reported in Table 17.

Table 17: Nickel loading of $x\text{Ni}/\text{SiO}_{2, \text{sph}}$ catalysts

Number of coatings	Nickel Loading (%)
1	0.799
2	1.078
3	1.517

As previously observed during microscopy, nickel did not form a uniform layer over the silica core. It was therefore important to confirm that the silica did not thermally degrade, appearing in the TGA results as a mass loss. To confirm this, uncoated SiO_2 was tested under reducing conditions in the TGA, Figure 45 shows the resulting TGA profile. A mass loss

centred around 525°C was present due to the thermal degradation of SiO₂ [210]. Thermal degradation was confirmed by repeating the analysis under nitrogen: a similar profile was observed. This ruled out that the mass loss at 525°C was due to a reduction process, Hu et al. report that silica does not reduce until temperatures greater than 800°C [148], silica reduction was not visible in the current results. It is important that the thermal decomposition of SiO₂ is prevented. SiO₂ evaporation into the fuel cell would not only degrade the reforming catalyst but it would poison the fuel cell [213]. It is therefore encouraging to see that as the silica is coated, the silica no longer thermally decomposes: Figure 44 shows no mass loss peak around 525°C. There is a mutually beneficial relationship between the silica and the nickel. The silica supports the nickel and a strong interaction between the metal and support prevents the silica from readily evaporating.

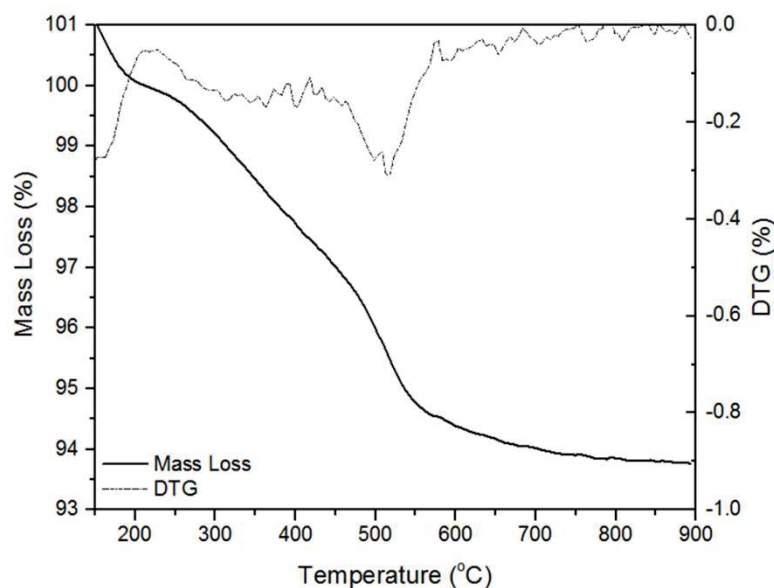


Figure 45: TGA results of uncoated SiO₂ under reducing conditions.

5.2.2 Ni@SiO₂

Figure 46 shows the TGA results of the as prepared NiO@SiO₂ catalyst, again tested under reducing conditions. The profile shows several reduction peaks from 325 to 500°C. For comparison, the TGA trace of 3Ni/SiO_{2, sph} is also shown in Figure 46. It is well known that the

strength of the interaction between the metal and support affects the reducibility of the catalyst [214]. Figure 46 shows that the Ni@SiO₂ catalyst is more readily reduced than the xNi/SiO_{2, sph} catalyst. The mass loss associated with nickel reduction occurs at a much lower temperature in the Ni@SiO₂ catalyst than in the Ni/SiO_{2, sph} catalysts. Therefore, it can be concluded that there is a stronger metal-support interaction in the xNi/SiO_{2, sph} catalysts. As previously mentioned, nickel phyllosilicates result in a strong interaction between the metal and support [204]. This leads to the Ni/SiO_{2, sph} catalyst having a higher reduction temperature.

Using the composition of the nickel species present, determined by XPS, the nickel loading of the Ni@SiO₂ catalyst was estimated to be 6.05%.

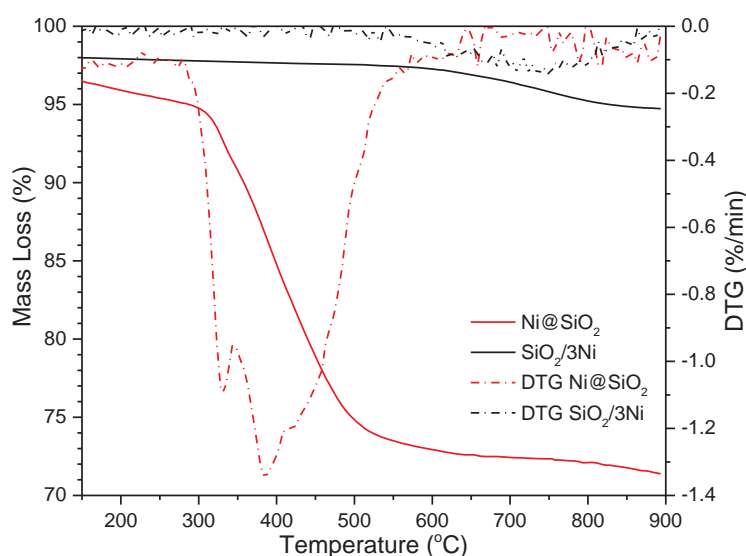


Figure 46: TGA profiles of Ni@SiO₂ catalyst and 3Ni/SiO_{2, sph} catalyst.

The DTG profile of Ni@SiO₂ shows that this catalyst reduced via a series of several different processes. Other studies have shown that this is possible when nickel species are present in different environments, both physical and chemical. Mile et al. used temperature programmed reduction (TPR) to investigate the location of NiO particles supported on silica based materials with a variety of porosities [209]. The supports used each contained pores

of multiple sizes, “smaller” pores $\sim 10\text{nm}$ and “larger” pores $\sim 100\text{nm}$. The proportion of small to large pores on each support varied. TPR results revealed reduction of NiO occurred at 2 temperatures; $\sim 400^\circ\text{C}$ and $\sim 500^\circ\text{C}$. NiO which was reduced at 400°C was evidenced as being located in the small pores whilst the NiO reduced at 500°C was associated with the larger pores. This could have been the result of nickel silicate formation leading to smaller particles which are more difficult to reduce, due to a lower rate of nucleation. Similarly, Rodriguez-Gomez and Cabellero investigated the impact of where nickel particles were located on porous supports on the reduction temperature [202]. The authors concluded that particles located inside mesopores were more difficult to reduce than particles on the outer of a pore. This resulted in a shift of the reduction peak by 150°C . Many authors have suggested temperatures for the reduction of nickel species in different chemical environments supported on silica, these are summarised in Table 18.

During this study the Ni@SiO₂ catalyst has been shown to reduce at three temperatures; 330°C , 365°C , and 435°C . Due to the low temperature of reduction and lack of evidence to support the presence of nickel silicate in other characterisation techniques, the presence of this species was omitted. Other than Ni₂O₃ which reduces at very low temperature [209], XRD and XPS showed that the nickel species present were purely NiO. The creation of 3 different reduction peaks must therefore be a result of the NiO being in different physical environments. As shown in the TEM images, 3 types of nickel oxide particle were present in the Ni@SiO₂ sample: uncoated, thinly coated and thickly coated.

Table 18: Reported temperatures for the reduction of nickel species supported on silica.

Reduction temperature of bulk NiO, interacting weakly with SiO ₂ (°C)	Reduction temperature NiO, interacting more strongly with SiO ₂ (°C)	Reduction temperature of nickel silicates (°C)	Reference
350-380	410-450	750+	[144]
417	499	609	[215]
380	-	1:1 500	[216]
-	<550	350-800	[199]
-	-	1:1 600 2:1 900	[206]
-	540-580	750-780	[217]
400	470	600	[204]
-	-	1:1 500-700 2:1 700-800	[211]
	400	600	[93]

Rodriguez-Gomez and Cabellero assigned the lowest temperature reduction peaks to the environments better exposed to the reduction gases [202]. The reduction peaks were therefore assigned as follows:

- The peak at around 330°C was assigned to the reduction of uncoated NiO.
- The peak at ~365°C was assigned to the intermediately reducible nickel which was found in thinly coated particles.
- The peak at ~435°C was assigned to the thicker coated Ni@SiO₂ catalyst.

In order to confirm this theory, work was initiated to vary the porosity of the silica shell. Li et al. report that by varying the amount of PVP used during synthesis, the size of the silica pores changed [117]. The synthesis described in Section 3.1.2 was therefore repeated. Three samples were synthesised, the first contained the full amount of PVP requested by the procedure, the second contained half the amount, and the final sample omitted PVP completely from the reagents.

The TGA profiles of the three Ni@SiO₂ catalysts were recorded and derivatives of the mass losses were peak fitted to clearly show the 3 reduction environments. TEM was recorded of the 3 catalysts and BET surface area analysis was carried out. The results are shown on the following page.

Figure 47A-D show that the 3 different catalysts have very different reduction profiles. The catalyst made with half the amount of PVP clearly contained a higher proportion of the NiO which was reduced at 365°C whilst the catalyst made without PVP contained a greater proportion of the easily reduced NiO with its main peak at ~330°C.

The TEM recorded confirmed the argument for the 330°C peak being due to uncoated NiO and the 365°C peak resulting from the thinly coated NiO, since the catalyst made with half the amount of PVP had a larger peak at 365°C and the TEM confirmed that the sample was almost entirely thinly coated NiO. The TEM of the Ni@SiO₂ catalyst made without PVP showed that the sample was predominantly uncoated NiO supported on SiO₂ flakes. It follows then that there is a larger peak at 330°C, representative of the uncoated NiO.

In order to determine the effect of the silica shell on the catalyst performance, NiO which was never coated with SiO₂ was also tested. The reduction profile of NiO in Figure 48, is comparable with that of Ni@SiO₂ as well as results obtained by Mile et al. [209]. Two differences from the Ni@SiO₂ catalyst were, however, apparent. The first is the presence of a very low temperature reduction peak at around 210°C. Mile et al. associate this peak with

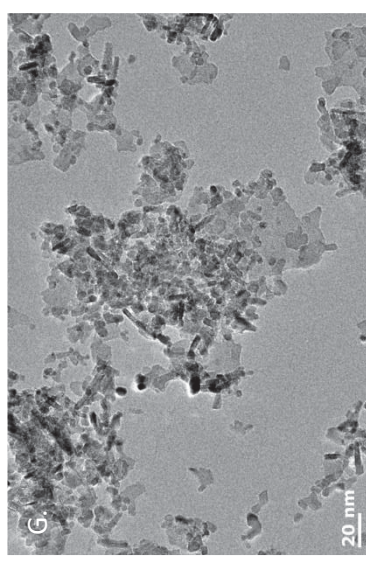
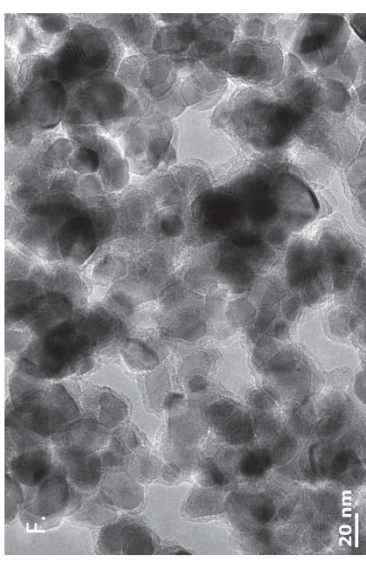
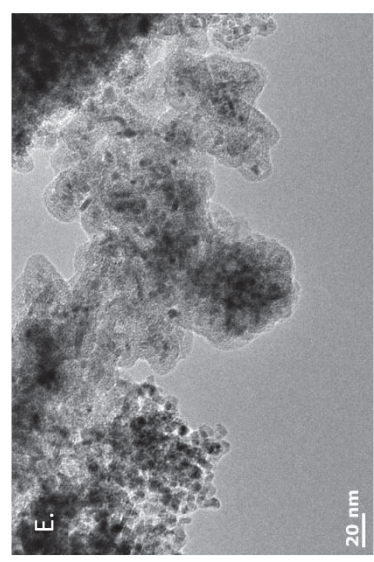
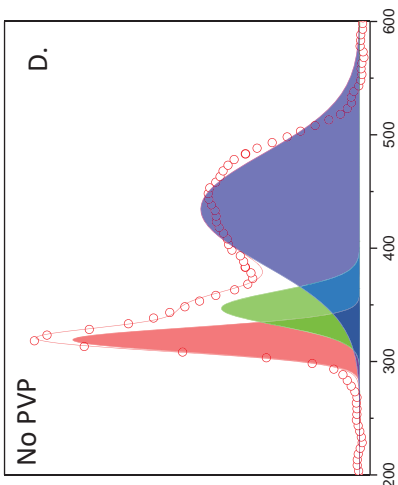
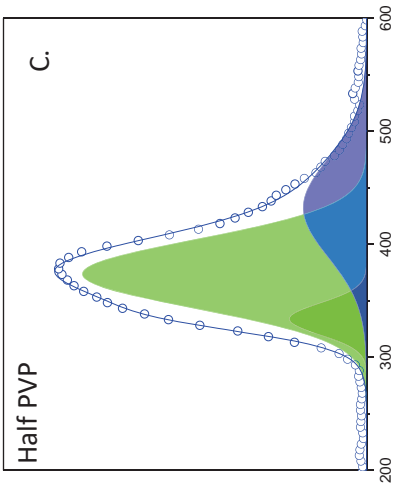
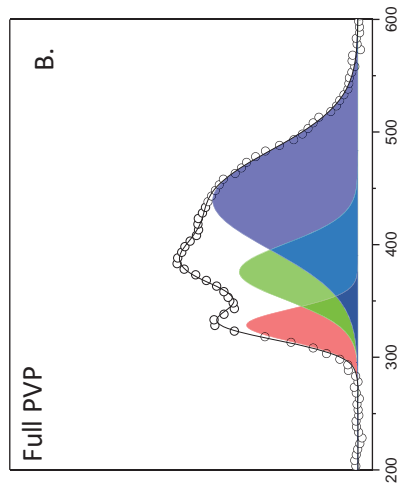
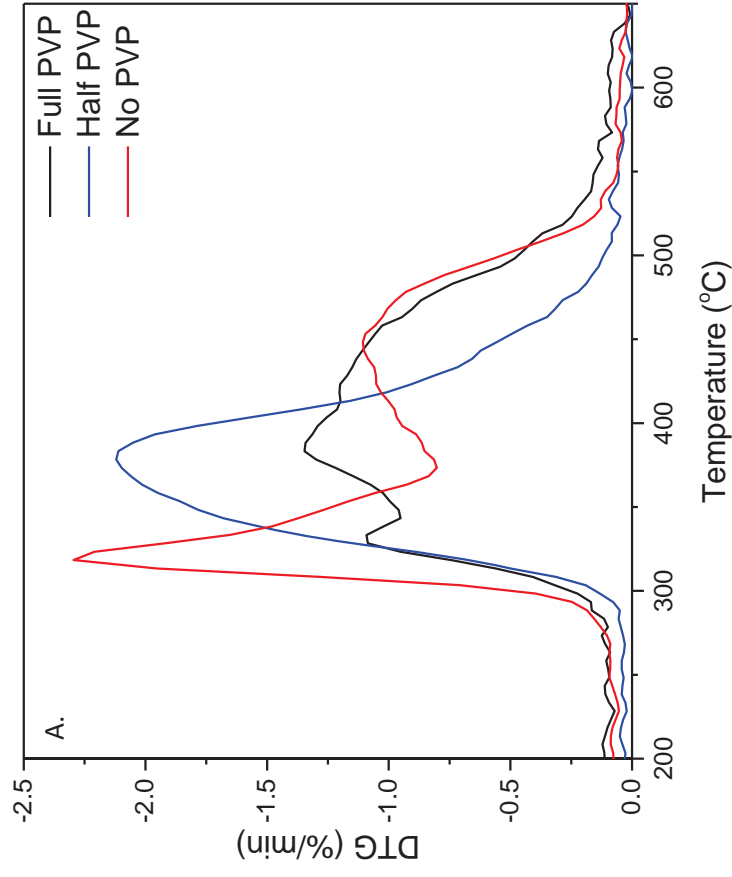


Table 19: Effect of varying PVP concentration in Ni@SiO₂.

	Peak 1 Area	Peak 2 Area	Peak 3 Area	BET (m ² g ⁻¹)
Position (°C)	327.2 ± 8.0	365.5 ± 18.5	435.4 ± 4.1	-
Full PVP	27.6	51.6	109.9	131.0
Half PVP	18.7	148.8	47.8	32.8
No PVP	52.6	35.3	133.5	162.4

Figure 47: Results of TGA, BET and TEM analysis of Ni@SiO₂ when synthesised with full, half and zero PVP.

the presence of Ni_2O_3 . Ni_2O_3 is a black substance, which explains the appearance of the as-synthesised “NiO” being a black powder rather than the expected green powder. The presence of some black Ni_2O_3 masked the appearance of any pale green NiO. Mile et al. suggested that the presence of Ni_2O_3 was somewhat random and that its presence or absence was insignificant to the results. Ni_2O_3 was also detected by XPS, as will be discussed later. The other difference between the NiO and the $\text{Ni}@\text{SiO}_2$ TGA trace is that the main reduction mass loss for NiO occurs in a single broad process, from 260°C to 560°C. The nickel oxide is reduced during a single process since there are no multiple NiO environments which have different reducibilities.

The methodology for determining the nickel content was reliable was confirmed, both the degree of reduction and composition of the sample from XPS data, and the mass loss from TGA were used to find the nickel loading of the NiO sample. If quantification was correct, the nickel loading would be close to 78.6 wt% since the NiO sample contained no silica. Mass loss associated with nickel reduction from TGA was 23.61 %. XPS of the fresh sample showed close to pure NiO. Therefore, it was assumed that mass lost from the sample was associated with NiO reduction to Ni^0 . Using the chemical formula of NiO the nickel loading of the sample was calculated to be 30.14 wt%, this would hold true if the sample had been fully reduced. From XPS data it was known that the sample did not fully reduce. From the XPS data it was determined that the nickel species present in the reduced NiO sample was composed of 63.69% NiO, 16.54% Ni_2O_3 , and 19.76% Ni^0 metal. The nickel not accounted for in the 23.61% oxygen mass loss was the 63.69% of NiO that was unchanged by reduction. As 16.54% of nickel species reoxidised to Ni_2O_3 , it was assumed that the oxygen for this to occur came from within the sample, since no oxidation mass gain was observed in the TGA.

Accounting for a 36.31% reduction meant that the determined nickel loading of 30.14% increased to 83.00%, close to the 78.3% predicted. Any deviation was likely to be the result of sample contamination and instrumental error. The method of determining nickel loading by TGA and XPS was therefore validated within an error of $\pm 6.0\%$.

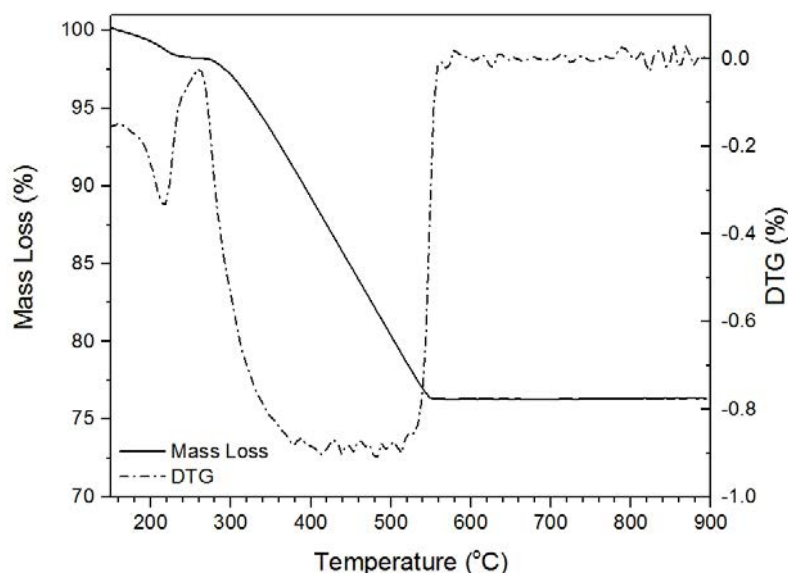


Figure 48: TGA profile of NiO under reducing conditions.

5.3 X-ray Diffraction (XRD)

5.3.1 $x\text{Ni}/\text{SiO}_{2, \text{sph}}$

Many authors report the XRD analysis of phyllosilicate containing compounds to result in a very weak diffraction pattern. The peak centres vary in literature due to this weak signal and high signal: noise ratio. Peaks around 34° , 38° , and 61° 2θ are common throughout literature [199,202,204]. At first investigation, analysis of the fresh $x\text{Ni}/\text{SiO}_{2, \text{sph}}$ catalyst showed no crystalline structure to be present. This is also a common conclusion drawn in literature due to very small and very well dispersed metal centres [201]. However, when a greater amount of sample was analysed, in order to magnify the signal, a weak XRD pattern was obtained which was indicative of ill-crystallised nickel phyllosilicates as reported in literature

[199,202,203,217]. Figure 49 shows the XRD patterns obtained from the fresh $x\text{Ni}/\text{SiO}_2, \text{sph}$ catalysts. The doubly and triply coated samples have been displaced in the y-direction to clearly display the results. The strength of the pattern increased with nickel loading as would be expected as the signal: noise ratio of the phyllosilicate peaks increases when there is a higher concentration of phyllosilicates. The analysis showed the broad peak at $22^\circ 2\theta$ resulting from the silica shell [144,199]. More intense peaks at 60.5 and $34^\circ 2\theta$ are indicative of nickel phyllosilicates as previously described.

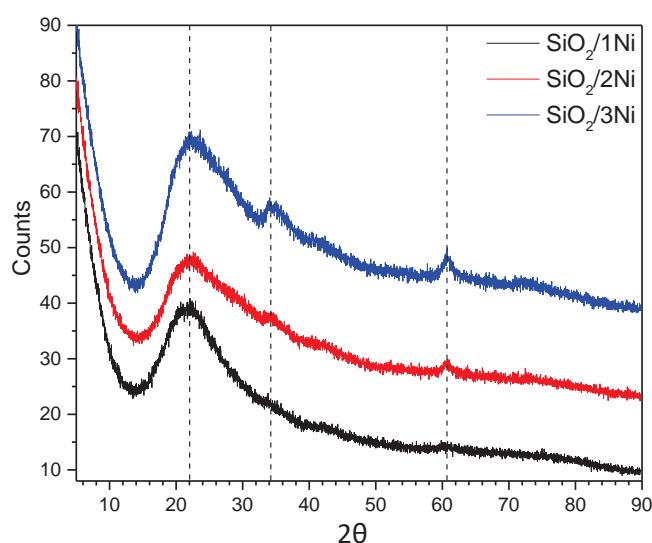


Figure 49: XRD analysis of fresh $x\text{Ni}/\text{SiO}_2, \text{sph}$.

On reduction, the weak patterns of phyllosilicates are not identifiable but some weak peaks associated with nickel metal are generated. The weak pattern again suggests small particles that are well dispersed on the support.

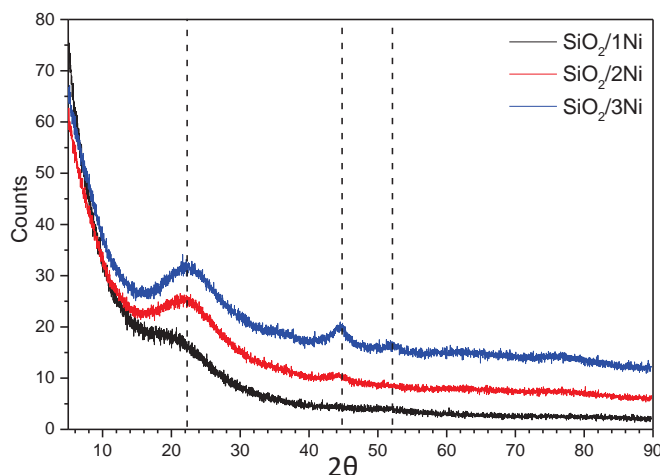


Figure 50: XRD analysis of reduced $x\text{Ni}/\text{SiO}_2, \text{sph}$.

5.3.2 Ni@SiO₂

XRD was carried out on NiO cores as well as the Ni@SiO₂ catalyst to see what happened to any crystallographic structures present, on reduction. The black spectrum in Figure 51 shows the XRD pattern of the as-prepared NiO cores. After reduction, a sample was taken and the red spectrum was recorded.

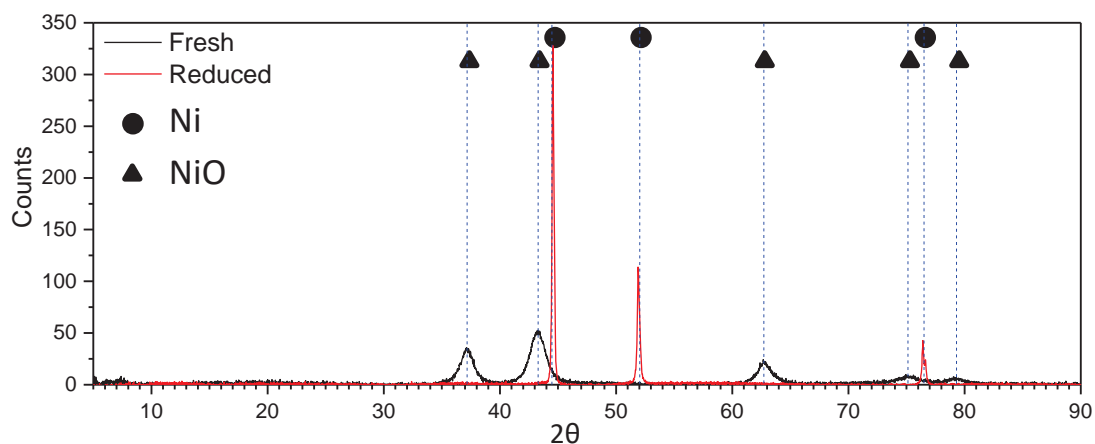


Figure 51: XRD spectra of fresh and reduced NiO.

The diffraction peaks were pattern-matched against the International Centre for Diffraction Data (ICDD), pdf 2 database of diffraction patterns. This suggested that the only crystalline phases in the as-prepared sample were NiO, indicated by the triangular markers.

Unfortunately, the diffraction peaks of oxidised nickel species are all very similar [218,219], and when nanoparticles are analysed by XRD, significant peak broadening is experienced.

Therefore, XRD is not the best method for distinguishing between oxidised nickel species, such as NiO or Ni₂O₃. XRD does allow rapid confirmation that reduction has been successful, however. The reduced sample showed no peaks associated with NiO. The pattern was replaced with the diffraction pattern of metallic Ni, indicated by circular markers. Therefore, the nickel oxide appeared to be fully reduced during the reduction procedure.

It is evident that the diffraction peaks became much sharper on reduction. The reduction in the full width half maximum of the diffraction peaks was evidence of nickel particle growth, agglomeration, as described in the Scherrer equation:

$$(19) \quad \tau = \frac{K \cdot \lambda}{\beta \cdot \cos \theta}$$

Where τ is the average size of the crystalline structures, K is a shape factor, λ is the wavelength of the incident X-rays, β is the full width half maximum of the diffraction peak, and θ is the Bragg angle at which the peak appears. Since the full width half maximum is part of the denominator; the sharper the peak, the larger the crystalline particle size [144].

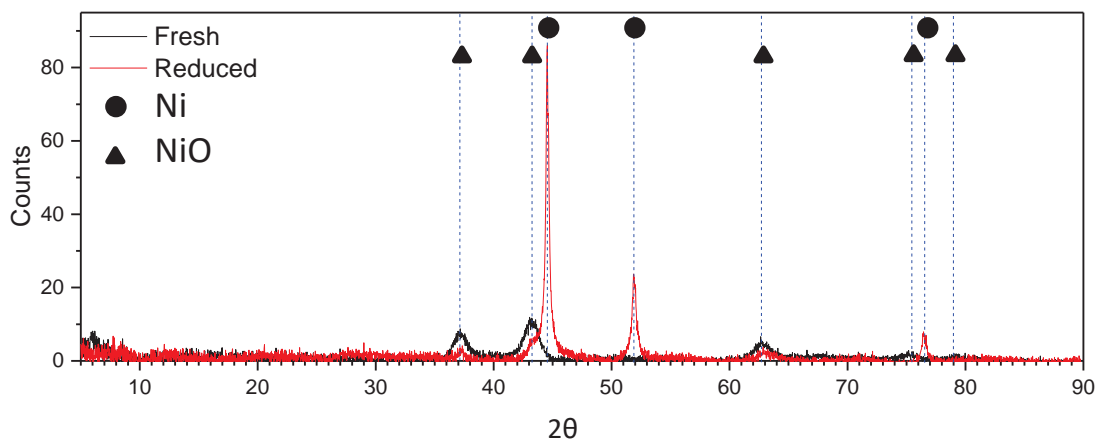


Figure 52: XRD patterns of fresh and reduced NiO@SiO₂.

Figure 52 shows the spectra recorded of the Ni@SiO₂ catalyst. The black, fresh, spectrum shows purely oxidised nickel species as the only crystalline substance present. This is unsurprising since the silica shell is amorphous and therefore is undetectable by XRD in a low concentration. The reduced sample contained a mixture of oxidised nickel and Ni⁰ metal. This suggests that the reduction procedure did not fully reduce the catalyst. It is proposed that the silica shell shields the NiO from the reduction gases, making the NiO less readily

reduced than uncoated NiO. Bian et al. note how silica shells increase the diffusion resistance of reactants [217].

5.4 X-ray Photoelectron Spectroscopy (XPS)

5.4.1 xNi/SiO_{2, sph}

Figure 53 shows the XPS survey scans of the xNi/SiO_{2, sph} catalysts before testing as well as the high resolution XPS of the Ni 2P 3/2 region with the background subtracted. Both figures show that with each subsequent coating, the nickel peak intensity increased. This is consistent with previous results showing that the nickel loading increased with subsequent nickel coatings. The atomic composition of the catalyst surface was calculated using the relative intensity of each of the atomic peaks. Table 20 shows the surface nickel content of the xNi/SiO_{2, sph} catalysts as synthesised and after reduction. The compositions calculated are only estimates since hydrogen contained in the nickel phyllosilicate is undetectable by XPS.

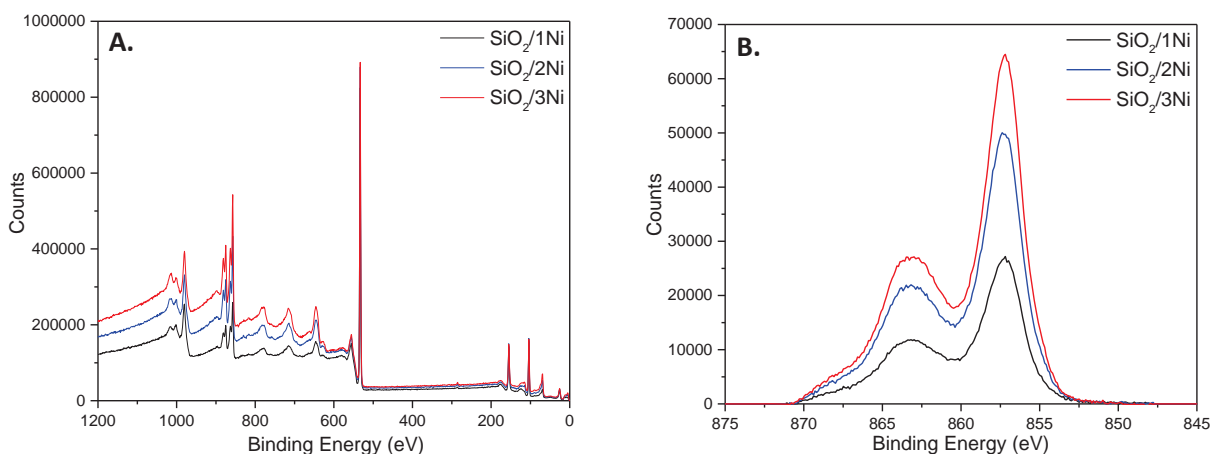


Figure 53: A. XPS survey spectrum of xNi/SiO_{2, sph} catalysts as synthesised. B. Ni 2P 3/2 region with background subtracted.

Table 20: Ni content at the surface of Ni/SiO_{2, sph} catalysts, measured with XPS

Catalyst	Fresh / %	Reduced / %
1Ni/SiO _{2, sph}	6.34	2.83
2Ni/SiO _{2, sph}	10.56	3.81
3Ni/SiO _{2, sph}	12.68	4.49

The results in Table 20 and Table 17 show that the nickel contents measured by XPS and by TGA were different. Variations can occur since TGA is a bulk analysis technique, i.e. the entire sample is reduced, therefore the nickel content of the entire sample is measured. In contrast, XPS is a surface sensitive measurement, therefore only the composition of the surface is measured. This varies from the bulk. Rodriguez-Gomez and Cabellero demonstrated the power of utilising both surface sensitive and bulk analysis methods in order to retrieve more information on catalysts [202]. In the case of the $x\text{Ni}/\text{SiO}_2, \text{sph}$ catalysts it is easy to imagine why there might be more nickel at the surface than in the bulk of the catalysts, since the silica cores have been coated in nickel. The surface composition should therefore show a greater proportion of nickel than the bulk analysis. The same difference can be seen here; the TGA results (bulk technique) show lower nickel content than the XPS analysis (surface technique) of the fresh catalysts. None the less, the trends in the data are equivalent and the numbers are similar, which was expected.

The nickel content of the samples decreased on reduction. It is proposed that this was not due to nickel leaving the sample by some thermally driven process, but that this was a result of a greater proportion of the underlying silica becoming visible to the spectrometer on reduction than when compared with the fresh sample. The fresh sample displayed whisker-like nickel phyllosilicate structures. As Figure 37 shows these structures interlock and form an irregular mesh over the surface of the silica. It then follows that when the phyllosilicates reduce into nickel nanoparticles the underlying silica surface is exposed. This makes the percentage of nickel on the surface of the catalyst appear to have reduced. It then follows that the atom% of nickel in the reduced catalyst, derived from XPS, should more closely resemble that which is presented in the TGA results, since the reduced sample had both

nickel and silica on the surface. This effect has been observed. Nickel content from XPS analysis remained higher than from TGA since the TGA results accounted for the entire mass of silica present in the sample, whereas XPS only accounted for silica present on the surface. A variety of peak positions are suggested in literature which can be assigned to different Ni^{2+} species. To name a few, Li et al. suggest that peaks at 854.7, 856.6 and 858.9 eV correspond to NiO, 1:1 Ni phyllosilicate, and 2:1 phyllosilicate, respectively [220]. Yang et al. associate peaks at 855.9 and 857.5 eV to 1:1 and 2:1 Ni phyllosilicate respectively [199]. Lehmann et al. suggest ranges of binding energies which should be used when associating peaks to Ni^{2+} species but the ranges in themselves are quite ambiguous [221]. A limited amount of literature on nickel silicates does not allow for confident determination of species or in fact a mixture of species. What appears clear from the literature available is that the 2:1 nickel phyllosilicate peak occurs at higher binding energies than the 1:1 peak and coupling XPS data with temperature programmed reduction data serves to aid species identification.

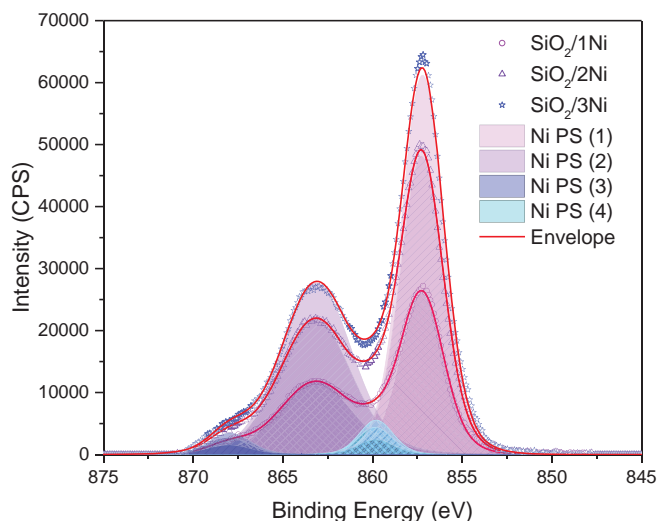


Figure 54: Fitted xNi/SiO_{2,sph} XPS data, Ni 2P 3/2 region.

Whilst the peak shape and binding energy of the Ni 2P 3/2 peaks from the high resolution XPS resembled that of $\text{Ni}(\text{OH})_2$ in the fresh xNi/SiO_{2,sph} catalysts, the dominant XPS peak was centred at 857.2eV, too high to be associated with any nickel metal (852.8-852.9 eV) or

oxide species (854.0-854.9 eV) [221]. It is not sensible to conclude this peak shows $\text{Ni}(\text{OH})_2$ species present due to the ease of reduction of $\text{Ni}(\text{OH})_2$ and a lack of a low temperature reduction peak in the TGA data. Lehmann et al. adopt the same strategy to distinguish between the overlapping peak positions of $\text{Ni}(\text{OH})_2$ and nickel phyllosilicates [221]. It is not surprising that the XPS peaks of $\text{Ni}(\text{OH})_2$ and nickel phyllosilicates look so comparable, given they both contain nickel atoms bonded to multiple hydroxide groups. Using evidence from TGA and TEM, it was therefore concluded that the nickel species were predominantly phyllosilicates in the fresh samples. Figure 54 shows the XPS data recorded in the Ni 2P 3/2 region along with the fitted data. Multiple peaks were assigned to the nickel phyllosilicate state. This was not because the nickel phyllosilicates were in different environments but it was a result of multiplet splitting as explained by Biesinger et al. [222].

The peak fitting model used in Figure 54 was used to identify the amount of nickel phyllosilicate species found in reduced and tested samples of $x\text{Ni}/\text{SiO}_2, \text{sph.}$

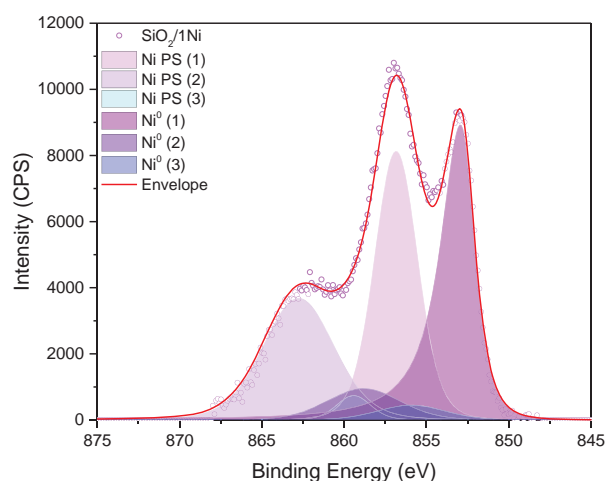


Figure 55: Reduced $x\text{Ni}/\text{SiO}_2, \text{sph.}$ XPS data, Ni 2P 3/2 region.

XPS of reduced samples showed peaks corresponding to both nickel metal and nickel phyllosilicates. Figure 55 shows the appearance of an additional nickel metal peak at lower binding energy, 852.9 eV. Again, the nickel metal had a number of associated peaks due to

the effect of multiplet splitting. The XPS results were consistent with TEM images which show that the $x\text{Ni}/\text{SiO}_{2, \text{sph}}$ catalysts were not fully reduced by the reduction procedure. The amount of reduced and oxidised nickel species in the (1-3) $\text{Ni}/\text{SiO}_{2, \text{sph}}$ samples is shown in Table 21.

Table 21: Oxidation state of Ni species present in $x\text{Ni}/\text{SiO}_{2, \text{sph}}$ catalysts after reduction

Sample	Amount of nickel species present as $\text{Ni}(\text{OH})_2$ (%)	Amount of nickel species present as Ni^0 (%)	Degree of reduction (%)
1Ni/SiO_{2, sph}	57.10	42.90	42.90
2Ni/SiO_{2, sph}	37.49	62.50	62.50
3Ni/SiO_{2, sph}	35.72	64.29	64.29

5.4.2 Ni@SiO₂

XPS results of the Ni@SiO₂ catalysts look radically different to the $x\text{Ni}/\text{SiO}_{2, \text{sph}}$ catalysts. Again, confirming that whilst in the $x\text{Ni}/\text{SiO}_{2, \text{sph}}$ catalysts, nickel phyllosilicates are present, the Ni@SiO₂ orientation does not exhibit these phyllosilicate structures. XPS results of the fresh Ni@SiO₂ catalyst show that the nickel is predominantly in the NiO state with small amounts of Ni₂O₃ also present. As previously mentioned, literature mentions that the presence of Ni₂O₃ is somewhat random and insignificant [209].

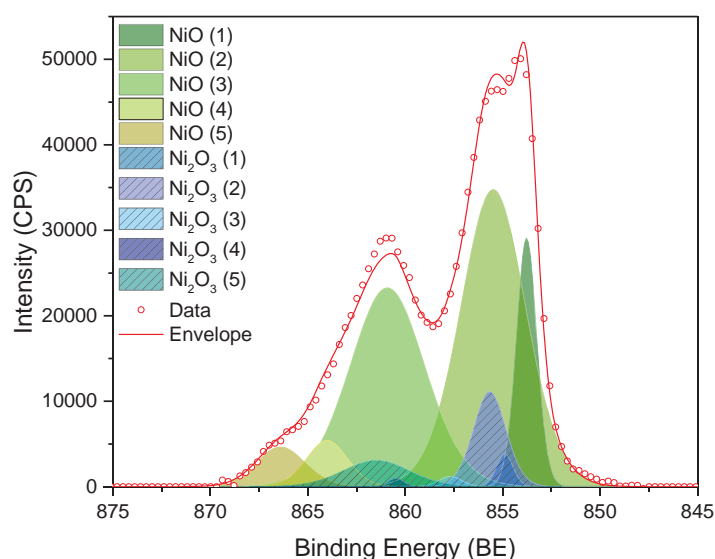


Figure 56: XPS of fresh Ni@SiO₂.

Quantification of the data shows that the nickel species in the fresh catalyst are made up of 88.24% NiO and 11.76% Ni₂O₃. This composition was taken into account when determining the nickel loading by TGA. XPS showed the nickel loading of the fresh Ni@SiO₂ catalyst to be 23.71%. This reduced to 13.24% when the reduced catalyst was analysed by XPS.

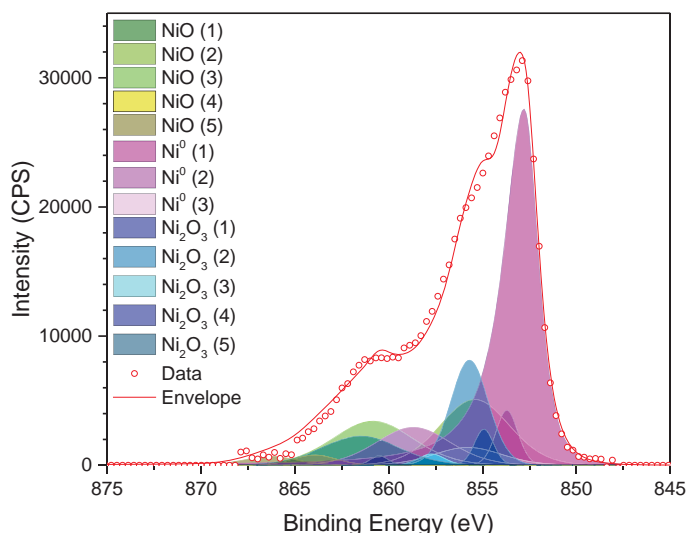


Figure 57: Ni 2P 3/2 peak of reduced Ni@SiO₂.

The reduced Ni@SiO₂ catalyst was confirmed to be predominantly Ni⁰ metal with some unreduced NiO and Ni₂O₃ species still present, as was suggested by the XRD results. Figure 55 shows the fitted XPS data of the reduced catalyst. Quantification revealed that the nickel species were as given in Table 22.

Table 22: Composition of nickel species, determined by XPS, in reduced Ni@SiO₂ catalyst.

NiO (%)	Ni ₂ O ₃ (%)	Ni ⁰ (%)	Degree of reduction (%)
27.35	19.65	53	53

The amount of Ni₂O₃ increased whilst the major source of reduction occurred by converting NiO to Ni⁰. It is proposed that the Ni₂O₃ is incredibly stable and therefore does not participate in reactions. The composition of the reduced catalyst again evidences that the catalyst was not fully reduced by the reduction profile.

5.5 Surface Area Analysis

5.5.1 $x\text{Ni}/\text{SiO}_{2,\text{sph}}$

BET surface area analysis revealed that the surface area of the $\text{Ni}/\text{SiO}_{2,\text{sph}}$ catalysts increased with increasing nickel loading. This was concurrent with the TEM results showing that the nickel dispersion was high across all the $x\text{Ni}/\text{SiO}_{2,\text{sph}}$ catalysts, particle size only marginally increased, but the density with which nickel nanoparticles packed onto the surface of the silica increased proportionally with the number of nickel coating cycles. The surface area therefore increased as more nickel nanoparticles were bound to the silica surface. As described in section 2.2, the increased active surface area would theoretically have a positive effect on the catalyst performance. An experimental failure resulted in the $1\text{Ni}/\text{SiO}_{2,\text{sph}}$ surface area analysis results being invalid. There was not enough sample remaining to repeat the results. However, the isotherms from the 2Ni and 3Ni catalysts both proved to be comparable in shape across both the fresh and reduced samples.

Table 23: BET surface area (m^2/g) of fresh, reduced and tested $x\text{Ni}/\text{SiO}_{2,\text{sph}}$ catalysts

Catalyst	Fresh	Reduced
$1\text{Ni}/\text{SiO}_{2,\text{sph}}$	N/A	N/A
$2\text{Ni}/\text{SiO}_{2,\text{sph}}$	61.8	63.4
$3\text{Ni}/\text{SiO}_{2,\text{sph}}$	86.5	89.9

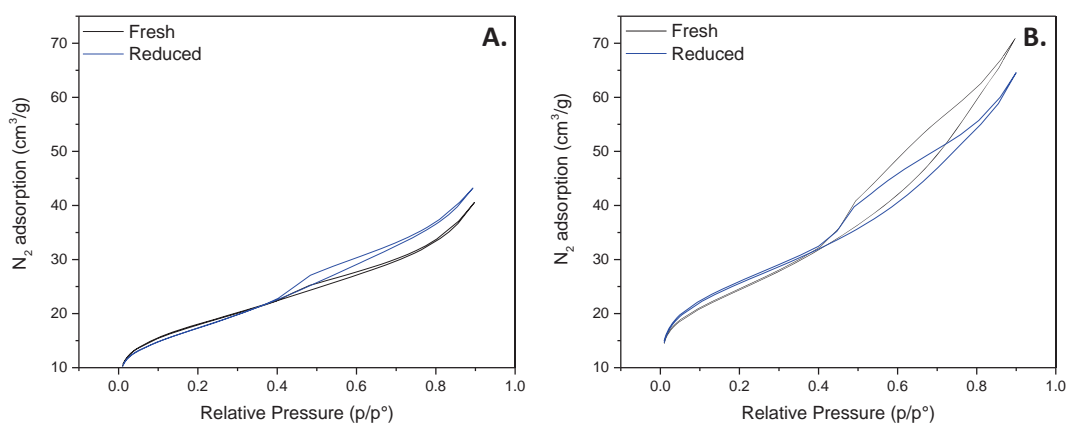


Figure 58: BET isotherms of A. $2\text{Ni}/\text{SiO}_{2,\text{sph}}$ and B. $3\text{Ni}/\text{SiO}_{2,\text{sph}}$.

The surface area of the samples increased slightly on reduction. This showed that the nickel nanoparticles were well dispersed on the surface of the silica. The even dispersion of nickel nanoparticles over the silica cores can be clearly seen in the TEM images, Figure 38A-C. The phyllosilicate structures acted as anchors between the nickel and silica, strongly bonding the two materials, as described in a series of in-depth studies by Burattin et al. [203,206,223]. The metal-support interaction was large enough to withstand large amounts of agglomeration, as might be expected, when the fibrous nickel phyllosilicates reduced into nickel nanoparticles supported on the silica surface.

5.5.2 Ni@SiO₂

Table 24 gives the surface area of the fresh and reduced Ni@SiO₂ catalyst. The surface area of the catalyst reduced significantly on reduction. This suggests that large amounts of Ni particle agglomeration occurred from the heat of reduction. This is also clear from the XRD data, as previously described. This is disadvantageous when it comes to the performance of the catalyst as previously described. However, the results show that the surface area of the reduced Ni@SiO₂ and the reduced xNi/SiO_{2, sph} catalysts were all within the same range, making performance of the catalyst independent of surface area for comparison of the two Ni/SiO₂ orientations.

Table 24: BET surface area (m²/g) of fresh, reduced, and tested Ni@SiO₂ catalyst.

Catalyst	Fresh	Reduced
Ni@SiO ₂	123.5	53.0

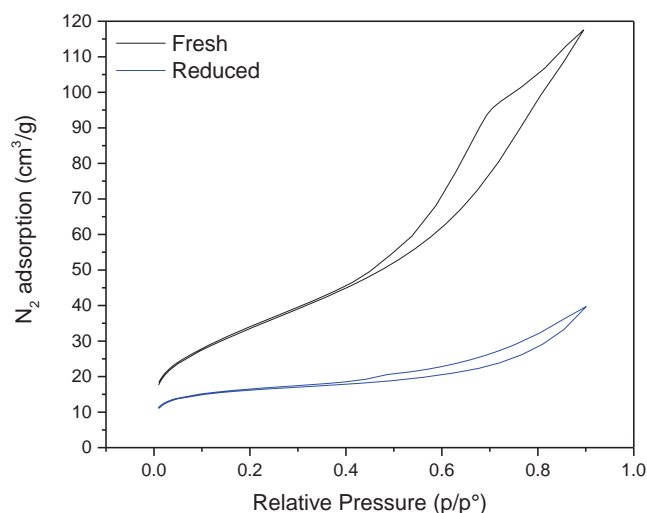


Figure 59: BET isotherms of fresh and reduced Ni@SiO₂

5.6 Summary

In summary, two different orientations of nickel supported catalysts were synthesised.

Nickel loading was varied in the xNi/SiO_{2, sph} catalyst and this chapter presented a full characterisation of the catalysts, prior to testing. Catalysts were analysed before and after reduction to observe any changes which occurred during this process.

It was confirmed that 2 different nickel supported catalysts had been prepared. The first catalyst was best described as nickel nanoparticles supported on spherical silica particles. The second catalyst consisted of nickel nanoparticles coated in a silica shell.

Table 25 summarises the physical properties determined for the catalysts in this chapter. It is clear that the nickel particle sizes on the different catalysts were comparable. The silica particle sizes were different, as would have been expected, but since the silica was a support, this was not deemed important. The size of the support would not affect the results. The surface area of the catalysts was also comparable. The differences which are

evaluated in subsequent chapters will therefore be dependent on the difference in the role of the silica and the resulting difference in Ni^{2+} species this results in.

Table 25: Summary of catalyst physical properties

	Ni/SiO₂, sph			Ni@SiO₂		
Number of coatings	1	2	3	N/A		
Average Nickel particle size (nm)	4.90	5.61	6.36	9.19	11.80	29.51
Average Silica particle size/shell thickness (nm)	151.16			8.54	2.71	0
Nickel content (TGA) (%)	0.80	1.08	1.52	6.05		
Nickel Content (XPS) (%)	2.83	3.89	4.49	13.24		
Abundant nickel oxide species present	Phyllosilicates			NiO, Ni ₂ O ₃		
Temperature of reduction (°C)	750			450		
Surface Area (m²/g)	N/A	63.4	89.9	52.97		

Chapter 6

CATALYTIC PERFORMANCE

6.1	Ni@SiO ₂ Catalyst Performance.....	130
6.1.1	Effect of Temperature on the Performance of Ni@SiO ₂ catalyst	130
6.1.2	Effect of CH ₄ :O ₂ Fuel Feed Ratio on the Performance of Ni@SiO ₂ catalyst	134
6.1.3	Effect of Gas Hourly Space Velocity (GHSV) on the Performance of Ni@SiO ₂ catalyst	137
6.1.4	Summary of testing over Ni@SiO ₂	138
6.2	Comparison of nickel nanoparticles and Ni@SiO ₂ for the POx of methane	138
6.3	xNi/SiO _{2, sph} Catalyst performance	144
6.3.1	Effect of Nickel loading on the performance of xNi/SiO _{2, sph} catalysts	144
6.3.2	Effect of Gas Hourly Space Velocity (GHSV) on the Performance of xNi/SiO _{2, sph} catalyst	148
6.3.3	Long term testing of xNi/SiO _{2, sph}	153
6.3.4	Summary of testing of xNi/SiO _{2, sph}	158
6.4	Comparison of Catalyst Performance between 3Ni/SiO _{2, sph} and Ni@SiO ₂	159
6.5	Summary	166

In this chapter the catalytic performance of the synthesised $x\text{Ni}/\text{SiO}_{2, \text{sph}}$ and $\text{Ni}@\text{SiO}_2$ catalyst is assessed in terms of methane conversion and hydrogen, carbon monoxide, and carbon dioxide yields. The catalysts were tested in a quartz tube fixed bed reactor as described in section 3.3. Catalytic activity was recorded by measuring the composition of reformed gases by gas chromatography. The performance was determined as a function of temperature, $\text{CH}_4:\text{O}_2$ ratio, and gas hourly space velocity (GHSV).

In this section the results of the $\text{Ni}@\text{SiO}_2$ catalyst are first examined and compared with the equilibrium data, collected in Chapter 4, to ensure that trends observed in the performance of the catalysts were as expected. The chapter then goes on to compare the performance of different catalysts. Secondly, $\text{Ni}@\text{SiO}_2$ is compared with bare Ni nanoparticles to assess the effect of the SiO_2 shell on performance stability. Next, the three $x\text{Ni}/\text{SiO}_{2, \text{sph}}$ catalysts are compared to assess the effect of nickel loading on their performance. Finally, $\text{Ni}@\text{SiO}_2$ is compared with $3\text{Ni}/\text{SiO}_{2, \text{sph}}$ to evaluate the influence of support role on activity. These two catalysts were chosen for comparison as a consequence of the results given in Chapter 5. These were the catalysts with the most comparable nickel particle size, loading, and surface area. Where appropriate, post-testing characterisation results have been included in this chapter to explain trends in catalytic performance.

It is important to comment here on the reaction products which are advantageous for this study. The intended application for the catalyst is natural gas reformation for SOFC.

Therefore, the desired reaction products constitute of anything that can be consumed in an SOFC to give electrical power. It is common for SOFC to electrochemically oxidise hydrogen as well as carbon monoxide as shown in Section 1.1.1. In addition, due to the high

temperature operation, it is possible to activate C-H bonds and directly oxidise hydrocarbons at the anode [224]. However, a major issue with direct hydrocarbon utilisation is deactivation due to carbon deposition. Subsequently, modified anodes are required to inhibit coking [225]. It is for these reasons that the highest conversion of methane to hydrogen and carbon monoxide is preferable, this is termed: syngas production selectivity. Complete oxidation of methane to carbon dioxide and water vapour is unfavourable since these products cannot be further utilised by the fuel cell.

6.1 Ni@SiO₂ Catalyst Performance

6.1.1 Effect of Temperature on the Performance of Ni@SiO₂ catalyst

Figure 60 shows results of an experiment in which the temperature of a Ni@SiO₂ fixed bed reactor was varied from 550°C to 950°C in 100°C intervals. Each temperature step was maintained for 2 hours and the performance indicators (CH₄ conversion as well as H₂, CO, and CO₂ yields) are presented relative to time. This temperature range was selected to cover the temperatures around which SOFC are operated and therefore the temperatures at which the catalyst could be required to operate at, if utilised as an IIR catalyst. The range includes low temperatures which could be used in the future for SOFC operation. Figure 60 shows that the performance of the catalyst was stable for the duration of each two-hour temperature interval. An average of the results for each temperature was calculated and these are shown in Figure 61 with respect to temperature.

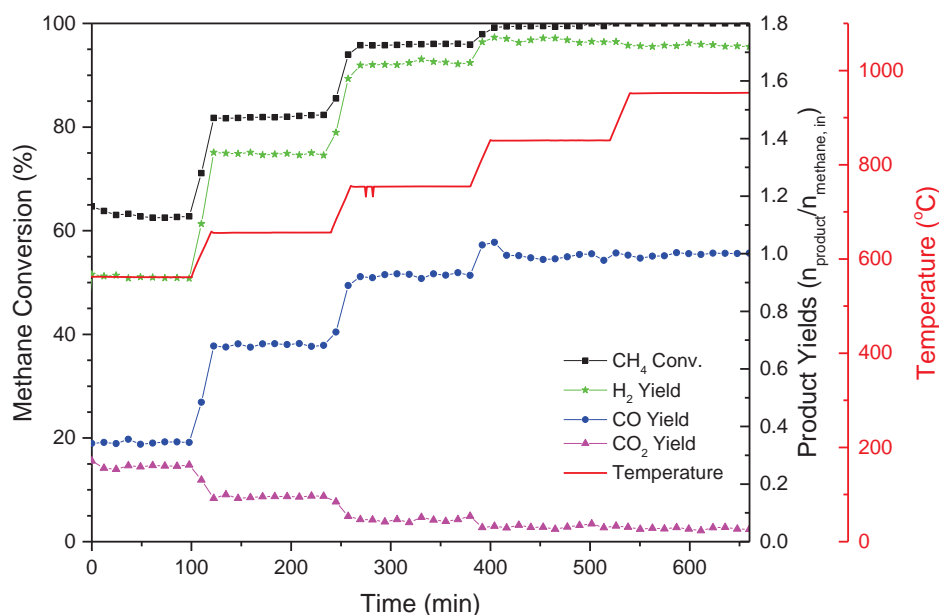


Figure 60: Effect of Temperature on Ni@SiO₂ Performance.

Figure 61 also shows the values of methane conversion and product yields at equilibrium, as calculated in Chapter 4. The equilibrium values are represented in Figure 61 by dashed lines. The shaded regions of the graph show an indication of error in the GC measurements.

Increasing the temperature of the reactor increased methane conversion and this was favourable for hydrogen and carbon monoxide yields, up to a maximum. Methane conversion over Ni@SiO₂ reached its maximum (close to 100%) at around 850°C, in good agreement with literature [191,193] and according to thermodynamic equilibrium. Past this temperature, complete methane conversion continued and product yields plateaued (H₂ = ~1.725, CO = ~1.0) since methane thermally decomposes at these temperatures [226] allowing for oxidation products to readily form.

At the tested GHSV (80640 ml.g⁻¹.h⁻¹), equilibrium was allowed to establish over the catalyst; Figure 61 shows that the methane conversion results closely match the conversion predicted by CEA. CO and CO₂ yields were also comparable. H₂ yield was lower than the expected

equilibrium value at all temperatures. This difference shows that significant amounts of water vapour were produced which were not recorded by the GC. The equilibrium analysis omitted water as a possible product due to the GC not being able to quantify this species. The equilibrium analysis therefore assumes all hydrogen atoms, generated by methane conversion, produce H_2 gas. It therefore follows that the actual H_2 yield is lower than the CEA results since, in reality, some hydrogen atoms are bound into water molecules. This was further confirmed by the observation of water accumulating in the water trap which was fitted after the reactor, before the GC.

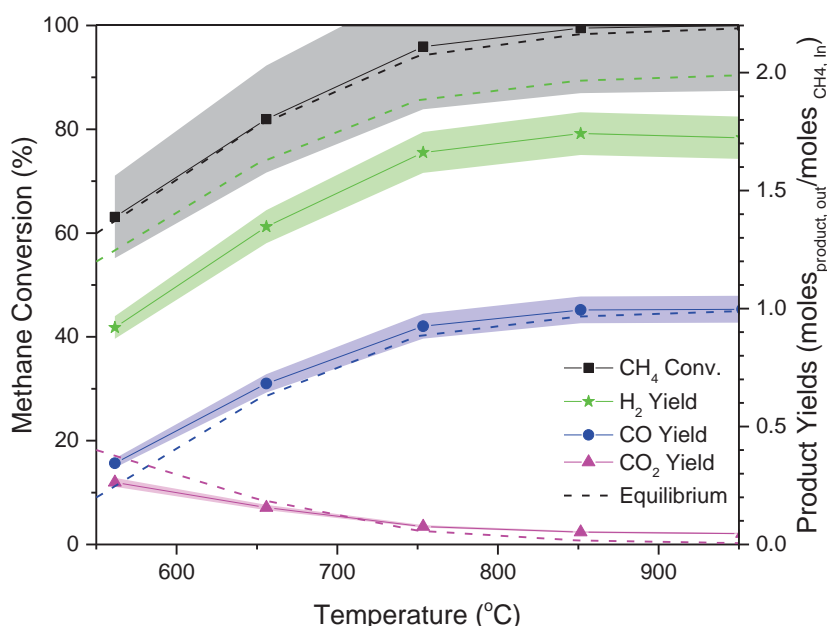


Figure 61: Average performance of Ni@SiO₂ with Increasing Temperature

It was confirmed that it was the catalyst enabling equilibrium to be reached at these reaction conditions by testing the methane conversion in a fixed bed reactor containing bare SiO₂ particles. When the catalyst was not present, the gas mixture did not reach equilibrium at this flow rate, as shown in Appendix H. This shows that the catalyst successfully increased the rate of partial oxidation.

At low temperatures there was evidence of complete oxidation governing the final product composition. Large amounts of CO_2 were recorded at low temperatures in contrast to high temperatures. Complete oxidation is perhaps a misleading term for the conversion of methane to carbon dioxide and water since it could suggest that all reactions have come to completion. It is known from the discussion in Chapter 4, however, that this is far from the case. As temperature increases, dry reforming (DR) and steam reforming (SR) reactions become energetically viable. These reactions consume the products of complete oxidation in order to produce more CO and H_2 , a process which overall results in the same reaction products as partial oxidation. The detection of CO_2 at low temperature and its subsequent consumption at high temperatures is evidence for the oxidation-reformation mechanism being exhibited on this catalyst at this GHSV.

As further evidence of both endothermic and exothermic reactions occurring, indicating the oxidation-reformation mechanism, the temperature of the reactor, close to the surface of the catalyst, was recorded using a thermocouple. As the furnace temperature was increased during the experiment, the difference between the set and measured temperatures reduced, as shown in Figure 62. This is consistent with the oxidation-reformation mechanism given that at low temperatures there is evidence of large proportions of additional furnace heating, i.e. exothermic oxidation reactions, and at higher temperatures, where SR and DR become viable, the cumulative effect of their endothermicity and the exothermicity of total oxidation, reduces the additional heating of the furnace. As described in Chapter 4, Figure 28, the overall reaction for partial oxidation is slightly exothermic. This explains why the temperature recorded by the thermocouple remains slightly higher than the temperature at which the furnace was set at all temperatures.

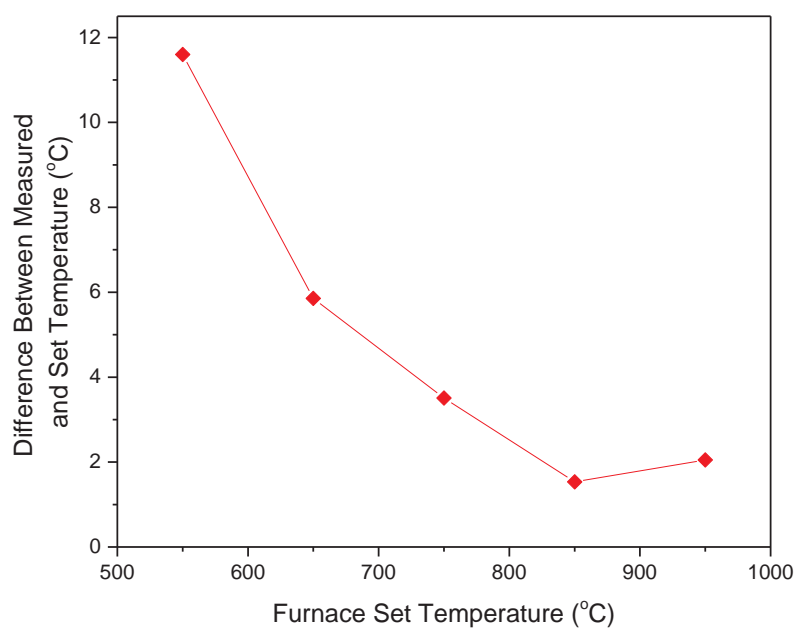


Figure 62: Difference in the temperature recorded near to the catalyst surface and the set furnace temperature with increasing furnace temperature.

6.1.2 Effect of $\text{CH}_4:\text{O}_2$ Fuel Feed Ratio on the Performance of $\text{Ni}@\text{SiO}_2$ catalyst

Figure 63 shows the effect of increasing oxygen content in the fuel feed on the catalyst performance. Again, error is indicated by the shaded regions and the expected equilibrium values are given by the dashed lines. All experiments were carried out with the furnace set to 750°C , and $\text{GHSV} = 80640 \text{ ml.g}^{-1}.\text{h}^{-1}$. Figure 63B shows the variation in temperature from the set point during the experiment.

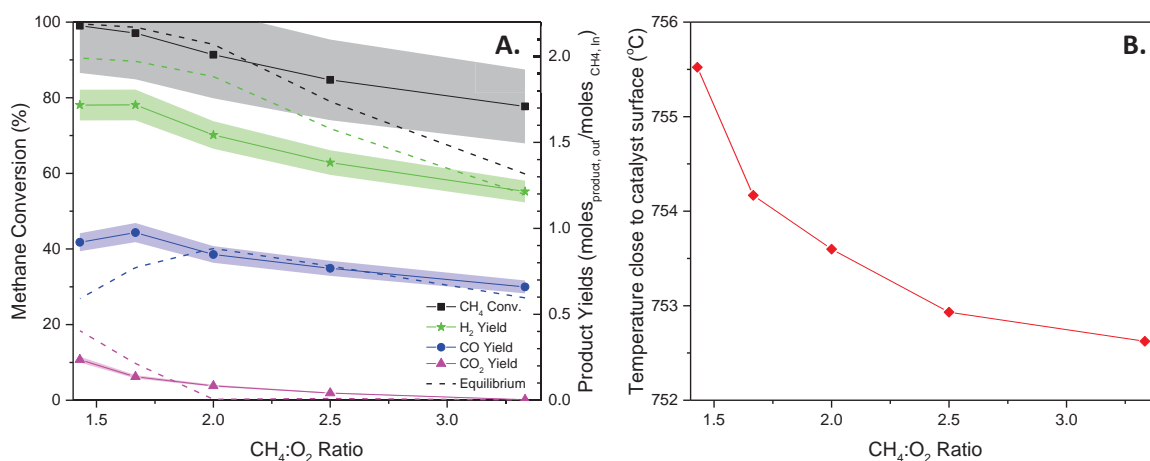


Figure 63: Effect of $\text{CH}_4 : \text{O}_2$ ratio on A. catalyst performance and B. reactor temperature.

Figure 63B shows that as more oxygen is introduced to the catalyst bed (lower $\text{CH}_4:\text{O}_2$ ratio), the overall partial oxidation reaction becomes more exothermic in nature. Complete oxidation is more highly favoured at higher oxygen contents. This is visible in the product yields; Figure 63A shows the CO_2 yield was higher at increased oxygen fuel feed contents. Further evidence of this is shown in the difference between the predicted and recorded H_2 yield. As with previous experiments, at low $\text{CH}_4:\text{O}_2$ ratio the hydrogen yield recorded was lower than that predicted by equilibrium analysis due to water formation. As the $\text{CH}_4:\text{O}_2$ ratio increased, the difference between the H_2 yield recorded and the equilibrium value reduced, showing that at low oxygen content fuel feeds, total oxidation was discouraged. The experiment suggests that when the $\text{CH}_4:\text{O}_2$ ratio is greater than 3.25 all water produced by complete oxidation is consumed in other reformation processes, since the equilibrium and results data meet.

Equilibrium predicts that the selectivity of the reaction towards syngas production peaks at the stoichiometric ratio of methane to oxygen for partial oxidation, $\text{CH}_4:\text{O}_2 = 2$. The results presented in Figure 63 show the peak in selectivity to be slightly lower than this; higher H_2 and CO yields were recorded at a $\text{CH}_4:\text{O}_2$ ratio of 1.67 than at $\text{CH}_4:\text{O}_2 = 2$. Under these conditions higher CO yields were recorded than the equilibrium data expected, on the other hand a lower CO_2 yield was recorded than was predicted. This suggests that the catalyst is effective in promoting the reformation pathways.

An alternative reason for the higher than equilibrium levels of CO being observed at low $\text{CH}_4:\text{O}_2$ ratios, was that the $\text{CH}_4:\text{O}_2$ ratio was varied from high to low. This could result in

oxygen in the fuel feed burning carbon off from the catalyst which may have been deposited during higher $\text{CH}_4:\text{O}_2$ ratio experiments. CEA analysis suggested coking would be an issue at high $\text{CH}_4:\text{O}_2$ ratios, Chapter 4, Figure 34. Although this explanation does not account for the higher H_2 yield at $\text{CH}_4:\text{O}_2$ of 1.67 than at a ratio of 2.

It is clear from experiments in which $\text{CH}_4:\text{O}_2$ ratio and temperature were varied that the CO yield recorded by GC more closely resembled the CO yield predicted by equilibrium analysis, than the H_2 yield. One reason for this has already been given, the inability of the GC to measure concentrations of water vapour. However, there is another reason which must also be considered. Figure 63 shows that the CO_2 product of total oxidation was present at low $\text{CH}_4:\text{O}_2$ ratio and this disappeared at $\text{CH}_4:\text{O}_2$ ratios > 2 as any CO_2 produced was consumed in dry reforming. Figure 63 also shows the difference of H_2 yield recorded from the equilibrium at low $\text{CH}_4:\text{O}_2$ ratios due to the presence of H_2O produced. As discussed, this difference only becomes negligible, indicating no H_2O present in the exhaust, at a $\text{CH}_4:\text{O}_2$ ratio > 3.25 . A similar trend is noted in Figure 61. CO_2 yield reduces to a small amount at $T > 750^\circ\text{C}$, whilst a difference in the recorded and expected H_2 yield, indicating the presence of H_2O , is present at all temperatures. These results suggest that CO_2 is more readily consumed than H_2O . This is due to the reverse water gas shift reaction contributing to the final product composition. This reaction consumes CO_2 and H_2 in order to make CO and H_2O , and is therefore unfavourable. As shown in Chapter 4, Figure 26, the reaction becomes viable at temperatures greater than 700°C . Nickel is known to be a great catalyst for a number of reactions due to its many oxidation states being readily accessible [227] including the water gas shift reaction and its reverse [228], this is one of the downsides of nickel being so catalytically active.

6.1.3 Effect of Gas Hourly Space Velocity (GHSV) on the Performance of Ni@SiO₂ catalyst

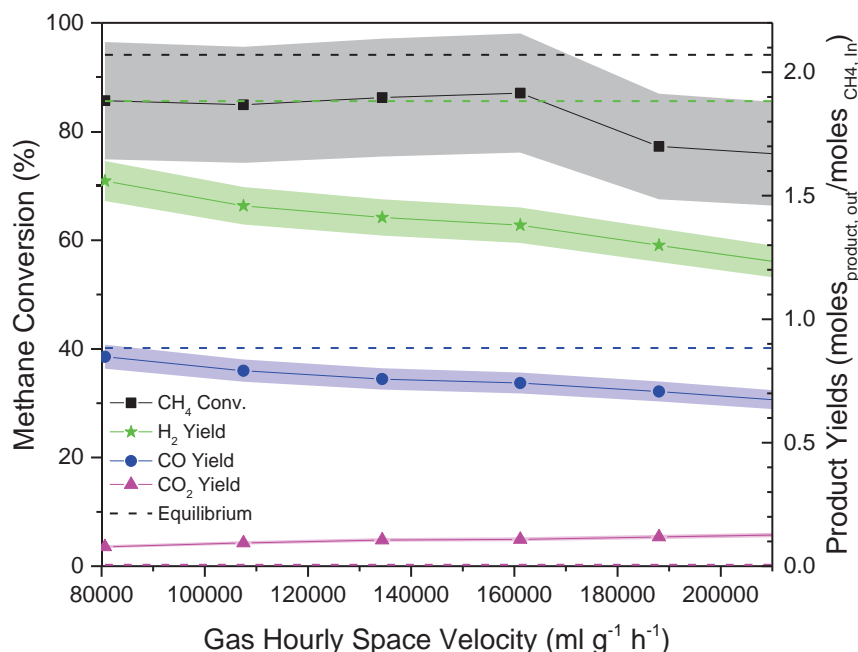


Figure 64: Effect of GHSV on catalyst performance recorded at a constant temperature of 750°C and a CH₄:O₂ ratio of 2.

GHSV was varied by changing the flow rate of the reactants over the catalyst bed. During this experiment the furnace temperature was set to 750°C and the CH₄:O₂ ratio was kept at the stoichiometric value of 2. This experiment was limited by the maximum flow rate of the mass flow controllers, only allowing GHSV of up to 214920 ml.g⁻¹.h⁻¹ to be tested.

Methane conversion remained at equilibrium until the GHSV exceeded ~160000 ml.g⁻¹.h⁻¹. Up to this point methane conversion reached the amount predicted by CEA, showing that the catalyst was effective in achieving equilibrium by increasing the rate of the partial oxidation. Past 160000 ml.g⁻¹.h⁻¹, kinetics prevented equilibrium being achieved. Nickel active sites were saturated with reactants and therefore additional reactants remained unconverted as there were no available nickel sites to increase the rate of their reactions. This saturation limit shows a boundary to which the catalyst can be deemed effective.

Figure 64 shows that as GHSV increased, the H₂ and CO yields gradually decreased. This is as a result of the kinetically sluggish SR and DR [193,229] reactions having less of an effect on the final product concentration due to a reduced amount of time that the reactants spend on the catalyst. The slowly increasing CO₂ yield is consistent with this conclusion.

6.1.4 Summary of testing over Ni@SiO₂

The Ni@SiO₂ catalyst was demonstrated as being an effective catalyst for the partial oxidation of methane to syngas. Methane conversion and syngas production selectivity over the catalyst increased with temperature up to 850°C, past which no further improvement was measured. The optimum CH₄:O₂ ratio for syngas production was shown to be 1.67 and the catalyst was demonstrated to be effective up to a GHSV of 160000 ml.g⁻¹.h⁻¹. The following section focuses on the importance of the silica shell in allowing this catalyst to operate.

6.2 Comparison of nickel nanoparticles and Ni@SiO₂ for the POx of methane

In order to determine the effect of the silica shell on the performance of the catalyst, uncoated NiO particles, prepared in the same way as the cores of the Ni@SiO₂ catalyst, were tested under the same reaction conditions. Figure 65 shows methane conversion and product yields recorded for the bare Ni nanoparticles and Ni@SiO₂ catalyst when they were tested for POx at different temperatures, ranging from 550°C to 950°C. As with previous experiments, the temperature was changed in 100°C intervals and each temperature step was maintained for 2 hours. As with previous experiments the CH₄:O₂ ratio was maintained at 2 and GHSV was fixed at 80640 ml.g⁻¹.h⁻¹. Figure 65 shows performance indicators relative to time, giving an indication of the catalyst stability.

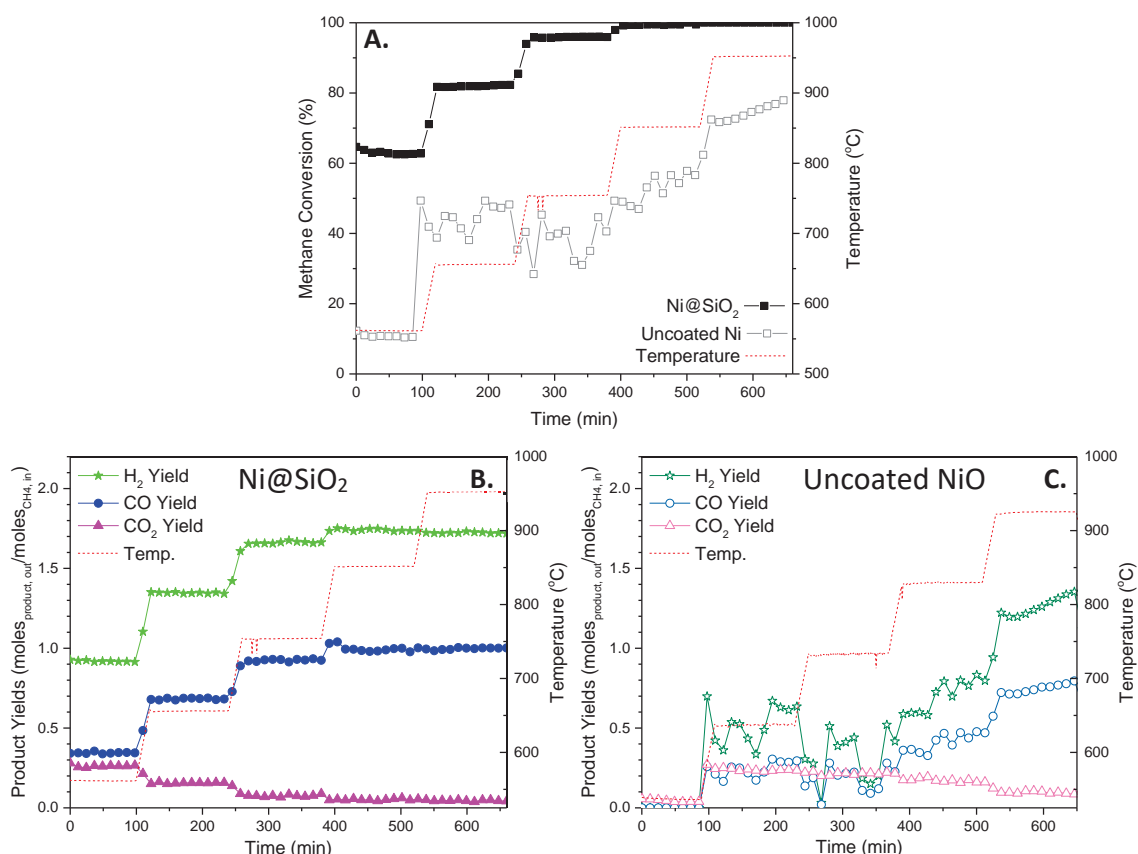


Figure 65: Comparing the catalytic performance of Ni and Ni@SiO₂ in terms of A. methane conversion and B-C. H₂, CO and CO₂ yield when tested under partial oxidation conditions at different temperatures. 5B shows results from Ni@SiO₂ whereas 5C. shows results from uncoated Ni.

During the 550°C temperature step, around 10% methane conversion was consistently achieved over the uncoated Ni catalyst. Van Looij and Geus [230] confirmed the nature of the nickel species responsible for POx in 1997. The authors observed that an oxidised nickel species would promote complete methane oxidation and reduced metallic sites were necessary to reform methane to syngas via SR and DR. Ding et al. depicted the processes which occur on the different nickel states, Figure 66 [100].

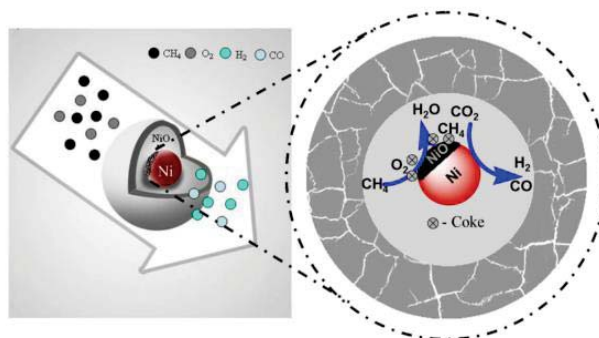


Figure 66: Partial oxidation proceeding over multiple oxidation states of nickel. Image taken from Ding et al. [98]

The nickel nanoparticles were reduced in-situ. However, when the POx gas mixture was introduced to the reactor the oxygen present was not consumed in methane conversion, therefore it re-oxidised the Ni nanoparticles to NiO. No oxygen was observed by the GC, and Figure 65C confirms that at 550°C no CO was produced and only low amounts of CO₂. Oxygen balancing revealed that around 20% of the input oxygen was unaccounted for in the evolved gases. It therefore follows that the oxygen must have been consumed in nickel oxidation. Van Looij and Geus comment on how the oxidising ability of the POx reactants is high when methane conversion is low [230]. Re-oxidation of the uncoated nickel particles was confirmed by XRD recorded after testing, Figure 67 shows the appearance of NiO diffraction peaks as a result of testing. During this low temperature step, all the methane conversion was attributed to total methane oxidation over NiO.

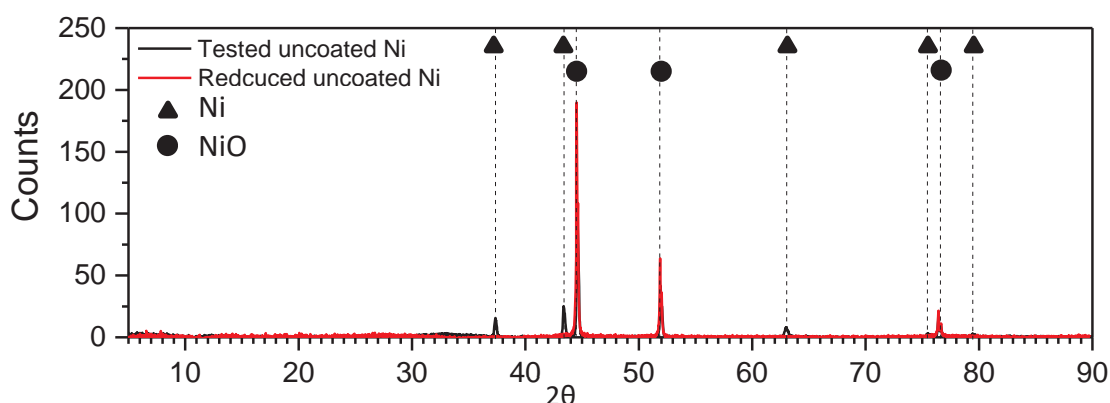


Figure 67: XRD of reduced and tested uncoated Ni nanoparticles.

What is initially apparent from Figure 65 is the difference in stability of the two powders. At all temperatures, the Ni@SiO₂ produced almost the same methane conversion and product yields for the duration of each of the two-hour time periods where the temperature remained constant. On the other hand, between 650 and 850°C the bare nickel nanoparticles resulted in an erratic amount of methane converted and the H₂, CO, and CO₂

yields were equally inconsistent. It is hypothesised that the instable performance of the uncoated nickel sample was due to re-oxidation of the nickel and subsequent redox cycling.

As described earlier, the reduced nickel powder was oxidised by unconsumed O₂ during the 550°C temperature step. Between the 550°C step and the 650°C step an activation process was evidenced; methane conversion rapidly increased from ~10% to above 45% and the production of H₂, CO, and CO₂ was kindled. Rashidi et al. showed reduction of NiO to commence at temperatures greater than 600°C under methane [231]. Alizadeh also reported NiO reducing at 600°C under methane, increasing in speed at higher temperatures and under higher concentrations of methane [232]. Given that NiO reduces to Ni under methane in the 550-650°C temperature range, the increase in methane conversion was attributed to this reduction process. In a similar manner other authors have attributed sharp increases in catalytic performance to catalyst reduction [233,234]. The increase in CH₄ conversion was mirrored in CO and H₂ production. CO and H₂ were produced in the reduction of NiO under CH₄ [231,232,235], as below, and also in the reformation of methane over metallic Ni [230]. Whilst methane conversion over NiO is possible to a certain extent (~10%), conversion is vastly improved over a nickel catalyst with a mixed oxidation state [230], >40% in this work. Metallic sites are critical in promoting syngas selectivity, evidenced by the evolution of H₂ and CO only once the catalyst is activated/reduced.



At temperatures between 650°C and 850°C methane conversion is still relatively low, compared with the conversion over Ni@SiO₂, and recorded values remain inconsistent. This variability was attributed to the redox cycling between nickel oxidation states since there

remains incomplete consumption of oxygen, due to low methane conversion. It was shown that when methane conversion was low, excess oxygen oxidised the nickel, NiO promotes total methane oxidation and a lack of Ni⁰ inhibits reformation. As a result, oxygen concentration falls and this spurred reduction of the NiO back to Ni⁰ due to the higher methane concentration. The mixed oxidation state of the nickel sites caused a spike in CH₄ conversion, and also in syngas production due to reformation reactions being catalysed over Ni⁰. This lowered the methane concentration. Methane conversion was still low, meaning the environment could tip back towards an oxidising one, and the cycle continued to repeat itself. The effects of this redox cycle are depicted in Figure 68.

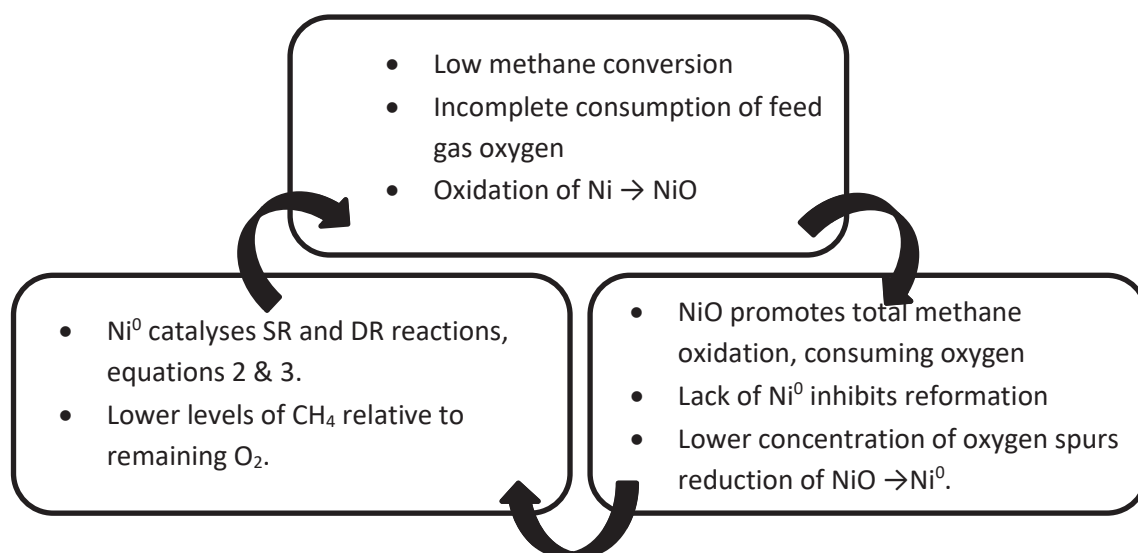


Figure 68: Redox cycling of nickel when tested for partial oxidation.

As the 950°C temperature step was reached, increased temperature drove faster reduction and more facile total methane oxidation. Methane conversion increased to a level where redox cycling was no longer possible, all oxygen was being consumed in methane oxidation. The erratic nature of the results therefore disappeared.

The Ni@SiO₂ catalyst did not exhibit redox cycling and therefore produced a stable level of methane conversion. XRD of the fresh and reduced catalysts showed that the silica shell made the reduction of the Ni@SiO₂ catalyst more difficult, Chapter 5, Figure 51 and Figure 52. The reduction procedure left the bare nickel particles fully reduced whereas the coated particles remained partially oxidised. In the same way, the silica shell protected the nickel against re-oxidation during the 550°C step. The mixed oxidation state of the nickel going into testing allowed for both combustion and reformation processes to occur. The silica shell was thereby making the Ni@SiO₂ a viable catalyst for the POx of methane to syngas. Silica shells control the flow of reactants and products to and from the catalysts surface. Pu et al. [236] investigated different materials with which to synthesise shells for nickel core, core@shell catalysts. The authors concluded the importance of the refinement of shell thickness in maintaining easy access of reactants to the catalysts surface. Silica was deemed to provide the thinnest shell of the tested materials, this resulted in the highest activity for the steam reforming of acetic acid. Song [237] also reported how the pore density of silica must be adjusted in order to achieve the highest catalytic activities due to facile movement of reactants. Cendrowski et al. [238] explain the increased time taken for iron oxide to further oxidise when magnetite is coated in a silica shell, the authors attributed the chemical stability of the core@shell particle to be due to the silica shell limiting the rate of oxygen diffusion to the iron surface. In this study, the uncoated nickel particles experienced oxidation which led to instability and deactivation the catalyst. The silica coated particles remained in their reduced state throughout testing, it is therefore concluded that the silica shell is critical in limiting the diffusion of oxygen to the nickel surface and thereby maintaining a high activity for syngas production by providing metallic nickel sites on which

reforming reactions were performed. Re-oxidation being inhibited was confirmed by XRD of the tested catalyst showing no NiO diffraction peaks, Figure 69.

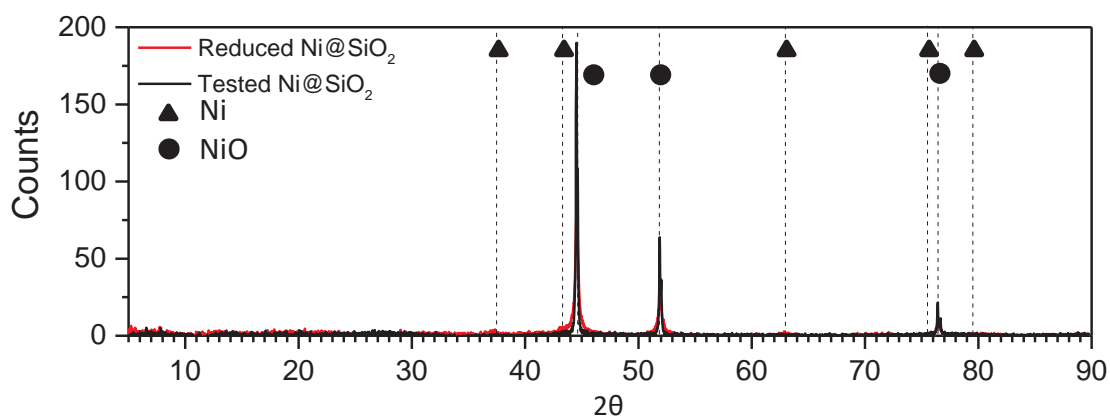


Figure 69: XRD of reduced and tested Ni@SiO₂.

These results highlight the importance of the silica shell in preventing the redox cycling of nickel species. By preventing the re-oxidation and subsequent redox cycling of Ni in Ni@SiO₂ the catalyst displayed stability unparalleled by bare nickel nanoparticles. In order to further investigate the importance of the silica shell in limiting oxygen diffusion and preventing reoxidation. It would be beneficial to prepare catalysts with varying degrees of porosity and pore size to determine a limit, past which maintaining the nickel in its reduced form is no longer possible.

6.3 xNi/SiO_{2, sph} Catalyst performance

6.3.1 Effect of Nickel loading on the performance of xNi/SiO_{2, sph} catalysts

Nickel loading had little effect on the performance of the catalysts when temperature was varied between 550 and 950°C, as represented in Figure 70. During these experiments the CH₄:O₂ ratio was maintained at 2 and the GHSV was 80640 ml.g⁻¹.h⁻¹. All catalysts operated close to equilibrium, resulting in similar performances. Any differences in CH₄ conversion/product yield could be associated to measurement error.

The same can be said for the effect of $\text{CH}_4:\text{O}_2$ ratio. As can be seen in Figure 71, the nickel loading did not change the CH_4 conversion or product yields to any significant degree since all catalysts were operating at equilibrium.

The similarity in these results was to be expected since the catalysts were generating equilibrium gas compositions and by definition, catalysts do not alter the position of equilibrium. Catalysts only change the rate at which equilibrium is reached. Differences could only be expected if the nickel content was lower than some minimum, where the reaction would be kinetically controlled. It was apparent that none of the catalysts had a nickel loading below this minimum. When GHSV was varied, differences were to be expected since this would highlight kinetics and the importance of the catalysts in speeding reactions up. It was also anticipated that some differences would be visible when the catalysts were tested for long periods of time since deactivation would occur at different rates depending on the amount of nickel present.

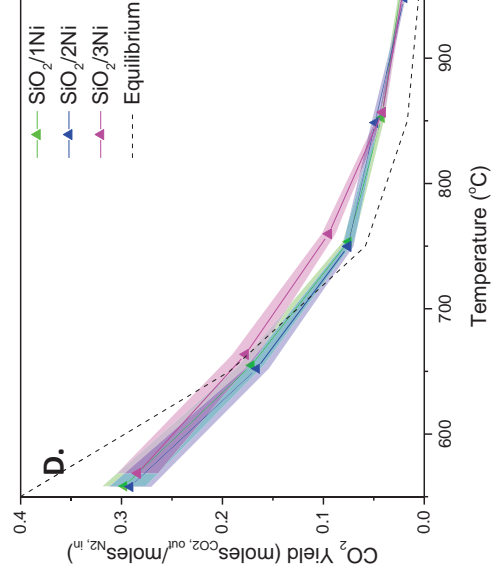
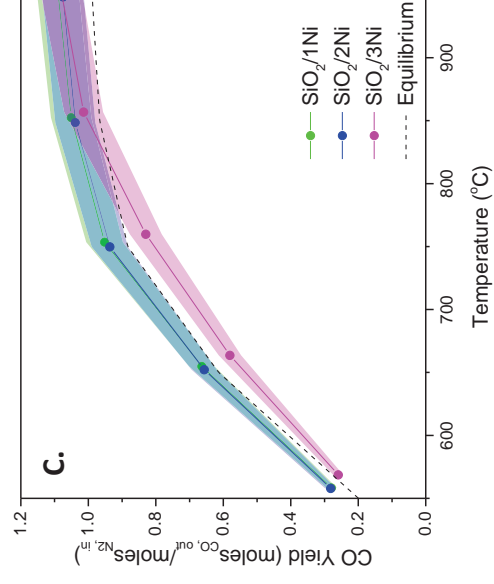
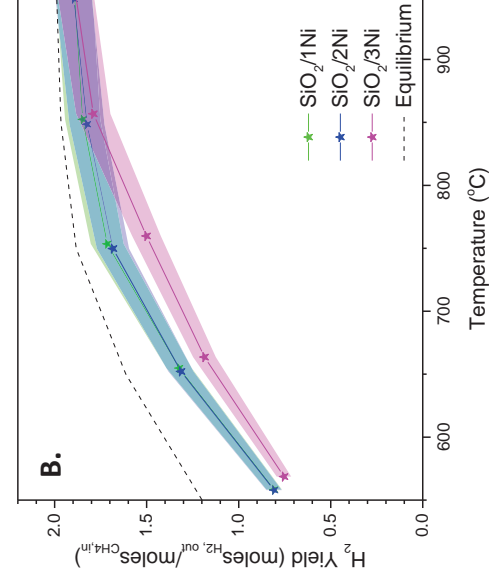
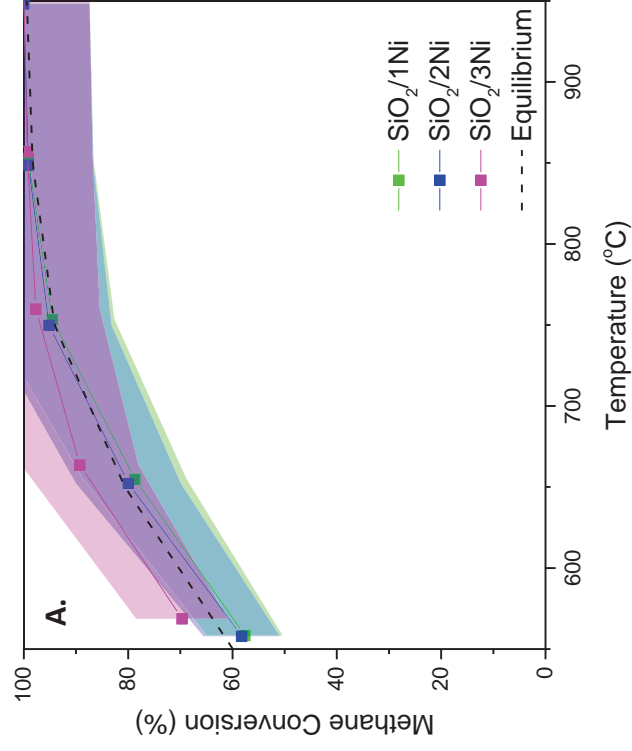


Figure 70: Effect of Temperature on (1-3)Ni/SiO_{2,sph} catalyst performance. Tested at a CH₄:O₂ ratio of 2 and a GHSV of 80640 ml g⁻¹ h⁻¹.

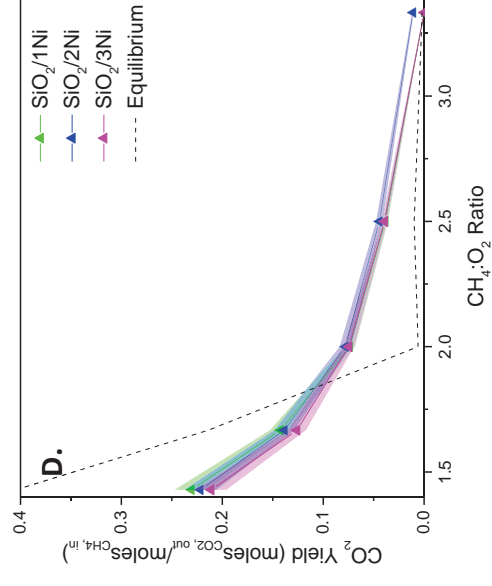
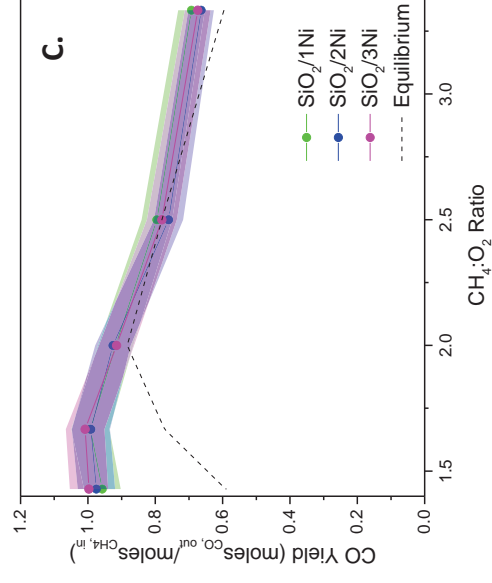
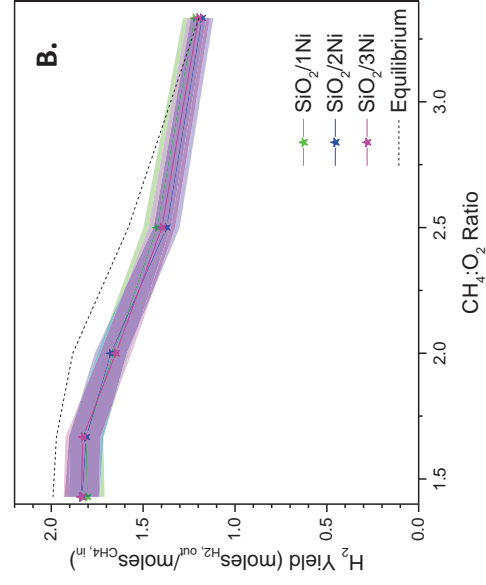
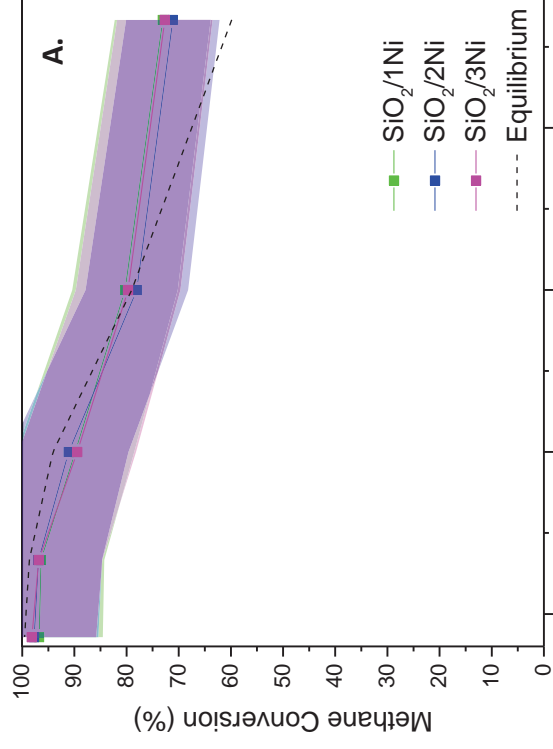


Figure 71: Effect of CH₄:O₂ ratio on (1-3)Ni/SiO₂,_{sph} catalyst performance. Tested at 750°C and a GHSV of 80640 ml g⁻¹ h⁻¹.

6.3.2 Effect of Gas Hourly Space Velocity (GHSV) on the Performance of xNi/SiO_{2, sph} catalyst

Varying the GHSV over the catalyst was limited by the maximum flow rates of the mass flow controllers. This meant that the range of GHSV which could be observed over 0.05 g of catalyst was limited to 80640 to 214920 ml.g⁻¹.h⁻¹. Over this range the methane conversion did not change for the xNi/SiO_{2, sph} catalysts, as shown in Figure 72. In this range of GHSV the selectivity of the catalysts towards syngas decreased, as with the Ni@SiO₂ catalyst this was due to the sluggish kinetics of the SR and DR reactions [146,193,229]. This is again evidence for the oxidation-reformation mechanism occurring over this catalyst at low GHSV. The extent to which H₂ and CO yield decreased did not remarkably change with increased nickel loading. It can be said that in the range of 80640 – 214920 ml.g⁻¹.h⁻¹, nickel loading had no effect on catalyst activity or selectivity towards syngas production.

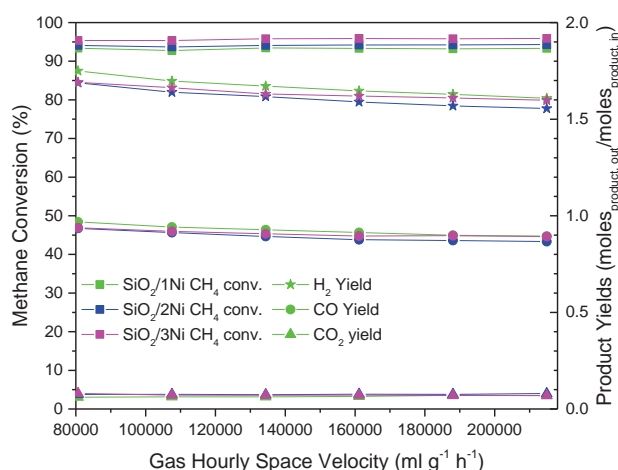


Figure 72: Effect of nickel loading in xNi/SiO_{2, sph} and GHSV on selectivity towards syngas production in the GHSV range 80640 to 214920 ml g⁻¹ h⁻¹.

No sharp drop-off from the equilibrium was noted in methane conversion when the GHSV was increased, as was observed with the Ni@SiO₂ catalyst. For this reason, higher GHSV were investigated. To achieve higher GHSV, the weight of the catalyst loaded into the fixed bed reactor was reduced from 0.05 to 0.0125 g and reduced further to 0.0063 g. This

allowed for the GHSV range to be extended to cover space velocities up to 1705714 ml.g⁻¹.h⁻¹. Figure 73 shows the results from these tests. The experiments where different weights of catalyst were used (0.05 g, 0.0125 g, and 0.0063 g) are shown in different colours in order to remind the reader that the experiments were completely different tests, run at different times.

GHSV is calculated by dividing the flow rate of reactants measured in ml.h⁻¹, by the weight of the catalyst. It therefore follows that when the weight of the catalyst is halved but the flow rate is doubled, the GHSV remains the same. It is for this reason that the data points cross over in the experiments that have utilised 0.0125 g and 0.0063 g of catalyst. There was a large discrepancy between the results recorded at the same GHSV but over different weights of catalyst. There is also a non-linearity between the results recorded over 0.05 g and 0.0125 g of catalyst. These jumps/discrepancies in the data were assigned to other factors than GHSV which could affect the catalyst performance when the weight of the catalyst in the fixed bed reactor was changed. Such factors include: changing the thermal efficiency of the reactor, changing the reactor length and decreasing the pressure drop across the reactor [239]. Nevertheless, trends in the data remain valid, particularly when it comes to the gradient with which conversion and selectivity decreases, relative to nickel loading.

Figure 73 shows that as the GHSV was vastly increased the effect of nickel loading began to play a significant role in both methane conversion and selectivity towards syngas production. At high GHSV methane conversion dropped more quickly in the 1Ni/SiO_{2, sph} catalyst than in the 2Ni and 3Ni catalysts. This was mirrored in the product yields, the 3Ni catalyst remaining

the most selective towards syngas production in both the 0.0125 g and 0.0063 g GHSV ranges.

It is concluded that the effect of nickel loading becomes more pronounced at higher GHSV. Higher Ni loading leads to a higher activity and selectivity towards syngas production. This is intuitive since the more nickel there is, the more active sites there are for reactions to occur. At low GHSV where values close to equilibrium are achieved the effect of having more nickel sites is not clear since the reactants have been allowed the time in which the catalyst can show its full potential. At higher GHSV the catalyst is asked to work much harder and convert reactants much quicker, at these GHSV having more active sites, more hands on deck, becomes vital.

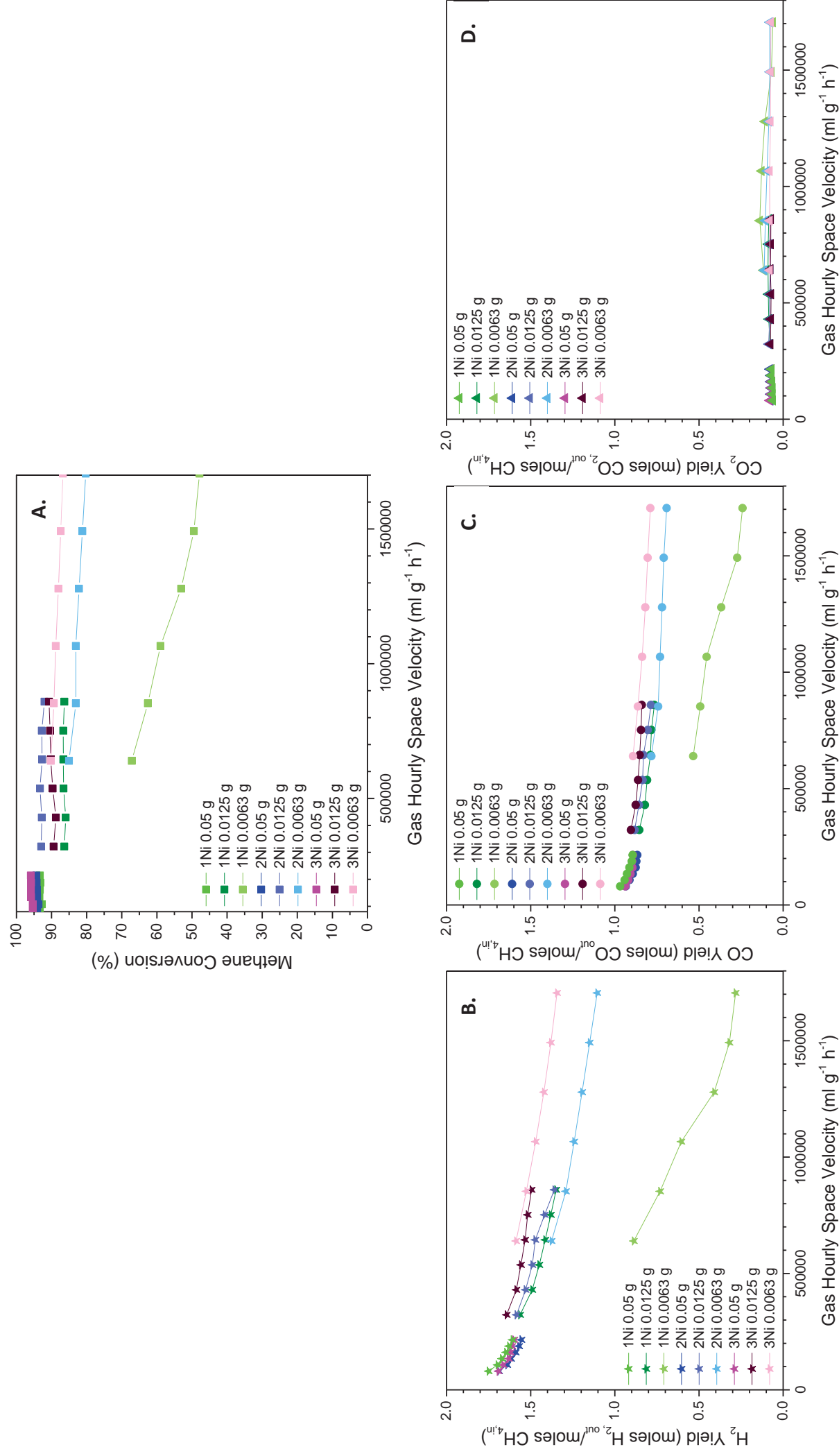


Figure 73: Effect of nickel loading in xNi/SiO₂_{sph} and GHSV on selectivity towards syngas production in the GHSV range 80640-1705714 $\text{ml g}^{-1} \text{h}^{-1}$.

CO₂ yield remains low over all tested GHSV, since the scale of Figure 73D has been matched to Figure 73B and C for comparison, the figure is not helpful for viewing the trends in CO₂ yield which were incredibly interesting. For this reason, the scale for the CO₂ yield was expanded and is shown in Figure 74.

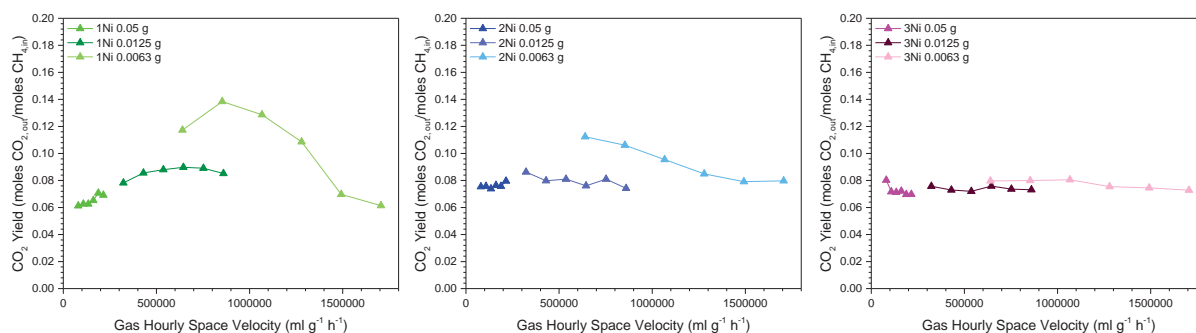
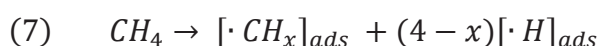


Figure 74: Effect of Ni loading on CO₂ yield when (1-3)Ni/SiO_{2, sph} catalysts were tested over a large range of GHSV.

The results from the 1Ni catalyst appear to go through a maximum, as does the CO₂ yield over the 2Ni catalyst, however, the maximum is a smaller one. The CO₂ yield at increasing GHSV over the 3Ni catalyst is almost linear. It has already been discussed how a decrease in syngas production selectivity mirrored by an increase of CO₂ yield is evidence for the oxidation-reformation mechanism. It seems apparent that the correlation between decreasing syngas selectivity and increasing CO₂ yield breaks down at higher GHSV. Several authors report that the direct mechanism for POx occurs at high GHSV [94,240,241]. The above results show tipping points between the oxidation-reformation and direct mechanisms. The GHSV at which the mechanism shifts is lower for catalysts with higher nickel loadings.

The break-down in the correlation between decreasing syngas production and increased CO₂ yield and therefore the switching of reaction mechanism appears at lower GHSV when nickel loading is increased. The direct mechanism for POx appears to dominate at all GHSV > 80640

ml.g⁻¹.h⁻¹ on the 3Ni catalyst, evidenced by linear CO₂ yield development with decreasing levels of syngas production. The direct mechanism for partial oxidation relies on homolytic dissociation of the reactants on the catalyst surface [242,243], via Equation 7, and it therefore follows that the mechanism will be favoured by higher nickel loadings since there will be more sites at which methane can dissociate.



6.3.3 Long term testing of xNi/SiO_{2, sph}

Testing the catalysts for longer periods of time revealed first insights into how the catalysts degrade. Figure 75 shows the GC results when each of the (1-3)Ni/SiO_{2, sph} catalysts were tested for 5 days at 750°C, at a CH₄:O₂ ratio of 2 and GHSV of 80640 ml g⁻¹ h⁻¹. The conversion and product yields vary depending on the external lab temperature; this daily temperature cycle does not affect the overall trend of degradation.

The methane conversion steadily decreased at a comparable rate across all 3 catalysts. The H₂ and CO yields were highest for the 2Ni/SiO_{2, sph} catalyst and selectivity towards syngas production decreased the most in the 1Ni/SiO_{2, sph} sample. Any decrease in H₂ and CO yield was mirrored by an increase in CO₂ yield.

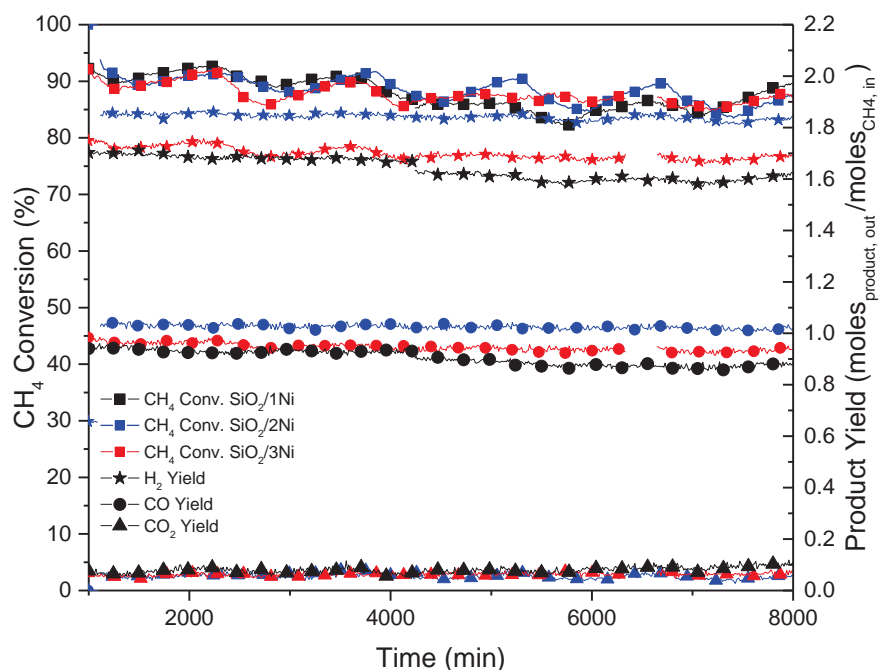


Figure 75: Long term stability of $x\text{Ni}/\text{SiO}_2, \text{sph}$ catalysts tested at 750°C , a $\text{CH}_4:\text{O}_2$ ratio of 2 and a GHSV of $80640 \text{ ml g}^{-1} \text{ h}^{-1}$.

Post-test characterisation revealed significant coking on the catalysts. TEM/EDS images showed that carbon nanotubes had grown, Figure 76. XPS (Figure 77A) and TGA under oxidising conditions (Figure 77B) showed that the extent of coking increased with nickel loading. Nickel particle agglomeration was also recorded to some extent evidenced in the particle size distributions, shown in Figure 78.

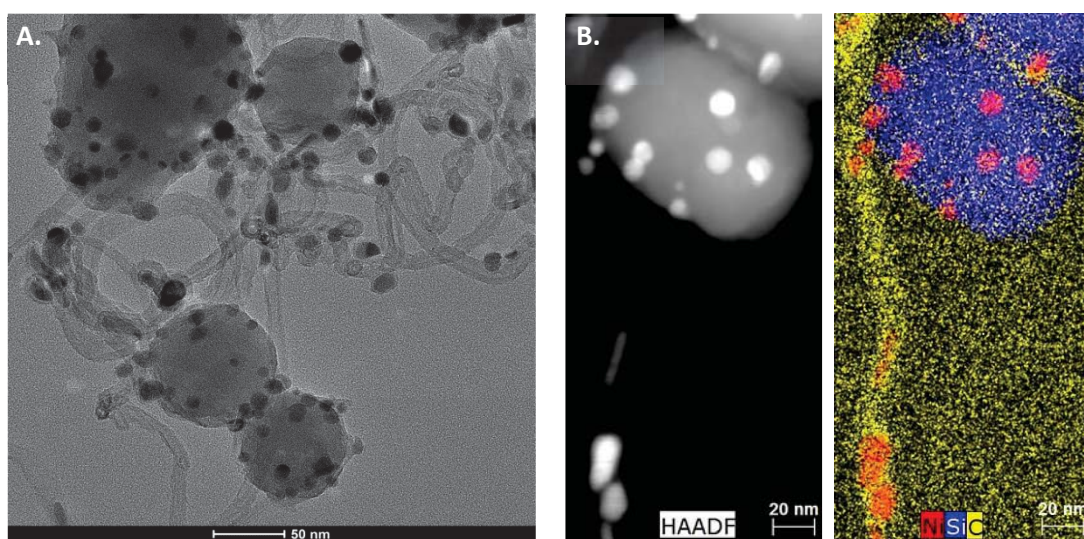


Figure 76: A. TEM, and B. EDS of tested $x\text{Ni}/\text{SiO}_2, \text{sph}$

As shown in Figure 76, some of the carbon nanotubes contain nickel particles at their tips. Yan et al. [244] describe how carbon nanotubes can form on Ni/SiO₂ catalysts. To form carbon nanotubes, carbon atoms must first deposit on the surface of the catalyst, then dissolve into the metal particles and finally realign to form carbon-carbon bonds. Formation of carbon nanotubes indicates a low rate of carbon deposition, since only under such conditions do carbon atoms have time for dissolution into the metal particles followed by realignment. If there was a higher rate of carbon deposition, Yan et al. suggest that the structure of the carbon species formed would be more onion like [244].

The mechanism for carbon nanotube formation can be described as either tip-growth or base-growth. The base growth mechanism results in empty nanotubes where-as tip growth results in carbon nanotubes with metal particles at their tips. Figure 76 shows that the mechanism for carbon nanotube growth in these experiments was tip-growth. The tip growth mechanism seen here was a consequence of the phyllosilicate bond between the nickel particles and the support being relatively weak. A stronger interaction between the metal and its support would have resulted in the base growth mechanism since the metal would not be so readily pushed away from the support when the carbon atoms realign. The base growth mechanism was observed for a Ni/MgO catalyst [245]. With the tip-growth mechanism, nickel particles are separated from the silica particles. With time the carbon nanotubes break [246,247], leading to a drastic reduction in the active surface area of the catalyst and therefore deactivation.

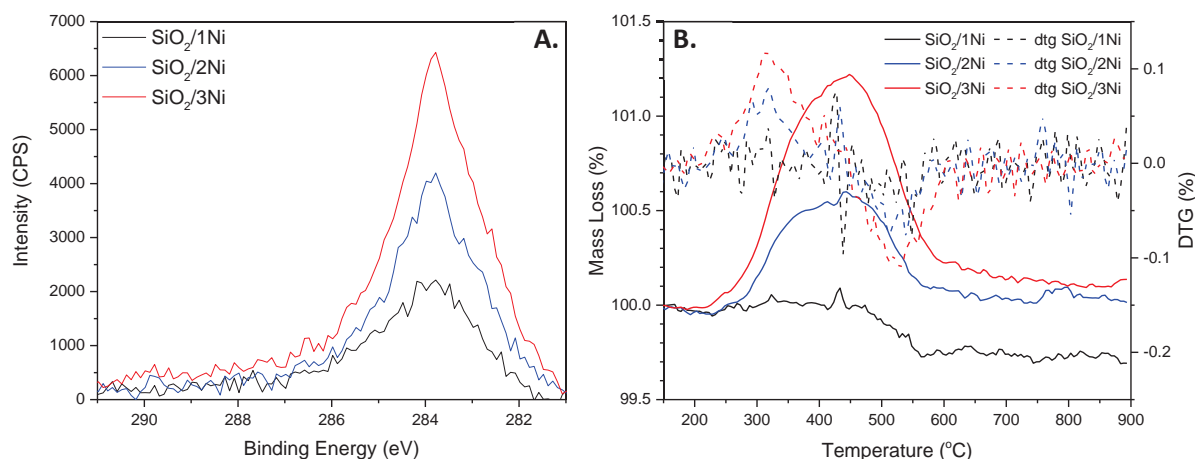


Figure 77: A. C1s peak from the XPS of tested (1-3)Ni/SiO_{2, sph} catalysts and B. TGA of tested (1-3)Ni/SiO_{2, sph}; the mass loss at 525°C resulted from carbon oxidation [220].

The extent of carbon deposition on the catalysts increased with increased nickel loading as shown by the TGA and XPS results. This same trend has been previously reported since nickel is not only an excellent catalyst for hydrocarbon reforming, but it also catalyses carbon deposition. Methane dissociates on nickel surfaces when the methane molecule adsorbs with an energy greater than 50 kJ.mol⁻¹, and it has adsorbed onto a nickel site with free neighbouring sites [243]. The probability of these requirements simultaneously occurring increases with nickel loading since there are a greater number of nickel sites on which to adsorb.

Zhang et al. [248] report coking and agglomeration over a Ni/ γ -Al₂O₃ catalyst, whilst post-test characterisation revealed these deactivation mechanisms to have occurred the extent of the catalysts degradation (which was high) did not match the extent of coking/agglomeration evidenced which is fairly low. The slow deactivation process observed over the 80 hours of testing was therefore attributed to phase transformation of the support and it was concluded that coking and agglomeration would play a more significant role in performance reduction after longer periods of testing. A drastic reduction in the catalytic

performance as would be expected from coking and Ni particle migration was not observed over the 100+ hours of testing in this study. It is therefore thought that the nickel particles remain catalytically active when they are inside carbon nanotubes, as previously reported [248]. The small amount of deactivation visible in the GC results was therefore assigned to metal particle agglomeration. The particle size distributions, Figure 78, show that agglomeration was comparable for all three catalysts. It follows that the degradation profiles over the 100+ hours tested were therefore similar.

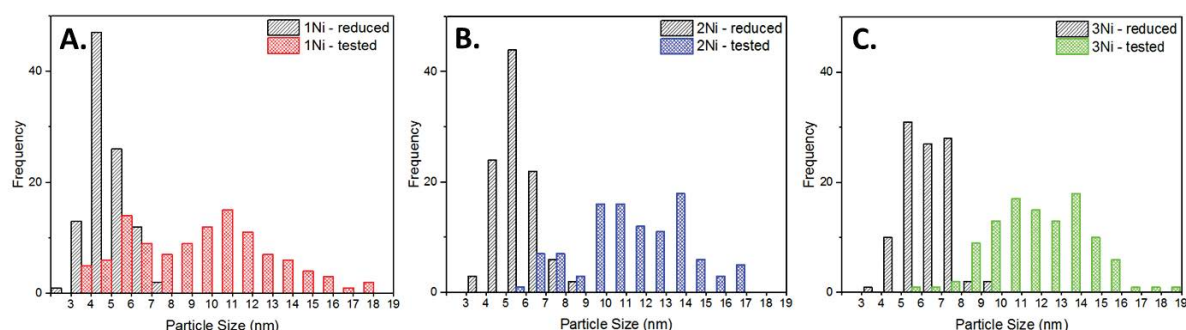


Figure 78: Particle size distribution for reduced and tested (1-3)Ni/SiO_{2, sph} catalysts respectively.

Table 26: The average Ni particle size of the xNi/SiO_{2, sph} catalysts before, and after testing.

	Reduced/nm	Tested/nm	Increase/nm	% increase
1Ni/SiO _{2, sph}	4.90	9.23	4.33	88.37
2Ni/SiO _{2, sph}	5.61	11.30	5.69	101.43
3Ni/SiO _{2, sph}	6.36	11.79	5.43	85.38

It would be expected that at some time the carbon nanotubes would begin to fracture, and nickel particle loss would cause more rapid degradation of catalyst performance. It would be expected that this would occur sooner on the 3Ni/SiO_{2, sph} catalyst given that the TGA and XPS results show larger degrees of coking in this catalyst.

6.3.4 Summary of testing of xNi/SiO_{2, sph}

In this section it was concluded that changing the nickel loading on a Ni/SiO_{2, sph} catalyst did not visibly impact on the catalyst performance when the following experiments were performed:

- Varying the temperature between 550 and 950°C with CH₄:O₂ = 2 and
GHSV = 80640 ml.g⁻¹.h⁻¹
- Varying the CH₄:O₂ ratio between 3.33 and 1.43, maintaining 750°C and
GHSV = 80640 ml.g⁻¹.h⁻¹
- Varying the GHSV between 80640 and 1705714 ml.g⁻¹.h⁻¹, maintaining 750°C and
CH₄:O₂ = 2

Changes in the catalytic performance arose when the catalysts were tested at very high GHSV at which time the direct mechanism for partial oxidation dominates and the 3Ni catalyst outperforms the catalysts with lower nickel loadings.

Over the 100+ hour period tested, the catalytic performance slowly reduced as a consequence of nickel particle agglomeration. Nickel loading had little impact on this and as such the catalysts degraded with comparable rates in the 100+ hour timeframe.

Carbon deposition was recorded on all three Ni/SiO_{2, sph} catalysts with larger amounts recorded on catalysts with higher nickel loadings. As a consequence of the mechanism for carbon deposition being tip growth, it is thought that with time the 3Ni/SiO_{2, sph} catalyst would degrade catastrophically in the shortest time period.

In the next section the 3Ni/SiO_{2, sph} catalyst will be compared with Ni@SiO₂ in order to show the effect of support role on catalyst performance.

6.4 Comparison of Catalyst Performance between 3Ni/SiO_{2, sph} and Ni@SiO₂

Given the results from Chapter 5, the catalytic performance of 3Ni/SiO_{2, sph} was compared with Ni@SiO₂ since these were the catalysts closest to one another in nickel loading and nickel particle size. Catalysts were compared to elucidate how the role of the support affected the catalytic ability. Comparison of the experiments where temperature, and CH₄:O₂ ratio were varied over Ni@SiO₂ and 3Ni/SiO_{2, sph} are given in Figure 79, both experiments were carried out at a GHSV of 80640 ml.g⁻¹.h⁻¹. During the experiment where the effect of temperature was investigated, the CH₄:O₂ ratio was maintained at a value of 2; when the CH₄:O₂ ratio was varied, the temperature was set at 750°C.

Figure 79 shows how the 3Ni/SiO_{2, sph} and Ni@SiO₂ catalysts performed comparably when the temperature, and CH₄:O₂ ratio were varied. It could be argued that the 3Ni/SiO_{2, sph} catalyst performed slightly better than the Ni@SiO₂ catalyst when conditions favoured total oxidation, i.e. at high temperature and low CH₄:O₂ ratio. Under these conditions the 3Ni/SiO_{2, sph} catalyst produced slightly elevated yields of CO and H₂ when compared with the Ni@SiO₂ catalyst. This could be due to the availability of more active nickel sites. The 3Ni/SiO_{2, sph} catalyst presented its nickel on the surface of the catalyst, reactants therefore had uninhibited access to the active sites. In the Ni@SiO₂ system, nickel was coated in a layer of porous silica. Therefore whilst reactants could access the nickel sites, they had to diffuse through the silica in order to do this.

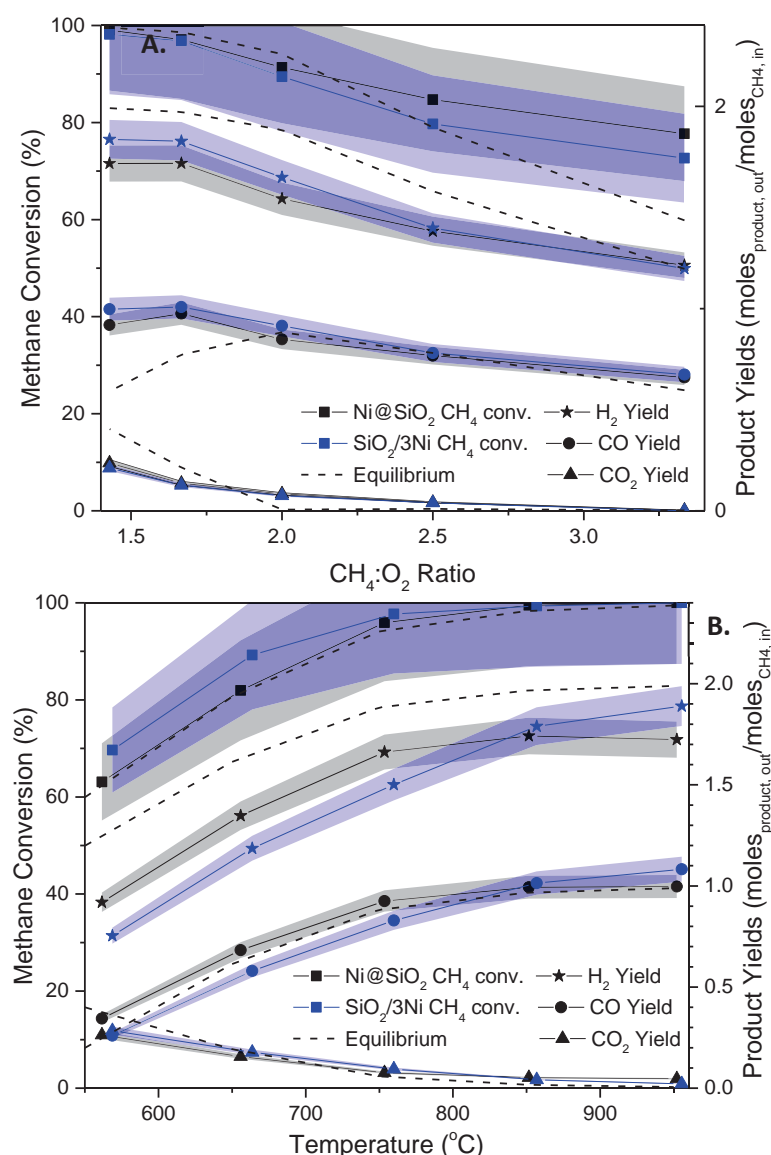


Figure 79: Comparison of $1\text{Ni}/\text{SiO}_{2,\text{sph}}$ and Ni@SiO_2 catalysts in experiments where A. temperature, and B. $\text{CH}_4:\text{O}_2$ ratio was varied.

At highly oxidising conditions, sluggish SMR and DR in the Ni@SiO_2 system due to limited access to catalytic sites reduced the amount of H_2 and CO produced. Zhang et al. showed the importance of tailoring the porosity and therefore the reactant diffusion resistance in nanoparticle shells in order to allow for effective particle agglomeration protection whilst allowing free movement of reactants and products [249].

Figure 80 shows the comparison of experiments where the GHSV was varied over the $3\text{Ni}/\text{SiO}_{2,\text{sph}}$ and $\text{Ni}@\text{SiO}_2$ catalysts. The $3\text{Ni}/\text{SiO}_{2,\text{sph}}$ catalyst showed levels of methane conversion close to equilibrium at all reactant flow rates. H_2 and CO yields gradually decreased while CO_2 yield gradually increased. The $\text{Ni}@\text{SiO}_2$ catalyst maintained equilibrium CH_4 conversion only up to $160000\text{ ml.g}^{-1}.\text{h}^{-1}$. H_2 and CO yields fell more rapidly, when compared with the $3\text{Ni}/\text{SiO}_{2,\text{sph}}$ catalyst. CO_2 yield increased also, again at a greater rate than was observed in the $3\text{Ni}/\text{SiO}_{2,\text{sph}}$ catalyst. It is clear that the $3\text{Ni}/\text{SiO}_{2,\text{sph}}$ catalyst had a higher specific activity than $\text{Ni}@\text{SiO}_2$, since $3\text{Ni}/\text{SiO}_{2,\text{sph}}$ clearly performed better than the $\text{Ni}@\text{SiO}_2$ catalyst at higher GHSV.

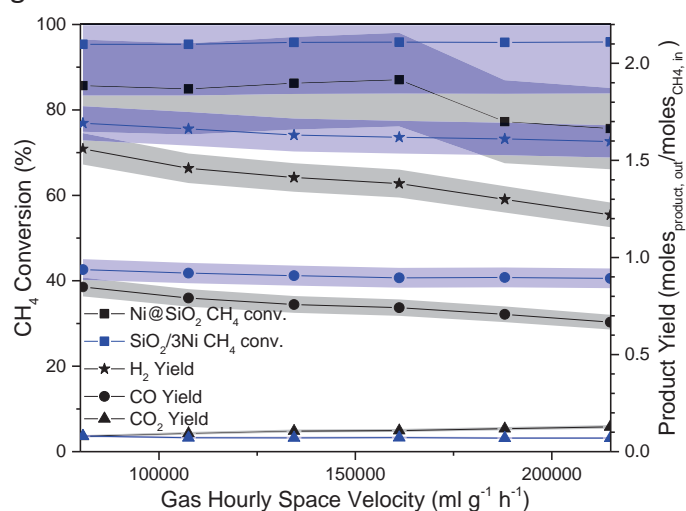


Figure 80: Comparison of $3\text{Ni}/\text{SiO}_{2,\text{sph}}$ and $\text{Ni}@\text{SiO}_2$ catalyst with varied GHSV

It is proposed that this is due to the active nickel species being more available to the flow of reactants in the $x\text{Ni}/\text{SiO}_{2,\text{sph}}$ system, than in the $\text{Ni}@\text{SiO}_2$ system. Since nickel nanoparticles are located on the surface of the catalyst in the $3\text{Ni}/\text{SiO}_{2,\text{sph}}$ system, there is less resistance to reactant diffusion than in the $\text{Ni}@\text{SiO}_2$ catalyst where reactants must diffuse through the mesopores of the silica shell in order to access the nickel. Bian et al. report a similar result [217]. Increased diffusion resistance also explains the greater effect of GHSV on product yields in the $\text{Ni}@\text{SiO}_2$ catalyst. Reduced access to Ni sites reduces the extent to which the

catalyst can activate the DR and SMR reactions, resulting in an exhaust stream with greater proportions of total oxidation products. The effect is emphasised at greater GHSV.

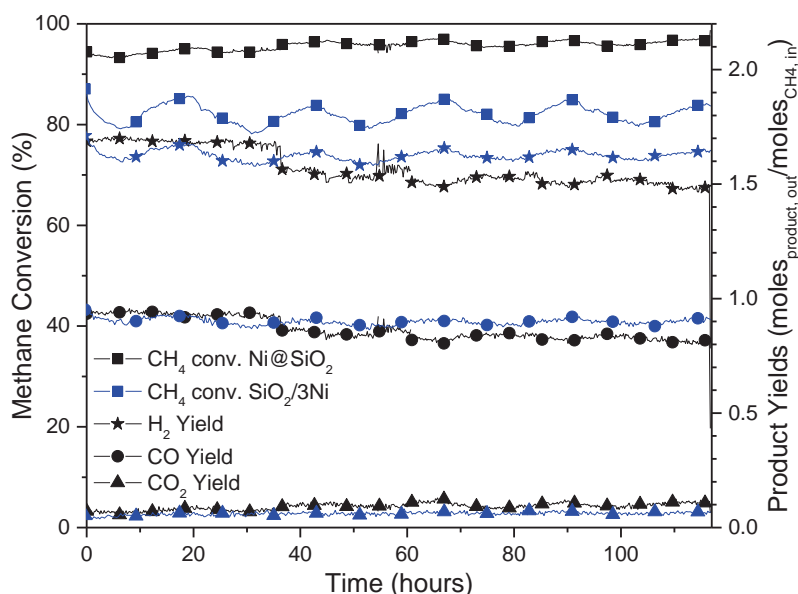


Figure 81: Long term stability of 3Ni/SiO_{2, sph} and Ni@SiO₂ catalysts tested at 750°C, a CH₄:O₂ ratio of 2 and a GHSV of 80640 ml g⁻¹ h⁻¹.

The long-term stability of the catalysts was determined by testing the activity of the catalysts at 750°C, a GHSV of 80640 ml⁻¹.g⁻¹.h⁻¹, and a CH₄:O₂ ratio of 2 for 120 hours. Figure 81 shows that the methane conversion of the two catalysts remains stable across the 100+ hour test period, additionally the conversion over the Ni@SiO₂ catalyst is shown to be markedly higher throughout the test.

However, the CO and H₂ yields gradually decrease for the Ni@SiO₂ catalyst whereas the selectivity towards syngas production appears to remain stable over the 3Ni/SiO_{2, sph} catalyst. In the Ni@SiO₂ test the decrease in H₂ and CO yields were mirrored by a gradual increase in CO₂ yield. This indicated a reduction in the extent of SR and DR, this could be caused by a reduced active surface area due to agglomeration. This was confirmed by TEM, XRD and BET.

Imaging of the tested Ni@SiO₂ catalyst and subsequent measurement of the particle size revealed that the average nickel particle size had increased from 9.19 nm to 12.4 nm. Distinguishing between a thinly and thickly coated nickel particle was not possible in the tested catalyst. Larger uncoated nickel agglomerates were still visible however. These were measured to range in size from 17.8 to 83.5 nm. It is proposed that the silica shell breaks down on the thinly coated particles and the resulting bare nickel agglomerates with the remaining uncoated nickel, evidence of large nickel particles with remnants of silica coatings are visible in Figure 82B. The particle size distribution of the uncoated Ni particles is also concurrent with this theory, Figure 82D, given that the distribution is not normal, indicating the existence of 2 different types of particles having been measured. XRD of the tested catalyst showed significant peak sharpening, Figure 69, indicative of particle growth. BET further confirmed that the active surface area was significantly reduced (Figure 83).

No carbon deposition was observed in the Ni@SiO₂ catalyst, none could be seen in the TEM images, Figure 82A and B, no mass loss was noted in the TGA trace of the tested catalysts measured under oxidising conditions, and the C1s peak in the XPS of reduced and tested samples were comparable, Figure 84.

As previously described, the small amount of deactivation in the 3Ni/SiO_{2, sph} catalyst is due to nickel particle agglomeration however catastrophic deactivation is predicted with time due to coking. The catalysts therefore exhibit deactivation mechanisms to a differing extent based on their support role assignment. When the silica was merely a structural support, the Ni/SiO_{2, sph} catalyst displayed small amounts of agglomeration whilst coking remained an

issue. On the other hand, when the silica was utilised as a protective shell, the Ni@SiO₂ catalyst resisted coking however agglomeration remained a problem.

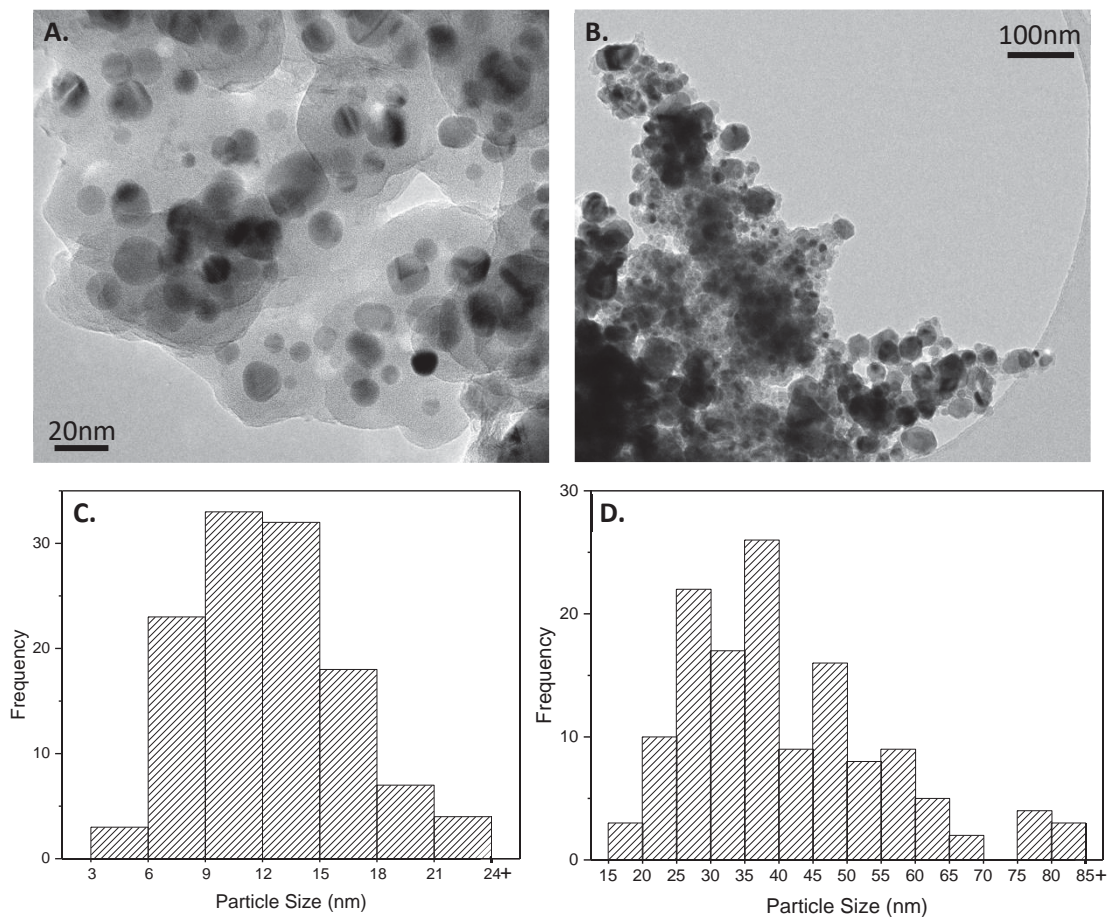


Figure 82: A-B TEM of Ni@SiO₂ and particle size distributions of C. coated and D. uncoated nickel particles.

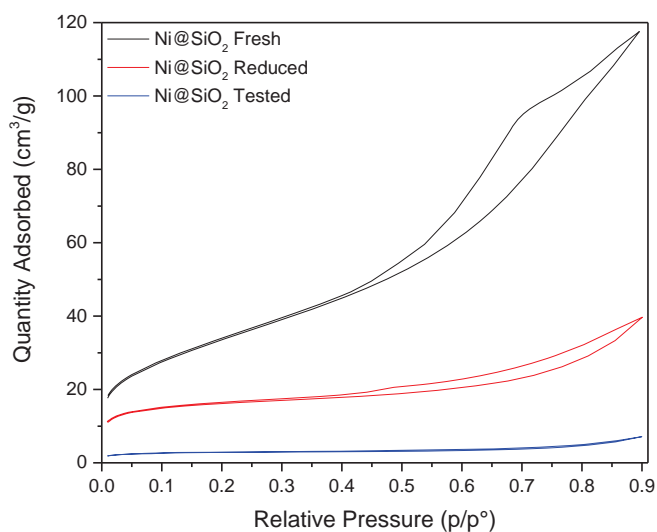


Figure 83: BET of fresh, reduced and tested Ni@SiO₂.

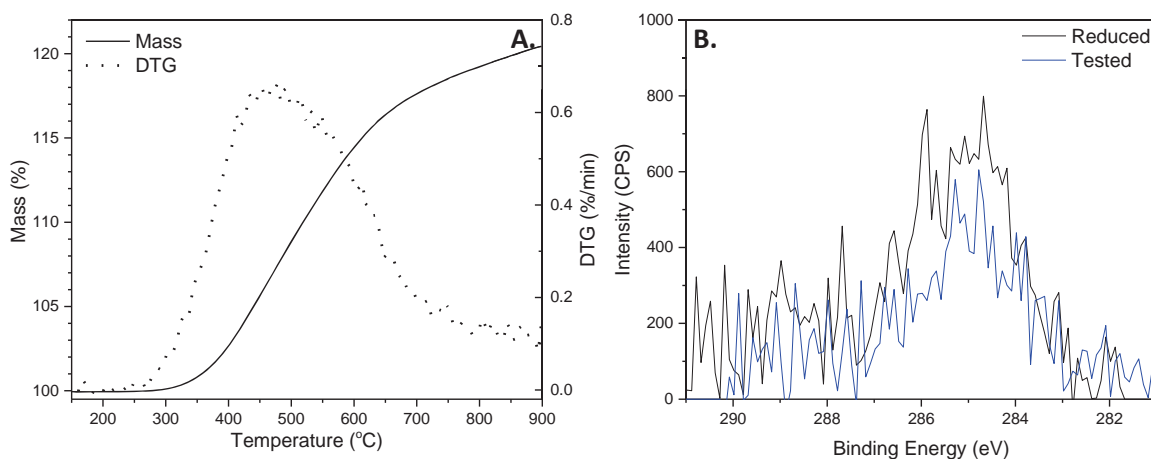


Figure 84: A. TGA and B. XPS of the tested Ni@SiO₂ catalyst.

In an attempt to accelerate the rate of degradation and elucidate which catalyst was more stable the catalysts were tested at a higher GHSV for 250 hours. 0.0125 g of each catalyst was loaded into the reactor and a CH₄:O₂ ratio of 2 was passed over the catalyst with a total flow rate of 112 ml.min⁻¹. This represented a GHSV of 537600 ml.g⁻¹.h⁻¹. The catalysts were tested at 750°C for 250 hours. The results obtained are shown in Figure 85.

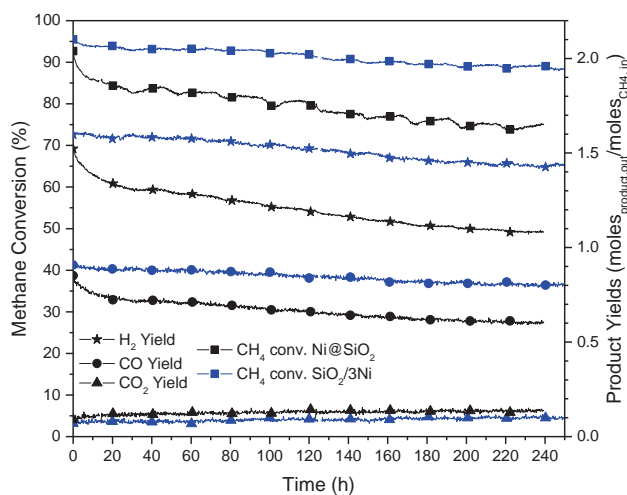


Figure 85: Long term testing of Ni@SiO₂ and 3Ni/SiO_{2, sph} at high GHSV.

The rate of degradation in the Ni@SiO₂ is higher in the first 20 hours of testing than the subsequent 220 hours of testing. The fast degradation during the first period is attributed to uncoated nickel particles rapidly agglomerating during this time, slower degradation is then

observed since the remaining particles are somewhat protected from agglomeration as previously mentioned.

A rapid decline in performance of the $3\text{Ni}/\text{SiO}_{2, \text{sph}}$ catalyst, as would be expected from the migration of nickel particles off the silica support due to carbon deposition, was not observed during the 250 hours of testing. This further reinforced the conclusion that degradation recorded in the $3\text{Ni}/\text{SiO}_{2, \text{sph}}$ catalyst was as a result of agglomeration rather than coking.

Excluding the first 20 hours of testing the rate of degradation was of the same order of magnitude although the $3\text{Ni}/\text{SiO}_{2, \text{sph}}$ catalyst was clearly more stable. Methane conversion dropped 5.5% in the $3\text{Ni}/\text{SiO}_{2, \text{sph}}$ catalyst whereas a 9.5% decrease was observed in the $\text{Ni}@\text{SiO}_2$ catalyst.

6.5 Summary

The effects of temperature, $\text{CH}_4:\text{O}_2$ fuel feed ratio, and GHSV on the performance of $\text{Ni}/\text{SiO}_{2, \text{sph}}$ and $\text{Ni}@\text{SiO}_2$ catalysts have been explored. The importance of the silica shell was investigated in the $\text{Ni}@\text{SiO}_2$ system and the effect of nickel loading was explored in the $\text{Ni}/\text{SiO}_{2, \text{sph}}$ system.

The SiO_2 shell was shown to be critical in protecting the nickel from rapid re-oxidation in the $\text{Ni}@\text{SiO}_2$ system. This prevented the catalyst from exhibiting Ni redox cycling and as a result the catalyst displayed a high activity and selectivity.

Increasing nickel loading was shown to improve the $\text{Ni}/\text{SiO}_{2, \text{sph}}$ catalyst performance at higher GHSV. Relative stability was shown over a 100+ hour testing period, however, post-

test characterisation revealed that carbon deposition remained an issue and worsened with increased nickel loading.

It was clear that the $3\text{Ni}/\text{SiO}_{2, \text{sph}}$ catalyst operated better than the $\text{Ni}@\text{SiO}_2$ catalyst at higher GHSV. The $3\text{Ni}/\text{SiO}_{2, \text{sph}}$ catalyst was also more stable than the $\text{Ni}@\text{SiO}_2$ catalyst when both were tested for longer periods of time. Different degradation methods dominated in each catalyst. Both suffered from agglomeration although the effects were greater in the $\text{Ni}@\text{SiO}_2$ system. The $\text{Ni}@\text{SiO}_2$ system resisted carbon deposition whilst this was largely apparent in the $3\text{Ni}/\text{SiO}_{2, \text{sph}}$ catalyst.

For the intended application, an indirect internal reforming catalyst, operating at 750°C is most interesting, 750°C being a common operating temperature for SOFC. At this temperature both catalysts provided a high methane conversion ($>95\%$) and showed a high selectivity towards syngas production. Both the $\text{Ni}@\text{SiO}_2$ and $\text{Ni}/\text{SiO}_{2, \text{sph}}$ catalysts were therefore considered as promising IIR catalysts and the following chapter describes the progress made in their integration into an SOFC.

Chapter 7

ACHIEVING INDIRECT INTERNAL REFORMING IN A FUEL CELL

7.1	Alumina fibres	170
7.2	Washcoating.....	171
7.3	Ex-situ testing of 1Ni/SiO _{2, sph} Fibre reactor	175
7.4	Ex-situ testing of Ni@SiO ₂ Fibre reactor	181
7.5	Ni@SiO ₂ Stub Reactor	184
7.6	Fuel Cell Testing	186
7.6.1	Long term testing on fuel cells	188
7.7	In-stream Gas Analysis	191
7.8	Summary	193

In this chapter, a method of achieving IIR within an SOFC is developed. Alumina hollow fibres are introduced as a novel material from which reforming bundles can be built. Alumina hollow fibres are high surface area tubes onto which catalysts can be mounted, the tubes can be bundled together to create a micro-reactor. In a similar fashion to that of monolithic reactors, alumina fibre bundle reactors offer a high catalytic activity and low pressure drop.

In this study, the $1\text{Ni}/\text{SiO}_{2,\text{sph}}$ and $\text{Ni}@\text{SiO}_2$ catalysts were washcoated onto the alumina fibres. Washcoating was selected as the method for mounting the catalyst onto the fibres due to the availability of resources, the facile nature and fine tune-ability of the procedure. The chapter describes the parameters which were optimised in order to achieve a fibre with a catalyst loading of 5 wt%.

The fibres were tested ex-situ from the fuel cell in a quartz tube reactor. The effect of the silica supports role on the fibre reactors performance are discussed. As a consequence of results showing the enhanced performance of the $\text{Ni}@\text{SiO}_2$ catalyst over the $\text{Ni}/\text{SiO}_{2,\text{sph}}$ catalyst, the latter catalyst was eliminated from further system integration.

The $\text{Ni}@\text{SiO}_2$ fibres were then tested in short lengths of tube of the same material as the fuel cell. These reactors were named “stub reactors”. Following promising results in the stub reactor the fibres were finally tested in an operational fuel cell.

The performances of the fuel cells were compared during operation on reformed gas from the fibre reactor and methane. The results show that $\text{Ni}@\text{SiO}_2$ has great potential as an IIR catalyst. The catalyst was fully integrated into the fuel cell, allowing for reformation of CH_4 directly fed into the fuel cell before the gases reached the anode. The fuel cell was operated

for over 160 hours and no evidence of damage to the reformer was observed at the end of testing.

7.1 Alumina fibres

Alumina hollow fibres were selected as the material from which to build an indirect internal reformer. Figure 86 shows a single hollow fibre, along with its dimensions, and an SEM image allowing the reader to visualise the high surface area of the fibres interior.

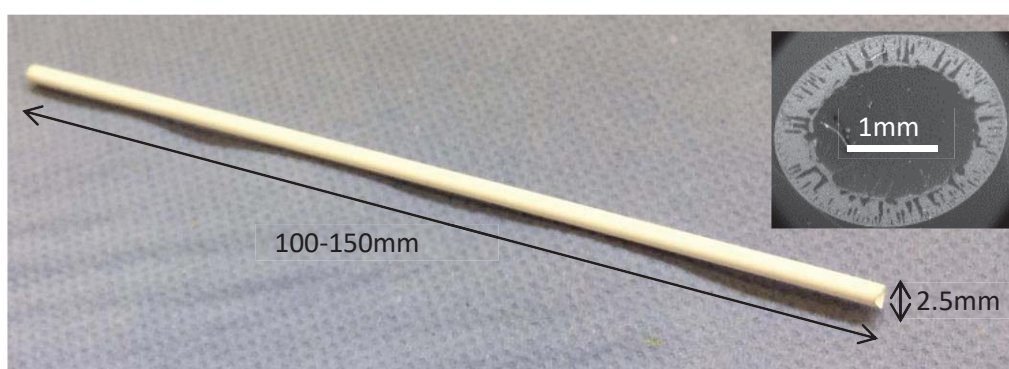


Figure 86: Alumina fibre showing dimensions and SEM of cross section.

Many thanks are attributed to Tao Li from the Li group at Imperial College London for supplying the fibres. The fibres were made by an immersion induced phase inversion process. An excellent summary of the process is given in the book, “Ceramic Membranes for Separation and Reaction” [250]. A polymer is dispersed in a solvent and the polymeric solution is then immersed in a non-solvent, the solvent diffuses out of the polymer whilst the non-solvent diffuses into the polymer. This exchange creates the unique finger like structures shown in the inset of Figure 86. The resulting hollow fibre structures can be applied across a number of applications including gas membrane separation, reactor synthesis, desalination, filtration and even fuel cell electrolytes/electrodes [251–255].

It was envisaged that the high surface area of the reactor wall would act as an intermediate between a wash-coated wall and a fixed bed reactor, containing high amounts of catalyst per unit volume while maintaining a low pressure drop. In addition, the non-linear channels would favour gas-catalyst contact and be beneficial to performance as in Fazeli and Behmans zig-zag configuration [181].

7.2 Washcoating

Figure 87A shows the effect of coating duration on the catalyst loading. During this experiment the washcoat was circulated at a pump rotation speed of 60 rpm. As the length of time which the fibre was subjected to the washcoating procedure for was increased the catalyst loading increased, linearly. Figure 87B shows the effect of increasing the speed at which the washcoat was circulated; all speeds were tested for 15 minutes. Increasing the speed at which the washcoat was circulated also increased the weight of catalyst loaded onto the fibre.

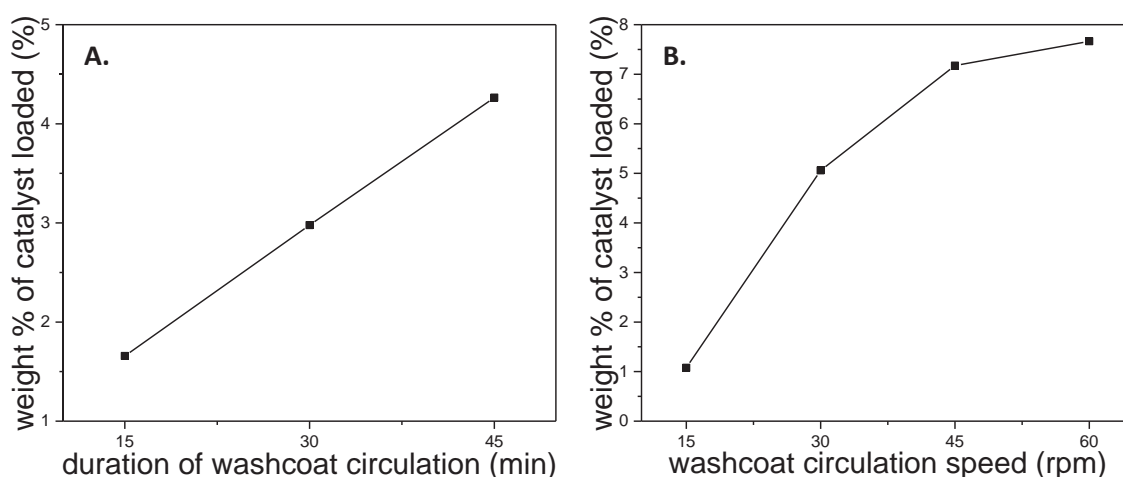


Figure 87: Effect of washcoat circulation duration and circulation speed on catalyst loading.

The effect of applying backpressure can be observed in Figure 88. 4 fibres were washcoated as per the details in Table 27. At both circulation speeds the catalyst loading increased when backpressure was applied.

Table 27: Range of experiments carried out to determine the effect of back pressure on catalyst loading.

Fibre #	Circulation Duration (min)	Circulation Speed (rpm)	Backpressure?
1	15	15	Yes
2	15	15	No
3	15	30	Yes
4	15	30	No

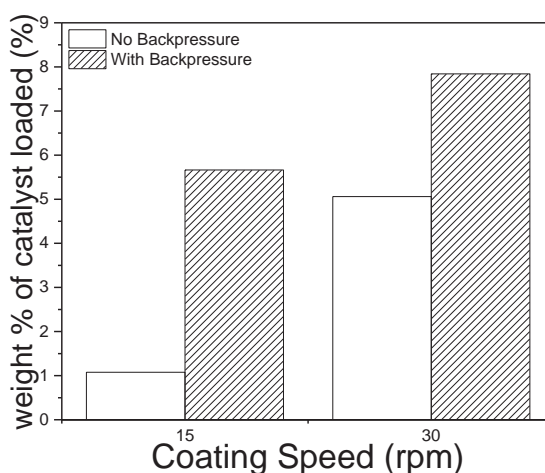


Figure 88: Effect of applying back pressure to catalyst loading of alumina fibre.

Figure 89 shows SEM/EDS images of a cross-section of the coated fibres. Some pores appear to be fully coated while others show no signs of catalyst. Not all pores within the fibre are connected to the fibre exterior due to the manufacturing process. However, it is assumed that the areas where the liquid washcoat will travel, as the washcoat is circulated through the fibre, are also the pores which reagents will pass through during testing. Therefore, so long as the desired catalyst loading is achieved, it is not important to focus on coating all the

pores of the fibre with catalyst. A well distributed and segregated layer of catalyst could also assist in thermal management as previously addressed by Settar et al. [174].

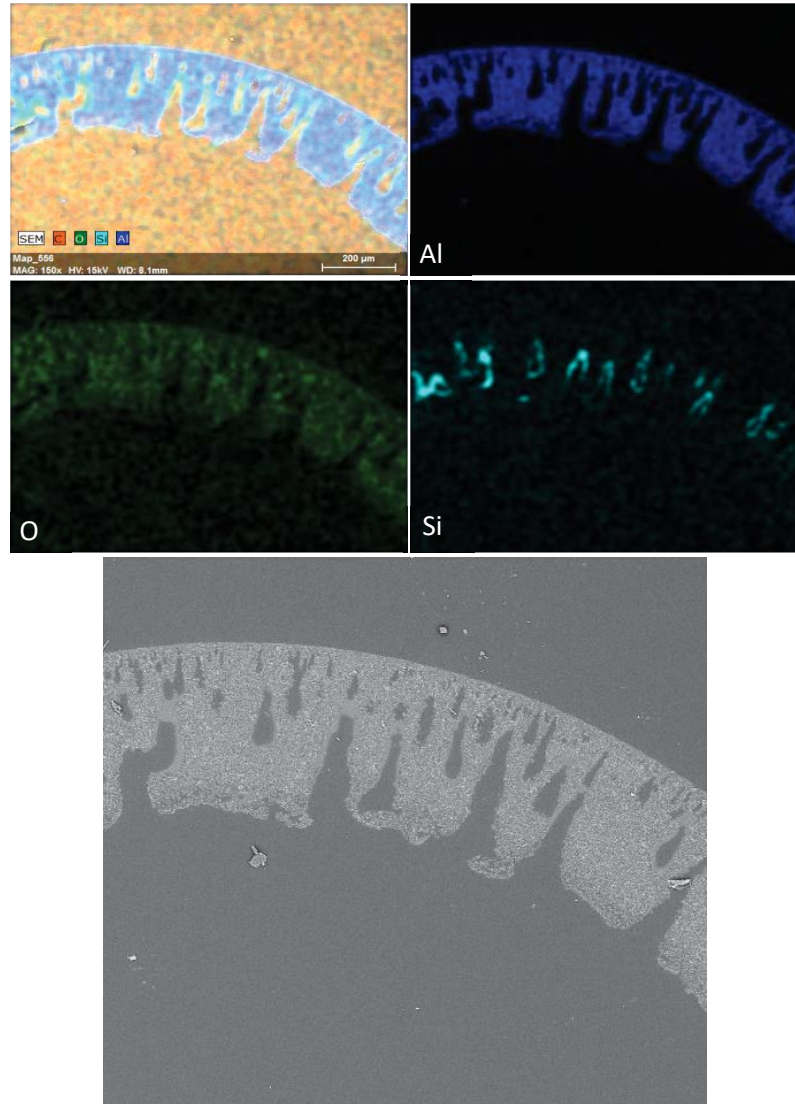


Figure 89: SEM/EDS of washcoated alumina fibre.

At low magnification as per Figure 89, no nickel was detected by the EDS since the particles were too small to be resolved. At higher magnification, Figure 90, nickel was detected in the catalyst layer, confirming that the catalysts were successfully deposited onto the alumina surface.

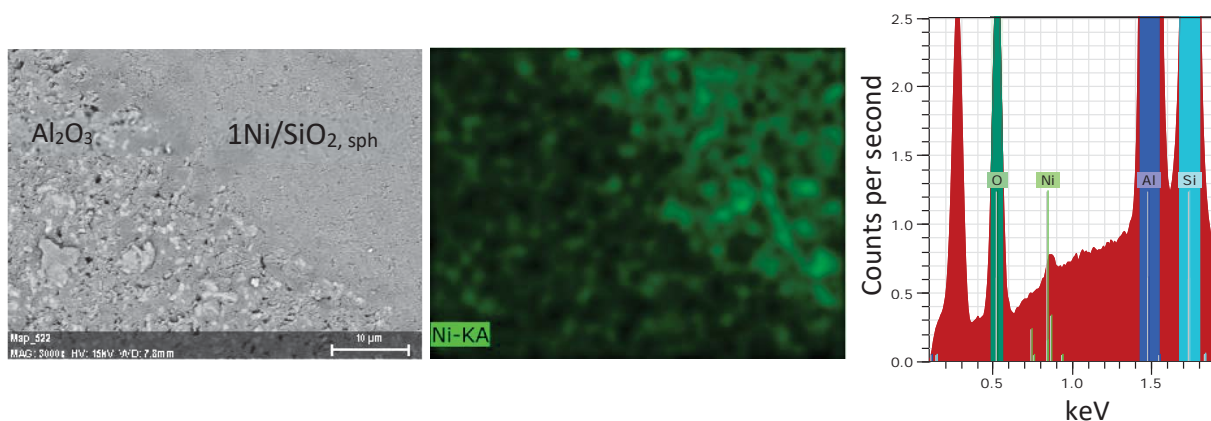


Figure 90: high magnification SEM/EDS of coated alumina fibre.

The remainder of the fibres were coated using the washcoating speed of 30 rpm for 15 min, while no back pressure was applied. This resulted in a catalyst loading of around 5 wt%. Multiple fibres coated under the same conditions resulted in loadings of 4.3, 5.8, 5.4, 5.1 and 6.7 wt%. The repeatability of the washcoating procedure was therefore demonstrated. It was calculated that when the fibres were bundled to be put into the fuel cell the resulting catalyst loading would be around 12.5 mg, comparable to some of the higher GHSV fixed bed reactors whose results were previously discussed in Chapter 6.

Fibres were cut to the length of the desired reactor, 40mm, and bundled to maximise the amount of catalyst in the reactor. Bundling also ensured a snug fit within the diameter of the fuel cell. Fibres were bundled by securing three lengths of fibre in a triangular fashion with tape. High temperature ceramic paste, Ceramabond, was applied to secure the fibres in place. The ceramabond was cured as per its manufacturer determined conditions; dried in air for several hours, heated to 93°C for 2 hours and then fired at 260°C for 2 hours. Figure 91 shows a picture of the resulting fibre assembled.

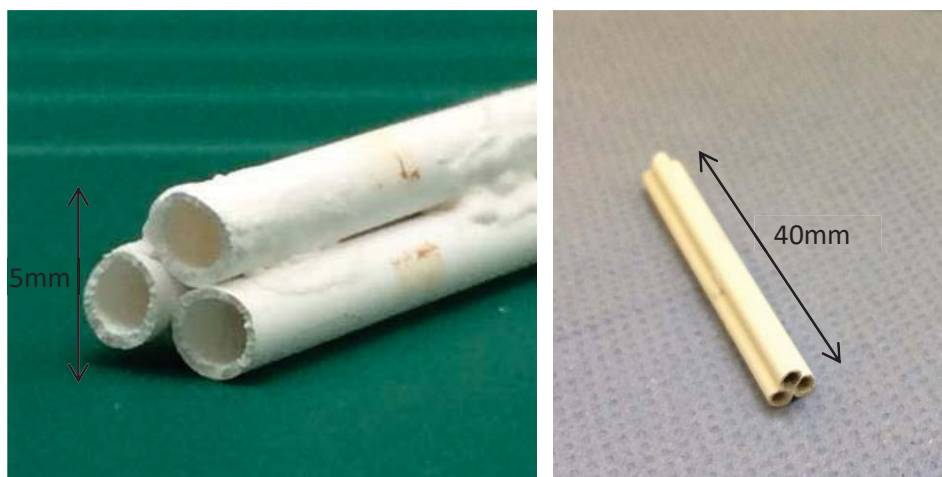


Figure 91: Assembled fibre bundle reactor.

7.3 Ex-situ testing of $1\text{Ni}/\text{SiO}_{2,\text{sph}}$ Fibre reactor

In order to compare the performance of the catalyst when it was held in a fixed bed reactor vs. its performance when the catalyst had been washcoated onto an alumina fibre, the fibre bundles were first tested ex-situ from the fuel cell. They were positioned inside a quartz tube of the same inner diameter as the fuel cell and the temperature of the furnace was varied from 550-950°C. the temperature was recorded close to the reactor using a thermocouple. A photograph of the experimental set up is shown below. As with the experiments in Chapter 6 the flow rate of the inlet gases was held at $67.2\text{ ml}\cdot\text{min}^{-1}$ during the experiment. The first fibre bundle tested contained 13 mg of $1\text{Ni}/\text{SiO}_{2,\text{sph}}$. This represented a GHSV of $308966\text{ ml}\cdot\text{g}^{-1}\cdot\text{h}^{-1}$. The $\text{CH}_4:\text{O}_2$ ratio was maintained at 2. As with the experiment in section 6.1 the temperature was varied in 100°C intervals and each temperature was maintained for a two-hour period. Figure 93A shows the methane conversion and product yields relative to time for this experiment. For comparison, the results of the same test carried out for the $1\text{Ni}/\text{SiO}_{2,\text{sph}}$ catalyst in a fixed bed reactor are shown in Figure 93B.



Figure 92: Photographs of fibre reactors held in quartz tubes and showing the position of thermocouple.

It was apparent that the catalyst did not perform well in the fibre reactor. In the fibre reactor, significant methane conversion was only recorded at $T > 850^{\circ}\text{C}$ with syngas production only being significant during the 950°C step. Methane conversion remained $\sim 10\%$ throughout all temperature steps up to 750°C , whereas in the fixed bed reactor methane conversion was greater than 55% at all temperatures. As was previously noted, methane conversion over NiO was approximately 10% . It was therefore hypothesised that the catalyst could have oxidised during the 550°C step and remained in its oxidised form until it was reduced at some temperature between the 750 and 850°C step. To test this hypothesis another $1\text{Ni}/\text{SiO}_{2, \text{sph}}$ fibre bundle reactor was tested directly at 750°C . It was thought that if the catalyst was not subjected to the lower temperature testing then it would not re-oxidise and so significant improvements in methane conversion and product yields would be observed.

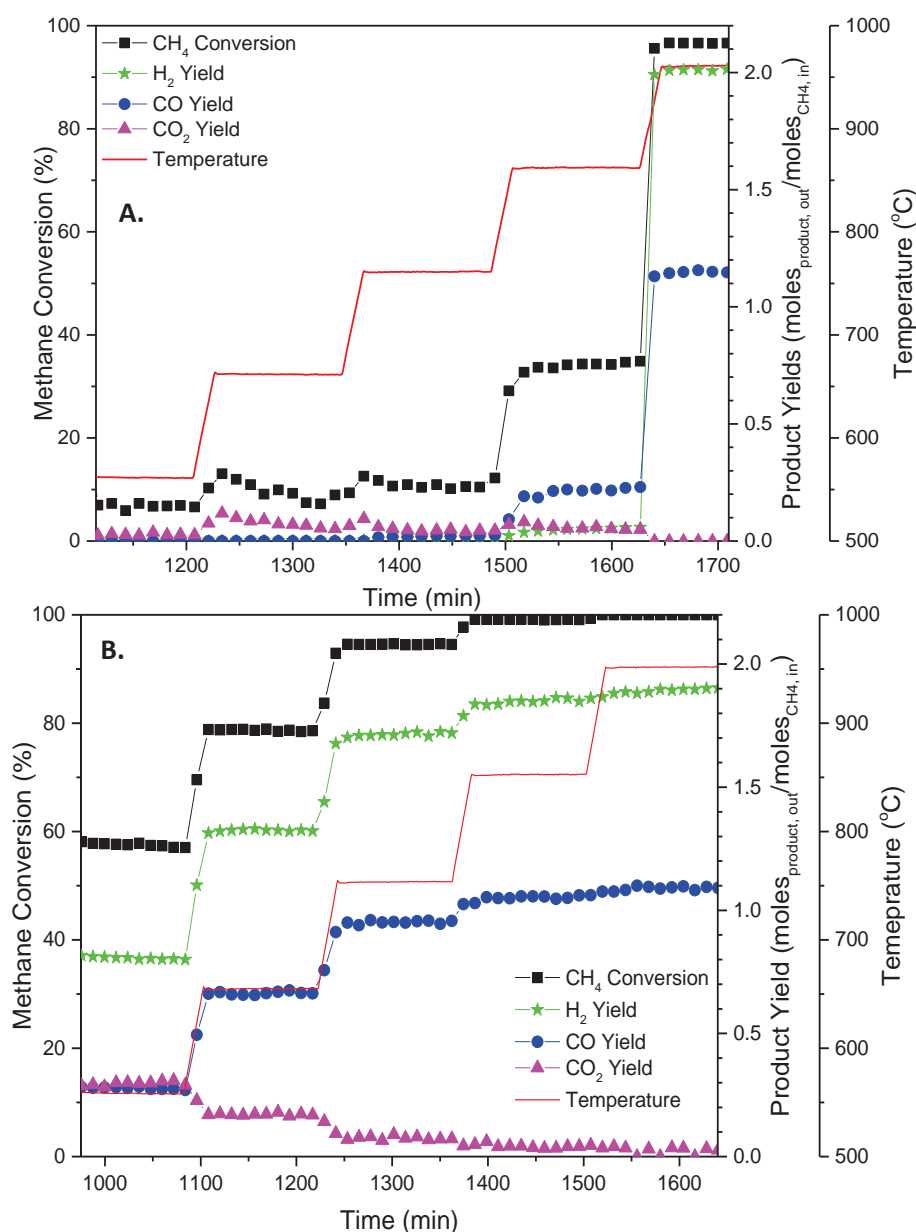


Figure 93: Effect of temperature on 1Ni/SiO_{2, sph} catalyst performance in A. Fibre bundle reactor and B. Fixed bed reactor.

The second bundle contained 12 mg of 1Ni/SiO_{2, sph} catalyst and was tested under the same reactant flow rate as in the above experiment. This represented a GHSV of 342275 ml.g⁻¹.h⁻¹. As with previous experiments, the fibre bundle was reduced overnight at 700°C and then was directly heated to 750°C at which point the reactants were introduced. The catalyst was left under these conditions until the methane conversion dropped back to 10%. The results are shown in Figure 94.

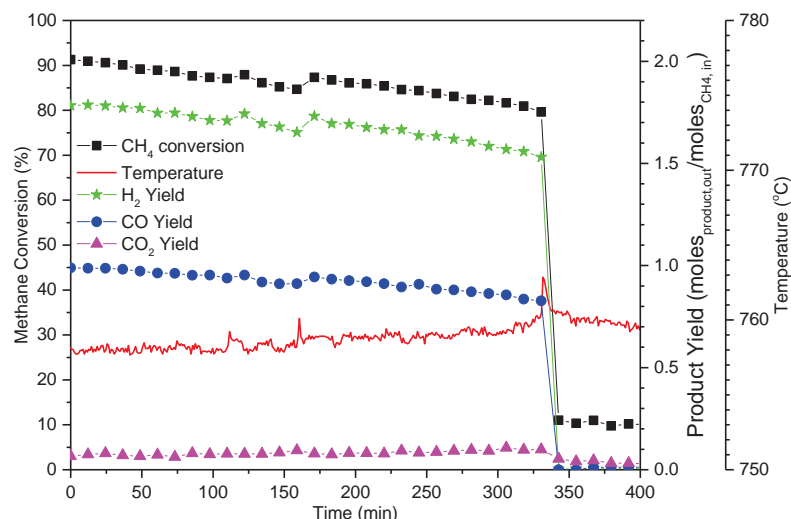


Figure 94: Immediately testing 1Ni/SiO_{2, sph} fibre bundle at 750°C, and a CH₄:O₂ = 2.

Testing directly at 750°C rather than previously testing the reactor at 550°C gave a remarkable improvement in the performance. Methane conversion at 750°C increased from ~10%, Figure 93A, to >90%, Figure 94. Syngas production selectivity was also high when the reactor was directly tested at 750°C whereas when the temperature was varied from 550°C, no syngas was produced at 750°C.

The methane conversion and syngas yields deteriorated over the course of 330 minutes, at which time a dramatic drop in performance was evidenced. This drop in performance was mirrored by a spike in the temperature recorded close to the reactor. The temperature spike was indicative of catalyst re-oxidation, since oxidation is an exothermic process.

The above results proved the hypothesis that catalyst re-oxidation at 550°C was the reason for low performance at 750°C during the experiment where the temperature was varied. Catastrophic catalyst deactivation caused by re-oxidation was also concluded. In an attempt to optimise the reaction conditions the CH₄:O₂ ratio was increased to 2.5 in order to reduce the oxidative power of the reactants. It was thought that this would slow down the rate of

catalyst re-oxidation. Again, the catalyst was directly tested at 750°C. The results are shown in Figure 95.

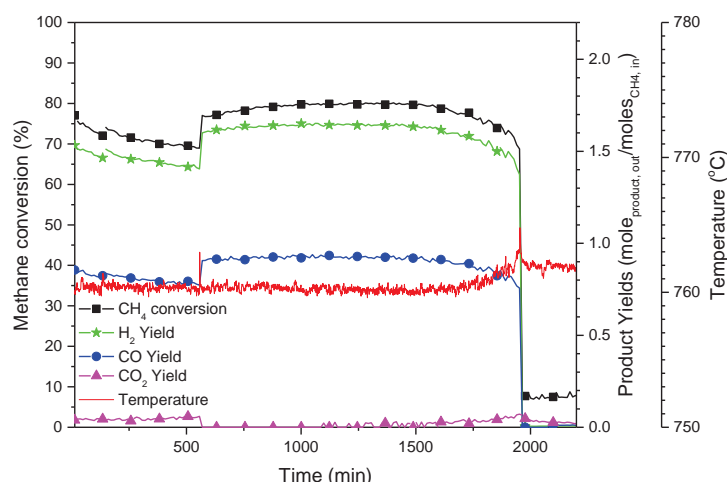


Figure 95: 1Ni/SiO₂, sph fibre reactor tested at 750°C, CH₄:O₂ = 2.5

Lowering the amount of oxygen in the reactant feed lowered the methane conversion by around 10%. This is consistent with the results obtained from the fixed bed reactor, Figure 71, Chapter 6. However, the sacrifice made in lowering the methane conversion resulted in a longer system lifetime. The reactor survived for almost 2000 minutes rather than the previously recorded 330 minutes.

To further show that re-oxidation was causing the catastrophic degradation of the catalyst, reduction of the degraded catalyst and re-testing was attempted. This was achieved by turning off the reactants and reintroducing 25% H₂/N₂ into the system. The catalyst was left under these conditions overnight. The next morning the hydrogen was turned off and the CH₄:O₂=2.5 gas mixture was reintroduced to the reactor. This cycle was repeated 3 times, the results are given in Figure 96. Product yields were omitted from the figure for simplicity, but full results can be seen in Appendix I.

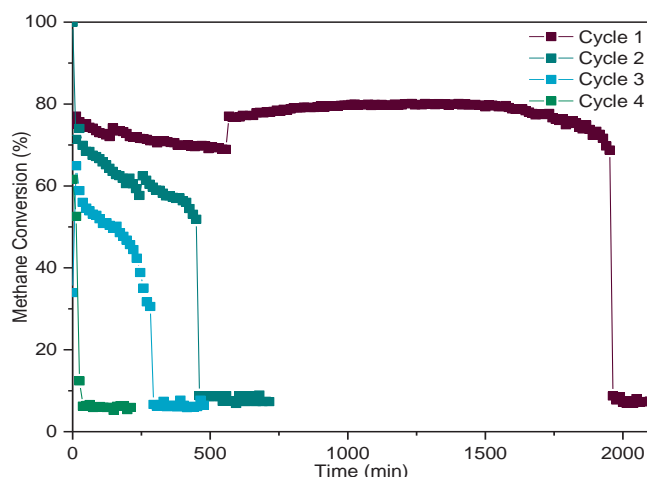


Figure 96: Regenerating the $1\text{Ni}/\text{SiO}_{2,\text{sph}}$ fibre reactor by in-situ reduction.

Each time the reactor was reduced the performance of the catalyst recovered. However, Figure 96 shows that with each regeneration the lifetime of the reactor diminished.

What is also visible in the results is a second form of degradation. During cycles 1 and 2 the catalyst appeared to degrade and then recover, without an external influence. This occurred at around 625 minutes in cycle 1, and around 275 minutes in cycle 2. The temperature profiles during these cycles are shown in Figure 97.

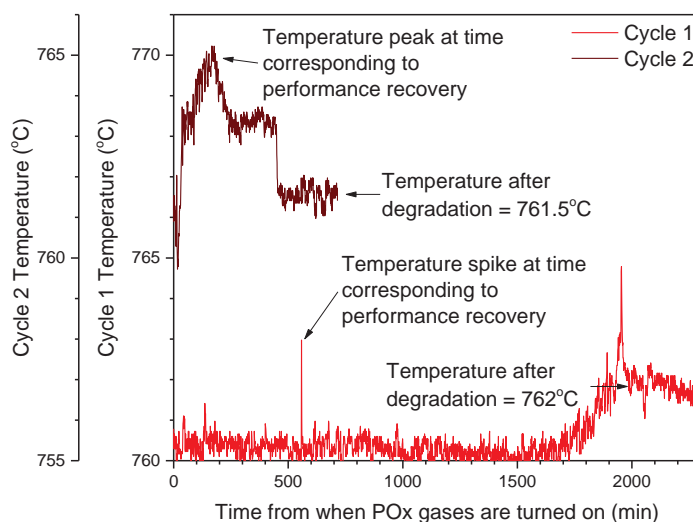


Figure 97: Temperature profiles of cycle 1 and 2 of the catalyst regeneration experiment.

Cycle 1 showed a clear spike in temperature, recorded at the same time as the recovery in performance was seen. It is thought that this spike in temperature was a result of carbon oxidation. It is believed that carbon was deposited on the catalyst during the first

625 minutes of testing. When the carbon was oxidised by oxygen in the reactant feed gas, an exothermic reaction was recorded. The removal of the deposited carbon caused the catalyst performance to recover. The temperature profile of cycle 2 did not display such a spike, the temperature can be described more accurately as building up to the time when performance was observed to recover. In between the two cycles, before reduction had occurred, there was a time when the catalyst was subjected to the methane and oxygen reactants with low degrees of conversion. It is thought that during this time carbon could deposit on the fibre reactor. What was then observed as the temperature building up was the deposited carbon being burned off. Again, once the carbon is removed, the performance increased.

Results from the ex-situ testing of the $1\text{Ni}/\text{SiO}_{2, \text{sph}}$ fibre reactor show that the $1\text{Ni}/\text{SiO}_{2, \text{sph}}$ catalyst was more prone to re-oxidation when it was tested in a fibre reactor, than when it was tested in a fixed bed reactor. As such the $\text{CH}_4:\text{O}_2$ ratio in the feed gas needed to be raised to achieve stability of the partial oxidation reaction for almost 2000 min. The catalyst eventually degraded by active nickel species re-oxidation. This was confirmed by reducing the catalyst in-situ and retesting the catalyst. Performance recovered on reduction, however, the lifetime of the catalyst drastically reduced with each redox cycle. The lifetime and performance of the $\text{Ni}/\text{SiO}_{2, \text{sph}}$ catalyst was poor in the alumina fibre reactor. Therefore, attempts at integration of the catalyst into an indirect internal reformer ceased.

7.4 Ex-situ testing of $\text{Ni}@\text{SiO}_2$ Fibre reactor

After learning from the $1\text{Ni}/\text{SiO}_{2, \text{sph}}$ fibre, the $\text{Ni}@\text{SiO}_2$ fibre was directly tested at 750°C , $\text{CH}_4:\text{O}_2$ ratio = 2.5. The $\text{Ni}@\text{SiO}_2$ fibre tested was loaded with 20 mg of catalyst representing a GHSV of $200597 \text{ ml.g}^{-1}.\text{h}^{-1}$. Figure 98 shows the results of this experiment. The fibre

showed no decrease in performance for over 4000 mins, over double the time that the 1Ni/SiO_{2, sph} fibre survived.

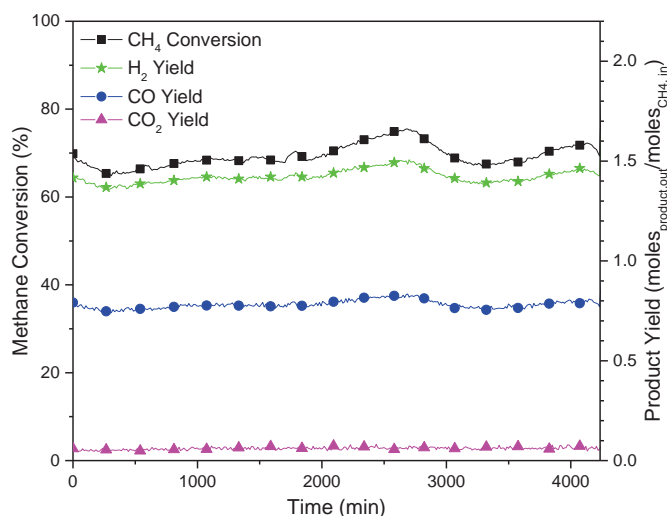


Figure 98: Ni@SiO₂ fibre bundle tested at 750°C, CH₄:O₂ = 2.5 GHSV = ml g⁻¹ h⁻¹.

Due to the observed stability of the catalyst, the CH₄:O₂ ratio was decreased to 2 to see if the catalyst could handle the more highly oxidising environment in a way which the 1Ni/SiO_{2, sph} catalyst could not. The gas composition was changed over the same fibre tested in Figure 98. Figure 99 shows the point at which the gases were changed and the resulting improvement in performance.

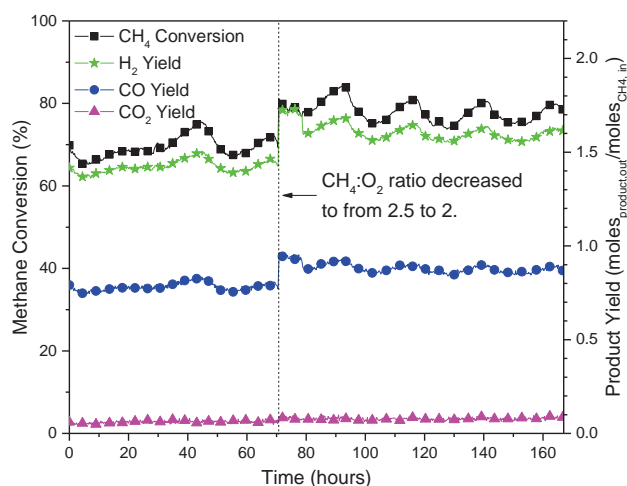


Figure 99: Ni@SiO₂ fibre reactor showing results after the gas composition was changed to a CH₄:O₂ ratio of 2.

The catalyst remained active for another 100 hours at which point the experiment was ended. The performance of the catalyst remained relatively stable throughout the duration

of the test. The major fluctuation resulted from the daily change in the external lab temperature. This fluctuation makes it difficult to measure the rate of catalyst degradation. It is estimated that when the $\text{CH}_4:\text{O}_2$ ratio was decreased to 2 the methane conversion dropped by a maximum of 5% during the next 100 hours.

The reactor was cooled down under a flow of N_2 and when the furnace was opened it was observed that the alumina fibre had disintegrated, as per Figure 100.



Figure 100: Disintegrated Ni@SiO₂ fibre after testing.

Since the GC results showed no massive decrease in performance as would be expected from this kind of disintegration, it was thought that the breakdown of the alumina fibre could have occurred during cooling. SEM of the broken fibre revealed carbon deposition had occurred, Figure 101. Rodrigues and Schmal reported a similar breakdown of their monolithic reactor due to carbon whisker formation during ethanol partial oxidation over nickel [256] and also cobalt catalysts [257]. Testing of the Ni@SiO₂ catalysts continued whilst being aware of the alumina fibre destruction which could occur.

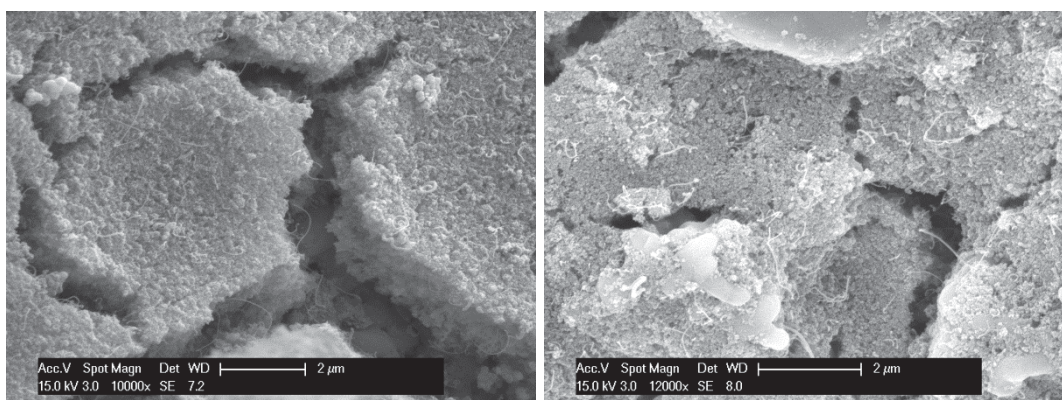


Figure 101: SEM of tested fibres showing carbon deposition on the alumina fibre.

Excellent performance of the Ni@SiO₂ catalyst washcoated and assembled into a fibre bundle was demonstrated. At a CH₄:O₂ ratio of 2.5, 70% methane conversion was achieved for 70 hours. The catalyst is resistant to re-oxidation in a way that the Ni/SiO_{2, sph} catalyst was not, being capable of operating comfortably with a CH₄:O₂ ratio of 2. With this fuel composition a methane conversion of around 80% was achieved for a further 100 hours. Catalyst performance was shown to be stable and therefore attempts at progression towards in-situ testing were attempted.

7.5 Ni@SiO₂ Stub Reactor

Due to the high cost of the microtubular fuel cells purchased for this study, a preliminary test to observe how the catalyst performed when held within the fuel cell tube was conducted. The tubular fuel cells purchased for this work were anode supported Ni-YSZ tubes (Ultra Electronics). The tubes are manufactured with a section of the tube being free of electrolyte and cathode, for an IIR catalyst to be inserted, as shown in Figure 102.

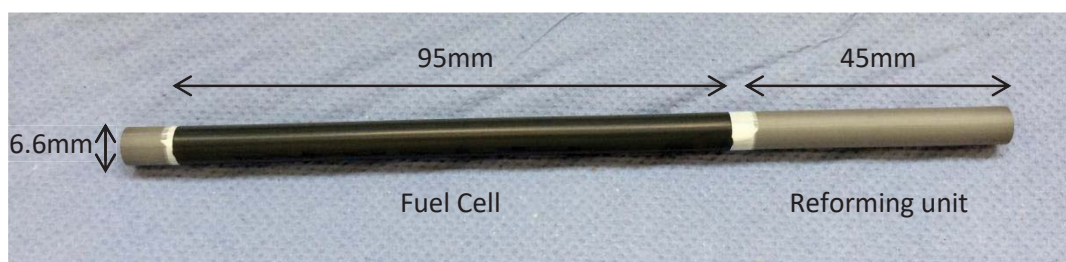


Figure 102: Ultra Electronics Ni/YSZ/YSZ/SDC/LSCF tubular fuel cells.

Previous work in the research group had utilised only the fuel cell part of tubes in order to build a stack to run on hydrogen. As such the reforming section was removed from the manufactured tubes leaving the lab with a stock of Ni-YSZ tube “stubs”. Alumina manifolds were attached to the stubs so that an alumina fibre could be positioned in the stub and

tested as a POx micro-reactor. A photograph of the arrangement of the stub reactor is shown in Figure 103.

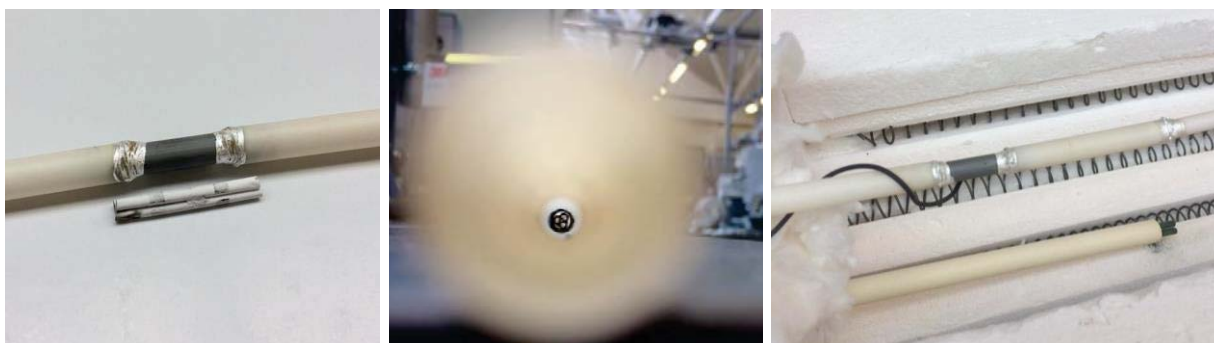


Figure 103: Stub reactor arrangement. Left: Alumina fibre next to the stub Middle: Alumina fibre positioned within the stub Right: Stub reactor in position in the furnace with a thermocouple in place.

Figure 104 shows the results of the stub reactor being tested at 750°C, at a CH₄:O₂ ratio of 2, and a total flow rate of 67.2 ml.min⁻¹. The figure also includes results from the fixed bed and alumina fibre reactor both tested under the same reaction conditions.

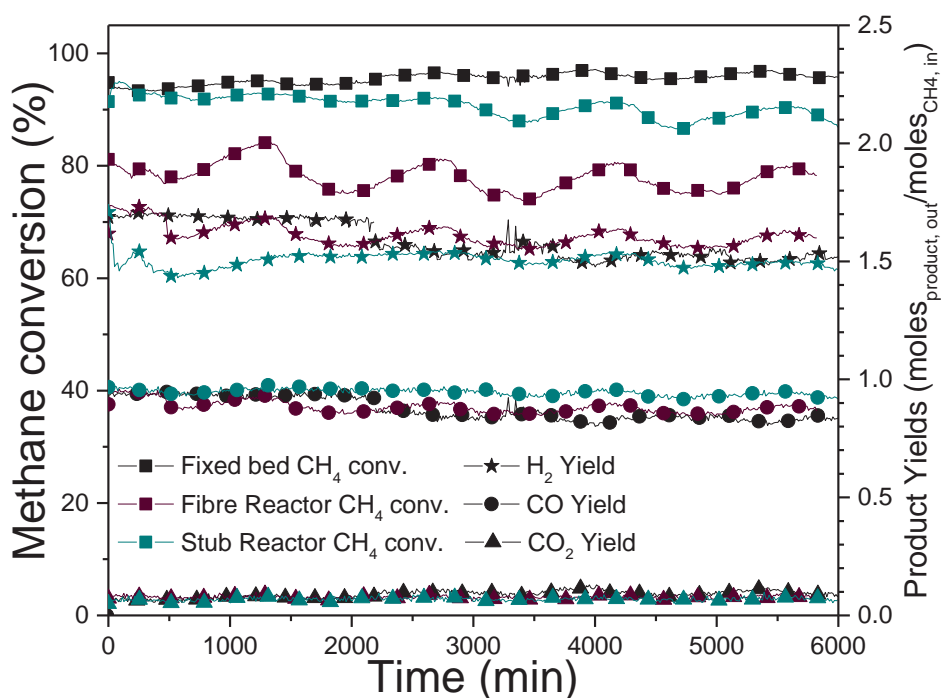


Figure 104: Comparison of different reactors all testing the Ni@SiO₂ catalyst at 750°C, CH₄:O₂ = 2 and GHSV approx. 80640 ml g⁻¹ h⁻¹.

The product yields of all 3 reactor arrangements are comparable. The methane conversion for the fibre reactor is significantly lower than the other two reactor arrangements. This

difference is attributed to the fact that the fibre reactor was tested at higher $\text{CH}_4:\text{O}_2$ ratio for more than 60 hours before the $\text{CH}_4:\text{O}_2 = 2$ composition was switched on. It is thought that during this time significant coking could have occurred which caused the lower than expected performance of the catalyst when tested at $\text{CH}_4:\text{O}_2 = 2$.

When the stub reactor experiment was finished the reactor was cooled under a flow of nitrogen and the alumina fibre was easily removed from the stub showing no signs of disintegration as was shown in Figure 100.

7.6 Fuel Cell Testing

It was firstly important to show that the alumina fibre reactors were capable of reforming gases at a fast enough rate in order to supply a fuel cell. For this reason, a fuel cell was assembled and the reactor was positioned at the fuel cell inlet. The fuel cell was tested on hydrogen for 2 days. During this time the catalyst was reduced and an indication of the fuel cell stability was obtained. At the start of testing, a current vs potential curve (IV curve) was measured between open circuit voltage (OCV) and 0.4V. This was repeated after 24 hours and the results are shown in Figure 105.

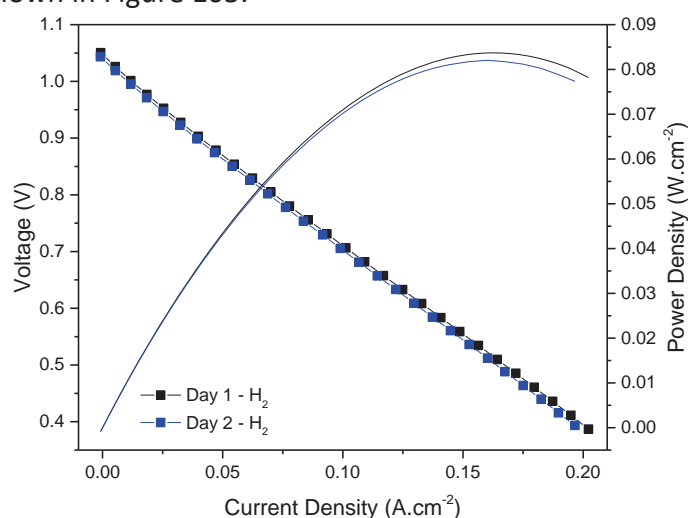


Figure 105: Fuel cell operating on H_2 . IV curve recorded at the start of the experiment and 24 hours later.

The maximum power density was recorded as 0.0835 W.cm^{-2} on day 1 and this dropped to 0.082 W.cm^{-2} over the next 24 hours. After the second IV curve was recorded the fuel gas was switched from hydrogen to the partial oxidation reactants, methane and oxygen. An IV curve was immediately recorded and Figure 106 shows the increase in power density recorded by switching the fuel feeds.

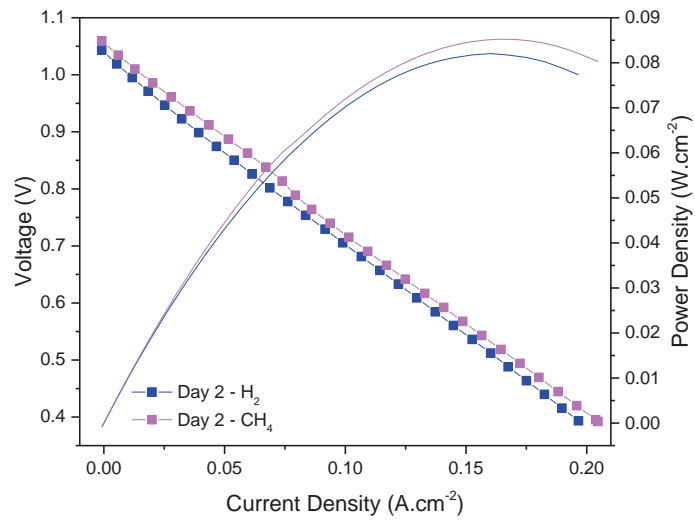


Figure 106: Increase in maximum power density when the fuel feeds are switched from H_2 to POx reactants.

Figure 106 shows that the alumina fibre was successful in reforming methane within a fuel cell so that the syngas produced could be oxidised by the fuel cell and generate power. Over the next 2 days, IV curves were recorded every 24 hours. The results are shown in Figure 107.

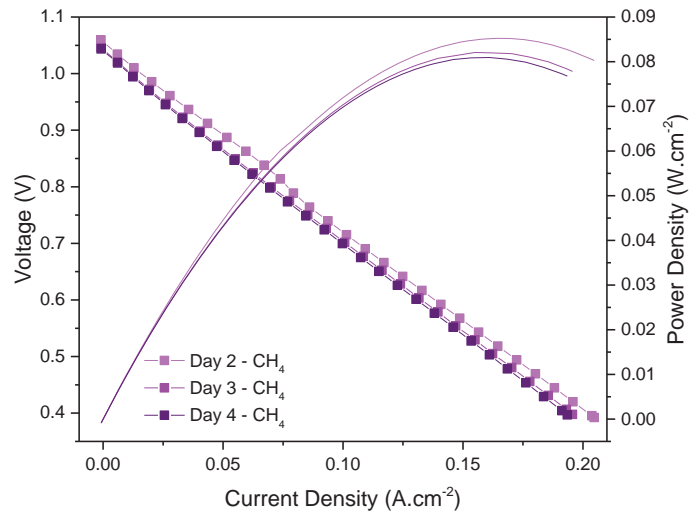


Figure 107: Fuel cell tested on reformed methane over the course of 48 hours.

The maximum power density decreased from 0.085 to 0.082 Wcm⁻² during the first day and over the next 24 hours the power density dropped to 0.081 Wcm⁻². This calculates to an average degradation rate of 0.002 Wcm⁻² per day. During the time when the cell was operated on hydrogen and when the cell was operating on reformed methane, the degradation rate remained comparable. Therefore, it was demonstrated that indirect internal reforming did not affect the performance of the tubular fuel cell during the 100 h of operation on H₂ and reformat.

When the experiment was turned off, the alumina fibre was removed from the cell intact, as shown in Figure 108.



Figure 108: Alumina fibre reactor removed from the fuel cell after testing.

7.6.1 Long term testing on fuel cells

To further evidence the effects of indirect internal reforming on microtubular SOFC performance, cells were tested for longer periods of time, until significant performance decay was evidenced. First of all, in order to determine the ability of the fuel cell to directly oxidise methane, a cell was tested under methane and nitrogen only. The total flow rate of reactants remained 67.2 ml.min⁻¹. Throughout all experiments the number of moles of hydrogen atoms delivered to the cell per minute was kept constant, i.e. double the amount of hydrogen was supplied than the amount of methane. The cells were held at a constant voltage of 0.7 V and an IV curve was recoded every 24 hours.

Figure 109 shows the current recorded at 0.7 V for the lifetime of the cell tested on methane and the daily IV curves.

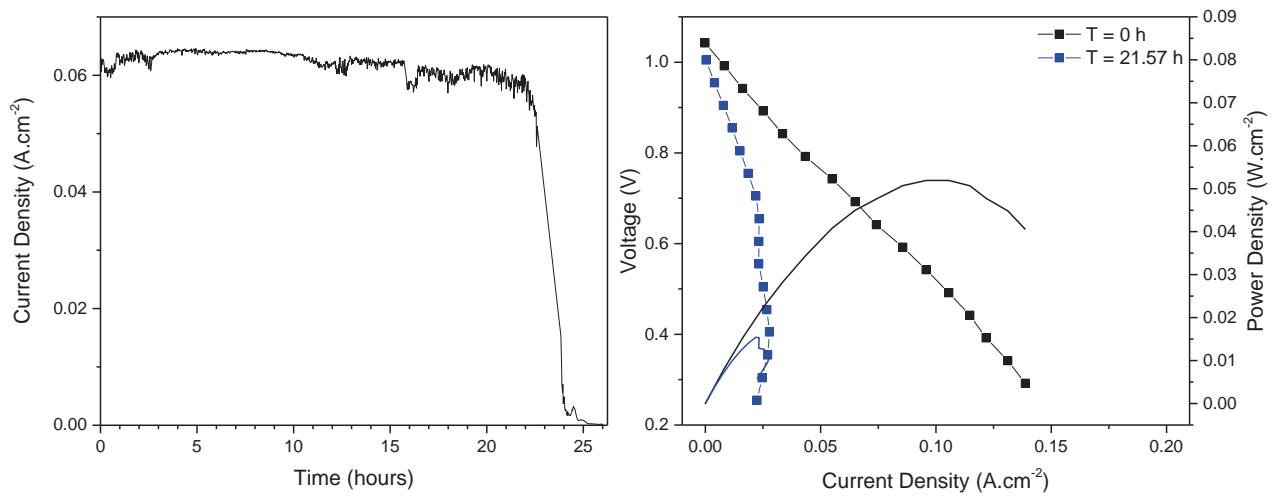


Figure 109: Cell testing under methane, cell death occurred after only 22 hours

Since the cell operated for a limited period of time it was clear that sustained operation under high methane concentrations was not possible. When the cell was removed from the test rig it was clear that high rates of carbon formation had blocked the tube and ultimately led to the cell failure. Figure 110 shows a photograph of the tube after testing. The cell completely cracked away from the manifold at the fuel cell exhaust and the interior of the cell was caked in coke.



Figure 110: Fuel cell which has been tested on methane. Left: fuel cell fractured away from the manifold Right: blocked fuel cell tube due to carbon deposition.

Another new cell was then tested on reformed methane using an alumina fibre bundle washcoated with Ni@SiO₂, placed at the cell inlet. The long term test results can be seen in Figure 111.

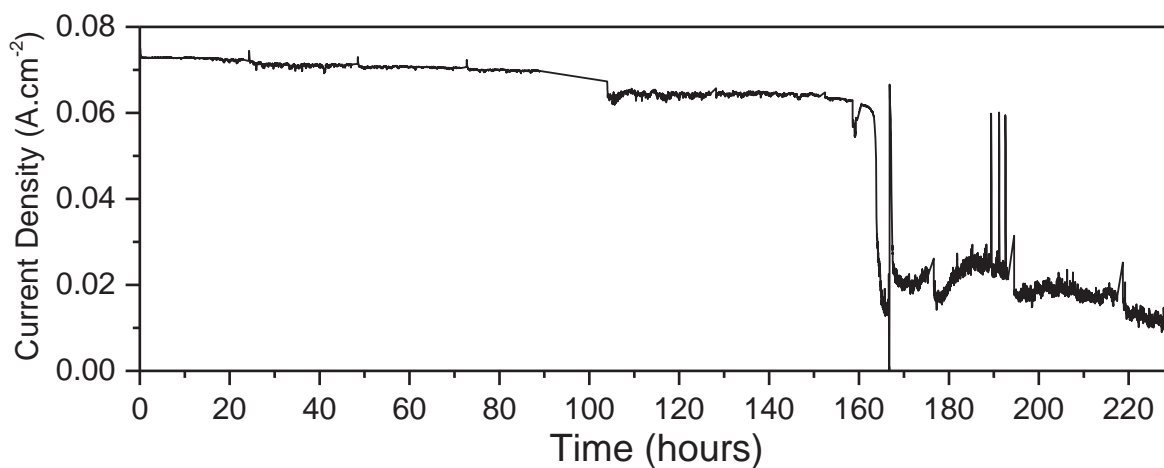


Figure 111: Long term fuel cell testing on reformed methane.

Figure 112 shows the daily IV curves recorded throughout this experiment. The alumina fibre and the fuel cell remained intact after testing.

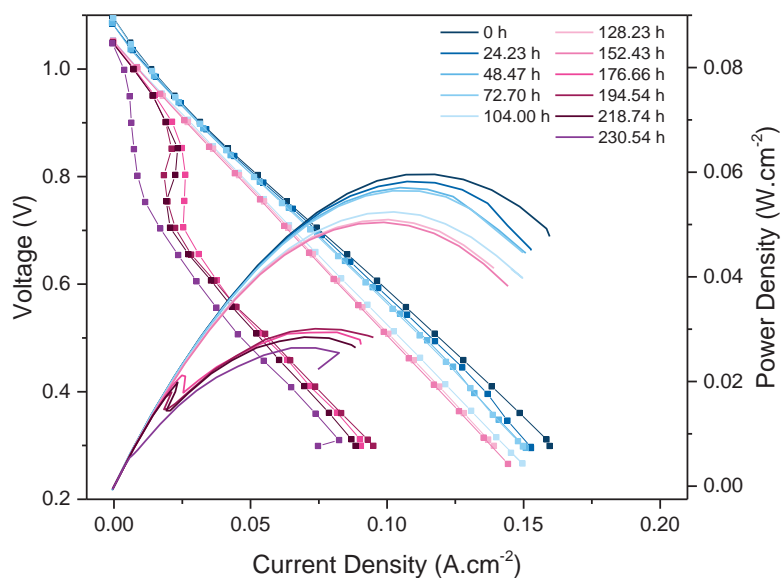


Figure 112: Daily IV curves recorded on fuel cell operated on reformed methane.

The cell showed a gradual degree of degradation followed by a catastrophic degradation event occurring after 160 hours. When the cell was removed from the furnace the fibre

reactor was intact and large degrees of carbon deposition, as was observed in the cell operated on methane, were not visible. Full integration of an IIR catalyst into a fuel cell was therefore demonstrated. Ni@SiO₂ showed large degrees of promise for this application.

It was believed that the fuel cell catastrophically degraded after 160 hours of operation due to no fault of the IIR since carbon deposition was not observed in the fuel cell. If the reforming catalyst was to significantly degrade large amounts of methane would enter the fuel cell and result in carbon deposition. In addition, the stability of the Ni@SiO₂ fibre bundles was previously demonstrated. Whilst the exact cause of fuel cell failure after 160 hours operation is not known, it is likely that the seal between the fuel cell and the alumina manifolds broke down with time on stream; this would lead to reactant crossover and fuel cell failure.

7.7 In-stream Gas Analysis

In order to further investigate the specific effect of an IIR state of health on the fuel cell performance, a method of characterising the gas stream between the IIR and fuel cell is needed.

The design of such a device was attempted in this work. In collaboration with the University of Strathclyde, it was envisaged that atomic absorption laser spectroscopy could be used to probe the methane concentration in-between the reformer and the fuel cell. The research group at Strathclyde have experience with applying gas characterisation technologies using lasers to gas-turbines [258] and also fuel cells [259,260]. Using the results collected from ex-situ testing the methane concentration could be related to the state of health of the catalyst. If this could be achieved the health of the fuel cell could be ensured by stopping operation

before serious carbon deposition occurred. Alternatively, if the catalyst allowed it, the composition of the reformer inlet could be changed in order to promote catalyst regeneration. Once this is achieved, normal operation could resume.

Initial design of this device consisted of a gas cell with a quartz window in each side, Figure 113. The reformer would be split from the fuel cell and each component would be secured to either side of the gas cell. An attempt was made to seal such a gas cell in which the fuel cell was imitated by sections of quartz tube, Figure 114.

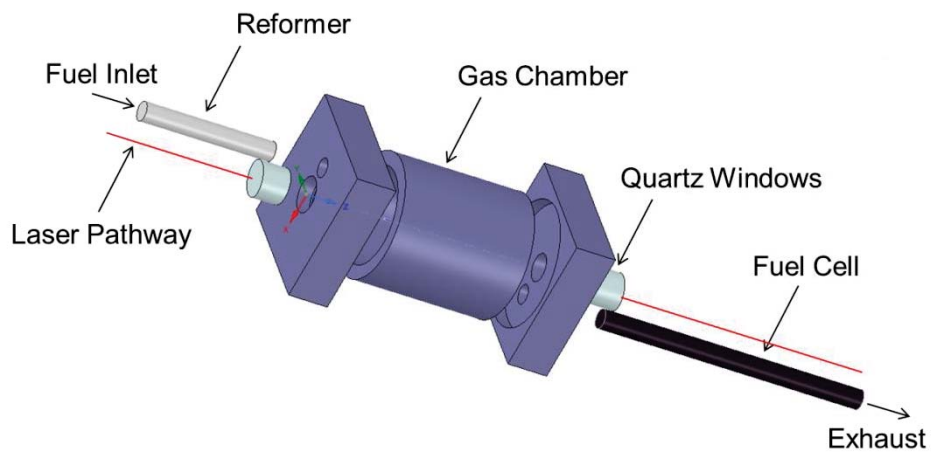


Figure 113: Initial design of the laser absorption spectroscopy device for determining the composition of gases between the reformer and fuel cell.

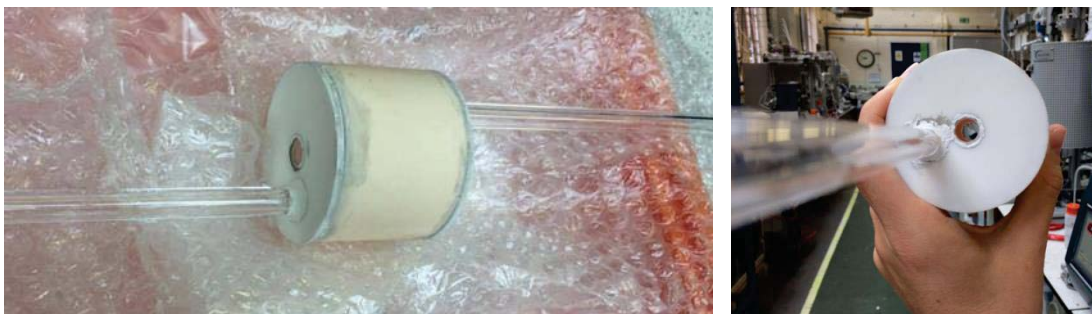


Figure 114: First attempt at building the gas cell.

The gas cell body was made from alumina and the end plates were made from Macor. The components were secured with ceramabond and sealed with a glass and silver seal. After

repeated attempts to seal the unit, leaks were still observed when the cell was tested at high temperatures. The length of the PhD did not allow further development of the design, however, it was envisaged that 3D printing of the ceramic components in a single unit would have helped to obtain a good seal.

7.8 Summary

The catalyst loading on an alumina fibre was demonstrated to increase with washcoating speed, duration and with the application of back pressure. For this work a catalyst loading of 5 wt% was achieved using the following washcoating parameters; 30rpm, 15min, without the application of backpressure. The process proved to be highly repeatable with the catalyst loading ranging from 4.3 wt% to 6.7 wt% for 5 fibres coated using the same procedure. Fibre bundle reactors were assembled using both the $1\text{Ni}/\text{SiO}_{2, \text{sph}}$ and $\text{Ni}@\text{SiO}_2$ catalysts from previous chapters and tested for their suitability in IIR reactors.

The $1\text{Ni}/\text{SiO}_{2, \text{sph}}$ fibre bundle readily re-oxidised resulting in a low performance. Reducing the oxygen content of the fuel feed enabled the production of syngas for over 30 hours. In-situ reduction of the catalyst regenerated the performance. However, with each regenerative cycle the duration of the period over which syngas was produced, reduced.

The $\text{Ni}@\text{SiO}_2$ fibre bundle showed greater promise. The fibre bundle stably delivered syngas under a $\text{CH}_4:\text{O}_2$ ratio of 2.5 for 70 hours. At this point the $\text{CH}_4:\text{O}_2$ ratio was reduced to 2 and the catalyst remained stable for another 100 hours. Under the more oxidising conditions, the methane conversion increased around 10% as would be expected.

Testing the fibre in a short section of fuel cell anode tube revealed that the fibre bundle did not cause cracking of the fuel cell material.

The Ni@SiO₂ fibre bundle was then fully integrated into an operating fuel cell. The degradation rate of the fuel cell when operated on hydrogen and on reformed methane was shown to be comparable, at an insignificant reduction in maximum power density of around 0.002 W.cm⁻² per day.

Longer tests were then carried out and a fuel cell was operated on reformed methane utilising the Ni@SiO₂ fibre bundle for 160 hours, demonstrating the potential of washcoated alumina fibres as IIR reactors.

Chapter 8

CONCLUSIONS

Two silica-nickel catalysts were prepared and characterised. The catalysts had distinctly different requirements of their silica components. One catalyst utilised the silica as merely a structural support. Nickel phyllosilicate bonds held 5 to 6 nm nickel particles onto the surface of spherical silica particles of approximately 150 nm diameter. The opposing catalysts consisted of 9 to 12 nm nickel particles coated in thick (8.5 nm) or thin (2.7 nm) silica shells. The catalyst adopted a core@shell arrangement and the support serviced as an inert coating on the nickel in an attempt to prevent carbon deposition and nickel particle agglomeration. The catalysts were named $\text{Ni/SiO}_{2, \text{sph}}$ and Ni@SiO_2 , respectively.

The Ni@SiO_2 catalyst was observed to be inhomogeneous by TEM, the catalyst consisted of three different classifications of particles: uncoated nickel, nickel in a thin coating of SiO_2 , and nickel coated in a thick layer of SiO_2 . The reduction profile of the catalyst showed three distinct reduction processes which were attributed to each of these different types of particles. The reduction treatment did not fully reduce the Ni@SiO_2 catalyst, whereas nickel which was not coated in SiO_2 was shown to fully reduce under the same conditions. It was therefore concluded that the SiO_2 shell shielded the catalyst from the reducing agent, making it more difficult to reduce.

The catalytic performance of the prepared Ni@SiO₂ catalyst and uncoated nickel particles were compared. The stability and performance of the Ni@SiO₂ catalyst could not be matched by the uncoated nickel. It was shown that the uncoated sample suffered from catalyst re-oxidation when methane conversion. Redox cycling of the nickel particles was evidenced. The Ni@SiO₂ catalyst showed no signs of this redox cycling and it was therefore concluded that the SiO₂ shell was essential in controlling the flow of reagents to and from the catalyst surface. In this way re-oxidation of the nickel was prevented and the available reduced nickel sites are critical in ensuring high syngas product yields.

The nickel loading in the Ni/SiO_{2, sph} catalyst was varied and as nickel loading increased the average particle size of the nanoparticles grew, as well as the catalysts surface area. It was demonstrated that by increasing the nickel loading on the Ni/SiO_{2, sph} catalysts the performance of the catalysts when tested at high GHSV was improved.

By observing the trends in product yields it was possible to determine the preferred reaction mechanism at various GHSV. At lower GHSV a drop in CO and H₂ product yield was mirrored by an increase in CO₂ yield, signifying the oxidation-reformation pathway. At higher GHSV, CO₂ yield did not increase with falling levels of CO and H₂. This suggested that CO and H₂ were the primary products of the reaction and therefore the direct pathway was occurring. It was concluded that the direct pathway was favoured at lower GHSV when a catalyst with a higher nickel loading was utilised due to the greater availability of nickel sites on which nickel dissociation could occur. Coupled with this was the conclusion that with increased nickel loading on the Ni/SiO_{2, sph} catalysts, carbon deposition increased, again due to the availability of nickel sites which promoted methane dissociation.

When the performance of the Ni/SiO_{2, sph} and Ni@SiO₂ catalysts were compared the Ni/SiO_{2, sph} catalyst performed better at higher GHSV. The silica shell was shown to restrict the flow of reactants to the nickel surface and at high GHSV, the effectiveness of the catalyst was restricted.

Post-testing characterisation revealed that different degradation mechanisms prevailed in the catalysts. The Ni/SiO_{2, sph} catalyst suffered from carbon deposition, the silica shell inhibited carbon growth in the Ni@SiO₂ system. It was concluded that the method of carbon growth on the Ni/SiO_{2, sph} catalyst was tip growth, meaning that the carbon lifted the nickel particles away from the silica support. Both catalysts suffered from nickel particle agglomeration. The coated nickel particles in the Ni@SiO₂ catalyst were measured to have increased in size by 3.21 nm, the uncoated particles massively agglomerated however, reaching sizes of up to 83.5nm. It was hypothesised that the agglomeration of the “coated” particles occurred due to incomplete encapsulation of the nickel particles in silica. The nickel particles on the Ni/SiO_{2, sph} catalyst grew an average of 5.15 nm. The measured performance of the catalysts was comparable over a test period of 120 hours. Since the degradation profiles were comparable, as was the rate of agglomeration in the supported particles, it was concluded that the recorded degradation was caused by agglomeration. It was hypothesised that eventually carbon deposition in the Ni/SiO_{2, sph} catalyst would cause severe deactivation due to a loss in active sites which would be caused by the carbon filaments breaking.

Both the Ni/SiO_{2, sph} and Ni@SiO₂ catalysts were washcoated onto alumina hollow fibres for incorporation into a fuel cell system. It was found that increasing the rate at which the washcoat was circulated around the hollow fibre increased the catalyst loading onto the

fibre. Additionally, applying back pressure and lengthening the duration of the washcoating procedure, increased catalyst loading.

Fibre bundles were prepared which were each coated in approximately 12.5 mg of either Ni@SiO₂ or Ni/SiO_{2, sph}. After testing it was found that the Ni/SiO_{2, sph} catalyst was more prone to re-oxidation when it was mounted in a fibre than when it was tested in a fixed bed reactor. It was not possible to operate the catalyst at low temperatures (550 to 650°C) and only when the catalyst was operated directly at 750°C was a high methane conversion and syngas selectivity achieved. However, the catalyst degraded by re-oxidation in only 5.5 hours. Lowering the oxygen content in the fuel feed extended the lifetime of the catalyst to around 33 hours. However, this came at a sacrifice in the form of a lower methane conversion and syngas yield. Regeneration of the catalyst, in-situ, was demonstrated by reduction of the spent catalyst. With each regeneration cycle the performance of the catalyst recovered however the lifetime of the catalyst diminished with each cycle. It was concluded that the Ni/SiO_{2, sph} catalyst was not appropriate for use as an IIR catalyst when mounted on an alumina hollow fibre due to the higher tendency for nickel re-oxidation.

When the Ni@SiO₂ fibre bundle was tested ex-situ the reactor showed comparable performance as when it was tested in a fixed bed reactor. The catalyst achieved >80% methane conversion for over 100 hours without showing any critical signs of degradation as had been witnessed in the Ni/SiO_{2, sph} catalyst.

The Ni@SiO₂ fibre bundle proved to maintain temperature gradients within the tolerable limits of the microtubular Ni-YSZ anode supported fuel cells used in this study. When the

bundle was tested within a fuel cell “stub” the stub showed no signs of cracking and methane conversion of >90% was observed.

A Ni@SiO₂ fibre bundle tested in a functional fuel cell demonstrated the performance of the fuel cell was comparable on both hydrogen and reformed methane, proving the concept of IIR. The fibre bundle was removed from the fuel cell, intact, at the end of testing. As a further proof of concept a new fuel cell was tested only on reformed methane until its performance significantly dropped. The fuel cell achieved more than 160 hours of operation on methane reformed by partial oxidation using the Ni@SiO₂ fibre bundle.

It has been shown that both Ni@SiO₂ and Ni/SiO_{2, sph} catalysts can be effective partial oxidation catalysts when tested in a fixed bed reactor. The stability of the Ni/SiO_{2, sph} catalyst is greater than the prepared Ni@SiO₂ catalyst. Although, further investigation into the complete encapsulation of the Ni@SiO₂ catalyst in SiO₂, could result in a catalyst resistant to both nickel particle agglomeration, and coking. The Ni@SiO₂ catalyst outperformed the Ni/SiO_{2, sph} catalyst when tested in an alumina fibre reactor, since the Ni/SiO_{2, sph} catalyst suffered from nickel particle re-oxidation, which was not observed in the Ni@SiO₂ catalyst. Positive results from ex-situ trials of Ni@SiO₂ fibre bundle reactors translated into the successful operation of a fuel cell on methane, reformed by partial oxidation, in an indirect internal manner. Thus this work serves as a proof of concept of the indirect internal reforming of methane by partial oxidation for solid oxide fuel cells.

8.1 Further Work

In order to eliminate a reformer fault from the possible causes of fuel cell failure after 160 hours, it is necessary to be able to determine the concentration of gases in between the

reformer and fuel cell. If this was possible the state of health of the reformer could be assessed which would provide more information as to the cause of fuel cell failure. To achieve this, a gas characterisation device based on atomic absorption laser spectroscopy has been proposed. Further work would therefore aim to successfully integrate this device into a reformer/fuel cell system. Investigation into effective high temperature sealants are required to achieve this.

Areas for further catalyst development would include further investigation into the Ni@SiO₂ catalyst preparation to achieve a homogenous sample consisting only of thickly coated nickel particles. It is thought that further investigation into the PVP concentration used in catalyst preparation would achieve this. By achieving a catalyst fully coated in inert SiO₂ it is envisaged that nickel particle agglomeration would be eradicated. Coating of the Ni/SiO_{2, sph} catalyst in a further layer of SiO₂ to protect the catalyst against carbon deposition would also be worthwhile.

APPENDICES

Appendix A - Calculation of Gibbs Free Energy of Partial Oxidation Reaction

POx reaction: $CH_4 + \frac{1}{2} O_2 \rightarrow 2H_2 + CO$

$$\Delta G (kJ.mol^{-1}) = \Delta H(kJ.mol^{-1}) - T(K)\Delta S(J.K^{-1}.mol^{-1})$$

Species	Enthalpy of formation, ΔH_f^0 (kJ.mol ⁻¹)	Entropy, S (J.K ⁻¹ .mol ⁻¹)
CO (g)	-110.54	197.9
CH ₄ (g)	-74.85	186.27
H ₂ (g)	0	130.59
O ₂ (g)	0	205.03

$$\Delta H = \sum \Delta H_f^0 (products) - \sum \Delta H_f^0 (reactants)$$

For POx : $((2*0) + (-110.54)) - ((-74.85) + (0.5*0)) = -35.69 \text{ kJ.mol}^{-1}$

$$\Delta S = \sum S (products) - \sum S (reactants)$$

For POx: $((2*130.59) + (197.9)) - ((186.27) + (0.5*197.9)) = 173.86 \text{ J.K}^{-1}.\text{mol}^{-1}$

Temperature (°C)		Calculation	$\Delta G (kJ.mol^{-1})$
200	473.15	$-35.69 - (473.15 * 173.86 \times 10^{-3})$	-117.26
400	673.15	$-35.69 - (673.15 * 173.86 \times 10^{-3})$	-152.72
600	873.15	$-35.69 - (873.15 * 173.86 \times 10^{-3})$	-187.50
800	1073.15	$-35.69 - (1073.15 * 173.86 \times 10^{-3})$	-222.27

Appendix B - Gibbs Free Energy Diagrams

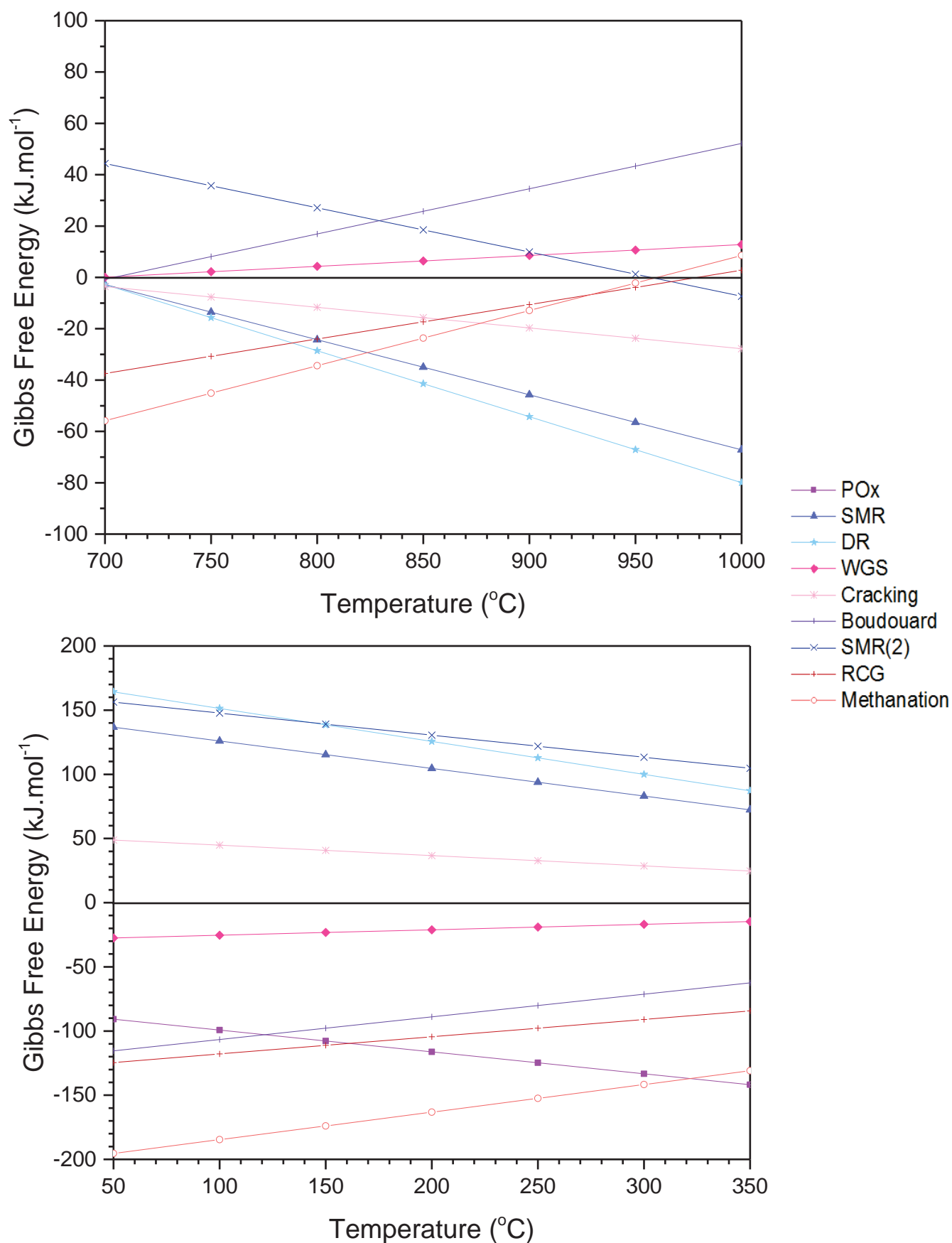


Figure 115: Effect of temperature on the Gibbs free energy of reactions.

Appendix C - Split Ratio

The split ratio defines how much the aliquot of sample is diluted before it enters the column. In the injector the sample is mixed with a controlled amount of carrier gas in order to dilute the sample, in this way less analytes enter the column. The more dilute the aliquot the narrower the peaks, since there are less molecules of analyte to move through the column. Peaks are less broad resulting in better separation. However, better separation is coupled with smaller peak areas. Since fewer analytes enter the column the changes in thermal conductivity recorded at the detector are reduced. This reduces the margin for error since small changes in peak area become large percentage errors, whereas any small variations in area in a larger peak represent a smaller percentage error. In summary the higher the split ratio the better the peak separation, but the less accurate the system becomes.

Split ratios are reported as a single number where the number gives the number of portions of carrier gas to sample. E.g. a method using a split ratio of 3 represents an injector which is diluting the sample by 1 part sample to 3 parts carrier gas.

Figure 116 shows that as the split ratio is increased from 20 to 35, the separation of the nitrogen and carbon monoxide peaks increases. The signal almost returns to the baseline in between the peaks. However, also clearly visible from the methane peak, is the diminishing peak area with increasing split ratio.

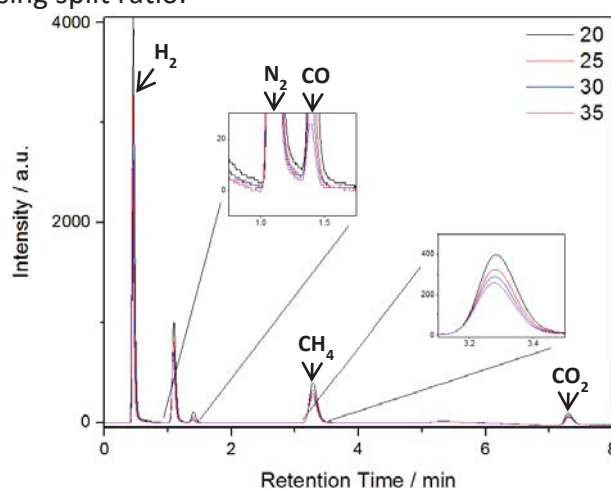


Figure 116: Effects of varying split ratio on GC spectrum

Appendix D - Column Flow Rate

The column flow rate determines the speed at which gases move through the column. At lower flow rates the analytes have more time to interact with the column. Analytes are therefore better separated at low flow rates. However, this comes at the expense of measurement time. A lower flow rate means that the gas with the most affinity for the column will take even longer to travel through the column. At lower flow rates, peaks also become broader since the longer time spent on the column means that the separated gas portions have more time to interact with the column. The peaks become more diffuse rather than being pushed through the column as one sharp peak.

It is important to note that when the column flow rate is changed, the make-up gas flow rate must also be changed. The make-up gas is a volume of gas added to the column effluent to make the volume of gas flowing over the column filament and the reference filament in the detector equal.

Figure 117 shows that decreasing the column flow rate from 10.3 to 5 ml min⁻¹ results in a greater separation of the nitrogen and carbon monoxide peaks however at lower flow rates, 5 and 6 ml min⁻¹, the carbon dioxide peak is not recorded in the acquisition time of 8 minutes. A longer acquisition time is required for these flow rates. Peak broadening at lower flow rates is

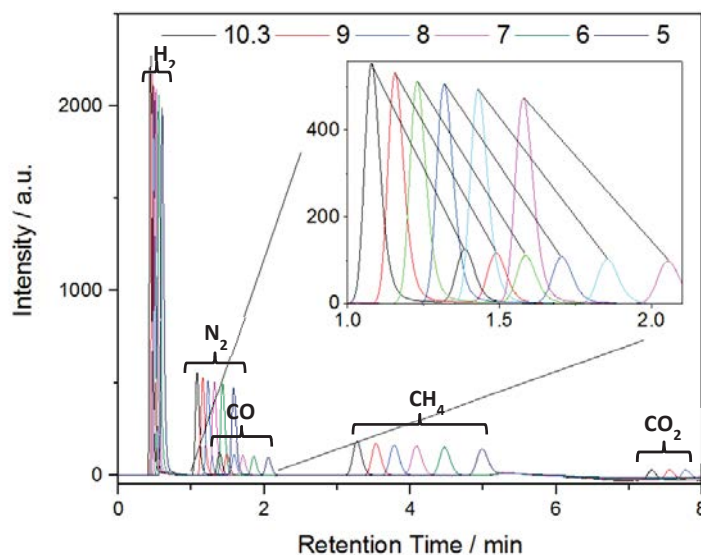


Figure 117: The Effect of Column Flow Rate on GC Spectrums
Flow rates are given in ml min⁻¹.

Appendix E - Column Temperature Profile

Changing the temperature at which the column is held changes the speed at which analytes move through the column. Generally the lower the column temperature the slower the gases move and therefore the better the separation of analytes. If gases are already well separated, however, a higher column temperature may be selected to increase the speed at which analytes move through the column to achieve a shorter run time. For observing a continuous process such as a catalytic process, as is investigated in this work, a shorter run time is preferable because it allows the user to take more data points per unit of time.

The column is capable of starting at a low temperature to allow good separation of molecules with a low affinity for the column. The column can then be heated to a higher temperature, in order to force molecules with a higher affinity through the column quicker to reduce run times. The column must then cool down at the end of the run before the column is deemed “ready” and the next sample can be taken.

Something to consider when varying the column temperature is the amount of time taken for the column to cool down in between runs. A higher start temperature is preferential as cooling the column to close to room temperature takes longer. A higher temperature will also give a flatter baseline at the start of each spectrum since a “ready” column is achieved more efficiently in between measurements. A lower final column temperature is preferential as it will take less time for a column to cool down from a lower temperature than a higher one. Shorter cooling periods are beneficial as they increase the number of data points you are able to collect per unit of time.

Figure 118 shows that using a higher initial column temperature a flatter baseline is achieved which means more reliable peak integration and results are achievable. However, this comes at the cost of a poorer nitrogen/carbon monoxide peak separation.

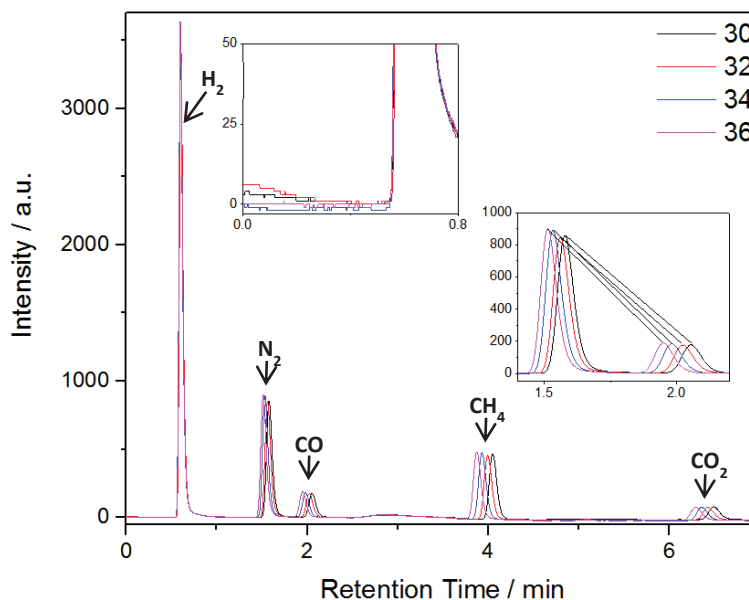


Figure 118: Effect of initial column temperature on GC spectrums.

When the temperature of the column is increased the column will “bleed”. This results in variations in the baseline which cannot be avoided. To ensure that these variations do not affect the integration of analyte peaks it is best to change method parameters so that peaks appear in areas where there is a relatively flat baseline. Figure 119 shows that at lower temperatures the methane peak is shifted to a retention time where the baseline is more flat. Though, this comes at the expense of run time. However, coupled with this longer measurement is a shorter column cool down period since the column is cooling from a lower temperature.

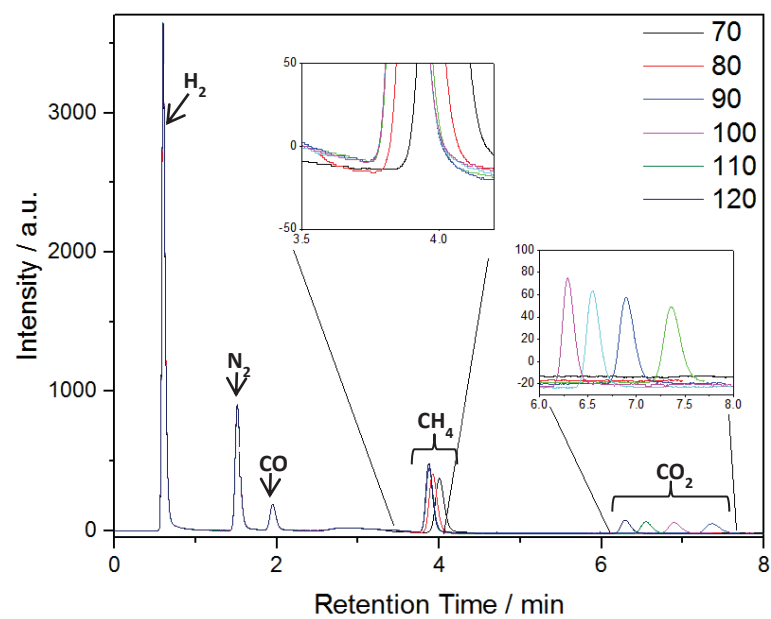


Figure 119: Effects of Final Column Temperature on GC Spectrums.

Appendix F - Detector Current

Finally, the detector current can be increased in order to achieve better sensitivity in the instrument. A higher current results in a larger signal for analytes, resulting in larger peaks and a larger margin for error.

Detectors have maximum operation temperatures and currents when they are used with different carrier gases. If the detectors are operated beyond these temperatures and currents the detector is at risk of failure. Figure 120 shows the maximum current possible at different operating temperatures. These charts are supplied by the detector manufacturer. The operating temperature is limited by the column temperature. The detector cannot be operated at a higher temperature than the column.

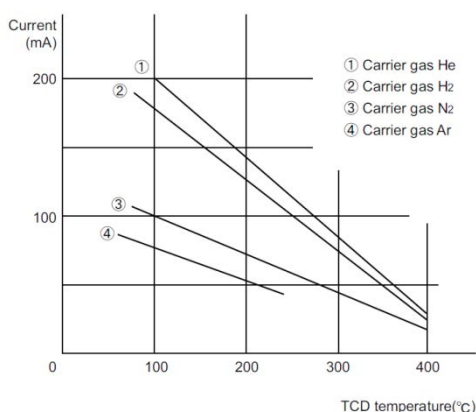


Figure 120: Detector operation limits

Figure 121 shows that with increased detector current, peak areas significantly increase.

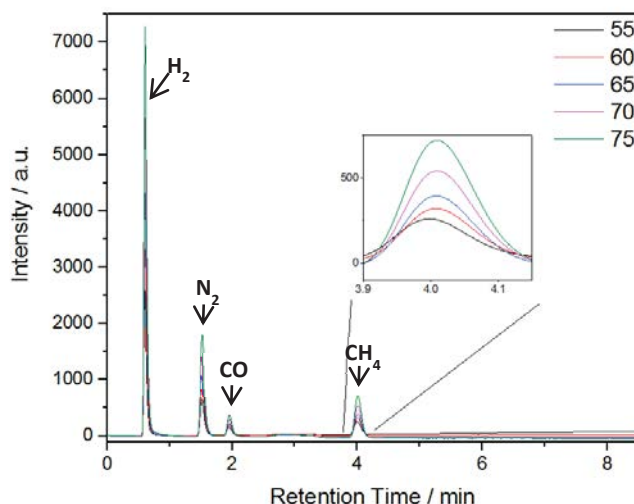


Figure 121: Effect of Detector Current on GC Spectrums.
Detector currents are given in mA.

Appendix G - Identification of GC peaks

Once an adequate separation is achieved in GC, it is important to identify which peak corresponds to which gas.

Each gas was sampled individually so that each peak could be attributed to its corresponding gas. Figure 122 shows the spectra when 100% H₂, O₂, N₂, CO, CH₄, and CO₂ where each independently sampled. This gives the retention time for these gases when sampled with this GC using the method parameters given in 3.3.1. These retention times are then used for peak identification later, when a sample is being measured.

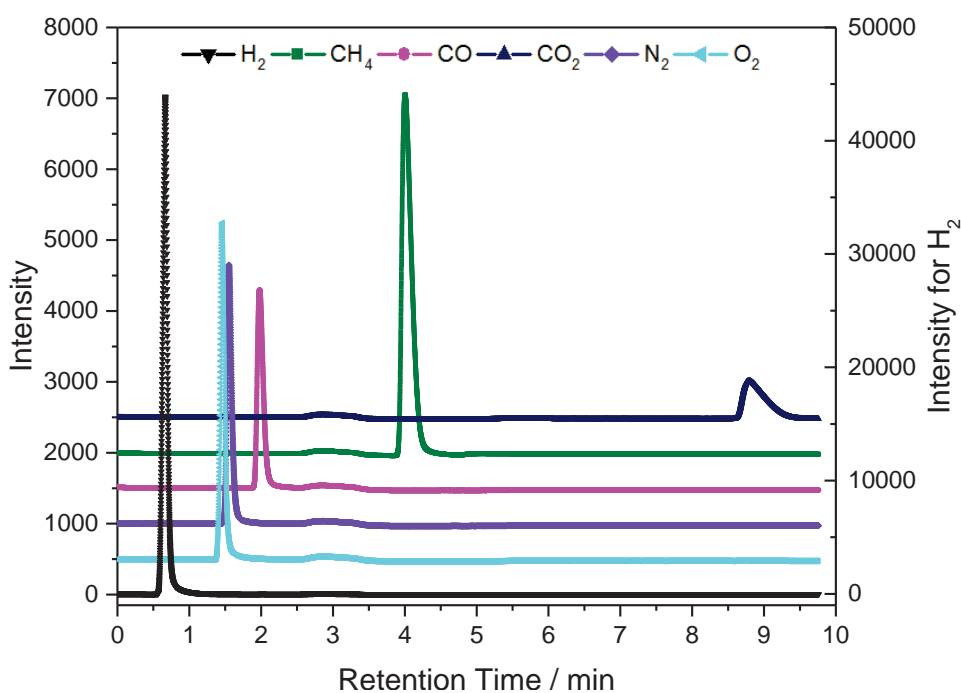


Figure 122: Spectra from individually sampling each gas in order to obtain the retention time.

Figure 122 also highlights the variable sensitivity of the GC to different gases. The GC gives a much larger response for hydrogen than it does for carbon dioxide even though in both cases 100% of the analyte is being measured. The sensitivity of the GC towards a gas can be adjusted by changing the reference gas used in the detector. E.g. if you specifically wanted

to investigate carbon dioxide you would use helium as the reference gas. Since hydrogen is of most interest in this work, argon was selected.

Appendix H –

Methane conversion and product yields when partial oxidation reactants were passed over a fixed bed reactor containing only SiO_2 . The same reaction conditions were used as when testing the effect of temperature on the catalysts.

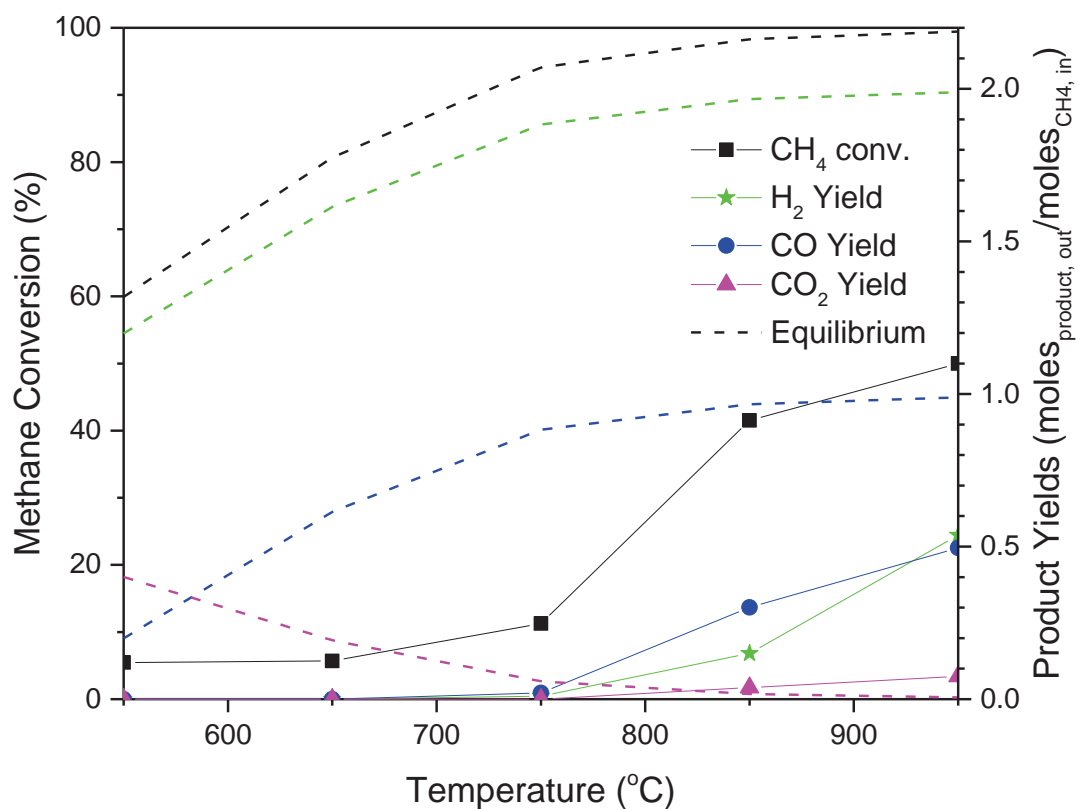


Figure 123: Catalytic activity of SiO_2 for partial oxidation of methane.

Appendix I - Product yields of the regeneration cycles of 1Ni/SiO_{2, sph} fibre bundle.

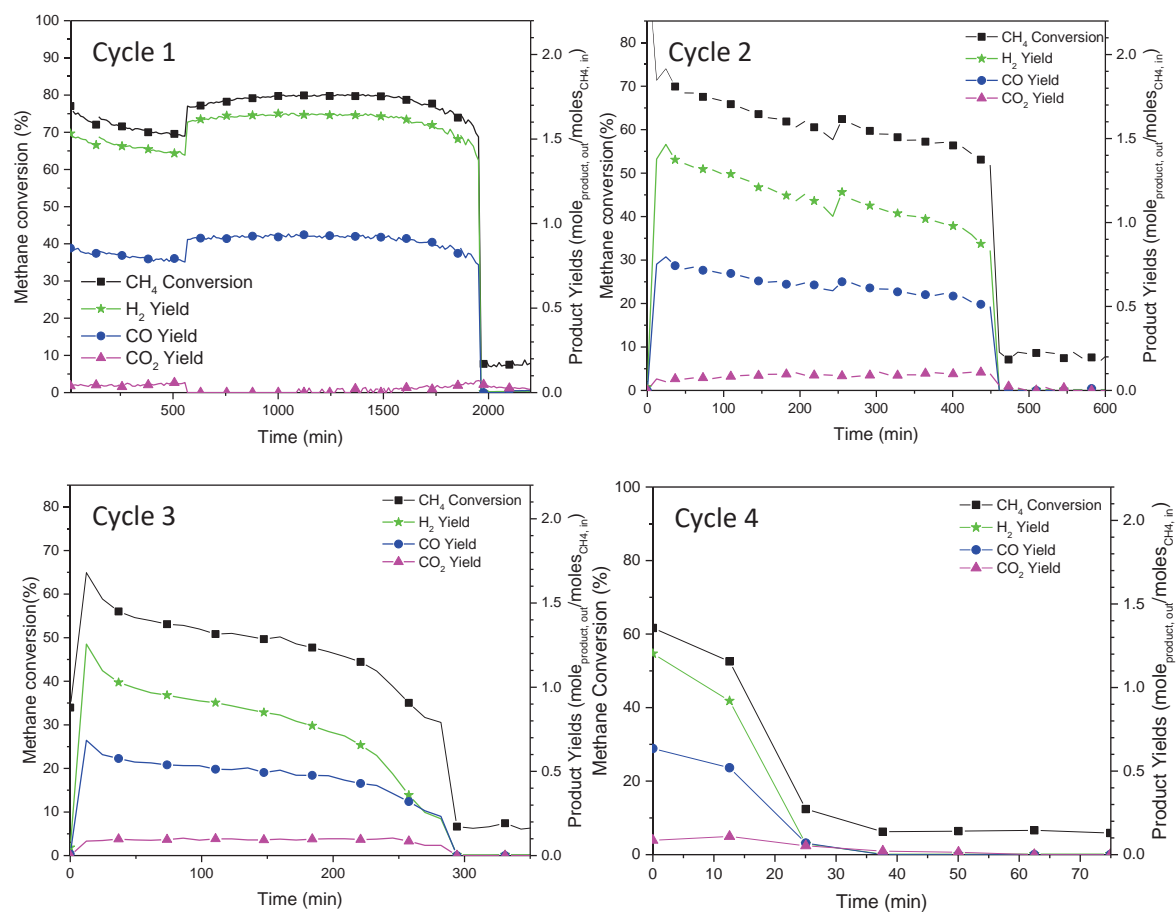


Figure 124: Regeneration of 1Ni/SiO_{2, sph} Fibre bundle showing product yields.

Bibliography

- [1] The World Bank, 2014, *Energy use (kg of oil equivalent per capita)*, IEA Stat., accessed 17 May 2018, <https://data.worldbank.org/indicator/EG.USE.PCAP.KG.OE>.
- [2] Statista, 2018, *World energy consumption from 2015 to 2050, by region*, Statista, accessed 17 May 2018, <https://www.statista.com/statistics/268297/world-energy-consumption-outlook/>.
- [3] Shafiee S., Topal E., 2009, 'When will fossil fuel reserves be diminished?', *Energy Policy*, 37, 181–9.
- [4] Rostrup-Nielsen JR., 2004, 'Fuels and Energy for the Future : The Role of Catalysis Fuels and Energy for the Future', *Catal Rev.*, 46, 247–70.
- [5] Steinberger-Wilckens R, Radcliffe J, Al-Mufachi N, Dodds PE, Abad AV, Jones O, et al., 2017, 'The Role of Hydrogen and Fuel Cells in Delivering Energy Security for the UK', *Supergen*, London, 1-24.
- [6] van Nes EH, Scheffer M, Brovkin V, Lenton TM, Ye H, Deyle E, et al., 2015, 'Causal feedbacks in climate change', *Nat. Clim. Chang.*, 5, 445–8.
- [7] Climate Focus, 2015, 'The Paris Agreement', report by *Climate Focus*
- [8] Mudway IS, Dundad I, Wood HE, Marlin N, Jamaludin JB, Bremner SA, et al., 2018, 'Impact of London's low emission zone on air quality and children's respiratory health: a sequential annual cross-sectional study.', *Lancet Public Heal*, 4, 28–40.
- [9] Sergi B, Azevedo I, Xia T, Davis A, Xu J., 2019, 'Support for Emissions Reductions Based on Immediate and Long-term Pollution Exposure in China.', *Ecol Econ*, 158, 26–33.
- [10] BEIS, 2018, 'UK Energy Statistics, Q3', *Department for Business Energy & Industrial Strategy*, London.
- [11] DECC, 2014, 'UK Energy Statistics.', *Department of Energy & Climate Change*, London.
- [12] Wilson IAG, Styring P., 2017, 'Why Synthetic Fuels Are Necessary in Future Energy Systems.', *Front Energy Res*, 5, 1–10.
- [13] BEIS, 2017, 'The Clean Growth Strategy: Leading the way to a low carbon future. *Department for Business Energy & Industrial Strategy*, London
- [14] Crawley M, Stoppato A, Benato A, Cavazzini G, Perez Diaz J, Blazquez F, et al., 2017, *Energy Storage*. First ed. World Scientific, Singapore.
- [15] Balat H, Kirtay E., 2010, 'Hydrogen from biomass - Present scenario and future prospects.', *Int J Hydrogen Energy*, 35, 7416–26.
- [16] Bockris J., 2013, 'The hydrogen economy: Its history.' *Int J Hydrogen Energy*, 38, 2579–88.

- [17] Moliner R, Lázaro MJ, Suelves I., 2016, 'Analysis of the strategies for bridging the gap towards the Hydrogen Economy.', *Int J Hydrogen Energy*, 41, 19500–8.
- [18] International Energy Agency, 2012, 'Energy Technology Perspectives', *IEA*, London, 1-443.
- [19] Cadent Gas, Keele University, ITM Power, Northern Gas Networks, Health & Safety Laboratory, Progressive Energy, et al., 2018, 'HyDeploy Project Report', *Hydeploy*, Coventry.
- [20] Progressive Energy Ltd., 2017, 'The Liverpool-Manchester Hydrogen Cluster: A Low Cost, Deliverable Project', *Progressive Energy*, Stonehouse.
- [21] Sadler D, Cargill A, Crowther M, Rennie A, Watt J, Burton S, et al., 2016, 'Leeds City Gate', *H21 Team*, Leeds.
- [22] Mac Kinnon M, Shaffer B, Carreras-Sospedra M, Dabdub D, Samuelsen GS, Brouwer J., 2016, 'Air quality impacts of fuel cell electric hydrogen vehicles with high levels of renewable power generation', *Int J Hydrogen Energy*, 41, 16592–603.
- [23] Behling NH., 2013, *Fuel Cells Current Technology Challenged and Future Research Needs*, first ed., *Elsevier*, Oxford.
- [24] Singhal SC, Kendall K., 2004, *High Temperature Solid Oxide Fuel Cells: Fundamentals, Design and Applications.*, first ed., *Elsevier*, Bodmin.
- [25] Baur E, Preis H., 1937, 'Über Brennstoff-Ketten mit Festleitern.', *Z Elektrochem*, 727–37.
- [26] Bleischwitz R, Bader N., 2010, 'Policies for the transition towards a hydrogen economy: The EU case', *Energy Policy*, 38:5388–98.
- [27] Steenberghen T, López E., 2008, 'Overcoming barriers to the implementation of alternative fuels for road transport in Europe', *J Clean Prod*, 16, 577–90.
- [28] Patil AC, Weijnen M., 2005, 'Actionable Solutions to Tackle Future Energy Uncertainties', *Int. Conf. Syst. MAN Cybern.*, 3705–10.
- [29] Elam CC, Padrã CEG, Sandrock G, Luzzi A, Lindblad P, Fjermestad E., 2003, 'Realizing the hydrogen future : the International Energy Agency ' s efforts to advance hydrogen energy technologies', *Int J Hydrogen Energy*, 28, 601–7.
- [30] Ogden J, Yang C, Nicholas M, Fulton L., 2014, 'NextSTEPS White paper: The Hydrogen Transition', *UC Davis*, California.
- [31] Kim JW, Boo KJ, Cho JH, Moon I., 2014, 'Key challenges in the development of an infrastructure for hydrogen production, delivery, storage and use.', first ed., *Woodhead Publishing Limited*, Cambridge.

- [32] Wang J., 2015, 'Barriers of scaling-up fuel cells: Cost, durability and reliability.', *Energy*, 80:509–21.
- [33] Andrews J, Shabani B., 2014, 'The role of hydrogen in a global sustainable energy strategy', *Wiley Interdiscip Rev Energy Environ*, 3, 474–89.
- [34] Edwards PP, Kuznetsov VL, David WIF, Brandon NP., 2008, 'Hydrogen and fuel cells: Towards a sustainable energy future', *Energy Policy*, 36, 4356–62.
- [35] Edwards P., Kuznetsov V., David WI., 2007, 'Hydrogen energy', *Philos Trans R Soc A Math Phys Eng Sci*, 365, 1043–56.
- [36] Gray EM., 2007, 'Hydrogen storage - status and prospects', *Adv Appl Ceram 2007*, 106, 25–8.
- [37] Ali DM, Salman SK., 2006, 'A comprehensive review of the fuel cells technology and hydrogen economy.', *IEEE*, vol. 1, Newcastle.
- [38] Berry KJ., 2003, 'Fuel Cell Commercialisation: Hydrogen Infrastructure Economic and Technical Barriers', *IEEE Trans Power Electron*, 149–56.
- [39] Balat M, Kirtay E., 2010, 'Major technical barriers to a "hydrogen economy."', *Energy Sources, Part A*, 32, 863–76.
- [40] Hyundai Motor Company, 2014, 'ix35 Fuel Cell: Specifications', *Hyundai*, South Korea.
- [41] Toyota Motor Corporation, 2014, 'Outline of the Mirai', *Toyota*, Japan.
- [42] Cherryman SJ, King S, Hawkes FR, Dinsdale R, Hawkes DL., 2008, 'An exploratory study of public opinions on the use of hydrogen energy in Wales', *Public Underst Sci*, 17, 397–410.
- [43] Page S, Krumdieck S., 2009, 'System-level energy efficiency is the greatest barrier to development of the hydrogen economy', *Energy Policy*, 37, 3325–35.
- [44] Sealy C., 2008, 'The problem with platinum', *Materials Today*, 11, 65–8.
- [45] Larin N, Zgonnik V, Rodina S, Deville E, Prinzhofer A, Larin VN., 2015, 'Natural Molecular Hydrogen Seepage Associated with Surficial, Rounded Depressions on the European Craton in Russia', *Nat Resour Res*, 24, 369–83.
- [46] Dincer I, Acar C., 2014, 'Review and evaluation of hydrogen production methods for better sustainability', *Int J Hydrogen Energy*, 40, 11094–111.
- [47] Nikolaidis P, Poullikkas A., 2017, 'A comparative overview of hydrogen production processes', *Renew Sustain Energy Rev*, 67, 597–611.
- [48] Hosseini SE, Wahid MA., 2016, 'Hydrogen production from renewable and sustainable energy resources: Promising green energy carrier for clean development', *Renew Sustain Energy Rev*, 57, 850–66.

- [49] Balat M., 2008, 'Potential importance of hydrogen as a future solution to environmental and transportation problems', *Int J Hydrogen Energy*, 33, 4013–29.
- [50] Mehmeti A, Angelis-Dimakis A, Arampatzis G, McPhail S, Ulgiati S., 2018, 'Life Cycle Assessment and Water Footprint of Hydrogen Production Methods: From Conventional to Emerging Technologies', *Environments*, 5, 24.
- [51] Bui M, Adjiman CS, Bardow A, Anthony EJ, Boston A, Brown S, et al., 2018, 'Carbon capture and storage (CCS): the way forward', *Energy Environ Sci*, 1062–176.
- [52] Hart D, Howes J, Madden B, Boyd E., 2016, 'Hydrogen and Fuel Cells: Opportunities for Growth', *E4Tech*, London.
- [53] Sadler D, Cargill A, Crowther M, Rennie A, Watt J, Burton S, et al., 2016, 'H21 Leeds City Gate.' *H21 Team*, Leeds.
- [54] Gigler J, Weeda M., 2018, 'Outlines of a Hydrogen Roadmap', *Topsector Energie*, Netherlands.
- [55] Goldstein B, Robles J., 2018, 'Renewable Hydrogen Roadmap', *Energy Independence Now*, California.
- [56] International Energy Agency, 2015, 'Technology Roadmap Hydrogen and Fuel Cells', *IEA*, Paris.
- [57] Randolph K, Miller E, Peterson D, Lyubovsky M, Cierpik-Gold K, Sink C, et al., 2017, 'Hydrogen Production Tech Team Roadmap', *US Drive Department of Energy*, Washington.
- [58] Office of Energy Efficiency and Renewable Energy, 2015, 'Fuel Cell Technologies Office Multi-Year Research, Development, and Demonstration Plan', *Department of Energy*, Washington.
- [59] Singh S, Jain S, Ps V, Tiwari AK, Nouni MR, Pandey JK, et al., 2015, 'Hydrogen: A sustainable fuel for future of the transport sector', *Renew Sustain Energy Rev*, 51, 623–33.
- [60] Mastanduno R, Roychoudhury S, Etemad S., 2014, 'Onboard Hydrogen Generation for IC Engine Emissions Reduction', *ASME 2014 Intern. Combust. Engine Div. Fall Tech. Conf.*, vol. 1, Indiana.
- [61] Xu X, Liu X, Xu B., 2016, 'A survey of nickel-based catalysts and monolithic reformers of the onboard fuel reforming system for fuel cell APU applications', *Int J Energy Res*, 1157–77.
- [62] Lee DH, Lee JO, Kim KT, Song YH, Kim E, Han HS., 2012, 'Hydrogen in plasma-assisted hydrocarbon selective catalytic reduction', *Int J Hydrogen Energy*, 37, 3225–33.
- [63] Lee DH, Lee JO, Kim KT, Song YH, Kim E, Han HS, 2011, 'Characteristics of plasma-assisted hydrocarbon SCR system', *Int J Hydrogen Energy*, 36, 11718–26.

- [64] Lebouvier A, Cauneau F, Fulcheri L, Lebouvier A, Cauneau F, Fulcheri L, et al., 2011, '2D Axisymmetric Coupled Computational Fluid Dynamics – Kinetics Modeling of a Nonthermal Arc Plasma Torch for Diesel Fuel Reforming'. *Energy Fuels*, 25, 2833–2840.
- [65] EG&G Technical Services Inc., 2004, 'Fuel Cell Handbook', *Department of Energy*, West Virginia.
- [66] Ji C, Dai X, Wang S, Liang C, Ju B, Liu X., 2013, 'Experimental study on combustion and emissions performance of a hybrid syngas-gasoline engine', *Int J Hydrogen Energy*, 38, 11169–73.
- [67] Li G, Zhang Z, You F, Pan Z, Zhang X, Dong J, et al., 2013, 'A novel strategy for hydrous-ethanol utilization: Demonstration of a spark-ignition engine fueled with hydrogen-rich fuel from an onboard ethanol/steam reformer', *Int J Hydrogen Energy*, 38, 5936–48.
- [68] Frigo S, Gentili R., 2013, 'Analysis of the behaviour of a 4-stroke Si engine fuelled with ammonia and hydrogen', *Int J Hydrogen Energy*, 38, 1607–15.
- [69] Kirillov VA, Sobyannin VA, Kuzin NA, Brizitski OF, Terentiev VY., 2012, 'Synthesis gas generation on-board a vehicle: Development and results of testing', *Int J Hydrogen Energy*, 37, 16359–66.
- [70] Ji C, Dai X, Ju B, Wang S, Zhang B, Liang C, et al., 2012, 'Improving the performance of a spark-ignited gasoline engine with the addition of syngas produced by onboard ethanol steaming reforming', *Int J Hydrogen Energy*, 37, 7860–8.
- [71] Chen SC, Kao YL, Yeh GT, Rei MH, 2017, 'An onboard hydrogen generator for hydrogen enhanced combustion with internal combustion engine', *Int J Hydrogen Energy*, 42, 21334–42.
- [72] Sall ED, Morgenstern DA, Fornango JP, Taylor JW, Chomic N, Wheeler J., 2013, 'Reforming of ethanol with exhaust heat at automotive scale', *Energy and Fuels*, 27, 5579–88.
- [73] Ma Z, Jiang Q-Z, Wang X, Zhang W-G, Ma Z-F., 2012, 'CO₂ reforming of dimethyl ether over Ni γ -Al₂O₃ catalyst', *Catal Commun*, 49–53.
- [74] Fernández IA, Gómez MR, Gómez JR, López-González LM., 2017, 'H₂ production by the steam reforming of excess boil off gas on LNG vessels', *Energy Convers Manag*, 134, 301–13.
- [75] Fuen C, Longhan C, Xin X, Xiang L, Lan Y., 2016, 'Test bed for farm vehicle onboard hydrogen production system with microwave plasma', *Int J Agric Biol Eng*, 9, 65–74.
- [76] Xu X, Li P, Shen Y., 2013, 'Small-scale reforming of diesel and jet fuels to make hydrogen and syngas for fuel cells: A review', *Appl Energy*, 108, 202–17.
- [77] Lin J, Walluk MR, Smith DF, Trabold TA., 2012, 'Mitigation of Carbon Formation During

Autothermal Reforming of Biodiesel for Solid Oxide Fuel Cell Applications', *ASME 2012 10th Int. Conf. Fuel Cell Sci. Eng. Technol. collocated with ASME 2012 6th Int. Conf. Energy Sustain.*, San Diego, California.

- [78] Karatzas X, Creaser D, Grant A, Dawody J, Pettersson LJ., 2011, 'Hydrogen generation from n-tetradecane, low-sulfur and Fischer-Tropsch diesel over Rh supported on alumina doped with ceria/lanthana', *Catal Today*, 164, 190–7.
- [79] Martinez AS, Brouwer J, Samuelsen GS., 2015, 'Comparative analysis of SOFC-GT freight locomotive fueled by natural gas and diesel with onboard reformation', *Appl Energy*, 148, 421–38.
- [80] Krummrich S, Llabrés J., 2015, 'Methanol reformer - The next milestone for fuel cell powered submarines', *Int J Hydrogen Energy*, 40, 5482–6.
- [81] Nikiforov B V., Chigarev A V., 2011, 'Problems of designing fuel cell power plants for submarines', *Int J Hydrogen Energy*, 36, 1226–9.
- [82] Bisaria V, Smith RJB., 2013, 'Hydrogen production by onboard gasoline processing - Process simulation and optimization', *Energy Convers Manag*, 76, 746–52.
- [83] Tanim T, Bayless DJ, Tremblay JP., 2014, 'Modeling a 5 kWe planar solid oxide fuel cell based system operating on JP-8 fuel and a comparison with tubular cell based system for auxiliary and mobile power applications', *J Power Sources*, 245, 986–97.
- [84] Varady MJ, Fedorov AG., 2011, 'Fuel reformation and hydrogen generation with direct droplet impingement reactors: Model formulation and validation reformers', *Ind Eng Chem Res*, 50, 9514–24.
- [85] Mai A, Iwanschitz B, Weissen U, Denzler R, Haberstock D, Nerlich V, et al., 2009, 'Status of Hexis SOFC Stack Development and the Galileo 1000N Micro-CHP System', *ECS Trans*, 25, 149–58.
- [86] Ito H., 2016, 'Economic and environmental assessment of residential micro combined heat and power system application in Japan', *Int J Hydrogen Energy*, 41, 15111–23.
- [87] Xu X, Shuai K, Xu B., 2017, 'Review on Copper and Palladium Based Catalysts for Methanol Steam Reforming to Produce Hydrogen', *Catalysts*, 7, 183.
- [88] Sheintuch M., 2015, 'Pure hydrogen production in a membrane reformer: Demonstration, macro-scale and atomic scale modeling', *Chem Eng J*, 278, 363–73.
- [89] Song L, Li X., 2013, 'Hydrogen production from partial oxidation of dimethyl ether by plasma-catalyst reforming', *J Cent South Univ*, 20, 3764–9.
- [90] Jolaoso LA, Zaman SF, Podila S, Driss H, Al-Zahrani AA, Daous MA, et al., 2018, 'Ammonia decomposition over citric acid induced γ -Mo₂N and Co₃Mo₃N catalysts', *Int J Hydrogen Energy*, 43, 4839–44.
- [91] Chen F, Huang X, Cheng DG, Zhan X., 2014, 'Hydrogen production from alcohols and

ethers via cold plasma: A review', *Int J Hydrogen Energy*, 39, 9036–46.

- [92] Heitnes K, Lindberg S, Rokstad OA, Holmen A., 1995, 'Catalytic partial oxidation of methane to synthesis gas', *Catal Today*, 211–6.
- [93] Ding C, Wang J, Ai G, Liu S, Liu P, Zhang K, et al., 2016, 'Partial oxidation of methane over silica supported Ni nanoparticles with size control by alkanol solvent', *FUEL*, 175, 1–12.
- [94] Hickman DA, Schmidt LD., 1993, 'Production of Syngas by Direct Catalytic Oxidation of Methane', *Science*, 343–6.
- [95] van Looij F, van Giezen JC, Stobbe ER, Geus JW., 1994, 'Mechanism of the partial oxidation of methane to synthesis gas on a silica-supported nickel catalyst', *Catal Today*, 21, 495–503.
- [96] Au CT, Wang HY., 1996, 'Pulse study of methane partial oxidation to syngas over SiO₂-supported nickel catalysts', *Catal Letters*, 41, 159–63.
- [97] Yuan R, He Z, Zhang Y, Wang W, Chen C, Wu H, et al., 2016, 'Partial Oxidation of Methane to Syngas in a Packed Bed Catalyst Membrane Reactor', *Am Inst Chem Eng J*, 62, 2170–6.
- [98] Takenaka S, Umebayashi H, Tanabe E, Matsune H, Kishida M., 2007, 'Specific performance of silica-coated Ni catalysts for the partial oxidation of methane to synthesis gas', *J Catal*, 245, 392–400.
- [99] Jun JH, Lim TH, Nam SW, Hong SA, Yoon KJ., 2006, 'Mechanism of Partial Oxidation of Methane Over a Nickel-Calcium Hydroxyapatite Catalyst', *Appl Catal A Gen*, 312, 27–34.
- [100] Ding C, Gao X, Han Y, Ma X, Wang J, Liu S, et al., 2015, 'Effects of surface states over core-shell Ni@SiO₂ catalysts on catalytic partial oxidation of methane to synthesis gas', *J Energy Chem*, 24, 45–53.
- [101] Xu S, Wang X., 2005, 'Highly active and coking resistant Ni/CeO₂ZrO catalyst for partial oxidation of methane', *Fuel*, 84, 563–7.
- [102] Tsipouriari VA, Zhang Z, Verykios XE., 1998, 'Catalytic Partial Oxidation of Methane to Synthesis Gas over Ni-Based Catalysts', *J Catal*, 179, 283–91.
- [103] Prettre M, Eichner CH, Perrin M., 1945, 'The Catalytic Oxidation of Methane to Carbon Monoxide and Hydrogen', *Trans Faraday Soc*, 42, 335–9.
- [104] Van Looij F, Stobbe ER, Geus JW., 1998, 'Mechanism of the partial oxidation of methane to synthesis gas over Pd', *Catal Letters*, 50, 59–67.
- [105] Hayakawa T, Harihara H, Andersen AG, Suzuki K, Yasuda H, Tsunoda T, et al., 1997, 'Sustainable Ni / Ca_{1-x}Sr_x TiO₃ catalyst prepared in situ for the partial oxidation of methane to synthesis gas', *Appl Catal A Gen*, 149, 391–410.

- [106] Basile F, Basini L, Amore MD, Fornasari G, Guarinoni A, Matteuzzi D, et al., 1998, 'Ni / Mg / Al Anionic Clay Derived Catalysts for the Catalytic Partial Oxidation of Methane Residence Time Dependence of the Reactivity Features', *J Catal*, 173, 247–56.
- [107] Hickman DA, Schmidt LD., 1992, 'Synthesis Gas Formation by Direct Oxidation of Methane over Pt Monoliths', *J Catal*, 282, 267–82.
- [108] Hickman DA, Hauptfear EA, Schmidt LD., 1993, 'Synthesis gas formation by direct oxidation of methane over Rh monoliths', *Catal Letters*, 17, 223–37.
- [109] Drago RS, Jurczyk K, Kob N, Bhattacharyya A, Masin J., 1998, 'Partial oxidation of methane to syngas using NiO-supported catalysts', *Catal Letters*, 51, 177–81.
- [110] Choudhary VR, Rajput AM, Prabhakar B., 1993, 'Nonequilibrium Oxidative Conversion of Methane to CO and H₂ with High Selectivity and Productivity over Ni-Al₂O₃ at Low Temperatures', *J Catal*, 139, 326–8.
- [111] Au CT, Wang HY, Wan HL., 1996, 'Mechanistic Studies of CH₄ / O₂ Conversion over SiO₂ -Supported Nickel and Copper Catalysts', *J Catal*, 343–8.
- [112] Balint I, Miyazaki A, Aika K., 2003, 'The relevance of Ru nanoparticles morphology and oxidation state to the partial oxidation of methane', *J Catal*, 220, 74–83.
- [113] Salazar-Villalpando MD, Berry D a., Cugini A., 2010, 'Role of lattice oxygen in the partial oxidation of methane over Rh/zirconia-doped ceria: Isotopic studies', *Int J Hydrogen Energy*, 35, 1998–2003.
- [114] Zhu J, Vanommen J, Bouwmeester H, Lefferts L., 2005, 'Activation of O₂ and CH₄ on yttrium-stabilized zirconia for the partial oxidation of methane to synthesis gas', *J Catal*, 233, 434–41.
- [115] Otsuka K, Wang Y, Sunada E, Yamanaka I., 1998, 'Direct Partial Oxidation of Methane to Synthesis Gas by Cerium Oxide', *J Catal*, 160, 152–60.
- [116] Sadykov V A., Sazonova NN, Bobin AS, Muzykantov VS, Gubanova EL, Alikina GM, et al., 2011, 'Partial oxidation of methane on Pt-supported lanthanide doped ceria–zirconia oxides: Effect of the surface/lattice oxygen mobility on catalytic performance', *Catal Today*, 169, 125–37.
- [117] Li L, He S, Song Y, Zhao J, Ji W, Au C-T., 2012, 'Fine-tunable Ni@porous silica core–shell nanocatalysts: Synthesis, characterization, and catalytic properties in partial oxidation of methane to syngas', *J Catal*, 288, 54–64.
- [118] Özdemir H, Öksüzömer M a. F, Gürkaynak MA., 2014, 'Effect of the calcination temperature on Ni/MgAl₂O₄ catalyst structure and catalytic properties for partial oxidation of methane', *Fuel*, 116, 63–70.

- [119] Mette K, Kühl S, Tarasov A, Willinger MG, Kröhnert J, Wrabetz S, et al., 2016, 'High-Temperature Stable Ni Nanoparticles for the Dry Reforming of Methane', *ACS Catal*, 6, 7238–48.
- [120] Özdemir H, Faruk Öksüzömer M A., Ali Gürkaynak M., 2010, 'Preparation and characterization of Ni based catalysts for the catalytic partial oxidation of methane: Effect of support basicity on H₂/CO ratio and carbon deposition', *Int J Hydrogen Energy*, 35, 12147–60.
- [121] Maniecki TP, Bawolak K, Gebauer D, Mierczynski P, Jozwiak WK., 2009, 'Catalytic activity and physicochemical properties of Ni-Au/Al₃CrO₆ system for partial oxidation of methane to synthesis gas', *Kinet Catal*, 50, 138–44.
- [122] Oh H, Kang J, Heo E, Lee S, Choi J., 2014, 'Kinetic Investigation of CO₂ -CH₄ Reaction over Ni/La₂O₃ Catalyst using Photoacoustic Spectroscopy', 35, 2615–20.
- [123] Song Y-Q, He D-H, Xu B-Q., 2008, 'Effects of preparation methods of ZrO₂ support on catalytic performances of Ni/ZrO₂ catalysts in methane partial oxidation to syngas', *Appl Catal A Gen*, 337, 19–28.
- [124] Nogare DD, Degenstein NJ, Horn R, Canu P, Schmidt LD., 2011, 'Modeling spatially resolved data of methane catalytic partial oxidation on Rh foam catalyst at different inlet compositions and flowrates', *J Catal*, 277, 134–48.
- [125] Lu J, Fu B, Mayfair KC, Xiao G, Elam JW, Kung HH, et al., 2012, 'Coking and Sintering Resistant Palladium Catalysts Achieved Through Atomic Layer Deposition', *Science*, 335, 1205–9.
- [126] Verlato E, Barison S, Cimino S, Dergal F, Lisi L, Mancino G, et al., 2014, 'Catalytic partial oxidation of methane over nanosized Rh supported on Fecralloy foams', *Int J Hydrogen Energy*, 39, 11473–85.
- [127] Zhu T, Flytzani-stephanopoulos M., 2001, 'Catalytic partial oxidation of methane to synthesis gas over Ni – CeO₂', *Appl Catal A Gen*, 208, 403–17.
- [128] Ding C, Ai G, Zhang K, Yuan Q, Han Y, Ma X, et al., 2015, 'Coking resistant Ni/ZrO₂@SiO₂ catalyst for the partial oxidation of methane to synthesis gas', *Int J Hydrogen Energy*, 40, 6835–43.
- [129] Zhang C, Zhu W, Li S, Wu G, Ma X, Wang X, et al., 2013, 'Sintering-resistant Ni-based reforming catalysts obtained via the nanoconfinement effect', *Chem Commun*, 49, 9383–5.
- [130] Helveg S, Lopez-Cartes C, Sehested J, Hansen PL, Clausen BS, Rostrup-nielsen JR, et al., 2004, 'Atomic-scale imaging of carbon nanofibre growth', *Nature*, 427, 426–9.
- [131] Liu H, He D., 2010, 'Physicochemical Properties of Ni/γ -Al₂O₃ -AlN and Effects of AlN on Catalytic Performance of Ni/γ -Al₂O₃ -AlN in Partial Oxidation of Methane', 13716–21.

- [132] Ballarini A, Benito P, Fornasari G, Scelza O, Vaccari A., 2013, 'Role of the composition and preparation method in the activity of hydrotalcite-derived Ru catalysts in the catalytic partial oxidation of methane', *Int J Hydrogen Energy*, 38, 15128–39.
- [133] Li Z, Kathiraser Y, Ashok J, Oemar U, Kawi S., 2014, 'Simultaneous Tuning Porosity and Basicity of Nickel @ Nickel – Magnesium Phyllosilicate Core – Shell Catalysts for CO₂, Reforming of CH₄', *Langmuir*, 48, 14694–14705.
- [134] Majewski AJ, Wood J., 2014, 'Tri-reforming of methane over Ni@SiO₂ catalyst', *Int J Hydrogen Energy*, 39, 12578–85.
- [135] Kim HW, Kang KM, Kwak H-Y., 2009, 'Preparation of supported Ni catalysts with a core/shell structure and their catalytic tests of partial oxidation of methane', *Int J Hydrogen Energy*, 34, 3351–9.
- [136] Liu Z, Zhou J, Cao K, Yang W, Gao H, Wang Y, et al., 2012, 'Highly dispersed nickel loaded on mesoporous silica: One-spot synthesis strategy and high performance as catalysts for methane reforming with carbon dioxide', *Appl Catal B Environ*, 125, 324–30.
- [137] Chou Y-S, Huang M-H, Hsu N-Y, Jeng K-T, Lee R-Y, Yen S-C., 2016, 'Development of ring-shape supported catalyst for steam reforming of natural gas in small SOFC systems', *Int J Hydrogen Energy*, 41, 12953–61.
- [138] Majewski AJ, Wood J, Bujalski W., 2013, 'Nickel–silica core@shell catalyst for methane reforming', *Int J Hydrogen Energy*, 38, 14531–41.
- [139] Joo SH, Park JY, Tsung C-K, Yamada Y, Yang P, Somorjai G A., 2009, 'Thermally stable Pt/mesoporous silica core-shell nanocatalysts for high-temperature reactions', *Nat Mater*, 8, 126–31.
- [140] Cargnello M, Montini T, Polizzi S, Wieder NL, Gorte RJ, Graziani M, et al., 2010, 'Novel embedded Pd@CeO₂ catalysts: a way to active and stable catalysts', *Dalton Trans*, 39, 2122–7.
- [141] Seipenbusch M, Binder A., 2009, 'Structural Stabilization of Metal Nanoparticles by Chemical Vapor Deposition-Applied Silica Coatings', *J Phys Chem C*, 20606–10.
- [142] Yu K, Wu Z, Zhao Q, Li B, Xie Y., 2008, 'High-Temperature-Stable Au @ SnO₂ Core / Shell Supported Catalyst for CO Oxidation', *J Phys Chem Lett C*, 2244–7.
- [143] Arnal PM, Comotti M, Schüth F., 2006, 'High-temperature-stable catalysts by hollow sphere encapsulation', *Angew Chem Int Ed Engl*, 45, 8224–7.
- [144] Xia W, Hou Y, Chang G, Weng W, Han G, Wan H., 2012, 'Partial oxidation of methane into syngas (H₂ + CO) over effective high-dispersed Ni / SiO₂ catalysts synthesized by a sol - gel method', *Int J Hydrogen Energy*, 37, 8343–53.

- [145] Guo S, Wang J, Ding C, Duan Q, Ma Q, Zhang K, et al., 2018, 'Confining Ni nanoparticles in honeycomb-like silica for coking and sintering resistant partial oxidation of methane', *Int J Hydrogen Energy*, 43, 6603–13.
- [146] Jing QS, Zheng XM., 2006, 'Combined catalytic partial oxidation and CO₂ reforming of methane over ZrO₂-modified Ni/SiO₂ catalysts using fluidized-bed reactor', *Energy*, 31, 2184–92.
- [147] Sadegh SM, Davarani H, Hashemipour H, Talebizadeh A., 2017, 'Oleylamine-modified impregnation method for the preparation of a highly efficient Ni/SiO₂ nanocatalyst active in the partial oxidation of methane', *Chem Ind Chem Eng Q*, 23, 259–67.
- [148] Hu J, Yu C, Bi Y, Wei L, Chen J, Chen X., 2014, 'Preparation and characterization of Ni/CeO₂-SiO₂ catalysts and their performance in catalytic partial oxidation of methane to syngas.' *Chinese J Catal*, 35, 8–20.
- [149] Li B, Xu X, Zhang S., 2013, 'Synthesis gas production in the combined CO₂ reforming with partial oxidation of methane over Ce-promoted Ni/SiO₂ catalysts', *Int J Hydrogen Energy*, 38, 890–900.
- [150] Li L, Lu P, Yao Y, Ji W., 2012, 'Silica-encapsulated bimetallic Co – Ni nanoparticles as novel catalysts for partial oxidation of methane to syngas', *CATCOM*, 26, 72–7.
- [151] Li L, Yao Y, Sun B, Fei Z, Xia H, Zhao J, et al., 2013, 'Highly Active and Stable Lanthanum-doped Core – Shell- structured Ni@SiO₂ Catalysts for the Partial Oxidation of Methane to Syngas', *Chem Cat Chem*, 5, 3781–7.
- [152] Sivaiah M V., Petit S, Beaufort MF, Eyidi D, Barrault J, Batiot-Dupeyrat C, et al., 'Nickel based catalysts derived from hydrothermally synthesized 1:1 and 2:1 phyllosilicates as precursors for carbon dioxide reforming of methane', *Microporous Mesoporous Mater*, 140, 69–80.
- [153] Wang SG, Cao DB, Li YW, Wang J, Jiao H., 2009, 'Reactivity of surface OH in CH₄ reforming reactions on Ni(1 1 1): A density functional theory calculation', *Surf Sci*, 603, 2600–6.
- [154] Ashok J, Ang ML, Terence PZL, Kawi S., 2016, 'Promotion of the Water-Gas-Shift Reaction by Nickel Hydroxyl Species in Partially Reduced Nickel-Containing Phyllosilicate Catalysts', *ChemCatChem*, 8, 1308–18.
- [155] Clarke SH, Dicks AL, Pointon K, Smith TA, Swann A., 1997, 'Catalytic aspects of the steam reforming of hydrocarbons in internal reforming fuel cells', *Catal Today*, 38, 411–23.
- [156] Aguiar P, Chadwick D, Kershenbaum LS., 2004, 'Dynamic effects in autothermal systems: Application to a coated-wall internally reformed solid oxide fuel cell', *Chem Eng Res Des*, 82, 259–66.
- [157] Dokmaingam P., 2015, 'Configuration development of autothermal solid oxide fuel

cell: A review', *Eng J*, 19, 1–13.

- [158] Majewski AJ, Bossel U, Steinberger-Wilckens R., 2018, 'Catalytic Reforming System Suitable for Transportation Applications', *Fuel Cells*, 18, 535–42.
- [159] Jiang B, Maeder T, Santis-Alvarez AJ, Poulikakos D, Muralt P., 2015, 'A low-temperature co-fired ceramic micro-reactor system for high-efficiency on-site hydrogen production', *J Power Sources*, 273, 1202–17.
- [160] Corigliano O, Fragiaco P., 2017, 'Numerical modeling of an indirect internal CO₂ reforming solid oxide fuel cell energy system fed by biogas', *Fuel*, 196, 352–61.
- [161] Jahn M, Heddrich M, Weder A, Reichelt E, Lange R., 2013, 'Oxidative Dry-Reforming of Biogas: Reactor Design and SOFC System Integration', *Energy Technol*, 48–58.
- [162] Peters R, Riensche E, Cremer P., 2000, 'Pre-reforming of natural gas in solid oxide fuel-cell systems', *J Power Sources*, 86, 432–41.
- [163] Peters R, Dahl R, Kluttgen U, Palm C, Stolten D., 2002, 'Internal reforming of methane in solid oxide fuel cell systems', *J Power Sources*, 106, 238–44.
- [164] Lim LT, Chadwick D, Kershenbaum L., 2005, 'Achieving Autothermal Operation in Internally Reformed Solid Oxide Fuel Cells: Simulation Studies', *Ind Eng Chem Res*, 44, 9609–18.
- [165] Dokmaingam P, Irvine JTS, Assabumrungrat S, Charojrochkul S, Laosiripojana N., 2010, 'Modeling of IT-SOFC with indirect internal reforming operation fueled by methane: Effect of oxygen adding as autothermal reforming', *Int J Hydrogen Energy*, 35, 13271–9.
- [166] De Lorenzo G, Fragiaco P., 2018, 'Electrical and thermal analysis of an intermediate temperature IIR-SOFC system fed by biogas', *Energy Sci Eng*, 6, 60–72.
- [167] Aguiar P, Chadwick D, Kershenbaum L., 2002, 'Modelling of an indirect internal reforming solid oxide fuel cell', *Chem Eng Sci*, 57, 1665–77.
- [168] Majewski AJ, Dhir A., 2016, 'Direct Utilization of Methane in Microtubular-SOFC', *J Electrochem Soc*, 163, F272–7.
- [169] Boder M, Dittmeyer R., 2006, 'Catalytic modification of conventional SOFC anodes with a view to reducing their activity for direct internal reforming of natural gas', *J Power Sources*, 155, 13–22.
- [170] Dokmaingam P, Assabumrungrat S, Soottitantawat A, Laosiripojana N., 2010, 'Modelling of tubular-designed solid oxide fuel cell with indirect internal reforming operation fed by different primary fuels', *J Power Sources*, 195, 69–78.
- [171] Fischer K, Seume JR., 2009, 'Impact of the Temperature Profile on Thermal Stress in a Tubular Solid Oxide Fuel Cell', *J Fuel Cell Sci Technol*, 6, 1–9.

- [172] Fellows R., 1998, 'A novel configuration for direct internal reforming stacks', *J Power Sources*, 71, 281–7.
- [173] Aguiar P, Chadwick D, Kershenbaum L., 2004, 'Effect of methane slippage on an indirect internal reforming solid oxide fuel cell', *Chem Eng Sci*, 59, 87–97.
- [174] Settari A, Lebaal N, Abboudi S., 2018, 'Numerical analysis of catalytic-coated walls of an indirect internal reforming solid oxide fuel cell: Influence of catalyst coating distribution on the reformer efficiency', *Energy Convers Manag*, 176, 357–71.
- [175] Cimino S, Lisi L, Russo G., 2012, 'Effect of sulphur during the catalytic partial oxidation of ethane over Rh and Pt honeycomb catalysts', *Int J Hydrogen Energy*, 37, 10680–9.
- [176] Lee M tsang, Greif R, Grigoropoulos CP, Park HG, Hsu FK., 2007, 'Transport in packed-bed and wall-coated steam-methanol reformers', *J Power Sources*, 166, 194–201.
- [177] Simsek E, Avci AK, Önsan ZI., 2011, 'Investigation of catalyst performance and microstructured reactor configuration for syngas production by methane steam reforming', *Catal Today*, 178, 157–63.
- [178] Karim A, Bravo J, Gorm D, Conant T, Datye A., 2005, 'Comparison of wall-coated and packed-bed reactors for steam reforming of methanol', *Catal Today*, 110, 86–91.
- [179] Kim-Lohsoontorn P, Priyakorn F, Wetwatana U, Laosiripojana N., 2014, 'Modelling of a tubular solid oxide fuel cell with different designs of indirect internal reformer', *J Energy Chem*, 23, 251–63.
- [180] Rodrigues CP, Kraveva E, Ehrich H, Noronha FB., 2016, 'Structured Reactors as an Alternative to Fixed-bed Reactors: Influence of catalyst preparation methodology on the partial oxidation of ethanol', *Catal Today*, 273, 12–24.
- [181] Fazeli A, Behnam M., 2010, 'Hydrogen production in a zigzag and straight catalytic wall coated micro channel reactor by CFD modeling', *Int J Hydrogen Energy*, 35, 9496–503.
- [182] Majewski AJ, Dhir A., 2016, 'Direct Utilization of Methane in Microtubular-SOFC', *J Electrochem Soc*, 163, F272–7.
- [183] Schwiedernoch R, Tischer S, Correa C, Deutschmann O., 2003, 'Experimental and numerical study on the transient behavior of partial oxidation of methane in a catalytic monolith', *Chem Eng Sci*, 58, 633–42.
- [184] Nakajo A, Wullemmin Z, Van herle J, Favrat D., 2009, 'Simulation of thermal stresses in anode-supported solid oxide fuel cell stacks. Part I: Probability of failure of the cells', *J Power Sources*, 193, 203–15.
- [185] Qi D, Lin C, Zhao H, Liu H, Lü T., 2016, 'Size regulation and prediction of the SiO₂ nanoparticles prepared via Stöber process', *J Dispers Sci Technol*, 38, 70–4.

- [186] Atkins P, Overton T, Rourke J, Weller M, Armstrong F., 2010, 'Inorganic Chemistry', fifth ed. *Oxford University Press*, Oxford.
- [187] NPL Training, 2019, 'Measuring the Surface Chemistry of Nanoparticles Using XPS: XPS Peaks', Online training course.
- [188] Thommes M, Kaneko K, Neimark A V., Olivier JP, Rodriguez-Reinoso F, Rouquerol J, et al., 2015, 'Physisorption of gases, with special reference to the evaluation of surface area and pore size distribution', *IUPAC Technical Report*, 87.
- [189] Choudhary V., Mamman A., 1999, 'Oxidative conversion of methane to syngas over NiO/MgO solid solution supported on low surface area catalyst carrier', *Fuel Process Technol*, 60, 203–11.
- [190] Chan SH, Ding OL, Hoang DL., 2004, 'A Thermodynamic View of Partial Oxidation, Steam Reforming, and Autothermal Reforming on Methane', *Int J Green Energy*, 1, 265–78.
- [191] Smith MW, Shekhawat D., 2011, 'Catalytic Partial Oxidation, Fuel Cells Technol. Fuel Process', *Elsevier B.V*, 73–128.
- [192] Chen WH, Lin MR, Lu JJ, Chao Y, Leu TS., 2010, 'Thermodynamic analysis of hydrogen production from methane via autothermal reforming and partial oxidation followed by water gas shift reaction', *Int J Hydrogen Energy*, 35, 11787–97.
- [193] Zhu J, Zhang D, King KD, 2001, 'Reforming of CH₄ by partial oxidation: thermodynamic and kinetic analyses', *Fuel*, 80, 899–905.
- [194] Burgoyne JH, Hirsch H, 1954, 'The Combustion of Methane at High Temperatures', *Proc R Soc Lond A Math Phys Sci*, 227, 73–93.
- [195] Monnerat B, Kiwi-Minsker L, Renken A., 2001, 'Hydrogen production by catalytic cracking of methane over nickel gauze under periodic reactor operation', *Chem Eng Sci*, 56, 633–9.
- [196] Horn R, Williams KA, Degenstein NJ, Bitsch-Larsen A, Dalle Nogare D, Tupy SA, et al., 2007, 'Methane catalytic partial oxidation on autothermal Rh and Pt foam catalysts: Oxidation and reforming zones, transport effects, and approach to thermodynamic equilibrium', *J Catal*, 249, 380–93.
- [197] Kumar S, Kumar S, Prajapati JK., 2009, 'Hydrogen production by partial oxidation of methane: Modeling and simulation', *Int J Hydrogen Energy*, 34, 6655–68.
- [198] Modrow H., 2004, 'Tuning Nanoparticle Properties—The X-ray Absorption Spectroscopic Point of View', *Appl Spectrosc Rev*, 39, 183–290.
- [199] Yang M, Jin P, Fan Y, Huang C, Zhang N, Weng W, et al., 2015, 'Ammonia-assisted synthesis towards a phyllosilicate-derived highly-dispersed and long-lived Ni/SiO₂ catalyst', *Catal Sci Technol*, 5, 5095–9.

- [200] Ocana M, Gonzalez-Elipse A., 1999, 'Preparation and characterization of uniform spherical silica particles coated with Ni and Co compounds', *Colloids Surfaces A Physicochem Eng Asp*, 157, 315–24.
- [201] Yan L, Liu X, Deng J, Fu Y., 2017, 'Molybdenum modified nickel phyllosilicates as a high performance bifunctional catalyst for deoxygenation of methyl palmitate to alkanes under mild conditions', *Green Chem*, 19, 4600–9.
- [202] Rodriguez-Gomez A, Caballero A., 2017, 'Identification of Outer and Inner Nickel Particles in a Mesoporous Support: How the Channels Modify the Reducibility of Ni/SBA-15 Catalysts', *ChemNanoMat*, 3, 94–7.
- [203] Burattin P, Che M, Louis C., 1998, 'Molecular Approach to the Mechanism of Deposition–Precipitation of the Ni(II) Phase on Silica', *J Phys Chem B*, 102, 2722–32.
- [204] Zhao B, Chen Z, Yan X, Ma X, Hao Q., 2017, 'CO Methanation over Ni/SiO₂ Catalyst Prepared by Ammonia Impregnation and Plasma Decomposition', *Top Catal*, 60, 879–89.
- [205] Kim J-H, Suh DJ, Park T-J, Kim K-L., 2000, 'Effect of metal particle size on coking during CO₂ reforming of CH₄ over Ni–alumina aerogel catalysts', *Appl Catal A Gen*, 197, 191–200.
- [206] Burattin P, Che M, Louis C., 1999, 'Metal Particle Size in Ni/SiO₂ Materials Prepared by Deposition–Precipitation: Influence of the Nature of the Ni(II) Phase and of Its Interaction with the Support', *J Phys Chem B*, 103, 6171–8.
- [207] Dahlberg KA, Schwank JW., 2012, 'Synthesis of Ni@SiO₂ Nanotube Particles in a Water-in-Oil Microemulsion Template', *Chem Mater*, 24, 2635–44.
- [208] Hermida L, Abdullah AZ, Mohamed AR., 2018, 'FT-IR and TGA of MCF Silica-Supported Nickel', *Catalyst*, 2508, 2328–33.
- [209] Mile B, Stirling D, Zammitt MA, Lovell A, Webb M., 1988, 'The location of nickel oxide and nickel in silica-supported catalysts: Two forms of "NiO" and the assignment of temperature-programmed reduction profiles', *J Catal*, 114, 217–29.
- [210] Kim Y, Kim J, Ha S, Kwon D, Lee J., 2014, 'Polyimide nanocomposites with functionalized SiO₂ nanoparticles: enhanced processability, thermal and mechanical properties', *RSC Adv*, 4, 43371–7.
- [211] Li Z, Kawi S., 2018, 'Multi-Ni@Ni phyllosilicate hollow sphere for CO₂ reforming of CH₄: Influence of Ni precursors on structure, sintering, and carbon resistance', *Catal Sci Technol*, 8, 1915–22.
- [212] Kong X, Zhu Y, Zheng H, Li X, Zhu Y, Li YW., 2015, 'Ni Nanoparticles Inlaid Nickel Phyllosilicate as a Metal-Acid Bifunctional Catalyst for Low-Temperature Hydrogenolysis Reactions', *ACS Catal*, 5, 5914–20.

- [213] Haga K, Adachi S, Shiratori Y, Itoh K, Sasaki K., 2008, 'Poisoning of SOFC anodes by various fuel impurities', *Solid State Ionics*, 179, 1427–31.
- [214] Turlier P, Praliaud H, Moral P, Martin GA, Recherches D., 1985, 'Influence of the nature of the support on the reducibility and catalytic properties of nickel: evidence for a new type of metal support interaction', *Appl Catal*, 19, 287–300.
- [215] Mo L, Saw ET, Du Y, Borgna A, Ang ML, Kathiraser Y, et al., 2015, 'Highly dispersed supported metal catalysts prepared via in-situ self-assembled core-shell precursor route', *Int J Hydrogen Energy*, 40, 13388–98.
- [216] Louis C, Cheng ZX, Che M. Characterization of Ni/SiO₂ Catalysts during Impregnation and Further Thermal Activation Treatment Leading to Metal Particles. *J Phys Chem* 1993;97:5703–12.
- [217] Bian Z, Kawi S., 2018, 'Sandwich-like silica@Ni@silica multicore-shell catalyst for low temperature dry reforming of methane: confinement effect against carbon formation', *ChemCatChem*, 320–8.
- [218] Nie S, Dong X, Peng C, Li B, Hong N, Hu Y., 2013, 'The growth mechanism of multi-wall carbon nanotubes produced by pyrolyzing polypropylene composite', *J Polym Res*, 20, 4–8.
- [219] Gong J, Tian N, Wen X, Chen X, Liu J, Jiang Z, et al., 2014, 'Synergistic effect of fumed silica with Ni₂O₃ on improving flame retardancy of poly(lactic acid)', *Polym Degrad Stab*, 104, 18–27.
- [220] Li Z, Mo L, Kathiraser Y, Kawi S., 2014, 'Yolk – Satellite – Shell Structured Ni – Yolk @ Ni @ SiO₂ Nanocomposite : Superb Catalyst toward Methane CO₂ Reforming Reaction', *ACS Catal*, 4, 1526–36.
- [221] Lehmann T, Wolff T, Hamel C, Veit P, Garke B, Seidel-morgenstern A., 2012, 'Physico-chemical characterization of Ni / MCM-41 synthesized by a template ion exchange approach', *Microporous Mesoporous Mater*, 151, 113–25.
- [222] Biesinger MC, Payne BP, Grosvenor AP, Lau LWM, Gerson AR, Smart RSC., 2011, 'Resolving surface chemical states in XPS analysis of first row transition metals, oxides and hydroxides: Cr, Mn, Fe, Co and Ni', *Appl Surf Sci*, 257, 2717–30.
- [223] Burattin P, Che M, Louis C., 2000, 'Ni/SiO₂ Materials Prepared by Deposition–Precipitation: Influence of the Reduction Conditions and Mechanism of Formation of Metal Particles', *J Phys Chem B*, 104, 10482–9.
- [224] Zhao Y, Xia C, Jia L, Wang Z, Li H, Yu J, et al., 2013, 'Recent progress on solid oxide fuel cell: Lowering temperature and utilizing non-hydrogen fuels', *Int J Hydrogen Energy*, 38, 16498–517.
- [225] Gorte RJ, Vohs JM, McIntosh S., 2004, 'Recent developments on anodes for direct fuel utilization in SOFC', *Solid State Ionics*, 175, 1–6.

- [226] Cantelo RC., 1956, 'The Thermal Decomposition of Methane', *J Am Chem Soc*, 78, 2042–4.
- [227] Tasker SZ, Standley EA, Jamison TF., 2015, 'Recent Advances in Nickel Catalysis', *Nature*, 509, 299–309.
- [228] Catapan RC, Oliveira AAM, Chen Y, Vlachos DG., 2012, 'DFT study of the water-gas shift reaction and coke formation on Ni(111) and Ni(211) surfaces', *J Phys Chem C*, 116, 20281–91.
- [229] Hong JK, Zhang L, Thompson M, Wei W, Liu K., 2011, 'Effect of Sulfur Poisoning in High Pressure Catalytic Partial Oxidation of Methane over Rh - Ce / Al₂O₃ Catalyst', *Ind. Eng. Chem. Res.*, 1, 4373–80.
- [230] Van Looij F, Geus JW., 1997, 'Nature of the active phase of a nickel catalyst during the partial oxidation of methane to synthesis gas', *J Catal*, 168, 154–63.
- [231] Rashidi H, Ebrahim HA, Dabir B., 2013, 'Reduction kinetics of nickel oxide by methane as reducing agent based on thermogravimetry', *Thermochim Acta*, 561, 41–8.
- [232] Alizadeh R, Jamshidi E, Ale-Ebrahim H., 2007, 'Kinetic study of nickel oxide reduction by methane', *Chem Eng Technol*, 30, 1123–8.
- [233] Poirier MG, Jean G, Poirier MP., 1992, 'Partial Oxidation of Methane over a Praseodymium/Ruthenium Pyrochlore Catalyst', *Stud Surf Sci Catal*, 73, 359–66.
- [234] Dedov AG, Shlyakhtin OA, Loktev AS, Mazo GN, Malyshev SA, Tyumenova SI, et al., 2018, 'Partial oxidation of methane to synthesis gas: Novel catalysts based on neodymium–calcium cobaltate–nickelate complex oxides', *Pet Chem*, 58, 47–51.
- [235] Ghanbarabadi H, Khoshandam B., 2018, 'Controlled synthesis of Nix-Co(1-x) bimetallic nanoparticles using the thermogravimetric method', *Chem Eng Res Des*, 137, 174–85.
- [236] Pu J, Nishikado K, Wang N, Nguyen TT, Maki T, Qian EW., 2018, 'Core-shell nickel catalysts for the steam reforming of acetic acid', *Appl Catal B Environ*, 224, 69–79.
- [237] Song H., 2015, 'Metal Hybrid Nanoparticles for Catalytic Organic and Photochemical Transformations', *Acc Chem Res*, 48, 491–9.
- [238] Cendrowski K, Sikora P, Zielinska B, Horszczaruk E, Mijowska E., 2017, 'Chemical and thermal stability of core-shelled magnetite nanoparticles and solid silica', *Appl Surf Sci* 407, 391–7.
- [239] Chen J, Song W, Xu D., 2018, 'Computational Fluid Dynamics Modeling of the Catalytic Partial Oxidation of Methane in Microchannel Reactors for Synthesis Gas Production', *Processes*, 6, 83.
- [240] Vella LD, Specchia S., 2011, 'Alumina-supported nickel catalysts for catalytic partial oxidation of methane in short-contact time reactors', *Catal Today*, 176, 340–6.

- [241] Christian Enger B, Lødeng R, Holmen A., 2008, 'A review of catalytic partial oxidation of methane to synthesis gas with emphasis on reaction mechanisms over transition metal catalysts', *Appl Catal A Gen*, 346, 1–27.
- [242] Lapszewicz JA, Jiang XZ., 1993, 'Activation of Reactants by Metal Oxide Catalysts - A Key to Selectivity of Oxidative Methane Coupling?', *Prepr Am Chem Soc Div Pet Chem*, 37, 102.
- [243] Pena MA, Gomez JP, Fierro JLG., 1996, 'New catalytic routes for syngas and hydrogen production', *Appl Catal*, 144, 7–57.
- [244] Yan X, Bao J, Zhao B, Yuan C, Hu T., 2017, 'CO Dissociation on Ni / SiO₂: The Formation of Different Carbon Materials', *Top Catal*, 60, 890–7.
- [245] Yan X, Liu C., 2013, 'Effect of the catalyst structure on the formation of carbon nanotubes over Ni / MgO catalyst', *Diam Relat Mater*, 31, 50–7.
- [246] Claridge JB, Green MLH, Tsang SC, York APE, Ashcroft AT, Battle PD., 1993, 'A study of carbon deposition on catalysts during the partial oxidation of methane to synthesis gas', *Catal Letters*, 22, 299–305.
- [247] Anderson JR, Boudart M., 1985, 'Catalysis: Science and Technology', *Springer-Verlag*, Berlin.
- [248] Zhang Y, Xiong G, Sheng S, Yang W., 2000, 'Deactivation studies over NiO/ γ -Al₂O₃ catalysts for partial oxidation of methane to syngas', *Catal Today*, 63, 517–22.
- [249] Zhang Q, Lee I, Joo JIB, Zaera F., 2012, 'Core - Shell Nanostructured Catalysts'.
- [250] Li K., 2007, 'Ceramic Membranes for Separation and Reaction', *John Wiley & Sons Ltd*, London.
- [251] Rabuni MF, Li T, Punmeechao P, Li K., 2018, 'Electrode design for direct-methane micro-tubular solid oxide fuel cell (MT-SOFC)', *J Power Sources*, 384, 287–94.
- [252] Lu X, Li T, Bertei A, Cho JIS, Heenan TMM, Rabuni MF, et al., 2018, 'The application of hierarchical structures in energy devices: New insights into the design of solid oxide fuel cells with enhanced mass transport', *Energy Environ Sci*, 11, 2390–403.
- [253] Li T, Wu Z, Li K., 2014, 'Single-step fabrication and characterisations of triple-layer ceramic hollow fibres for micro-tubular solid oxide fuel cells (SOFCs)', *J Memb Sci*, 449, 1–8.
- [254] Li T, Wu Z, Li K., 2015, 'Co-extrusion of electrolyte/anode functional layer/anode triple-layer ceramic hollow fibres for micro-tubular solid oxide fuel cells-electrochemical performance study', *J Power Sources*, 273, 999–1005.
- [255] Li T, Lu X, Wang B, Wu Z, Li K, Brett DJL, et al., 2017, 'X-ray tomography-assisted study of a phase inversion process in ceramic hollow fiber systems – Towards practical structural design', *J Memb Sci*, 528, 24–33.

- [256] Rodrigues CP, Schmal M., 2011, 'Nickel-alumina washcoating on monoliths for the partial oxidation of ethanol to hydrogen production', *Int J Hydrogen Energy*, 36, 10709–18.
- [257] Rodrigues CP, da Silva VT, Schmal M., 2010, 'Partial oxidation of ethanol over cobalt oxide based cordierite monolith catalyst', *Appl Catal B Environ*, 96, 1–9.
- [258] Benoy T, Wilson D, Lengden M, Armstrong I, Stewart G, Johnstone W., 2017, 'Measurement of CO₂ Concentration and Temperature in an Aero Engine Exhaust Plume Using Wavelength Modulation Spectroscopy', *IEEE Sens J*, 17, 6409–17.
- [259] Lengden M, Cunningham R, Johnstone W., 2013, 'Tunable Diode Laser Based Concentration Measurements of Water Vapour and Methane on a Solid Oxide Fuel Cell', *J Light Technol*, 31, 1354–9.
- [260] Lengden M, Cunningham R, Johnstone W., 2011, 'Tuneable diode laser gas analyser for methane measurements on a large scale solid oxide fuel cell', *J Power Sources*, 196, 8406–8.